HAL
open science

Imagerie sismique haute résolution et quantification des incertitudes : de la zone de subduction au réservoir

Alexandrine Gesret

To cite this version:

Alexandrine Gesret. Imagerie sismique haute résolution et quantification des incertitudes : de la zone de subduction au réservoir. Géophysique [physics.geo-ph]. Sorbonne Universite, 2019. tel-03115009

HAL Id: tel-03115009

https://minesparis-psl.hal.science/tel-03115009

Submitted on 19 Jan 2021

HAL is a multi-disciplinary open access archive for the deposit and dissemination of scientific research documents, whether they are published or not. The documents may come from teaching and research institutions in France or abroad, or from public or private research centers.

L'archive ouverte pluridisciplinaire **HAL**, est destinée au dépôt et à la diffusion de documents scientifiques de niveau recherche, publiés ou non, émanant des établissements d'enseignement et de recherche français ou étrangers, des laboratoires publics ou privés.

Sorbonne Université

Manuscrit

rédigé en vue de la présentation en soutenance

Habilitation à Diriger des Recherches

par

Alexandrine GESRET

MINES ParisTech / Centre de Géosciences

Imagerie sismique haute résolution et quantification des incertitudes : de la zone de subduction au réservoir

Soutenance prévue le jeudi 10 octobre 2019 devant le jury composé de :

M. Jean Virieux	Université Grenoble Alpes	*Rapporteur*
M. Dominique Gibert	Université Rennes I	*Rapporteur*
M. Eric Beucler	Université de Nantes	*Rapporteur*
Mme Hélène Lyon-Caen	Ecole Normale Supérieure	*Examinatrice*
Mme Sylvie Leroy	Sorbonne Université	*Examinatrice*
M. Hervé Chauris	MINES ParisTech	*Examinateur*

Résumé

La quantification des incertitudes est une question primordiale en géophysique. Mes travaux de recherche présentés dans ce manuscrit sont axés sur le développement de méthodologies qui visent à améliorer la fiabilité des résultats et à estimer les incertitudes associées dans le cadre de la localisation des séismes et de l'imagerie sismique du sous-sol. Concernant l'imagerie, deux approches de caractérisation de la structure en profondeur sont considérées : la méthode des fonctions récepteur (sismologie passive) et la tomographie de temps de trajet (sismique active).

La première partie se focalise sur des analyses originales des ondes télésismiques converties de P en S aux interfaces sous les sismomètres. La sensibilité de la réponse en conversion à la fréquence du signal est caractérisée en calculant la réponse en ondelettes pour une couche à faible vitesse. L'application de l'analyse multi-échelle à des données recueillies en Grèce permet de caractériser la nature du toit de la subduction Hellénique sous le Péloponnèse. L'extension de la réponse en ondelettes aux ondes multiples réfléchies à la surface est ensuite présentée. Dans le cas d'interfaces pentées, la réponse des ondes converties est également sensible à l'angle d'incidence du rai. Cette variation de la réponse en fonction de l'incidence est utilisée pour contraindre la géométrie du toit de la subduction Hellénique sous quelques stations.

La deuxième partie se concentre sur la tomographie des temps de trajet, qui vise à estimer le modèle de vitesse de propagation des ondes dans le sous-sol à partir des temps d'arrivée des ondes sismiques pour des tirs actifs (sources connues). Le cadre bayésien est adapté pour quantifier les incertitudes mais avec la contrepartie d'un temps de calcul très élevé dû au grand nombre de simulations requis pour estimer la distribution a posteriori. Des algorithmes efficaces sont présentés pour résoudre le problème direct et le problème inverse. Même avec de tels algorithmes, les approches stochastiques ne peuvent être appliquées qu'avec un nombre restreint de paramètres décrivant le modèle de vitesse. Des paramétrisations parcimonieuses de modèles 1D et 2D sont proposées.

La dernière partie se focalise sur les avancées en termes de formulation de la localisation probabiliste des événements sismiques. Une méthode permettant de propager les incertitudes du modèle de vitesse aux incertitudes de localisation des événements sismiques est introduite. Cette formulation permet d'obtenir des localisations plus précises ainsi que des estimations fiables des incertitudes associées qui prennent en compte les erreurs de pointé et de modèle de vitesse. Dans les approches classiques, seuls les temps des premières arrivées des ondes P et S sont utilisés pour localiser les séismes ; ajouter d'autres types d'information (tels que les temps d'arrivée des ondes réfléchies ou la polarisation des ondes) permet d'améliorer la qualité la localisation et de diminuer l'incertitude de localisation.

Ce manuscrit présente des contributions dédiées à l'amélioration de la résolution et à l'estimation d'incertitudes avec des applications sur des données réelles à différentes échelles. Dans le dernier chapitre, je propose des perspectives qui permettraient d'étendre et de combiner les différentes approches présentées avec une application sur des données recueillies au Laboratoire du Rift de Corinthe.

Abstract

Uncertainty quantification is of primary importance in geophysics. My research activities are mainly dedicated to the development of methodologies to improve reliability and to estimate uncertainties in the context of earthquake location and seismic imaging. Regarding imaging, two approaches dedicated to structural characterization at depth are considered : the receiver function method (passive seismology) and the traveltime tomography (active seismic).

The first part focuses on original analyses of P to S teleseismic converted waves at interfaces beneath seismometers. I present the multiscale analysis in conversion that has been developed to establish and use the frequency dependent response variations in order to constrain the fine nature of the inclusion at the top of the Hellenic slab in Greece. The extension of the wavelet response to backscattered converted waves is also introduced. In case of dipping heterogeneities, the response of the converted waves depends on the incidence angle of the seismic ray. I use this variation of the response in conversion to constrain the geometry of the top of the Hellenic slab beneath a few seismometers.

The second part deals with traveltime tomography that aims to estimate the wave propagation velocity model from observed first arrival times generated by active shots. The bayesian framework is adapted to quantify uncertainties but it requires a long computation time due to the large number of simulations. Efficient algorithms are presented to solve both the forward and the inverse problems. Even with such algorithms, probabilistic approaches can be applied only for a restricted number of parameters describing the velocity model. Original parcimonious 1D and 2D parameterizations are presented.

The third part introduces new formulations of the probabilistic seismic event location. A method that allows to propagate velocity model uncertainties to seismic event location is described. This formulation gives reliable locations with the associated uncertainties that accounts for both picking errors and velocity model uncertainties. In standard approaches, only P and S first arrival times are generally used to locate seismic events ; adding other informations (such as arrival times of reflected waves or wave polarization) allows to improve the quality of event location and to decrease its uncertainty.

This manuscript presents contributions dedicated to improvment of the resolution and to uncertainty estimation with application to real data at different scales. In the last part, I propose perspectives to extend and combine the presented approaches with an application to real data recorded at the Corinth Rift Laboratory.

Remerciements

Mes premiers remerciements vont à Dominique Gibert, sans qui je ne me serais certainement pas orientée vers la géophysique. Un stage à ses côtés, stage encadré également par Stéphanie Gautier, m'a permis de découvrir la géophysique et les ondelettes. Son enthousiasme, son imagination ont très certainement contribué à mon envie de poursuivre en doctorat dans ce domaine. J'ai été particulièrement heureuse que Dominique Gibert me suive en participant ensuite à mon jury de thèse et enfin à ce jury d'HDR. Mon expérience s'est poursuivie durant ma thèse sous la direction d'Alfred Hirn. Je lui serai éternellement reconnaissante de cette formation rigoureuse (parfois très exigeante !) mais au combien passionnante et d'avoir partagé un peu de son immense culture. Un grand merci à Mark Noble qui, lors de mon arrivée à l'Ecole des Mines, a dédié beaucoup de temps à me former sur de nouvelles thématiques et m'a impliquée dans ses projets. De plus, c'est un collègue qui a de grandes qualités scientifiques et humaines avec qui c'est toujours un plaisir de travailler.

Je remercie sincèrement les membres de mon jury pour le temps consacré à évaluer mes travaux, pour leurs retours et surtout d'avoir fait de cette soutenance un moment d'échanges scientifiques passionnants. Je suis très reconnaissante à Eric Beucler pour sa lecture attentive et ses corrections pertinentes, à Sylvie Leroy pour son animation bienveillante de la soutenance, à Hélène Lyon-Caen avec qui j'ai un grand plaisir à travailler, à Jean Virieux pour son animation dynamique et pertinente des débats. Évidemment je remercie très chaleureusement Hervé Chauris qui m'a beaucoup motivée, encouragée et soutenue à passer mon HDR. Merci également pour sa confiance et d'avoir relu la première version de mon mémoire.

Je remercie les collègues de l'équipe de géophysique, Daniela Donno, Pierre Dublanchet et Veronique Lachasse avec qui c'est un plaisir d'échanger et les collègues du Centre de Géosciences, collègues auprès de qui j'ai apprécié de collaborer, une mention particulière à Nicolas Desassis et Thomas Romary pour l'aventure « géophysique stochastique » !

Les travaux introduits dans mon manuscrit n'auraient vu le jour sans les doctorants et étudiants, des personnes très enrichissantes avec qui j'ai beaucoup de plaisir à collaborer : Nidhal Belayouni, Elise Vhi Nu Ba, Jihane Belhadj, Keurfon Luu, Rita Abou Jaoude, Alexis Bottero, Ibrahim Almarouni.

Et je remercie également tous les chercheurs avec qui j'ai collaborés et je collabore, parmi eux, Maria Sachpazi, Maxime Godano, Emmanuel Gaucher, Sthéphanie Gautier, Christel Tiberi, Pierre Sochala, Olivier Le Maitre. Je m'excuse de ne pouvoir citer tous les collègues ici.

Enfin, un incommensurable merci à Benoît pour son soutien et sa patience et à mes filles pour leur aptitude (peut-être inconsciente) à relativiser !

Table des matières

Résumé **i**

Abstract **ii**

Remerciements **iii**

Table des matières **iii**

1 Introduction (contexte et motivations) **1**
1.1 Sismicité et structure dans les zones de subduction 1
1.1.1 Séismes 1
1.1.2 Imagerie sismique 4
1.1.3 Pourquoi les incertitudes ? 6
1.2 Sismicité et structure dans le contexte du monitoring microsismique 8
1.2.1 Séismes induits 8
1.2.2 Pourquoi les incertitudes ? 9

2 Imagerie haute résolution par les ondes télésismiques converties **15**
2.1 Méthode des fonctions récepteur (RF) 15
2.2 Développement d'une analyse multi-échelle des RF 18
2.2.1 Méthodologie : Réponse en ondelettes d'une couche à faible vitesse . . 19
2.2.2 Application : Caractérisation de la nature du toit du slab de la subduction Hellénique 20
2.2.3 Extension aux ondes multiples 21
2.3 Développement d'une analyse multi-azimutale des RF 24
2.3.1 Méthodologie : Réponse en conversion pour différents angles d'incidence 24
2.3.2 Application : Caractérisation de la géométrie du toit du slab de la subduction Hellénique 25
2.4 Sismicité et imagerie haute résolution de la segmentation du slab Hellénique 26
2.5 Conclusion 27

3 Estimation d'incertitudes par tomographie sismique probabiliste **31**
3.1 Méthode de la tomographie des temps de trajet 31
3.2 Développement d'algorithmes pour la résolution du problème direct 33
3.3 Développement d'algorithmes pour la résolution du problème inverse 35
3.3.1 Chaînes de Markov en interaction 35

3.3.2 Optimisation par essaim particulaire compétitive 38
3.4 Nouvelles paramétrisations parcimonieuses du modèle de vitesse 39
3.4.1 Paramétrisation basée sur la décomposition en ondelettes : application à des données réelles acquises dans le contexte du monitoring microsismique 40
3.4.2 Paramétrisation basée sur les cellules de Johnson-Mehl : application à des données synthétiques de sismique réfraction 2D 42
3.5 Conclusions 44

4 Estimation d'incertitudes par localisation probabiliste 47
4.1 Localisation probabiliste standard 47
4.2 Nouvelle formulation prenant en compte l'erreur du modèle de vitesse 48
4.3 Nouvelle formulation prenant en compte les ondes réfléchies 49
4.4 Nouvelle formulation prenant en compte la polarisation des ondes 53
4.5 Conclusions 54

5 Perspectives 55
5.1 Extension de la tomographie probabiliste des temps de trajet 55
5.1.1 Méta-modèles 55
5.1.2 Propagation d'incertitudes 57
5.2 Imagerie haute résolution du rift de Corinthe et quantification d'incertitudes 59
5.2.1 Contexte 59
5.2.2 Résultats préliminaires 60
5.2.3 Caractérisation des interfaces intracrustales 62
5.2.4 Inversion probabiliste des temps et polarités des converties 64
5.3 Conclusion 66

Bibliographie 67

6 Annexes 77
6.1 Curriculum Vitae 77
6.1.1 Expérience professionnelle 77
6.1.2 Formation 77
6.1.3 Enseignements 78
6.1.4 Encadremenent 78
6.1.5 Principaux projets de recherche 78
6.1.6 Autres implications 79
6.1.7 Publications 79
6.1.8 Conférences 80
6.2 Sélection d'articles 84

Chapitre 1

Introduction (contexte et motivations)

Quelle que soit l'échelle concernée, sismicité et structure sont intimement liés, la compréhension des mécanismes de nucléation des séismes nécessite une connaissance des propriétés du milieu (nature et propriétés des roches, présence de fluides,...). Il est donc primordial de caractériser la structure avec une haute résolution et si possible d'estimer l'incertitude associée dans le but de mener des interprétations fiables. Ce chapitre est divisé en deux grandes parties dans lesquelles j'introduis les deux champs d'application dans lesquels j'ai mené la majorité de mes travaux : la zone de subduction et la sismicité induite. Pour ces deux échelles, je tâche de présenter les problématiques qui m'ont menée à développer des approches pour améliorer la résolution et quantifier les incertitudes.

1.1 Sismicité et structure dans les zones de subduction

1.1.1 Séismes

Les zones de subduction sont un sujet de grand intérêt, elles sont responsables de phénomènes tectoniques majeurs (séismes, volcanisme . . .) et relâchent environ 90% de l'énergie sismique (Pacheco and Sykes, 1992). Les subductions résorbent dans le manteau la lithosphère océanique créée aux dorsales. L'interaction entre la lithosphère chevauchante et la lithosphère plongeante puis les modifications mécaniques et de pression-température dans le panneau plongeant (slab) en subduction donnent naissance à des séismes de différentes magnitudes et de différentes natures ainsi qu'à du volcanisme de type arc insulaire ou continental.

La subduction met en contact le toit de la plaque plongeante avec la plaque supérieure le long d'un méga-chevauchement. Le mouvement sur cette faille de grande dimension peut être accommodé par un glissement continu ou par des alternances entre état bloqué et état de glissement. Les grands séismes sont générés lorsqu'une zone de l'interplaque passe brutalement de l'état bloqué (phase intersismique) à la rupture (phase cosismique). Les interfaces de méga-chevauchement sont probablement les seules failles à pouvoir donner lieu à des magnitudes supérieures à 9 tels que les séismes d'Alaska (1964), de Sumatra (2004) ou de Tohoku (2011). Cette zone où nucléée la rupture est la portion sismogénique de la faille (Figure 1.1). La connaissance de la zone sismogénique est importante puisque sa limite la moins profonde peut être l'endroit où la nucléation d'un séisme génère un tsunami alors que sa limite la plus profonde est un facteur important à prendre en compte dans les études de risque sis-

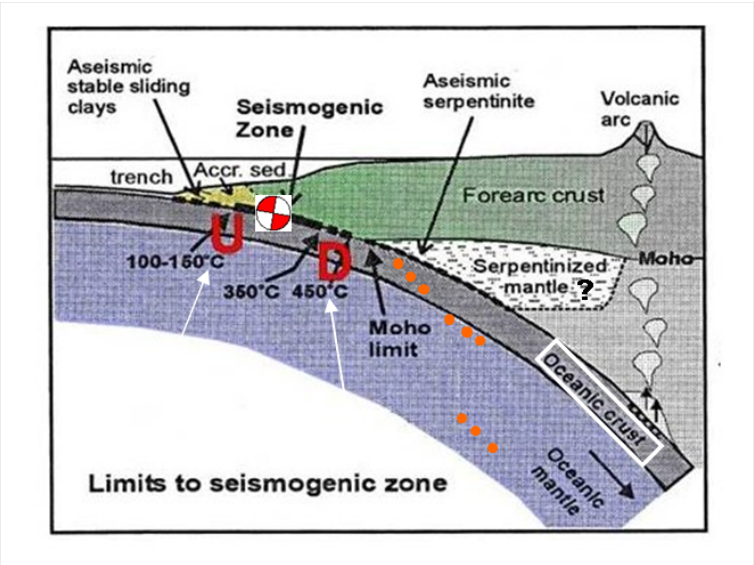

FIGURE 1.1 – Représentation schématique d'une zone de subduction avec limites thermiques et de composition de la zone sismogénique et localisation des séismes de Wadati-Benioff (ronds oranges). D'après Oleskevich et al. (1999).

mique des villes côtières. De plus, l'étendue de la zone sismogénique est étroitement liée à la magnitude maximale des séismes. Des facteurs autres que la température participent au contrôle des limites de la partie sismogénique tels que la nature et les propriétés physiques des matériaux, les hétérogénéités structurales du slab et de la croûte de la plaque supérieure ainsi que les fluides libérés à proximité de l'interplaque. Tous ces paramètres doivent être étudiés et contraints pour évaluer les limites de la zone sismogénique.

Les zones de subduction enregistrent également un autre type de séismes : la sismicité de profondeur intermédiaire (ronds oranges sur la Figure 1.1). Parmi les mécanismes permettant d'expliquer la rupture sismique à des pressions et températures bien plus élevées que pour les conditions normales dans les roches, la déshydratation a été communément considérée comme la principale responsable des séismes de slab (Abers et al., 2013). La libération d'eau à travers des réactions métamorphiques de déshydratation peut fragiliser les roches ("dehydration embrittlement"). Ces fluides peuvent favoriser la rupture sur une faille existante en augmentant la pression de pores ce qui réduit la contrainte normale effective à travers la faille. Ces transformations et les changements associés des propriétés physiques ont été associées à la sismicité de profondeur intermédiaire mais aussi aux trémors et aux séismes lents. Concernant la déshydratation et donc la présence d'eau en profondeur, plusieurs hypothèses existent associées à différentes profondeurs de sismicité (Hacker et al., 2003). La sismicité du plan supérieur de Benioff serait associée à l'éclogitisation des basaltes et gabbros de la croûte océanique (déshydratation des minéraux hydratés) et à la déserpentinisation du manteau supérieur. Quant aux séismes du plan inférieur de Benioff, ils seraient associés à la déserpentinisation du manteau inférieur. La désepentinisation exige une serpentinisation préalable, elle pourrait être due à l'introduction de fluides au niveau des fosses par des failles normales (Peacock, 2001) mais se pose alors le problème de leur pénétration. D'autres hypothèses sont donc proposées pour expliquer le second plan de sismicité telles

que la déflexure du slab ou des instabilités mécaniques périodiques dans des roches anhydres (Reynard et al., 2010). Des zones de déformation plastique suivant des zones de failles à l'endroit où la plaque océanique plongeante se déplie accumuleraient des contraintes qui se relâchent lors des séismes.

Zone de subduction Hellénique

Dans la zone de subduction Hellénique, le domaine Egéen avance vers le Sud-Ouest à une vitesse de 35 mm/an en chevauchant la lithosphère Ionienne de la plaque Africaine (Kahle et al., 2000). La partie Ouest de la zone de subduction Hellénique est complexe car sujette à des variations telles que le taux de convergence, l'occurence de sismicité profonde et d'extension de la plaque chevauchante. Dans la région des îles Ioniennes, la marge active de la subduction se transforme de subduction océanique au Sud à la subduction continentale au Nord (Figure 1.2) relié par la faille de Céphalonie (Anderson and Jackson, 1987).

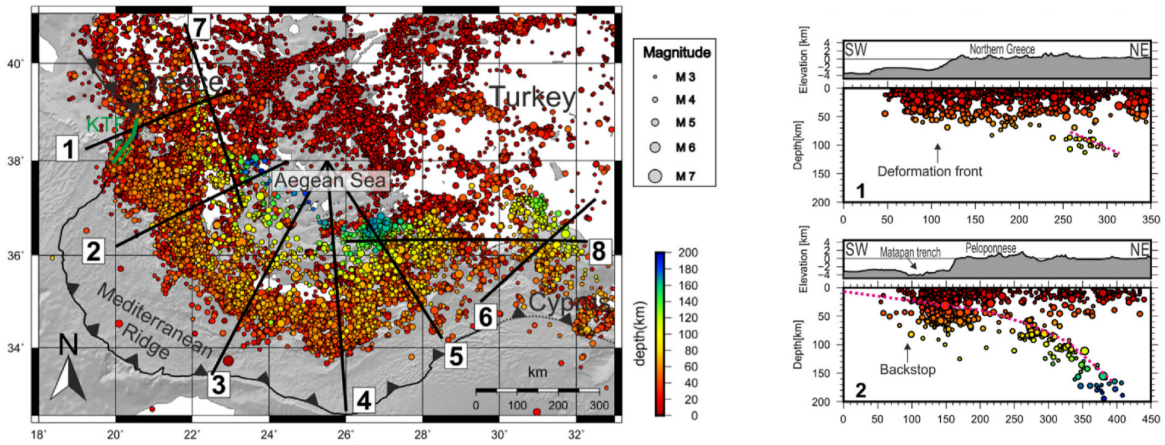

FIGURE 1.2 – Sismicité de l'International Seismological Centre pour la période 1964–2014. Seuls les séismes ayant une erreur inférieure à 10 km sont représentés sur la carte (gauche) et sur les sections (droite). L'échelle de couleur représente la profondeur et la taille correspond à la magnitude. La ligne pointillée indique le toit du slab. D'après Bocchini et al. (2018).

Actuellement c'est dans la zone Hellénique qu'est enregistrée la plus grande sismicité européenne. La zone de subduction Hellénique peut être sujette à des séismes de magnitude 8 comme ceux du 19eme et du 20eme siècle (Wyss and Baer, 1981) mais leurs magnitudes et localisations précises ne sont pas bien connues. Des séismes peu profonds en chevauchement révèlent une interplaque sismogénique active (Laigle et al., 2004). La localisation de ces grands séismes et leur mécanisme indiquent que la subduction Hellénique se poursuit jusqu'au Nord de l'île de Céphalonie. La sismicité en Grèce est caractérisée par de nombreux séismes superficiels (Figure 1.2), mais peu de séismes du slab. La distribution des hypocentres localisés par Papazachos et al. (2000) montrait une zone de Wadati-Benioff diffuse jusqu'à environ 200 km de profondeur. Bocchini et al. (2018) ont récemment localisé un grand nombre d'événements sur une période de 50 ans et ont attribué la terminaison de la sismicité de profondeur intermédiaire au Nord à la transition entre subduction océanique et subduction continentale. Le Golfe de Corinthe se trouve à l'aplomb de la limite d'une zone de Benioff

s'étendant jusqu'à 180 km de profondeur et une zone de Benioff peu active s'étendant jusqu'à 120 km de profondeur (Figure 1.2 droite).

La distribution des séismes ne permet pas d'imager la transition océanique à continentale en profondeur ni de caractériser la structure telle que la nature de la croûte au toit du slab, la caractérisation structurale nécessite donc d'utiliser des méthodes d'imagerie sismique.

1.1.2 Imagerie sismique

Afin de progresser dans la compréhension des séismes liés à la subduction, il est nécessaire de connaître les paramètres qui influent sur la nucléation de ces séismes, d'estimer leur mode de rupture et d'établir où ils se localisent exactement : à la surface ou à l'intérieur de la croûte océanique subduite, au manteau du slab, voire au coin mantellique. Il est donc important de caractériser la structure profonde des plaques et de localiser les fluides et cela de manière fiable. Les approches sismologiques sont un outil puissant pour imager la structure en profondeur. La croûte océanique a une vitesse sismique considérablement moindre que le manteau de l'arc de la plaque continentale et que le manteau de la plaque plongeante qui l'entourent (Hacker et al., 2003). Si une couche à faible vitesse est détectée au toit du slab, cela peut être la croûte océanique qui n'est pas encore éclogitisée (dépend de la température) mais cela peut aussi être une couche de manteau serpentinisé. Un moyen de discriminer entre les deux est de rechercher l'épaisseur de cette inclusion car celle de la croûte océanique est bien contrainte à $7-8$ km (White et al., 2002) ; si l'épaisseur est plus grande, cela ne peut être une simple croûte océanique. Un autre indicateur pertinent est le rapport V_p/V_s. En effet un fort rapport est généralement attribué à la présence de fluides (Audet et al., 2009 ; Audet et Bürgmann, 2014 ; Audet et Schwartz, 2013 ; Peacock et al., 2011) et peut révéler la présence de serpentine. Quelle que soit cette inclusion à faible vitesse au toit du slab, c'est elle qui peut apporter des informations sur la compréhension de la nucléation des séismes profonds et c'est donc elle qu'il faut caractériser.

Parmi les approches d'imagerie sismique, la sismique active (tirs et capteurs en surface) est particulièrement adaptée pour produire des modèles de vitesse de propagation des ondes dans le sous-sol (voir encart).

Objectif : reconstruction du modèle de vitesse $v(x)$

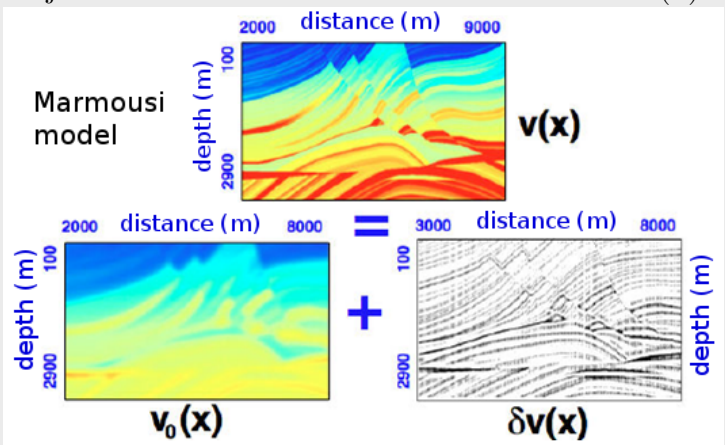

$v_0(x)$: macro-modèle de vitesse (grandes longueurs d'onde) obtenu par tomographie des temps de trajet des ondes transmises

$\delta v(x)$: modèle de réflectivité (petites longueurs d'onde) obtenu par migration
Résolution verticale : $\lambda/4$ à $\lambda/2$ où $\lambda = V_p/f$

La sismique réflexion est très puissante puisqu'elle permet d'imager les réflecteurs avec une

très haute résolution. La sismique a par exemple permis d'imager la partie sismogénique de l'interplaque à environ 15 km de profondeur dans la région des îles Ioniennes (Clément et al., 2000). Cette méthode n'ayant cependant pas une pénétration assez profonde pour permettre d'imager une plaque plongeante à la profondeur où nucléent les séismes de Wadati-Benioff, les méthodes de tomographie passive sont alors préférées. Les études tomographiques ont permis d'imager la zone de subduction Hellénique à des échelles très variées. A de grandes échelles, les tomographies régionales et télésismiques montrent une plaque d'épaisseur d'environ 150 km d'épaisseur (Figure 1.3 gauche) plongeant jusqu'à $1200 - 1400$ km de profondeur (Spakman et al., 1988; Bijwaard and Spakman, 1998; Piromallo and Morelli, 2003).

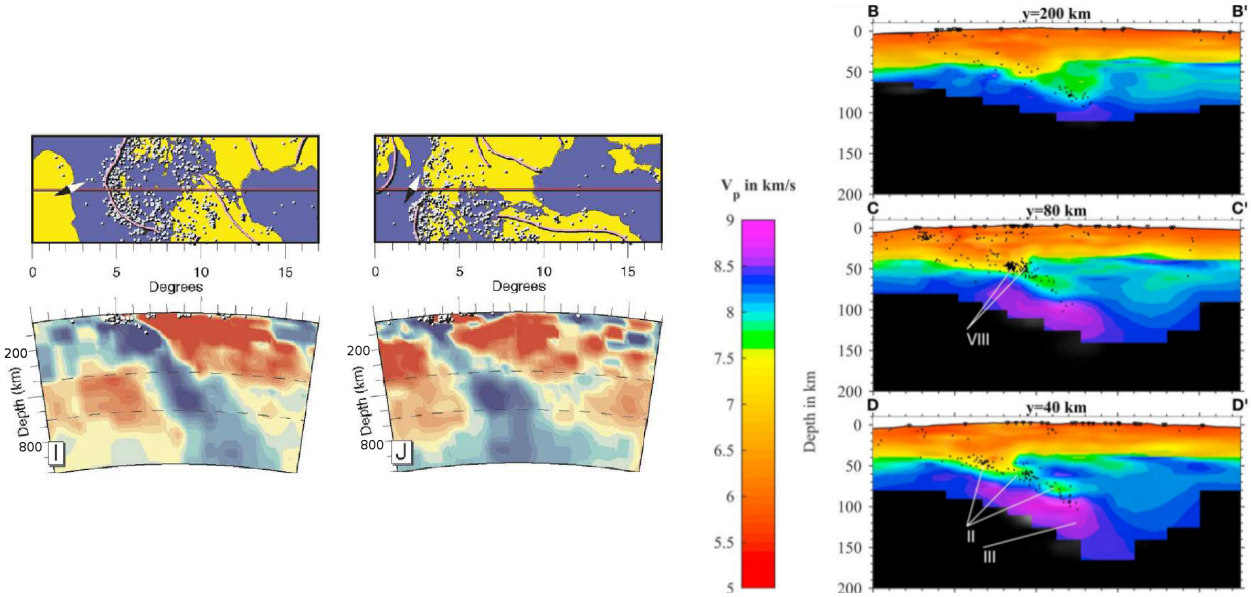

FIGURE 1.3 – Gauche : Images de tomographie globale des anomalies de vitesse P. D'après Bijwaard and Spakman (1998). Droite : Images de tomographie locale des anomalies de vitesse P. D'après Halpaap et al. (2018).

Ces images ont permis de montrer une discontinuité dans les modèles sous l'Ouest de la Grèce, discontinuité interprétée comme une déchirure du slab parallèle à la fosse qui se propage du Nord vers le Sud (Wortel and Spakman, 2000). Cependant la faible résolution de ces approches ne permettent pas de discuter la nature et la géométrie fine du toit du slab. A l'échelle locale, Papazachos and Nolet (1997) identifient le slab jusqu'à 140 km de profondeur avec un changement de pendage de $10°$ à $20 - 30°$ vers 70 km de profondeur cohérent avec la géométrie observée de la zone de Benioff (Papazachos et al., 2000). Cependant le toit du slab correspond ici à une anomalie rapide d'environ $20 - 25$ km d'épaisseur ne permettant pas de résoudre la nature du toit du slab. Récemment Halpaap et al. (2018) ont réalisé une tomographie des séismes locaux en utilisant la sismicité enregistrée par des réseaux permanents et temporaires. Ils ont imagé avec une très haute résolution (Figure 1.3 droite) une couche à faible vitesse $7-7.8$ km/s de pendage $20°$ vers le NE de 40 à 90 km de profondeur au-dessus d'une anomalie positive $8.4 - 8.9$ km/s de 50 à 180 km de profondeur. Cette tomographie permet d'imager une anomalie d'épaisseur inférieure à 10 km dans une zone d'extension de 50 km sur plusieurs coupes verticales orientées dans la direction de pendage du slab Hellénique. Les méthodes de tomographie des séismes, même des séismes locaux,

produisent des anomalies de vitesse par rapport à un modèle de référence qui consistent en des images lisses (voir encart). Elles ne sont donc pas les plus adaptées pour discuter de la nature et de la géométrie fine des hétérogénéités. La croûte océanique peut être caractérisée en analysant les ondes guidées dans cette couche à faible vitesse (e.g., Abers, 2000; Martin et al., 2003) ou par analyse des ondes télésismiques converties (e.g., Yuan et al., 2000; Audet et al., 2009). En effet, cette approche permet de concilier profondeur de pénétration et résolution puisqu'elle permet d'imager les interfaces en profondeur de manière similaire à la sismique réflexion. Cette technique des fonctions récepteur (RF) consiste à isoler les ondes converties aux interfaces sous la station en déconvoluant les composantes radiales des sismogrammes par la composante verticale. Depuis les années 2000, cette technique est très largement utilisée pour imager le toit du slab dans les zones de subduction, les résultats majeurs obtenus à 6 zones de subduction sont repris dans Audet and Kim (2016). De plus cette approche permet également d'investiguer le rapport V_p/V_s ; en effet des rapports élevés entre 1.8 et 2.4 ont été reportés à plusieurs zones de subduction (Audet and Burgmann, 2014) telles que les Cascades (Audet et al., 2009), le Mexique central (Kim et al., 2010), le Costa Rica (Audet and Schwartz, 2013), l'Alaska (Kim et al., 2014) et Nankai (Kodaira et al., 2004).

1.1.3 Pourquoi les incertitudes ?

Deux grands projets d'instrumentation ont été lancés dans la même période dans le but d'imager la subduction Hellénique avec les ondes télésismiques converties : le projet Medusa financé par la NSF avec un premier déploiement d'un profil Sud dans le Péloponnèse suivi du redéploiement des mêmes stations le long d'un profil Nord dans la Grèce continentale (Figure 1.4 gauche). Dans le cadre du projet européen "Thales was right", plusieurs dizaines

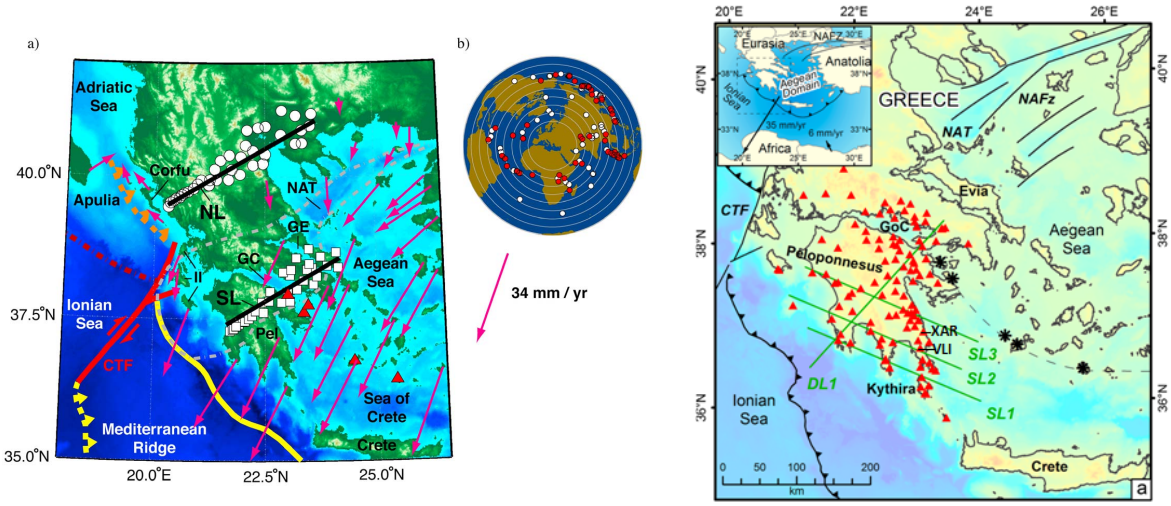

FIGURE 1.4 – Gauche : position des stations (ronds blancs) déployées le long d'un profil Sud puis d'un profil Nord dans le cadre du projet Medusa. D'après Pearce et al. (2012). Droite : position des stations (triangles rouges) déployées dans le cadre du projet européen "Thales was right". Ligne pointillée : arc volcanique, lignes fines noires : continuité de la faille Nord Anatolienne (NAFz) dans la mer Egée, GoC : Golf of Corinth, NAT : North Aegean Trough, CTF : Cephalonia Transform Fault. D'après Sachpazi et al. (2016).

de sismomètres temporaires ont également été déployés, mais cette fois dans une direction plutôt perpendiculaire à la direction de pendage, le long de l'Est du Péloponnèse et au Nord à travers le golfe de Corinthe (triangles rouges de la Figure 1.4 droite). Les travaux présentés dans la section 2 ont été obtenus avec les données recueillies dans le cadre de ce projet.

Le premier résultat d'imagerie des anomalies de vitesse obtenu avec les données télésismiques acquises dans le cadre du projet Medusa (Suckale et al., 2009), filtrées entre 0.03 et 0.03 Hz, montrait une inclusion à faible vitesse épaisse de $15 - 22$ km de pendage $21°$ (Figure 1.5 gauche). La figure du milieu montre une fonction récepteur (RF) unitaire obtenue pour un téléséisme enregistré à la station VLI de l'Observatoire National d'Athènes. Le même filtrage communément utilisé entre 3 et 13 s a été appliqué aux sismogrammes avant de calculer la RF. La RF Q montre clairement vers 6 s un lobe négatif suivi d'un lobe positif correpondant aux ondes converties à une couche à faible vitesse au toit du slab de la subduction Hellénique. L'écart temporel entre ces converties vaut 1.8 s ce qui correspond également à

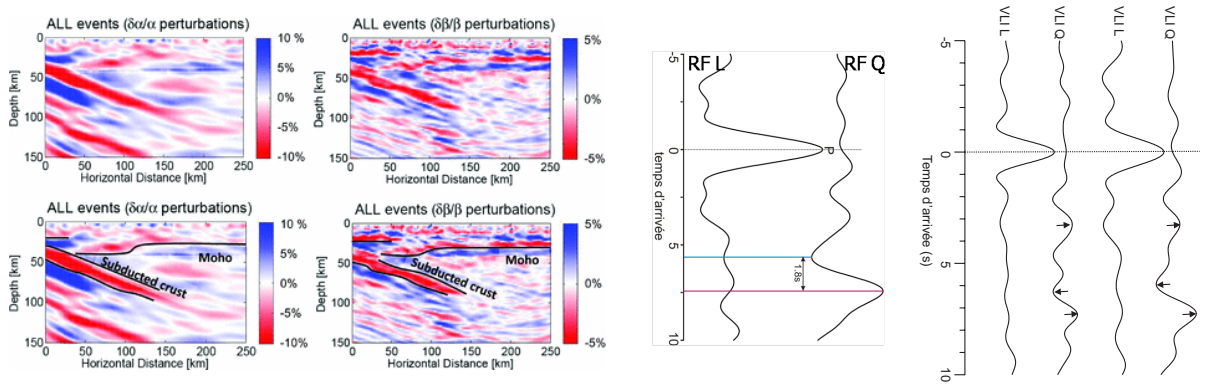

FIGURE 1.5 – A gauche : imagerie des anomalies de vitesse sous le profil Sud du projet Medusa. D'après Suckale et al. (2009). Au milieu et à droite, RF L (contient l'onde P incidente) et Q (contient les converties de P en S) unitaires pour différents filtrages et téléséismes enregistrés à la station VLI de l'Observatoire National d'Athènes. D'après Gesret et al. (2010).

une croûte d'environ 15 km d'épaisseur. Une telle épaisseur peut être interprétée comme une croûte océanique subduite avec une couche de sédiments et possiblement une couche de manteau serpentinisé au-dessus (Suckale et al., 2009) ou comme une subduction de type continental. Sur la figure de droite, sont représentées les RF unitaires pour deux séismes de Honshu de magnitude supérieure à 7 enregistrés à la station VLI, avec cette fois l'application d'un filtre entre 2 et 20 s. Une réponse en conversion sensiblement différente est observée : l'écart entre le lobe négatif et le lobe positif est respectivement d'environ 1.3 s et 1 s. Ceci illustre que le délai en temps entre le lobe négatif et le lobe positif est sensible à la fréquence du signal (selon le filtre appliqué et selon le contenu fréquentiel du téléséime) car ces lobes interfèrent. Ce phénomène implique une interprétation différente en termes d'épaisseur d'inclusion et illustre le risque de sommer des données avec un filtrage commun sans prendre en compte le contenu fréquentiel différent des événements car ce type de traitement peut entrainer une perte de résolution en créant des interférences entre données de différent contenu fréquentiel. En conclusion, les images obtenues par analyse ou migration des ondes converties sont très puissantes puisqu'elles permettent d'imager le Moho de la plaque chevauchante, les croûtes océaniques au toit des slabs, elles donnent même des indices de serpentinisation

et d'éclogitisation. Cependant l'amalgame de tous les téléséismes peut entrainer une perte de résolution, qui elle-même implique une surinterprétation de l'épaisseur et/ou du rapport V_p/V_s. En plus du risque de mauvaise interprétation, les approches globales peuvent masquer des informations sur la structure fine qui doivent pourtant être portées par ces données. Mes contributions se sont focalisées sur des développements méthodologiques visant une très haute résolution, principalement par une analyse fine de données unitaires. Une approche multi-échelle des RF est introduite dans le chapitre 2.2 qui permet d'améliorer la résolution. De la même manière, les analyses globales les plus usuelles ne tirent pas complètement partie de la variation de réponse en conversion due à la présence d'interfaces pentées, une approche multi-azimuthale est présentée dans la section 2.3 qui permet de contraindre précisément la géométrie du toit du slab Hellénique sous quelques stations.

A l'échelle de la zone de subduction, il est clair qu'une erreur dans l'imagerie entrainera une erreur d'interprétation de la sismicité, ce phénomène est tout aussi vrai dans le contexte du monitoring microsismique que j'introduis dans la section suivante bien que la plus petite échelle et la moindre profondeur impliquent généralement une meilleure connaissance de la structure.

1.2 Sismicité et structure dans le contexte du monitoring microsismique

1.2.1 Séismes induits

La sismicité induite regroupe les événements sismiques dont la nucléation n'est pas due à des processus physiques purement tectoniques. Les séismes induits sont des événements déclenchés directement ou indirectement par les activités humaines qui ont modifié le champ de contraintes. Le monitoring microsismique consiste principalement à localiser les événements sismiques générés par des processus de rupture dans les roches fragiles. La distribution spatio-temporelle de la sismicité permet ensuite de surveiller la dynamique de fracturation et d'estimer l'extension des réseaux de fractures ainsi créés (e.g., Phillips et al., 2002; Flewelling et al., 2013). Ce sujet a un fort impact puisqu'il s'applique à plusieurs échelles et dans des domaines très variés : champs géothermiques, exploitation des mines, réservoirs conventionnels et non conventionnels, réinjection des eaux usées, etc... Par exemple, la réinjection d'eaux, co-produites avec l'huile ont généré des milliers d'événements en Oklahoma et conduit à une augmentation considérable du taux de sismicité depuis 2009 (Ellsworth, 2013). Bien que la majorité des événements ait de faible magnitude, certains séismes atteignent des magnitudes supérieures à 5 et nécessitent donc de réévaluer l'aléa sismique dans ces régions. Actuellement les injections de fluide sont couramment utilisées par les industriels dans les secteurs pétroliers et géothermiques qui génèrent d'importantes séquences sismiques. Par exemple, le très grand nombre de microséismes enregistré au site géothermique français de Soultz-sous-Forêts a permis d'imager les failles et fractures majeures du réservoir profond (Sausse et al., 2010) et même de décrire son comportement hydro-mécanique pendant la stimulation (Cornet et al., 2007; Calo et al., 2011). Il est particulièrement important d'avoir des localisations précises car la sismicité induite par l'exploitation est souvent le seul outil disponible afin d'optimiser les méthodes et de maîtriser les risques inhérents à ce type d'exploitation.

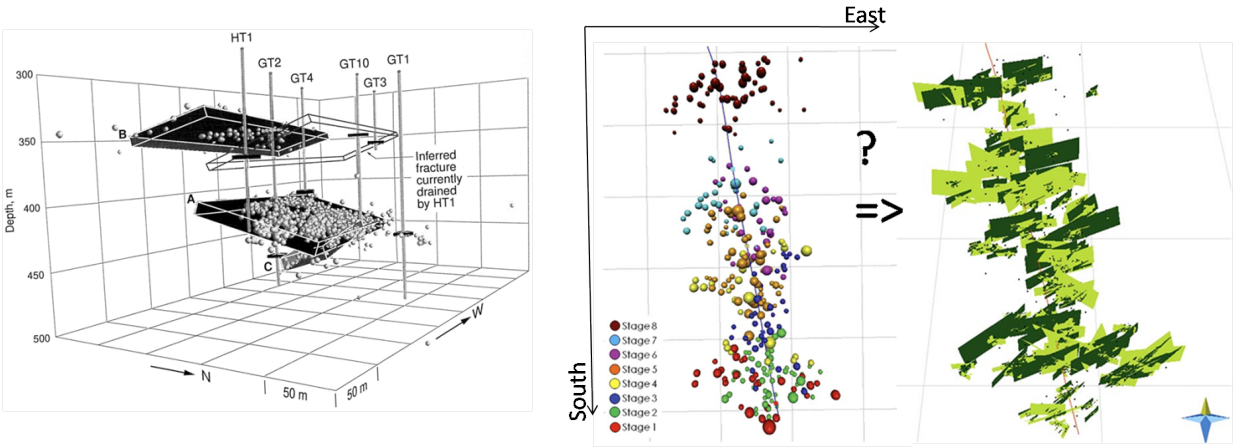

FIGURE 1.6 – Gauche : sismicité révélant les plans de fracture (Clinton County, Kentucky). D'après Rutledge et al. (1998). Droite : sismicité diffuse correspondant à 8 stages de stimulation (Williston Basin) et interprétation proposée avec réseaux de fractures. D'après Williams-Stroud et al. (2013).

La localisation d'un événement sismique consiste à résoudre un simple problème inverse. Connaissant les temps de première arrivée des ondes sismiques enregistrées à un ensemble de capteurs, on cherche à déterminer la position de l'hypocentre. Ceci nécessite d'abord de modéliser les temps de trajet entre une source et des récepteurs pour un modèle de vitesse de propagation des ondes dans le sous-sol donné. La deuxième étape vise à trouver le point de l'espace et le temps origine d'activation de la source qui minimisent l'écart entre ces temps d'arrivée synthétiques et les temps d'arrivée observés aux capteurs. Depuis mon arrivée à MINES ParisTech, j'ai travaillé et sur l'aspect modélisation et sur l'aspect inversion tout en m'attachant à appliquer mes développements méthodologiques dans le cadre de partenariats aussi bien académiques qu'industriels. J'ai travaillé sur des données acquises dans différents contextes tels que la mine ou sur des données acquises dans le contexte de la fracturation hydraulique.

1.2.2 Pourquoi les incertitudes ?

Dans ce contexte, la distribution des séismes est communément utilisée pour délimiter les failles ou les fractures. Dans certains cas, les séismes s'alignent bien et l'intepretation est aisée (Figure 1.6 gauche) mais dans d'autres cas, la sismicité est diffuse (Figure 1.6 droite). Se pose alors la question de savoir si la sismicité définit des plans de fracture ou si les séismes ne sont pas plutôt mal localisés ? Des alignements de sismicité peuvent être aussi dus à des artefacts d'algorithmes de localisation.

Afin d'interpréter cette sismicité de manière fiable, il est donc essentiel d'utiliser des approches qui permettent d'estimer des localisations ainsi que les incertitudes associées de manière fiable. Plusieurs facteurs impliquent des erreurs de localisation : la géométrie du réseau sismologique utilisé pour localiser, les incertitudes sur le pointé, les incertitudes sur le modèle théorique et enfin les incertitudes sur le modèle de vitesse. Le modèle de vitesse de propagation des ondes dans le sous-sol considéré dans la localisation est souvent une approximation de la réalité : méconnaissance de la structure, approximation haute fréquence,

hypothèse isotrope...La non prise en compte des incertitudes du modèle de vitesse est la plus grande source d'erreur de localisation des séismes. Dans le contexte de la fracturation hydraulique, le modèle de vitesse utilisé pour localiser les événements sismiques induits par l'exploitation est généralement un modèle de vitesse à couches. Celui-ci est construit à partir d'un log sonique, puis est calibré par tomographie grâce à des tirs de perforation dont la position est connue (Eisner et al., 2009; Maxwell, 2010). Mes contributions ont essentiellement porté sur l'estimation d'un modèle de vitesse fiable et des incertitudes associées dans le contexte de la tomographie des temps de trajet et sur des estimations de localisation des séismes fiables et de leurs incertitudes.

Tomographie des temps de trajet

La tomographie des temps de trajet est un problème inverse classique de la géophysique visant à estimer le modèle de vitesse de propagation des ondes dans le sous-sol à partir de temps de trajet (des ondes transmises) enregistrés à un ensemble de sismomètres (voir encart). On distingue la tomographie active pour laquelle les positions des sources sont connues de la tomographie passive pour laquelle les sources sont les séismes. Mes travaux portent sur la tomographie active pour laquelle les sources générant les ondes sismiques sont connues. La tomographie se résume alors en un problème d'optimisation numérique où on cherche à estimer le modèle de vitesse qui minimise une fonction coût entre les temps d'arrivée observés et les temps d'arrivée synthétiques générés en résolvant le problème direct. Le plus souvent, ce problème inverse est résolu avec des approches locales de linéarisation itérative qui reposent sur le calcul du gradient de cette fonction coût (e.g., Zelt and Barton, 1998; White, 1989; Day et al., 2001; Taillandier et al., 2009). Cependant ces approches locales peuvent ne pas être robustes dans le cas où la fonction coût n'est pas une fonction lisse avec un minimum global bien défini. Lorque la relation entre le modèle et les données est fortement non linéaire, la surface de la fonction coût a une forme complexe. Elle peut être multimodale avec un minimum global représentant la solution la plus probable et d'autres minima représentant d'autres solutions possibles. Elle peut aussi être plus sensible à certains paramètres du modèle qu'à d'autres et présenter des vallées pour lesquelles la fonction coût varie très peu. La linéarisation fait l'hypothèse d'une solution unique. Pour réduire l'espace des solutions possibles, une procédure de régularisation est appliquée (Menke, 2012). Cela est généralement réalisé en imposant la solution d'être proche d'un modèle initial a priori. Si la solution initiale est trop loin de la solution globale, l'inversion peut être stoppée dans un minimum local ou dans une zone où la fonction coût ne change pas significativement comme illustré pour cet exemple simpliste de tomographie sismique (Figure 1.7). Le vrai modèle de vitesse de propagation des ondes consiste ici en un simple modèle à 2 couches, 6 sources disposées en $X = 0$ m génèrent des ondes qui sont enregistrées à 6 capteurs déployés en $X = 20$ m (Figure 1.7). La profondeur de l'interface étant connue, les deux seuls paramètres à estimer sont donc les vitesses de propagation des ondes dans chacune des couches. Sur la figure de droite, les lignes représentent les valeurs de la fonction coût et les flèches les directions de descente.

Il est clair que la solution estimée par une approche d'optimisation locale basée sur le calcul du gradient de la fonction coût dépendra du modèle initial. Si le modèle initial se trouve en A, une approche locale convergera vers une une solution finale erronée pour la-

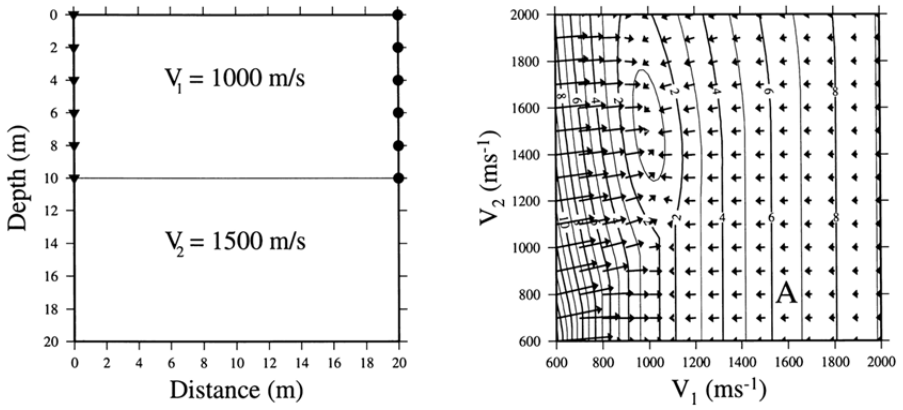

FIGURE 1.7 – Exemple simple de tomographie sismique. Gauche : dispositif d'acquisition et vrai modèle de vitesse. A droite : Isovaleurs de la fonction coût et directions de descente fonction des deux paramètres à inférer. D'après Wéber (2000).

quelle $V_2 = 800$ m/s. On peut tirer deux conclusions de cet exemple très simpliste : d'une part l'intérêt d'utiliser des approches d'optimisation qui ne soient pas sensibles au modèle initial, c'est-à-dire les approches d'optimisation globale. D'autre part, il y a un intérêt à estimer les incertitudes sur les paramètres à inverser. Pour ce petit exemple, on souhaiterait retrouver une incertitude faible sur le paramètre V_1 comparée à celle de V_2. Les approches locales ne sont pas adaptées pour estimer des incertitudes fiables. Rawlinson et al. (2014) font une description complète des méthodes existantes pour estimer les incertitudes et illustrent qu'un échantillonnage probabiliste de la distribution a posteriori dans un cadre bayésien est bien plus adapté. En effet, l'échantillonnage d'importance permet d'échantillonner la fonction coût de manière proportionnelle à la probabilité. Cet échantillonnage est généralement réalisé en utilisant des algorithmes de type Markov Chain Monte Carlo (Mosegaard and Tarantola, 1995; Sambridge and Mosegaard, 2002). L'inconvénient de cet échantillonnage est le coût de calcul requis par le grand nombre de simulations. Mes contributions, décrites dans le chapitre 3 ont principalement porté sur le développement d'algorithmes efficaces de modélisation des temps de trajet et d'inversion et également sur la proposition de paramétrisations parcimonieuses. En effet, le nombre de simulations dépend du nombre de paramètres du modèle à inverser. Les approches probabilistes sont actuellement limitées à $200 - 300$ paramètres. Il est important de souligner que les méthodes locales sont très efficaces et peuvent donc être appliquées à d'immenses jeux de données (milliers de sources et de capteurs) et à des modèles contenant de l'ordre du million de paramètres. Jusqu'ici, mes travaux ne se placent pas dans ce domaine d'applications.

Localisation des séismes

La localisation d'un séisme est également un problème inverse classique qui peut être résolu avec des approches d'optimisation locale telles qu'implémentées dans des softwares toujours largement utilisés (e.g., Lee and Lahr, 1975; Lahr, 1989, 2002). Ces algorithmes visent à retrouver la solution la plus probable qui correspond au minimum de la fonction coût entre les temps d'arrivée (P et S) observés et synthétiques. La localisation souffre des

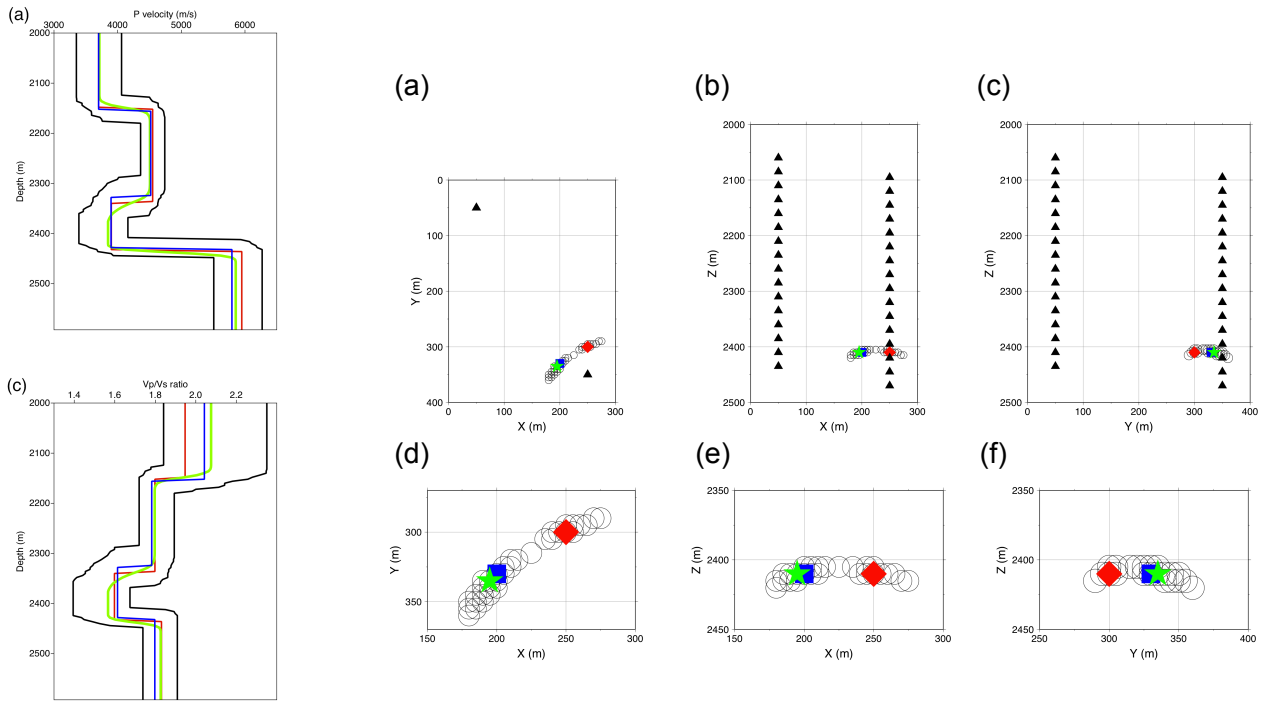

FIGURE 1.8 – Influence du modèle de vitesse sur la localisation d'un séisme enregistré à 32 capteurs (triangles noirs), representée pour les plans XY (a), ZX (b) et ZY (c). Le diamant rouge indique la position du séisme simulé dans le modèle de vitesse rouge P (en haut à gauche) et S (en bas à gauche). Les hypocentres estimés (ronds) sont représentés pour 170 modèles proches du vrai modèle. (d)-(f) Zooms sur les localisations. D'après Gesret et al. (2015).

mêmes inconvénients que la tomographie puisqu'elle produit une solution déterministe qui peut être erronée et l'estimation d'incertitudes se base généralement sur l'hypothèse forte que la fonction coût a un seul minimum et une forme quadratique. La forme de cette fonction coût est particulièrement complexe dans le cas d'une faible courverture du réseau sismologique ou d'un milieu hétérogène. Depuis les travaux de Tarantola and Valette (1982), la formulation probabiliste est souvent préférée (e.g., Moser et al., 1992; Wittlinger et al., 1993; Lomax et al., 2001; Husen et al., 2003) car elle permet de retrouver le minimum global de la fonction coût et d'estimer l'incertitude associée même pour une solution non-linéaire/multimodale. La solution finale n'est plus un seul point mais la fonction de densité de probabilité a posteriori (pdf) de la localisation. Même si la formulation probabiliste est plus fiable, la qualité de l'hypocentre estimé dépend essentiellement de la précision du modèle de vitesse utilisé (Husen and Hardebeck, 2010). Par exemple Kinnaert et al. (2016) ont montré que la sismicité enregistrée à 3 km de profondeur au champ géothermique de Rittershoffen (France) peut être déplacée latéralement de plusieurs centaines de mètres quand une faille locale est introduite dans le modèle de vitesse. Prenons ici un exemple simple avec deux puits dans lesquels sont déployés 2×16 capteurs (Figure 1.8). On simule un séisme (diamant rouge) dans le modèle de vitesse vrai (profils rouges sur la figure de gauche). A partir de ces temps d'arrivée, on localise l'événement dans différents modèles de vitesse. Bien que ces modèles de vitesse soient proches du modèle vrai, certains vont donner des localisations éloignées de plus de 50 m de

la vraie position du séisme. Par exemple les profils de vitesse P et S verts (resp. bleus), pourtant très similaires au modèle de vitesse vrai, donnent une localisation représentée par l'étoile verte (resp. le carré bleu) éloignée du vrai hypocentre. Cet exemple illustre clairement l'importance du modèle de vitesse qui est utilisé dans la localisation. Dans le chapitre 4, je me focaliserai sur des développements méthodologiques qui permettent d'estimer des localisations ainsi que les incertitudes associées qui prennent en compte cette incertitude du modèle de vitesse. Des approches menant à des localisations plus fiables en intégrant plus d'informations seront également introduites dans ce chapitre.

Chapitre 2

Imagerie haute résolution par les ondes télésismiques converties

Ce chapitre reprend les principaux résultats obtenus sur l'imagerie de la zone de subduction Hellénique dans le cadre de collaborations principalement avec Maria Sachapazi de l'Observatoire National d'Athènes, Alfred Hirn de l'Institut de Physique du Globe de Paris et Mireille Laigle de Geoazur. Les approches présentées dans les parties 2.2 et 2.3 visent à utiliser les ondes télésismiques converties pour imager avec une haute résolution la nature des hétérogénéités (Gesret et al., 2010) et leur géométrie (Gesret et al., 2011). Dans la section 2.4, la segmentation du slab imagée par une analyse plus globale des données est succintement présentée (Sachpazi et al., 2016).

2.1 Méthode des fonctions récepteur (RF)

L'objectif de la méthode des fonctions récepteur (RF) est d'imager la structure sous un sismomètre en utilisant les ondes télésismiques converties de P en S aux interfaces. La méthode des RF repose sur un principe simple. Pour des incidences télésismiques, l'onde P est quasi verticale, les ondes converties de P en S aux interfaces sous les sismomètres sont donc enregistrées sur les composantes horizontales. Dans le cas où l'interface est horizontale et les milieux isotropes, l'onde Ps, vibrant dans le plan perpendiculaire à la direction de propagation, est essentiellement visible sur la composante radiale. L'onde Ps étant nettement moins énergétique que l'onde P directe, un traitement est nécessaire pour extraire les ondes converties du signal enregistré. Les effets de source et de trajet du rai peuvent être éliminés en déconvoluant les ondes S de la composante radiale par le signal des ondes P de la composante verticale (voir encart). Préalablement à l'étape de déconvolution, les sismogrammes horizontaux Nord et Est sont tournés dans la direction radiale et tangentielle.

Principe des RF par déconvolution dans le domaine spectral
Les sismogrammes peuvent être considérés comme la convolution d'une fonction source effective $s(t)$ avec la réponse impulsionnelle de la structure locale g :
$z(t) = s(t) * g_z(t)$ où $z(t)$ est la composante verticale
$r(t) = s(t) * g_r(t)$ où $r(t)$ est la composante radiale
La fonction source effective $s(t)$ est la forme d'onde d'un téléséisme qui contient les effets de rupture, la complexité de la région source ainsi que les effets de propagation le long du rai et elle est supposée semblable pour les traces horizontales et verticale. En supposant que le sismogramme vertical est dominé par l'arrivée P, la réponse impulsionnelle radiale peut être retrouvée par déconvolution, en utilisant par exemple la division spectrale :
$G_r(w) \approx \frac{R(w)}{Z(w)}$
Pour éviter des divisions par des valeurs proches de 0, les valeurs trop faibles peuvent être remplacées par une valeur seuil, le "water level".

Les fonctions récepteur ont d'abord été calculées en utilisant la déconvolution dans le domaine spectral (Langston, 1979) puis, dans les années 90, certains groupes ont préféré utiliser la déconvolution par filtre inverse (Kind et al., 1995) basée sur la théorie de Berkhout (1977) ou dans les années 2000, la déconvolution itérative dans le domaine temporel (Ligorria and Ammon, 1999) ainsi que la technique de "Multiple-Taper Spectral Correlation" (Park and Levin, 2000 ; Helffrich, 2005). Ces méthodes constituent les principales approches toujours utilisées bien que certaines équipes cherchent toujours à développer de nouvelles techniques (e.g., Bodin et al., 2014; Dettmer et al., 2015).

Les résultats présentés dans ce manuscrit ont principalement été obtenus en utilisant la déconvolution par filtre inverse du logiciel Seismic Handler développé par Stammler (1993). Cette approche présente l'avantage de se placer dans le repère local du rai du rai P émergent P,Sv,Sh (aussi appelé repère LQT) ce qui apparaît plus adapté pour la déconvolution puisque tout le signal des ondes P est sur la composante L (longitudinale) qui peut alors être déconvoluée des composantes Q et T. De plus, l'avantage d'utiliser la composante Q au lieu de la composante radiale est la disparition de l'énergie de l'onde P incidente sur la RF Sv en $t = 0s$. Ceci permet d'isoler des ondes converties à de très petites profondeurs, qui sont mêlées à l'onde première P et donc difficilement identifiables lorsque les composantes verticale et radiale sont utilisées. Le critère de rotation correcte est respecté si la RF Q s'annule en zéro. Enfin, cette méthode cherche à obtenir l'ondelette à phase nulle, qui représente l'onde P sur la composante L. Cette ondelette nous sera nécessaire pour le prolongement de l'étude lorsque les effets fréquentiels seront étudiés par calcul de RF synthétiques à partir de cette ondelette.

Les RF Q et T résultantes de la déconvolution sont alors constituées de lobes positifs et négatifs qui correspondent aux ondes converties aux différentes interfaces rencontrées par l'onde P (voir schéma 2.1). La RF T sera nulle sauf en cas d'interfaces pentées ou en présence d'anisotropie. Dans le cas d'une interface horizontale, l'amplitude de l'onde Ps dépend à la fois de l'incidence initiale de l'onde P et des caractéristiques des deux milieux de part et d'autre de l'interface : principalement de la vitesse des ondes S mais aussi de la vitesse des ondes P et de la densité. L'expression des coefficients de transmission à une interface implique qu'un lobe positif sur la RF Q indique une augmentation de la vitesse avec la profondeur tandis qu'un lobe négatif indique une diminution de la vitesse avec la profondeur. Le temps d'arrivée de l'onde Ps par rapport à celui de l'onde P transmise est proportionnel à la profondeur de

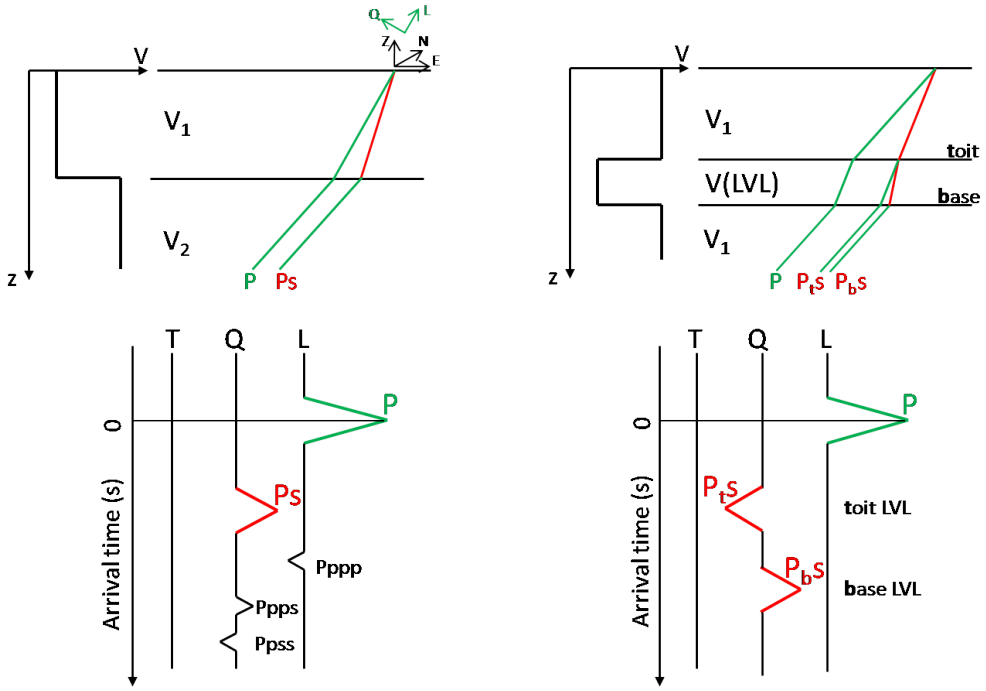

FIGURE 2.1 – À gauche, trajets des rais P et Ps pour pour une interface et RF associées. À droite, trajets des rais P et Ps pour une inclusion à faible vitesse et RF associées.

la discontinuité et à la différence des lenteurs dans la première couche. Il dépend aussi du paramètre de rai de l'onde P. Dans le cas d'une interface pentée, l'amplitude et le temps d'arrivée dépendent aussi de la valeur du pendage de la discontinuité et du backazimut de l'onde P incidente. Une interface sismique produit aussi des multiples d'amplitude significative qui se réverbèrent entre la discontinuité et la surface libre. Les multiples des couches superficielles peuvent parfois rendre difficile l'observation des converties de couches plus profondes en les masquant ou ils peuvent être interprétés comme étant des ondes converties primaires.

Dans le cas d'une couche à faible vitesse horizontale (LVL pour Low Velocity Layer), l'écart théorique τ_1 entre l'onde convertie au toit de la LVL (lobe négatif) et l'onde convertie à la base de la LVL (lobe positif) dépend de l'épaisseur de la LVL d, des vitesses V_p et V_s dans cette couche et du paramètre de rai p, il ne dépend donc pas du milieu au-dessus.

$$\tau_1 = d \times \left(\sqrt{\frac{1}{V_s^2} - p^2} - \sqrt{\frac{1}{V_p^2} - p^2} \right) \tag{2.1}$$

Les caractéristiques des hétérogénéités en profondeur peuvent théoriquement être déduites des RF, sur l'exemple de droite de la figure 2.1, l'écart Δ_1 obtenu en pointant les temps d'arrivée des maxima des lobes négatif et positif de la RFQ sera bien égal au délai théorique τ_1 (équation 2.1). Cependant, lorsque des données réelles sont analysées, la présence de bruit et surtout des interférences entre longueur d'onde du signal et taille de l'hétérogénéité peuvent rendre l'interprétation plus ardue. La section suivante introduit une approche multi-échelle qui permet de bénéficier de la variation de la réponse en conversion fonction de la fréquence

afin de contraindre de manière fiable la nature fine des hétérogénéités en profondeur.

2.2 Développement d'une analyse multi-échelle des RF

Les analyses multi-échelle basées sur des transformées en ondelettes ont été utilisées avec succès dans divers domaines (e.g., Goupillaud et al., 1984; Mallat and Hwang, 1992; Alexandrescu et al., 1995). En effet la transformée en ondelettes permet de caractériser les discontinuités dans un signal. La transformée en ondelettes d'un signal est le résultat de la convolution de ce signal par une famille d'ondelelettes, obtenue en dilatant une ondelette analysante. Pour une fonction homogène $c(\lambda z) = \lambda^\alpha c(z)$ (dont la réponse est homogène à toutes les échelles d'analyse) avec α le degré d'homogénéité de la discontinuité, l'amplitude de la ligne d'extrema de sa transformée en ondelettes suit une loi puissance d'exposant α par rapport à la dilatation de l'ondelette, c'est-à-dire une ligne droite dans un diagrammme $\log_2 - \log_2$ (Mallat and Hwang, 1992). Ceci permet donc d'identifier le degré d'homogénéité de la singularité, $\alpha = 0$ correspondant à une fonction Heaviside, $\alpha = 1$ à une fonction rampe et $\alpha = -1$ à une fonction Dirac. Une extension de la transformée en ondelette est la réponse en ondelettes (Le Gonidec et al., 2002) qui est obtenue en remplaçant l'opérateur de convolution par l'opérateur de propagation. En pratique, ils analysaient dans des expériences de laboratoire les ondes acoustiques réfléchies d'un milieu possédant des variations de vitesse fonction de la prodondeur. Nous avons démontré que la réponse en ondelettes s'appliquait aux ondes converties de P en S en transmission (Gesret et al., 2010). Cette section illustre le potentiel de cette méthode pour caractériser les discontinuités en profondeur par application d'une analyse en ondelettes des RF pour une hétérogénéité multi-échelle (dont la réponse n'est pas homogène à toutes les échelles d'analyse) : une couche à faible vitesse. Ces RF Q synthétiques sont calculées pour une famille d'ondelettes de Ricker sur la RF L. La famille d'ondelettes est aisément construite en faisant varier la dilatation a dans l'équation

$$R(t/a) = (1 - 2\pi^2 f_p^2 (t/a)^2) \exp^{-\pi^2 f_p^2 (t/a)^2} . \tag{2.2}$$

Cette formule fait apparaître la fréquence pic f_p qui correspond au maximum du spectre. Cependant ce n'est pas la seule définition de la période pour une ondelette de Ricker, d'autres définitions sont plus pertinentes lorque les critères de résolvabilité des couches minces sont étudiées (Widess, 1973). On peut en effet utiliser la période centrale T_c qui est égale à deux fois l'écart entre les points d'inflection du lobe central ou la période dominante T_b qui représente la largeur du lobe central de l'ondelette, c'est-à-dire l'écart temporel entre les deux lobes négatifs. C'est cette dernière mesure qui est utile dans la définition des limites de résolution, en effet c'est le rapport adimensionnel T_b/τ ou de manière équivalente λ_b/d qui permettra de définir les domaines de résolvabilité. Dans le cas de la réponse en conversion P en S à deux discontinuités, τ correspond à l'écart théorique en temps entre les converties P en S aux deux discontinuités (équation 2.1).

2.2.1 Méthodologie : Réponse en ondelettes d'une couche à faible vitesse

L'hétérogénéité analysée correspond à une fonction fenêtre. Celle-ci est intéressante puisqu'elle représente une couche à faible vitesse dans un profil de vitesse. Ce type de couche est attendue par exemple au toit des zones de subduction puisque la croûte océanique est incluse entre le manteau de la plaque chevauchante et le manteau de la plaque subduite. La réponse en ondelettes d'une croûte océanique typique de $V_p = 6.5$ km/s, $V_p/V_s = 1.8$ et d'épaisseur 7 km localisée à 60 km de profondeur incluse dans un milieu de vitesse attendue pour du manteau lithosphérique ($V_p = 8$ km/s, $V_p/V_s = 1.75$) est représentée sur la figure 2.2.

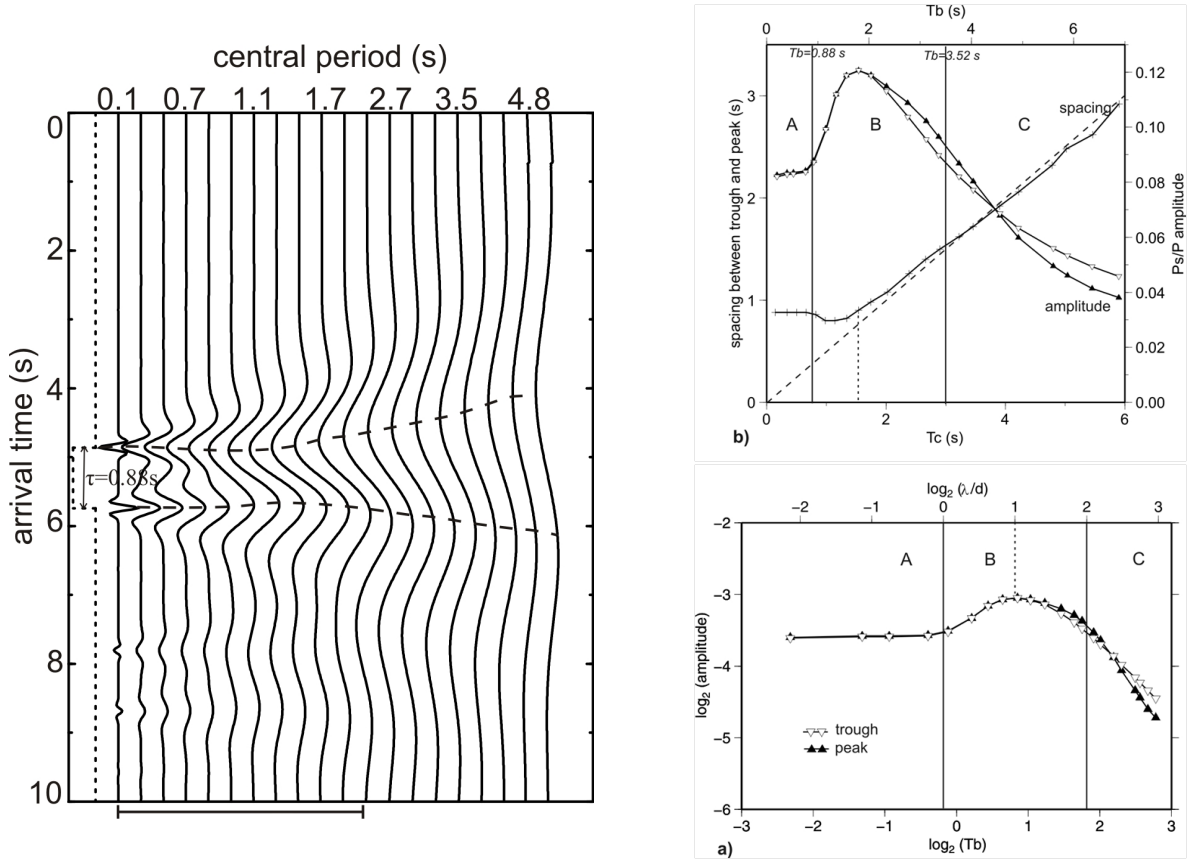

FIGURE 2.2 – À gauche, scalogramme représentant la réponse en conversion d'une LVL à une famille d'ondelettes de Ricker. En haut à droite, évolution de l'amplitude du lobe négatif (triangles inversés blancs) et du lobe positif (triangles noirs) fonction de la période dominante et évolution de l'écart entre ces lobes en fonction de la période centrale. En bas à droite, évolution de l'amplitude des lobes en fonction de la période dominante et du rapport λ/d en diagramme $\log_2 - \log_2$. D'après Gesret et al. (2010).

Il est clair que l'épaisseur apparente d'une couche déduite de l'écart entre lobes Δt dépend de la fréquence du signal. Les amplitudes des lobes négatif et positif ainsi que l'écart entre ces lobes sont mesurés pour les différentes périodes du signal et représentés en fonction de la période dominante et de la période centrale. Trois domaines peuvent être identifiés : (A) le domaine de non-interaction ($\lambda/d = T/\tau < 1$) pour lequel la convertie au toit de la couche et

la convertie à la base de la couche n'interfèrent pas. Chacune de ces interfaces est identifiée comme une discontinuité isolée de Heaviside ($\alpha = 0$ dans le diagramme $\log_2 - \log_2$), l'écart entre les lobes est donc constant. (B) le domaine d'interférences ($1 < \lambda/d = T_b/\tau < 4$) pour lequel les converties interfèrent, l'écart entre les lobes diminue légèrement avant d'augmenter. Le maximum d'amplitudes est atteint pour les interférences constructives pour lesquelles $T_b/\tau = 2$. (C) le domaine des couches minces ($T_b/\tau > 4$), la couche n'est plus résolue et est vue comme une discontinuité de Dirac ($\alpha = -1$ dans le diagramme $\log_2 - \log_2$), l'écart augmente linéairement avec la période centrale du signal.

Cette simulation montre que les caractéristiques d'une LVL ne pourront être déduites de RF que si $\lambda/d = T_b/\tau < 1$. Dans le cas d'une croûte océanique typique, cela implique une période dominante du signal inférieure à $0.88s$ nécessitant des filtrages très haute fréquence, rarement utilisés dans le traitement des RF.

2.2.2 Application : Caractérisation de la nature du toit du slab de la subduction Hellénique

Dans le cadre du projet européen Thales was right des stations sismologiques ont été déployées dans le Péloponnèse (Figure 1.4 droite). La figure 2.3 illustre l'application de l'analyse multi-échelles pour un séisme enregistré à deux stations déployées dans le Péloponnèse. En effet, la méthode de déconvolution par filtre inverse utilisée pour calculer les RF vise à obtenir une ondelette à phase nulle sur la RF L et nous permet donc de calculer la réponse en ondelettes en conversion. Le téléséisme choisi est exceptionnel puisqu'il a nucléé à 600 km de

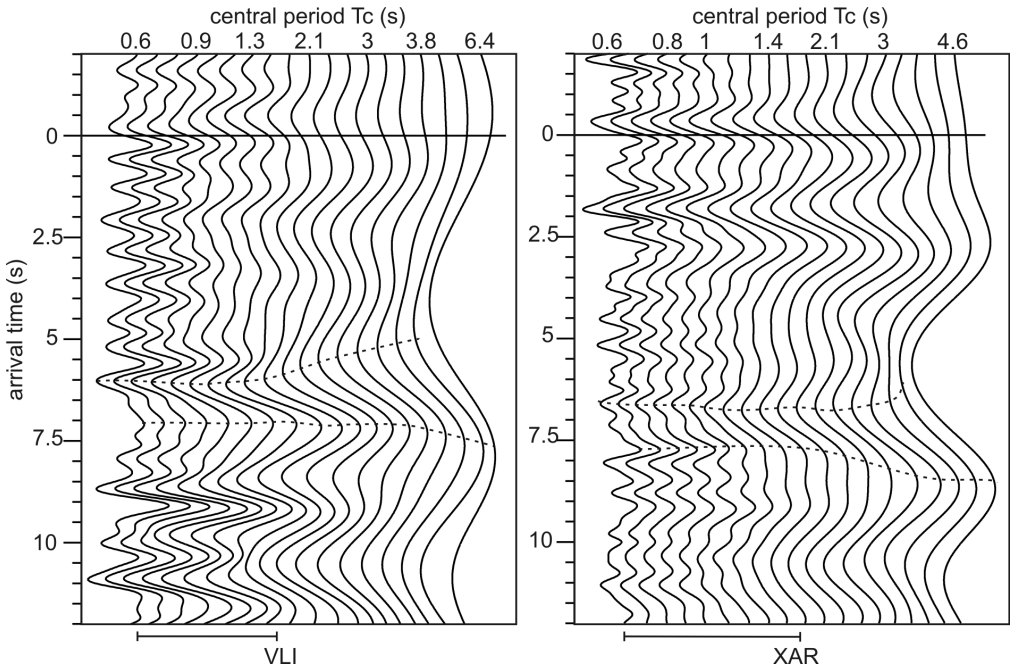

FIGURE 2.3 – Scalogrammes de RF pour les stations VLI et XAR obtenues pour un téléséisme haute fréquence de la mer d'Okhostk à 600 km de profondeur. D'après Gesret et al. (2010).

profondeur et a un contenu très haute fréquence. Dans ce cas de données réelles, la réponse en

ondelettes est obtenue en appliquant des filtres de bande passante croissante. Sur ces scalogrammes, il apparaît que l'épaisseur apparente sera bien inférieure pour les hautes fréquences puisque l'écart entre lobes est alors de l'ordre de la seconde correspondant à une épaisseur d'environ 8 km pour une vitesse de 6.5 km/s et un $V_p/V_s = 1.8$. Dans ce cas, l'analyse multi-échelle a donc permis pour la première fois de prouver que la subduction est bien de type océanique sous le Péloponnèse (Gesret et al., 2010). De plus nous avons également illustré qu'une couche plus épaisse subductait sous le Nord de la Grèce, que nous attribuons à une subduction de type continental. Pearce et al. (2012), en réanalysant les données du profil Sud de Medusa et en ajoutant le profil Nord, ont obtenu des résultats cohérents avec ceux-ci en terme d'épaisseur de croûte.

2.2.3 Extension aux ondes multiples

Le réponse en ondelettes peut également être appliquée aux ondes multiples qui se réfléchissent et se convertissent à la surface libre (voir schéma 2.4). Ces ondes sont très largement utilisées par de nombreuses équipes pour caractériser les toits des zones de subduction et également la limite Lithosphère-Asténosphère.

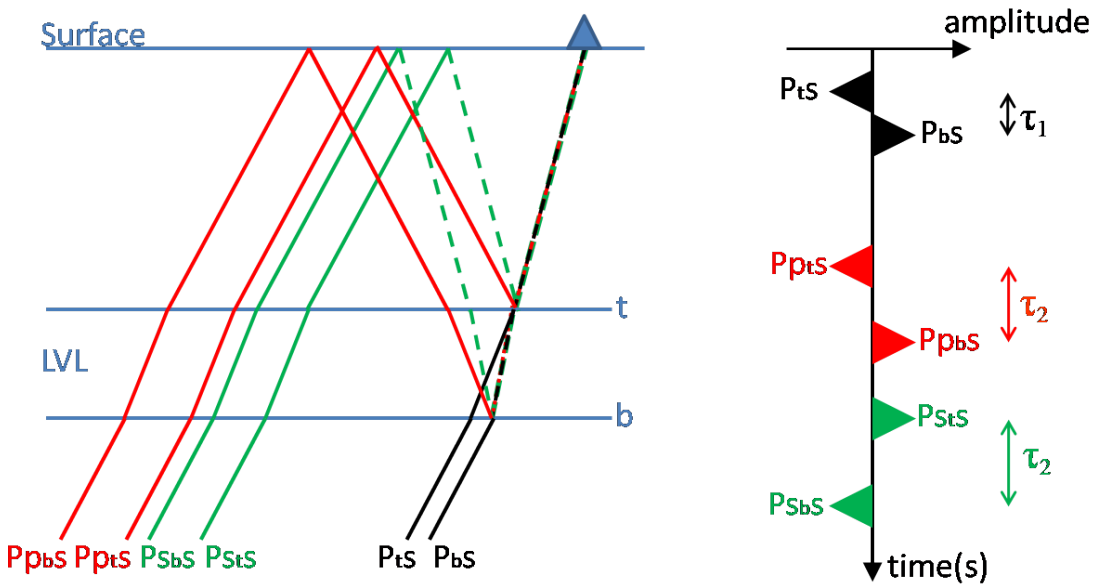

FIGURE 2.4 – Gauche : rais P (traits pleins) et S (traits pointillés) des converties Ps (en noir), des multiples Pps (en rouge) et Pss (en vert) converties au toit (t) et à la base (b) de la LVL. Droite : conversions associées sur la RF Q.

L'avantage de travailler avec la LVL est que les délais entre converties sont indépendants du milieu au-dessus permettant de s'affranchir du problème rencontré lors de la modélisation par exemple pour laquelle les temps à une profondeur donnée sont dépendants des caractéristiques (épaisseur, V_p,V_s) du milieu au-dessus.

$$\begin{aligned} \tau_2 &= d \times \left(\sqrt{\frac{1}{V_s^2} - p^2} + \sqrt{\frac{1}{V_p^2} - p^2} \right), \\ \tau_3 &= 2d \times \left(\sqrt{\frac{1}{V_s^2} - p^2} \right) \end{aligned} \tag{2.3}$$

Il apparaît que $\tau_1 = \tau_3 - \tau_2$, ceci implique que les temps d'arrivée des ondes primaires sont contenues dans les trajets des ondes multiples Pps et Pss. Si clairement identifiées, ces ondes sont donc suffisantes pour investiguer le milieu. Ce point est important car ces ondes sont plus résolvantes comme discuté ci-dessous.

La même approche que dans la section 2.2.1 est suivie. Les RF synthétiques sont calculées pour un modèle de vitesse contenant une LVL d'épaisseur 7 km ($V_p = 6.5$ km/s, $V_p/V_s = 1.8$) à 65 km de profondeur. Ces caractéristiques correspondent à des délais théoriques $\tau_1 = 0.88$ s, $\tau_2 = 2.95$ s et $\tau_3 = 3.83$ s. Le scalogramme est représenté sur la figure 2.5 gauche. Cette

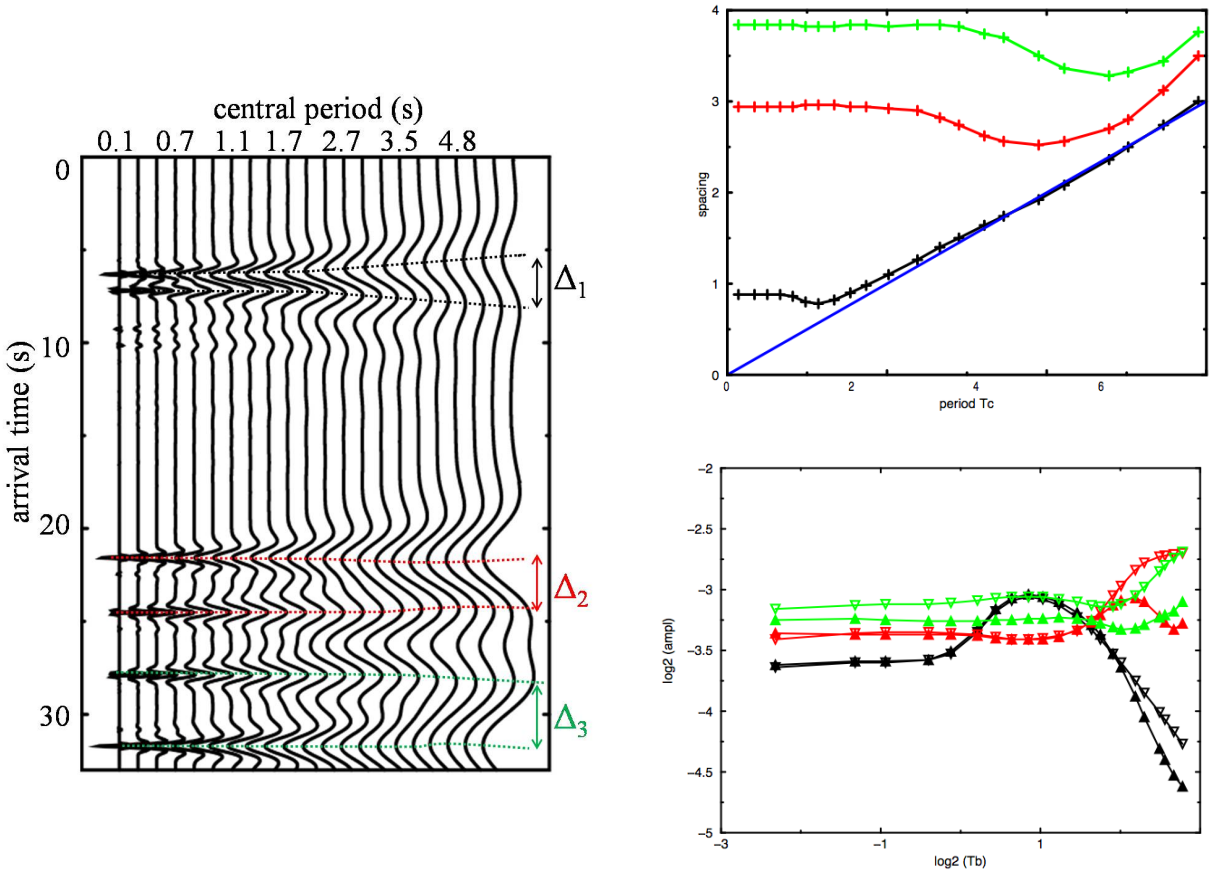

FIGURE 2.5 – À gauche, scalogramme représentant la réponse en conversion d'une LVL à une famille d'ondelettes de Ricker. En haut à droite, évolution de l'écart au toit et à la base de l'inclusion Δ_1 entre les converties Ps (noir), Δ_2 entre les converties Pps (rouge) et Δ_3 entre les converties Pss (vert). En bas à droite, évolution de l'amplitude des lobes négatifs (triangles inversés) et des lobes positifs (triangles à l'endroit) fonction de la période dominante en diagramme $\log_2 - \log_2$ (Gesret et al., in prep.).

figure montre clairement que les temps d'arrivée et amplitudes des 6 ondes sont sensibles

à la fréquence du signal. Afin de quantifier cet effet fréquentiel, l'écart observé entre les converties au toit et à la base de l'inclusion (Δ) est représenté (Figure 2.5 en haut à droite) en fonction de la période centrale pour chaque type d'ondes : Δ_1 pour les Ps (noir), Δ_2 pour les Pps (rouge) et Δ_3 pour les Pss (vert). Les amplitudes sont representées en fonction de la période dominante dans un diagramme $\log_2 - \log_2$ (Figure 2.5 en bas à droite) comme fait classiquement dans les transformées/réponses en ondelettes.

Comme dans le cas des ondes primaires, le domaine de non-interaction est défini pour $T_b/\tau_i < 1$. L'écart entre lobes décroît ensuite avant de réaugmenter. Cependant pour les multiples, le comportement de couche mince pour lequel $\Delta t(T_c) = T_c/2$ n'est pas identifié car les ondes Pps et Pss interfèrent compliquant la réponse. Cette réponse en ondelettes illustre la bien meilleure résolution des ondes multiples, si seules les ondes Pps et Pss sont utilisées, une inclusion typique d'une croûte océanique pourra être caractérisée pour des périodes dominantes du signal d'environ 3 s.

Des auteurs (e.g., Audet et al., 2009) ont estimé le V_p/V_s dans les inclusions au toit des slabs à partir des mesures de rapport d'écart Δ. En effet les rapports τ_2/τ_1, τ_3/τ_1 ou τ_3/τ_2 permettent de faire disparaître l'épaisseur de l'inclusion (équations 2.1 et 2.3), cependant cela nécessite que l'écart Δ soit bien égal au délai théorique τ et donc de se situer dans le domaine de non-interaction. Sur la figure 2.6 est représenté, en fonction de la période dominante du signal, le V_p/V_s qui sera déduit du rapport $\Delta_2(Pps)/\Delta_1(Ps)$ (gauche), du rapport $\Delta_3(Pss)/\Delta_1(Ps)$ (milieu) et du rapport $\Delta_3(Pss)/\Delta_2(Pps)$ (droite). Le V_p/V_s est

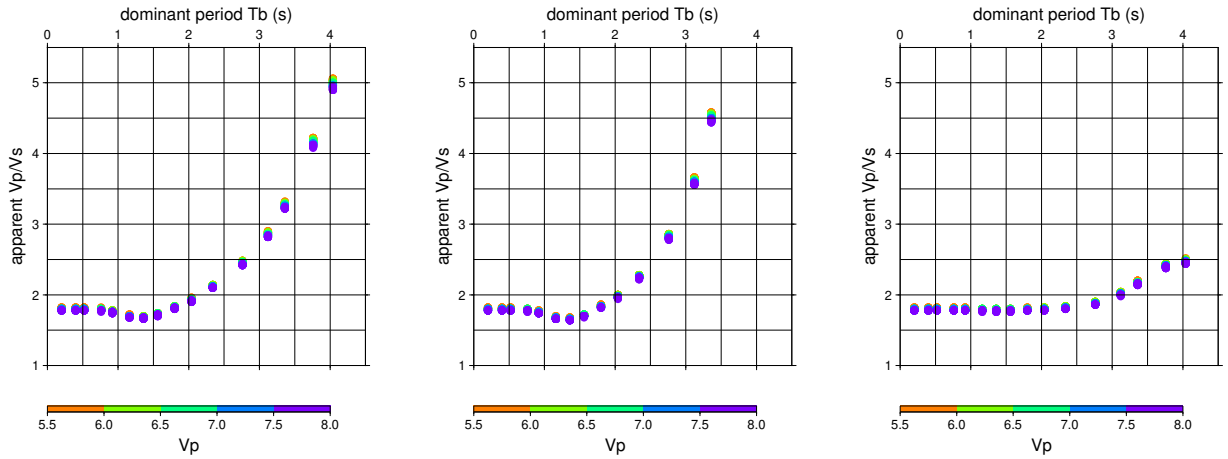

FIGURE 2.6 – V_p/V_s déduit des rapports d'écarts mesurés entre converties en fonction de la période dominante. A gauche, pour le rapport $\Delta_2(Pps)/\Delta_1(Ps)$, au milieu pour le rapport $\Delta_3(Pss)/\Delta_1(Ps)$ et à droite, pour le rapport $\Delta_3(Pss)/\Delta_2(Pps)$. L'échelle de couleur indique le V_p considéré (Gesret et al., prep).

presque insensible au V_p considéré. Il est clair que le V_p/V_s estimé de $\Delta 2(Pps)/\Delta 1(Ps)$ ou de $\Delta 3(Pss)/\Delta 1(Ps)$ sera en erreur dès que la période est supérieure à 0.9 s. Il sera légèrement inférieur à la vraie valeur (jusque 1.66) pour des périodes $0.9 < T_b < 1.8$ s puis il augmente extrêmement rapidement pour des périodes $T_b > 1.8$ s. Cette analyse prouve le risque de surestimation du V_p/V_s à partir des rapports d'écart et pourrait expliquer que des V_p/V_s extrêmement grands aient parfois été estimés dans certaines subductions. Pour contraindre de manière fiable ce rapport, soit seules les ondes multiples doivent être utilisées

mais les ondes Pss ne sont pas souvent aisément identifiables, soit les données doivent être regardées à des périodes inférieures à 1 s impliquant des filtrages très haute fréquence qui, à ma connaissance, ne sont pas communément utilisés. En revanche, si les fréquences de signal utilisé correspondent bien au domaine de non-interaction, le rapport des écarts est un excellent moyen pour contraindre le rapport V_p/V_s. La prochaine étape sera d'appliquer cette approche multi-échelle des ondes primaires et multiples pour le cas de données réelles, cette perspective est détaillée dans la section 5.2.

Les RF ne sont pas seulement sensibles aux interférences dues à la fréquence du signal, elles sont également sensibles à l'incidence du rai télésismique, en particulier dans le cas d'interfaces pentées. Les données doivent donc être regardées avec attention lorsque les origines des sources sont différentes, j'introduis dans la section suivante une approche qui permet de bénéficier de cette variation de réponse.

2.3 Développement d'une analyse multi-azimutale des RF

Les ondes converties de P en S aux interfaces pentées montrent des variations de polarité et de temps d'arrivées qui sont fonction du backazimut et de l'angle d'incidence du rai P par rapport à la direction et à la valeur du pendage. Si la majorité des interprétations des RF reposent sur une hypothèse de milieu 1D, plusieurs études datant du début de l'application de la technique des RF ont utilisé ces propriétés de variations pour contraindre des géométries d'interface pentée (Langston, 1977; Owens et al., 1988; Lapp et al., 1990; Cassidy, 1992; Baker et al., 1996).

2.3.1 Méthodologie : Réponse en conversion pour différents angles d'incidence

Les interfaces pentées dévient les ondes P et S du plan de propagation vertical P-Sv, c'est pourquoi de l'énergie est observée sur la composante tangentielle. Dans le cas d'une interface isolée, l'onde P directe aura de l'énergie sur la composante T contrairement au cas d'une inclusion, pour laquelle l'onde P retrouve l'azimut et l'angle d'incidence qu'elle avait dessous.

La majorité des auteurs a considéré des variations liées aux backazimuts différents. Par exemple, la variation de temps d'arrivée pour une incidence donnée aura un comportement symétrique par rapport à la direction updip-downdip avec des temps d'arrivée plus grands observés pour la direction de propagation updip. De la même manière, pour un angle d'incidence donné, les amplitudes des RF T sont antisymétriques par rapport à la direction updip-downdip. Cela signifie que la direction de pendage d'une discontinuité peut être contrainte si une inversion de polarité sur la composante T est observée. Cependant l'interprétation des RF peut être rendue plus ardue car des variations notables peuvent aussi émerger dues à des variations d'angle d'incidence (donc de distance épicentrale). Par exemple, si l'angle d'incidence est inférieur à la valeur de pendage, il y aura une inversion de polarité de la RF Q pour les téléséismes ayant des azimuts downdip (Figure 2.7).

L'interprétation des signaux est aussi complexifiée si les polarités sont analysées sur la composante T, en effet les polarités peuvent être opposées pour un même backazimut et un

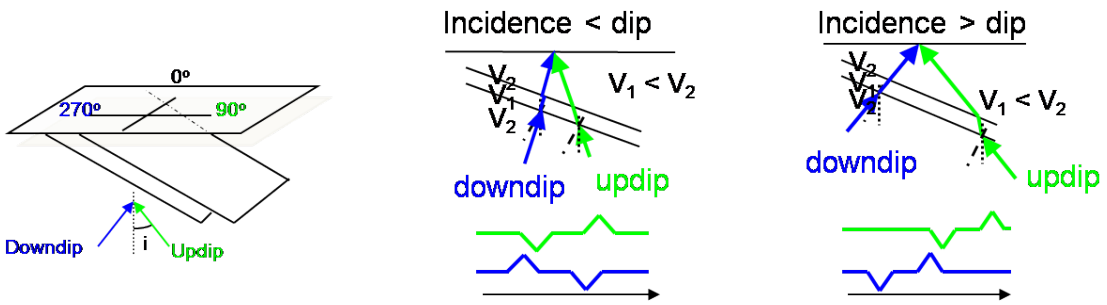

FIGURE 2.7 – Représentation schématique de la variation de réponse d'une LVL en termes de temps d'arrivée et de polarité sur la RF Q pour différents angles d'incidence et différents backazimuts.

angle d'incidence différent (Figure 2.8).

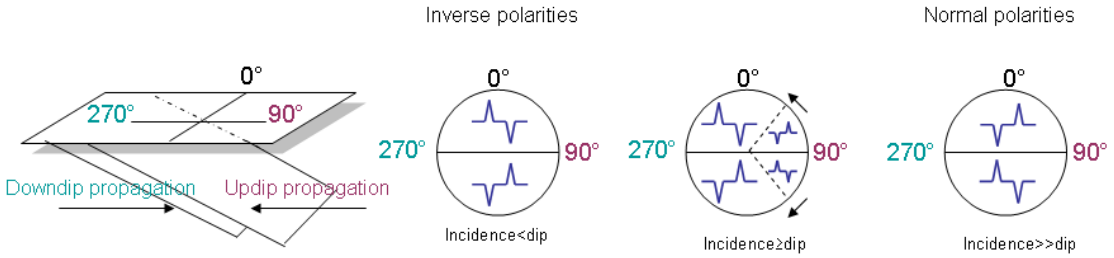

FIGURE 2.8 – Représentation schématique de la variation de réponse d'une LVL en termes de polarité sur la RF T pour différents angles d'incidence et différents backazimuts.

Un pendage ne peut donc être contraint en regardant seulement les variations fonction du backazimut. Ces variations impliquent que les RF ne doivent pas être sommées si elles ont des incidences différentes même si elles ont même backazimut car la correction de moveout devrait être différente de celle du milieu 1D ; en effet, le signal sera élargi par manque de cohérence des temps d'arrivée. De plus, la conversion peut même être masquée en cas de sommation de signaux ayant des polarités opposées dues à des angles d'incidence différents.

La complexité de la réponse dans le cas d'hétérogénéités pentées ne permet pas d'interpréter les données de manière évidente. Cependant cette variété implique une grande richesse d'informations portée par les données qui sera exploitée dans la section suivante pour contraindre la géométrie du toit de la subduction Hellénique. En effet, la diversité des sources enregistrées à quelques stations permet de rechercher les paramètres de pendage qui produisent des temps et polarités synthétiques ajustant au mieux les observations.

2.3.2 Application : Caractérisation de la géométrie du toit du slab de la subduction Hellénique

Dans la section 2.2.2, j'ai illustré que des interfaces séparées de moins de 10 km peuvent être résolues par la méthode des RF et qu'une fine couche à faible vitesse typique d'une

croûte océanique a pu être contrainte pour la première fois sous le Péloponnèse en utilisant la variation de la réponse en fonction de la fréquence du signal (Gesret et al., 2010). Cette section s'intéresse à la possibilité de contraindre la géométrie de cette inclusion en utilisant cette fois la variation de réponse en fonction de l'incidence du rai P. Certains sismomètres déployés dans le cadre du projet Thales was right ont été installés assez longtemps pour obtenir une bonne couverture azimutale et de distance épicentrale. Les RF obtenues montrent des variations claires en termes de temps d'arrivée et de polarités (Figure 2.9 en haut à gauche).

L'approche proposée consiste à trouver les trois paramètres (valeur et direction de pendage, profondeur) produisant des polarités et temps synthétiques ajustant au mieux les observations. Une exploration de l'espace des trois paramètres permet de contraindre la profondeur du slab sous la station VLI à 54 km de profondeur, une direction de pendage de $N35°E$ et une valeur de pendage de 16°. Ces valeurs des paramètres correspondent au misfit minimum entre polarités synthétiques et polarités observées et au misfit minimum entre temps d'arrivée synthétiques et temps d'arrivée observés pour l'ensemble des 44 téléséismes. Les vrais points de conversion sont calculés pour ce modèle ainsi que les résidus associés à chaque observation. Ces résidus montrent une bonne répartition des résidus autour de zéro.

La même approche appliquée à 2 stations déployées dans le Péloponnèse donne des résultats similaires c'est-à-dire des valeurs de pendage entre 16° et 18° dans une direction comprise entre $N20°E$ et $N40°E$ (Gesret et al., 2011). Ces valeurs sont cohérentes avec les valeurs de profondeur de slab contraintes sous chacun des capteurs. Nous avons également échantillonné un segment de slab peu profond (52 km) au Nord du golfe de Corinthe et d'Evvia, cette faible profondeur indique que ce slab n'est pas en continuité avec le slab du Péloponnèse, puisque ces stations du Nord sont bien plus loin de la limite de subduction. A ces stations, une épaisseur plus grande de couche au toit du slab a également été estimée, cohérente avec une nature continentale du toit du slab. Une plus grande flottabilité associée serait en accord avec une profondeur et un pendage plus faible que ceux observés au Sud du Golfe de Corinthe. Ces variations en profondeur du slab sont cohérentes avec une déchirure de slab associée à des phénomènes de surface tels que l'amincissement de la croûte Egéenne (Sachpazi et al., 2007) et à une zone de déformation de surface (Papanikolaou and Royden, 2007).

Cette méthode pourrait être étendue en estimant les incertitudes associées, cette perspective sera détaillée dans la section 5.2.

2.4 Sismicité et imagerie haute résolution de la segmentation du slab Hellénique

Dans les deux sections précédentes, les analyses étaient focalisées sur quelques stations. Nous nous intéressons ici à l'imagerie plus globale de la zone de subduction Hellénique.

Dans le cadre d'une collaboration avec Maria Sachpazi de l'Observatoire National d'Athènes, nous avons imagé la structure sous le Sud de la Grèce en calculant les RF sous environ 100 stations (Sachpazi et al., 2016). L'utilisation de RF haute fréquence et surtout la densité de ce réseau a permis de résoudre une topographie complexe du toit du slab. En effet les images obtenues le long de sections verticales perpendiculaires à la direction de subduction montrent que le toit du slab est discontinu. Il est segmenté depuis le Golfe de Corinthe jusqu'au Sud

de l'île de Kythira en panneaux plongeants vers l'E-SE de largeur de $30 - 50$ km qui sont séparés par 9 failles (Figure 2.10). Le séisme d'interplaque de Methoni du 14/02/2008 de M_W 6.8 a nucléé dans la prolongation en mer de la faille F6 et ces répliques principales (ronds noirs) délimitent une zone de rupture coïncidente avec le panneau entre les failles F6 et F7. Ce panneau pourrait aussi délimiter la zone d'un grand tremblement de terre de 1867 (Wyss and Baer, 1981). Les zones de rupture des séismes d'interplaque de 1886 et 1903 pourraient aussi être délimitées par les failles. Les magnitudes de ces événements ont été réévaluées à la baisse à environ 7 (Papadopoulos et al., 2014), les longueurs de rupture associées correpondraient à la taille des panneaux. La segmentation du slab semble donc contrôler la taille et la localisation des séimes de chevauchement d'interplaque.

Les failles concentrent également la majorité de la sismicité mineure à modérée occurant à $60 - 80$ km de profondeur. La qualité des localisations permise par le réseau dense temporaire et permanent permet d'affirmer que la majorité de ces séismes a lieu au sein de la croûte du slab (carrés roses). Nous associons cette sismicité à de la déshydratation car ces séismes ont lieu au niveau des failles qui ont certainement pu être hydratées quand elles étaient en mer.

Enfin, les séismses d'Argos (M_W 5.0 du 18/06/08), de Leonidio (M_W 6.4 du 06/01/08) et de Kythira (M_W 6.7 du 08/01/06) sont localisés sur les failles F6, F7 et dans le prolongement de F9. Ces séismes seraient donc associés à la segmentation du slab.

2.5 Conclusion

L'analyse multi-azimutale est un premier pas vers les les incertitudes puisqu'elle vise à trouver le misfit minimum par grid search de l'espace des paramètres. En effet, il suffirait de transformer ce misfit en vraisemblance, gaussienne par exemple (si l'on suppose que les erreurs de mesure suivent une distribution gaussienne) et de considérer l'information a priori sous forme de densité de probabilité, pour estimer l'incertitude sur les paramètres que l'on cherche à inférer. J'introduis dans le chapitre suivant cette formulation probabiliste appliquée à la tomographie des temps de trajet. Dans la section 5.2 des perspectives, je détaillerai une formulation permettant d'étendre l'analyse multi-azimutale à une inversion probabiliste pour estimer les incertitudes associées aux paramètres de géométrie d'une hétérogénéité. Je proposerai également une approche qui exploite l'analyse en ondelettes pour déterminer le type des hétérogénéités (interface, gradient,...) en profondeur.

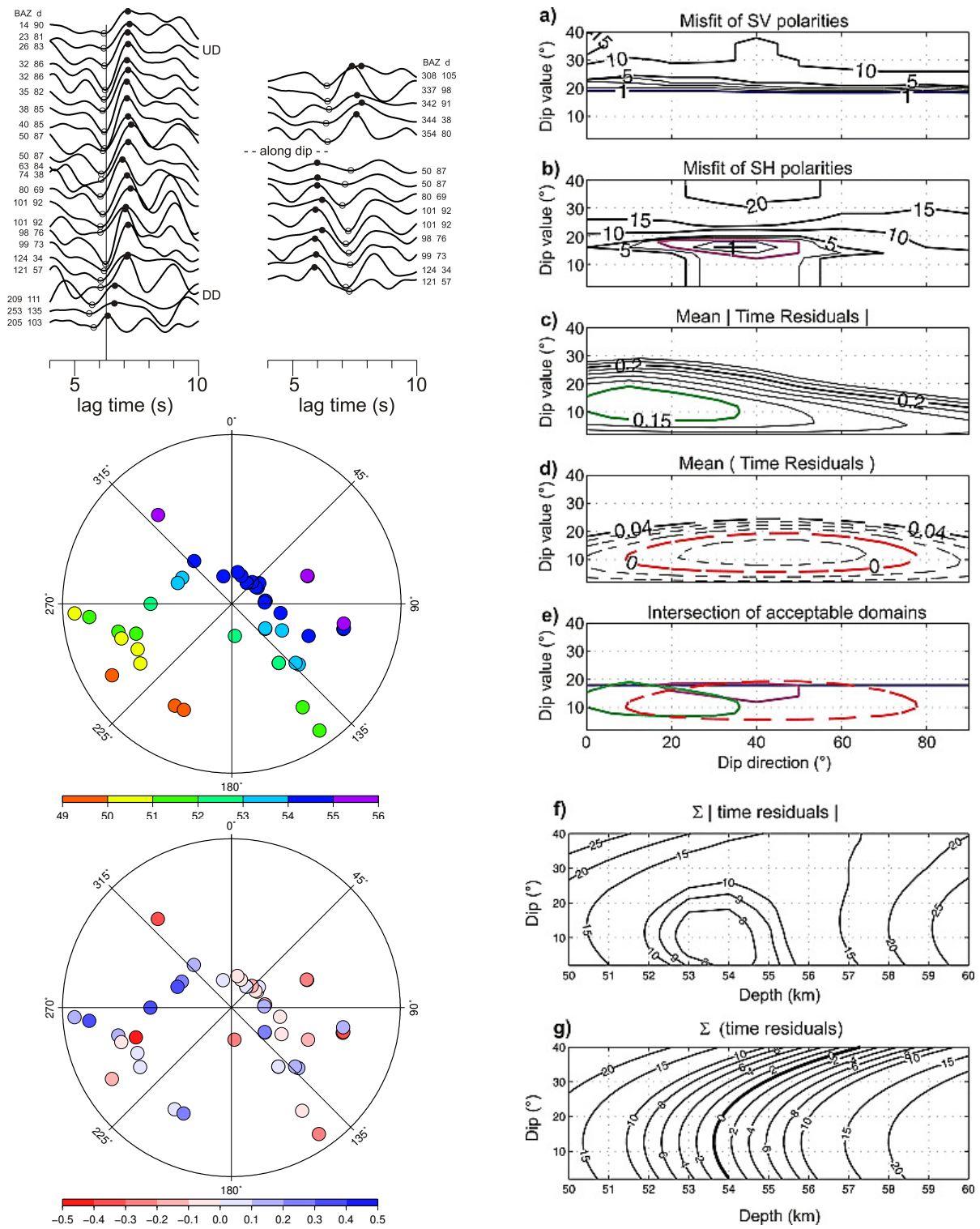

FIGURE 2.9 – En haut à gauche, observations des RF Q et T pour quelques téléséismes enregistrés à la station VLI. A droite, représentation des différences entre observations et synthétiques pour différentes valeurs des paramètres à inférer. A gauche, au milieu, points de conversion pour le meilleur modèle, la station est au centre du cercle. En bas, à gauche, résidus de temps d'arrivée pour le meilleur modèle. D'après Gesret et al. (2011).

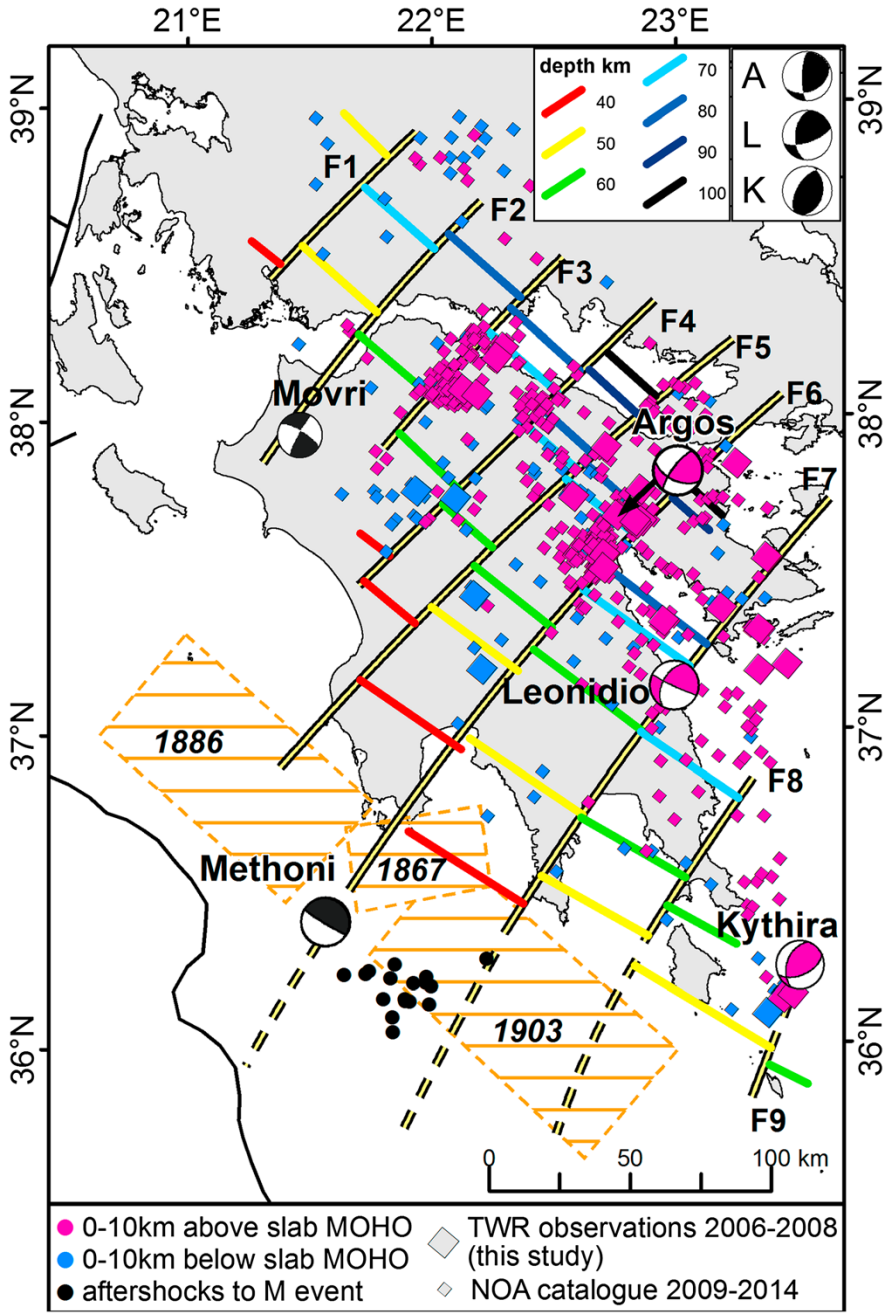

FIGURE 2.10 – Isoprofondeurs du Moho du slab (en couleur) et failles segmentant le slab (doubles lignes) imagées par migration des RF. Séismes mineurs à modérés représentés par les carrés dont la taille indique la magnitude et la couleur indique la profondeur. D'après Sachpazi et al. (2016).

Chapitre 3

Estimation d'incertitudes par tomographie sismique probabiliste

Ce chapitre présente les principaux résultats de travaux initiés peu après mon arrivée au Centre de Géosciences de MINES ParisTech. De part l'histoire de l'équipe de géophysique, j'ai été naturellement plongée dans les développements numériques liés à la simulation de la propagation d'onde dans les milieux hétérogènes. En effet, un algorithme très reconnu de calcul des temps de trajet, encore très largement utilisé par la communauté scientifique, est issu de l'équipe de Géophysique (Podvin and Lecomte, 1991). J'ai participé à l'élaboration d'un nouveau solveur principalement développé par Mark Noble, qui améliore significativement la précision des temps de trajet dans les milieux complexes 3D (Noble et al., 2014). Cet algorithme est succintement décrit dans la section 3.2. Les parties suivantes se focalisent sur des développements méthodologiques de tomographie probabiliste. La thématique de géophysique stochastique est née d'une collaboration avec l'équipe de Géostatistique initiée dès 2010 dans le cadre d'une action Carnot MINES. Les contributions sur cette thématique sont principalement méthodologiques axées sur la proposition de paramétrisations parcimonieuses adaptées à la tomographie stochastique et numériques avec le développement d'algorithmes. Les parties 3.3 et 3.4 reprennent les principaux résultats de quatre articles (Bottero et al., 2016; Belhadj et al., 2018; Luu et al., 2018, 2019) sur la tomographie probabiliste publiés par des étudiants que j'ai co-encadrés : Alexis Bottero dans le cadre d'un stage de Master 2, Jihane Belhadj et Keurfon Luu dans le cadre de leur thèse.

3.1 Méthode de la tomographie des temps de trajet

La tomographie des temps de trajet est un problème inverse classique de la géophysique visant à estimer le modèle de vitesse de propagation des ondes dans le sous-sol à partir de temps de trajet enregistrés à un ensemble de sismomètres (e.g., Rawlinson et al., 2010). Ce chapitre se concentre sur la tomographie active pour laquelle les sources générant les ondes sismiques sont connues en termes de position dans l'espace, de temps d'activation et de forme de l'ondelette source. Les inconnues sont alors les paramètres définissant le modèle de vitesse de propagation des ondes. La tomographie se résume alors en un problème d'optimisation numérique où on cherche à estimer le modèle de vitesse qui minimise une fonction coût

$S(\mathbf{m})$ entre les temps d'arrivée obervés $\mathbf{d}^{\text{obs}}$ et les temps d'arrivée synthétiques générés pour un modèle $\mathbf{m}$ avec l'opérateur du problème direct g. Comme rappelé dans la section 1.2.2, la tomographie est un problème inverse mal posé et afin de le résoudre de manière optimale, la formulation doit donc prendre en compte toute information a priori disponible sur les paramètres du modèle à inférer. Elle doit également représenter les incertitudes sur les observations. Pour répondre à ces exigences, la formulation probabiliste dans laquelle toutes les informations sont représentées par des distributions de probabilité est la plus adaptée (Tarantola and Valette, 1982). Le cadre bayésien permet en effet de transformer la distribution de probabilité a priori $\pi(\mathbf{m})$ en distribution de probabilité a posteriori $\pi(\mathbf{m}|\mathbf{d}^{\text{obs}})$:

$$\pi(\mathbf{m}|\mathbf{d}^{\text{obs}}) = \frac{\pi(\mathbf{d}^{\text{obs}}|\mathbf{m})\pi(\mathbf{m})}{\int \pi(\mathbf{d}^{\text{obs}}|\mathbf{m})\pi(\mathbf{m})d\mathbf{m}}. \tag{3.1}$$

Cette équation contient une intégrale sur l'espace des modèles au dénominateur, mais celle-ci peut être considérée comme une constante puisqu'elle ne dépend pas du modèle (Tarantola, 2005). La distribution a posteriori est donc connue à une constante près et peut s'écrire :

$$\pi(\mathbf{m}|\mathbf{d}^{\text{obs}}) \propto \pi(\mathbf{d}^{\text{obs}}|\mathbf{m})\pi(\mathbf{m}). \tag{3.2}$$

Cette distribution, proportionnelle au produit de la loi a priori $\pi(\mathbf{m})$ par la vraisemblance $\pi(\mathbf{d}^{\text{obs}}|\mathbf{m})$, résume comment l'information apportée par les données observées améliore la connaisance sur les paramètres du modèle. Une forme usuelle de la vraisemblance est la vraisemblance gaussienne (Mosegaard and Tarantola, 1995) pour laquelle on suppose que les erreurs de mesure (ici de pointés) et de modélisation suivent une distribution gaussienne :

$$\pi(\mathbf{d}^{\text{obs}}|\mathbf{m}) = \frac{1}{\sqrt{(2\pi)^{N_d}|\Sigma_d|}} \exp[-\frac{1}{2}(\mathbf{d}^{\text{obs}} - g(\mathbf{m}))^t \Sigma_d^{-1}(\mathbf{d}^{\text{obs}} - g(\mathbf{m}))]. \tag{3.3}$$

Les variances de ces erreurs sont donc contenues dans la diagonale de la matrice de covariance Σ_d. Très souvent, la matrice de covariance est diagonale sous l'hypothèse d'indépendance des erreurs.

$$\pi(\mathbf{m}|\mathbf{d}^{\text{obs}}) \propto \pi(\mathbf{m}) \exp[-\frac{1}{2}(\mathbf{d}^{\text{obs}} - g(\mathbf{m}))^t \Sigma_d^{-1}(\mathbf{d}^{\text{obs}} - g(\mathbf{m}))]. \tag{3.4}$$

Le théorème de Bayes permet de mettre à jour la distribution a priori en intégrant la théorie physique g (qui relie les paramètres du modèle aux observations) et les observations $\mathbf{d}^{\text{obs}}$ avec leurs incertitudes associées. Dans ce cadre bayésien, soit seul le modèle le plus probable est recherché ce qui correspond à de l'optimisation, soit la forme complète de la distribution est recherchée ce qui correspond à de l'échantillonnage. Le plus généralement, la solution la plus probable est estimée par une technique d'optimisation numérique, soit une approche d'optimisation locale basée sur le calcul du gradient de la fonction coût, soit une technique d'optimisation globale. Comme rappelé dans la section 1.2.2, l'inconvénient des méthodes locales est leur forte dépendance au modèle initial. Pour s'affranchir de ce défaut, il est préférable d'utiliser des méthodes d'optimisation globale. Dans ce dernier cas, il est plus probable que la solution obtenue sera proche de la vraie solution mais les incertitudes devront ensuite également être estimées autour de cette solution sous certaines hypothèses, le plus souvent une hypothèse de distribution gaussienne. Afin de s'affranchir de cette hypothèse, la

solution idéale est d'estimer la densité de probabilité a posteriori complète. Pour un faible nombre de paramètres du modèle $(3-4)$, la fonction densité de probabilité (pdf) a posteriori peut être estimée par recherche complète sur grille ("grid search") mais pour un plus grand nombre de paramètres à inférer, il est nécessaire de procéder à un échantillonnage d'importance en utilisant par exemple des algorithmes de type Markov Chain Monte Carlo (MCMC) qui sont particulièrement adaptés à l'échantillonnage (Robert and Casella, 2013). En effet ce type d'algorithme génère des modèles de vitesse quasi-indépendants qui sont distribués de manière proportionnelle à la distribution a posteriori (Koren et al., 1991; Mosegaard and Tarantola, 1995). En d'autres termes, la fréquence d'occurence approxime la densité de probabilté a posteriori $\pi(\mathbf{m}|\mathbf{d}^{\text{obs}})$. Cet échantillonnage de la distribution complète permet une estimation non biaisée des incertitudes du modèle de vitesse (Debski, 2010). La contrepartie est le temps de calcul requis par les algorithmes MCMC. En effet, un très grand nombre d'itérations est généralement requis avant que la chaîne ne converge vers une configuration stable proportionnelle à la distribution a posteriori. Un "thinning" de la chaîne est ensuite requis pour éviter la corrélation entre les états. Afin de réduire le temps de calcul, la procédure consiste généralement à lancer plusieurs chaînes indépendantes en parallèle et à aggréger les résultats, par exemple Bodin et al. (012a) lancent 96 chaînes indépendantes pour 3 millions d'itérations, éliminent la première moitié de chaque chaîne puis gardent un modèle tous les 250. Les approches de tomographie probabiliste requièrent donc un grand nombre de simulations (généralement de l'ordre du million), il est donc indispensable de disposer d'algorithmes efficaces en temps de calcul que ce soit pour la résolution du problème direct, qui sera appelé de très nombreuses fois, ou celle du problème inverse. Les deux premières sections présentent le développement de tels algorithmes. De plus, le nombre de paramètres à inverser doit être raisonnable, des paramétrisations parcimonieuses du modèle de vitesse 1D puis 2D sont introduites dans la dernière section.

3.2 Développement d'algorithmes pour la résolution du problème direct

Dans le cas de la tomographie des temps de trajet pour laquelle seuls les temps de première arrivée sont utilisés, l'équation Eikonal 3.5 peut être utilisée pour simuler ces temps t. L'équation Eikonal se déduit à partir de l'équation élastodynamique en approximation des hautes fréquences :

$$\left(\frac{\partial t}{\partial x}\right)^2 + \left(\frac{\partial t}{\partial y}\right)^2 + \left(\frac{\partial t}{\partial z}\right)^2 = \frac{1}{V^2(x,y,z)}, \tag{3.5}$$

où V représente la vitesse de propagation des ondes. L'approximation des hautes fréquences s'applique à des problèmes de propagation dans lesquels la longueur d'onde du signal est très petite vis-à-vis de la longueur caractéristique du milieu. Elle n'est donc licite que lorsqu'on observe une séparation d'échelle entre la longueur d'onde et la longueur de variation caractéristique des propriétés physiques du milieu.

Pour une position de source donnée, l'évaluation des temps de première arrivée en chaque point de la grille se fait en prenant en compte la possibilité d'avoir plusieurs fronts d'ondes localement indépendants. Ainsi, parmi les solutions candidates (correspondant à chaque front

d'onde), seul le temps minimal est retenu. Vidale (1988, 1990) est le premier à introduire un schéma aux différences finies permettant de propager les temps de première arrivée dans les modèles de vitesse 2D et 3D hétérogènes. Cette approche produit des temps de trajet relativement précis pour les modèles de vitesse lisses. Podvin and Lecomte (1991), en s'inspirant des travaux de Vidale, ont proposé une méthode alternative permettant de gérer les forts contrastes de vitesse. Cette amélioration est permise en utilisant une représentation physique du modèle de vitesse avec des mailles carrées de lenteur constante et en introduisant des opérateurs supplémentaires qui permettent de prendre en compte les ondes réfractées aux interfaces. Hole and Zelt (1995) et Afnimar and Koketsu (2000) ont amélioré la résolution en combinant les opérateurs des deux auteurs. Les opérateurs de différences finies impliquent une approximation d'ondes planes bien que, proche de la source, une approximation sphérique soit plus adaptée. L'approche la plus simple pour prendre en compte cette singularité proche de la source est de résoudre l'équation Eikonal factorisée (Zhang et al., 2005; Fomel et al., 2009), cependant cette approximation sphérique déteriore la précision loin de la source. Nous avons donc proposé un solveur hybride qui combine une approximation sphérique proche de la source et une approximation ondes planes loin de celle-ci (Noble et al., 2014). Afin de prendre en compte tous les types d'ondes (transmises, diffractées, réfractées), nous avons implémenté 16 opérateurs locaux comme suggéré par Afnimar and Koketsu (2000). Nous avons associé ces opérateurs locaux à une "Fast Sweeping Method" (Zhao, 2005) globale pour balayer la grille des temps de parcours dans des ordres alternés, permettant ainsi de prende en compte toutes les directions possibles de propagation d'ondes et la mise à jour des temps sur la totalité du modèle. Pour des milieux très hétérogènes, la "Fast Marching Method" (Rawlinson and Sambridge, 2004) serait certainement plus efficace mais elle est moins aisée à implémenter. Nous avons donc développé un nouveau solveur Eikonal qui gère la singularité à la source, des forts contrastes de vitesse et utilise une une grille avec des pas différents dans les 3 directions de l'espace. Une comparaison a été faite dans Noble et al. (2014) entre l'approximation ondes planes seule, l'approximation sphérique seule, le nouveau solveur hybride et l'algorithme de Podvin and Lecomte (1991).

Les résultats de cette comparaison (Figure 3.1 gauche) montrent que ce dernier permet de calculer de manière plus précise les temps de trajets avec des erreurs très faibles par rapport à la solution analytique dans un modèle bi-couche contenant un fort contraste de vitesse. La précision des temps de trajet obtenue avec ce nouveau solveur permet d'obtenir des dérivées de temps de trajet très précises. Dans le cadre de sa thèse que j'ai co-encadrée, Nidhal Belayouni a proposé des nouvelles formulations qui, en utilisant ces dérivées des temps très précises, permettent de calculer de nouveaux attributs de l'onde que sont l'angle à la source et l'amplitude de la première arrivée (Figure 3.2 gauche) en résolvant l'équation des angles et l'équation de transport.

Pour cet exemple de 3000×934 points de grille, des amplitudes très similaires sont obtenues entre le nouveau solveur et la modélisation des formes d'ondes complètes (Figure 3.2 droite) avec un temps de calcul nécessaire de 6 s à comparer aux 4 h nécessaires lorsque la modélisation des formes d'ondes est utilisée.

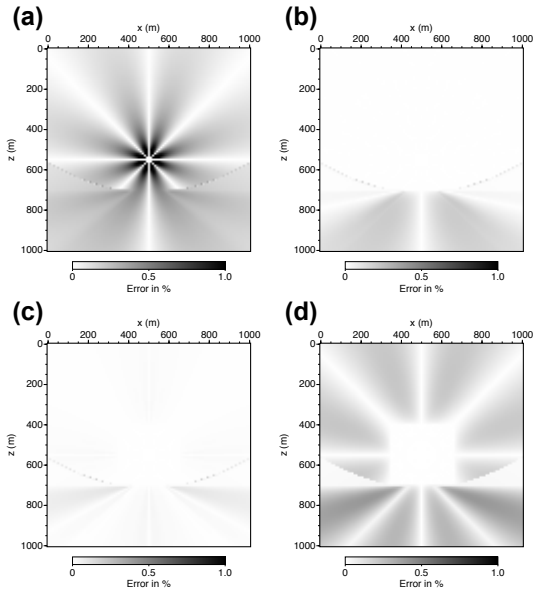

FIGURE 3.1 – A gauche : erreurs relatives entre solution analytique et numérique pour les opérateurs d'ondes planes seulement (a), d'ondes sphériques seulement (b), pour le nouveau schéma hybride (c) et pour l'algorithme de Podvin and Lecomte (1991) (d). D'après Noble et al. (2014).

3.3 Développement d'algorithmes pour la résolution du problème inverse

3.3.1 Chaînes de Markov en interaction

L'algorithme MCMC visant à échantillonner une distribution de probabilité le plus connu est certainement l'algorithme de Metroplis-Hastings (Hastings, 1970). Son implémentation est simple en deux étapes, depuis un état actuel m_i de la chaîne, un nouvel état m_{new} est proposé suivant une loi de proposition $q(m_{new}|m_i)$ qui décrit la probabilité de proposer un état m_{new} sachant que la chaîne est dans l'état m_i. Les deux lois les plus connues étant l'échantillonneur indépendant $q(m_{new}|m_i) = q(m_{new})$ où q est généralement la distribution a priori $\pi(m)$ qui, peut par exemple, suivre une loi uniforme (tous les états de la ditribution a priori sont équiprobables) et l'échantillonneur de marche aléatoire symétrique $q(m_{new}|m_i) = q(|m_{new} - m_i|)$ qui suit par exemple une loi normale centrée sur la valeur de l'état actuel et d'écart type fixé par l'utilisateur, $q = N(m_i, \sigma_m^2)$. Cet écart type est important car il a une forte influence sur les propriétés de mixage de la chaîne, ou sur son taux d'acceptance. La deuxième étape consiste à calculer la probabilité d'acceptation qui dépend du rapport entre densité de probabilité du nouvel état sur densité de probabilité de l'état actuel :

$$\alpha(m_i, m_{new}) = min\left(1, \frac{\pi(\mathbf{m_{new}}|\mathbf{d}^{\text{obs}})q(m_{new}|m_i)}{\pi(\mathbf{m_i}|\mathbf{d}^{\text{obs}})q(m_i|m_{new})}\right). \tag{3.6}$$

Si la transition est acceptée, $m_{i+1} = m_{new}$, sinon la chaîne reste dans son état actuel $m_{i+1} = m_i$. Si le nouvel état a une probabilité plus élevée, il sera forcément accepté. En

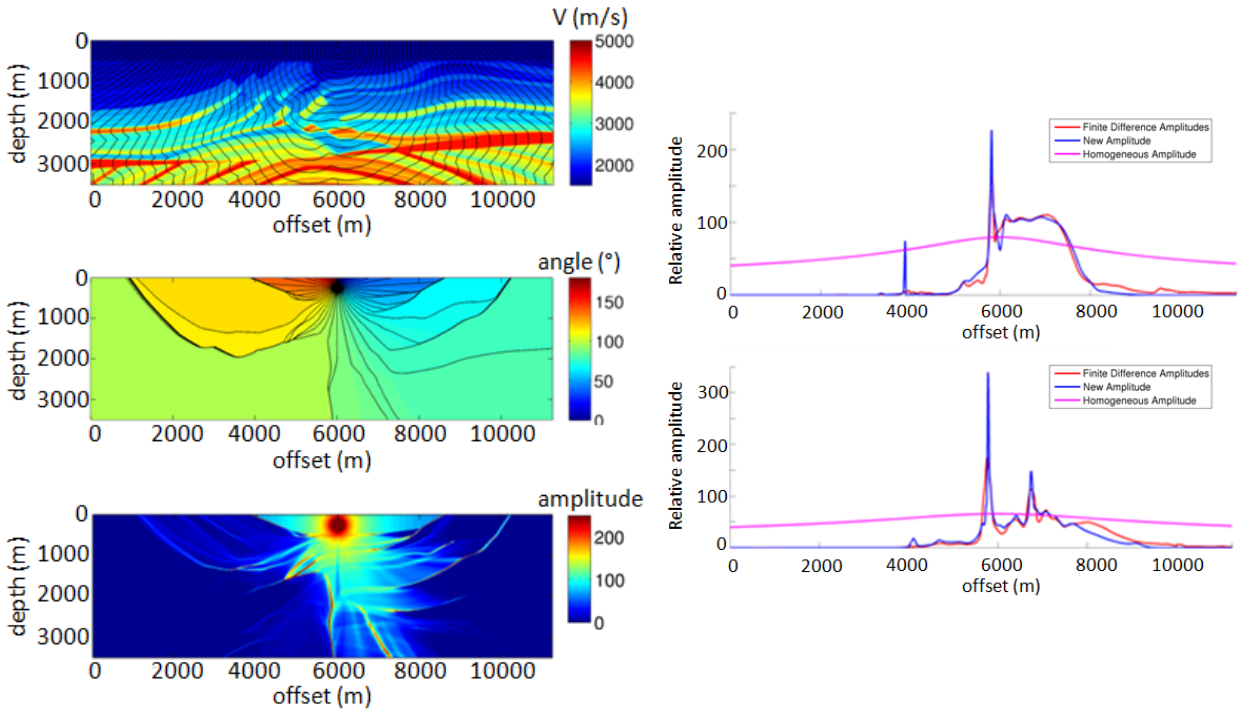

FIGURE 3.2 – A gauche : de haut en bas, isochrones des temps de trajet superposées au modèle de vitesse complexe, angles à la source et amplitudes déduites des dérivées des temps de trajet. A droite : Profils horizontaux de l'amplitude calculée avec la nouvelle formulation (en bleu) et celle calculée par modélisation de la forme d'onde complète (en rouge). D'après Belayouni (2013).

revanche, plus le nouvel état a une probabilité faible devant celle de l'état actuel, plus la probabilité de l'accepter sera faible également. Les échantillons obtenus par la chaîne après convergence sont ensuite utilisés pour calculer des estimateurs statistiques classiques tels que le modèle moyen et l'écart type associé, le modèle le plus probable ainsi que les intervalles de confiance basés sur les quantiles.

L'algorithme de Metroplis Hastings est simple d'implémentation cependant son efficacité en temps de calcul est limité. Afin d'accélérer la convergence, le recuit simulé introduit par Metropolis et al. (1953) puis généralisé par Kirkpatrick et al. (1983) peut lui être préféré. En effet, en ajoutant un paramètre, la température, la distribution a posteriori est déformée ce qui permet de faciliter l'exploration. Le recuit simulé est classiquement utilisé dans un but d'optimisation pour lequel le meilleur modèle est atteint quand la température est proche de 0. Lorsque la température est égale à 1, la distibution tempérée est la vraie distribution a posteriori et cette dernière peut alors être échantillonnée avec une exploration de Metropolis Hastings en laissant tourner l'algorithme. La figure 3.3 illustre l'effet de la température sur une simple distribution bimodale. Pour les grandes températures (courbe violette), la distribution à inférer est aplatie et la chaîne pourra aisément se "promener" dans cette distribution mais lorque la température diminue, la chaîne peut avoir des difficultés à sortir d'un maximum car les états proposés auront des probabilités trop faibles entraînant une probabilité d'acceptation faible également.

Une approche permettant de s'échapper d'un minimum local est de faire interagir plusieurs

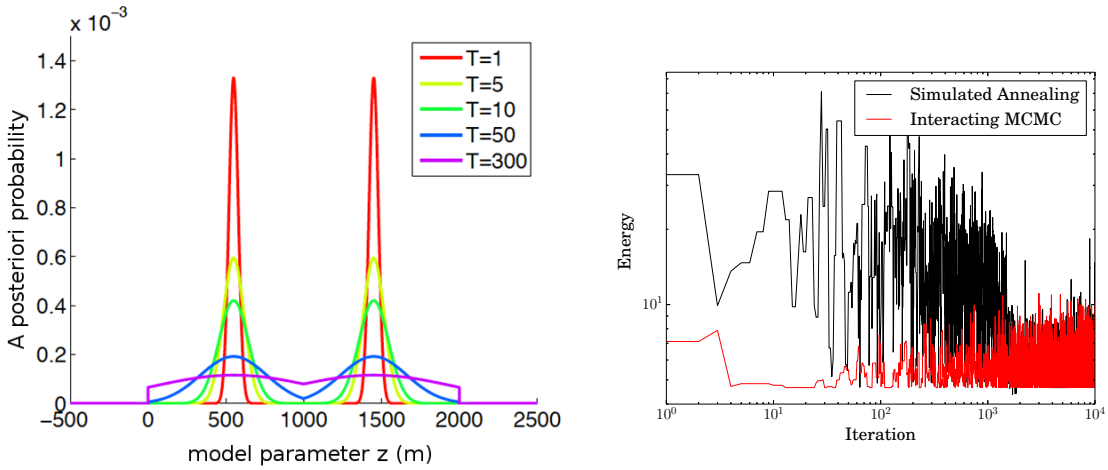

FIGURE 3.3 – À gauche, effet de la température sur la distribution a posteriori tempérée. À droite, comparaison de l'évolution de la fonction coût fonction de l'itération pour un recuit simulé (en noir) et l'IMCMC (en rouge). D'après Bottero et al. (2016).

chaînes comme proposé par Geyer (1991), ce qui permet également d'accélérer la convergence. Sambridge (2014) propose une application en géophysique de "Parallel Tempering" pour lequel des échanges entre des états simultanés de chaînes à des températures non adjacentes sont proposés. D'après les travaux de Romary (2009), les chaînes en interaction basées sur un rééchantillonnage d'importance de population (PIR) introduit par Andrieu et al. (2011), pour lesquelles des échanges dans l'histoire de la chaîne adjacente à la température supérieure sont permis, sont plus efficaces. Nous avons donc implémenté cet algorithme d'Interacting MCMC (IMCMC) et l'avons comparé à un recuit simulé classique (Bottero et al., 2016) pour une distribution multimodale (Figure 3.4 gauche). Pour cet exemple de distribution complexe, le recuit simulé résulte en une distribution a posteriori (Figure 3.4 milieu) qui ne permet pas d'identifier tous les modes, de plus le mode global ne correspond pas au mode principal. L'algorithme IMCMC est beaucoup plus performant que le recuit simulé puisqu'il permet d'identifier tous les modes et d'identifier le mode global comme le mode principal (Figure 3.4 droite). De plus, cet algorithme est beaucoup plus efficace, en témoigne l'évolution de la

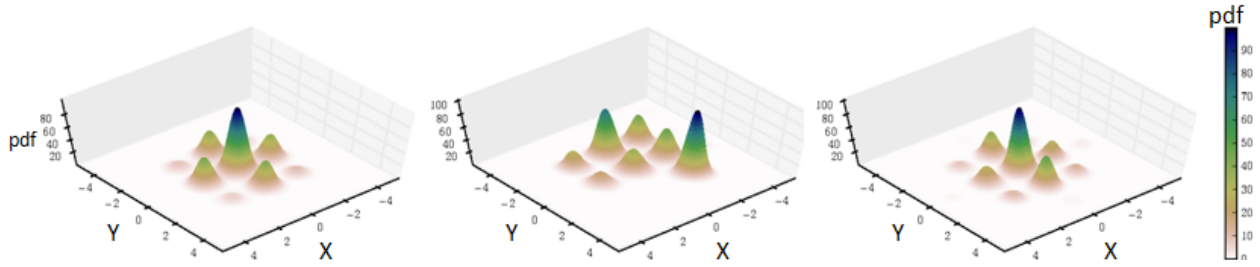

FIGURE 3.4 – À gauche : distribution à inférer, au milieu : distribution a posteriori obtenue par recuit simulé, à droite : distribution a posteriori obtenue avec l'algorithme IMCMC. D'après Bottero et al. (2016).

fonction coût en fonction des itérations (Figure 3.3 droite). Comme dans toutes les approches

d'inférence basées sur des algorithmes MCMC, des paramètres nécessitent d'être réglés, ici ils sont : le nombre de chaînes, la température maximale, la séquence des températures, l'échantillonneur à chaque température et la probabilité de proposer un échange. Cet algorithme n'est donc pas extrêment facile d'utilisation contrairement à l'optimisation par essaim particulaire introduite dans la section suivante.

3.3.2 Optimisation par essaim particulaire compétitive

Même si plusieurs chaînes de Markov peuvent être lancées en parallèle ou même interagir, ce sont des méthodes séquentielles qui ne permettent pas de profiter pleinement des structures type cluster. Les algorithmes évolutionnistes sont des méthodes d'optimisation globales inspirées de l'évolution naturelle des espèces puisqu'elles utilisent les principes de mutation, de recombinaison et de sélection. Ces approches sont intrinsèquement parallélisables et peuvent donc bénéficier pleinement des ressources informatiques actuelles. En effet chaque particule va explorer et évaluer la fonction coût d'un des modèles de la population simultanément aux autres particules de la population. Dans le cadre de la thèse de Keurfon Luu, nous nous sommes intéressés aux méthodes évolutionnistes en particulier à l'optimisation par essaim particulaire qui a été introduite assez récemment par Kennedy and Eberhart (1995) et a connu un grand succès dans le cadre de l'optimisation. La PSO (Particle Swarm Optimization) présente l'avantage d'être simple à implémenter (seulement 2 équations) et à utiliser (seulement 3 paramètres à régler). A une itération donnée, une particule est définie par le vecteur des paramètres du modèle et par un vecteur vitesse qui est ajusté en fonction de sa meilleure position visitée et du meilleur modèle de la population. Dans Luu et al. (2018), nous avons illustré que l'implémentation classique de la PSO peut souffrir de convergence prématurée et donc stagner dans un minimum local, en particulier si la fonction coût a une forme complexe. Nous avons donc proposé une PSO compétitive (CPSO) qui permet de s'échapper de ces minima locaux. L'idée est d'améliorer la diversité de la population en renouvelant une partie de la population et en ne gardant que les meilleurs modèles. Cette PSO compétitive montre un meilleur taux de convergence et une meilleure roubustesse au choix des paramètres de contrôle. Cette approche permet d'explorer un très grand nombre de modèles de manière très efficace. Luu et al. (2018) a proposé de sauvegarder tous les modèles visités par plusieurs runs depuis différentes populations initiales et d'estimer une densité de probabilité a posteriori avec tous ces échantillons. L'application de cet algorithme à des données réelles a montré des résultats comparables en termes d'incertitudes à ceux produits par une méthode MCMC.

Toujours dans le cadre de sa thèse, Keurfon Luu a ensuite comparé la PSO compétitive à deux autres algorithmes évolutionnistes : l'évolution différentielle (Storn and Price, 1997) et la Covariance Matrix Adaptation-Evolution Strategy (Hansen et al., 2003) pour un modèle de vitesse complexe (Figure 3.5). Il a montré que la Covariance Matrix Adaptation-Evolution Strategy est plus robuste en termes d'optimisation mais que la CPSO est plus adaptée pour estimer les incertitudes (Luu et al., 2019), en témoigne leurs valeurs par rapport à la couverture des rais (Figure 3.6 à droite au milieu).

Même avec de tels algorithmes tels que l'IMCMC ou la CPSO, l'échantillonnage de la distribution a posteriori reste coûteux et ce coût dépend du nombre de paramètres du modèle de vitesse que l'on cherche à inférer, d'où l'importance de proposer des modèles parcimonieux.

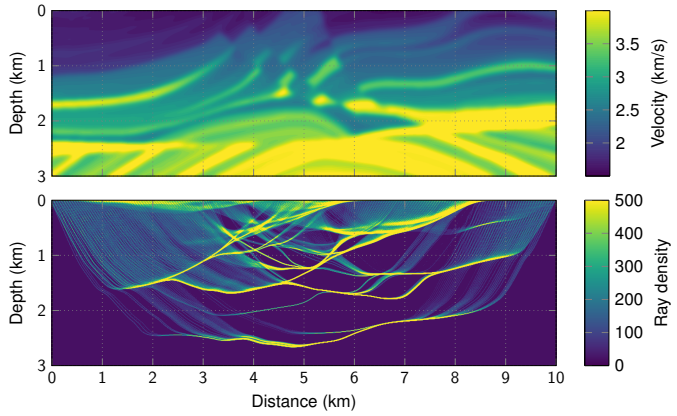

FIGURE 3.5 – En haut : vrai modèle de vitesse, en bas : couverture des rais dans le vrai modèle. D'après Luu et al. (2019).

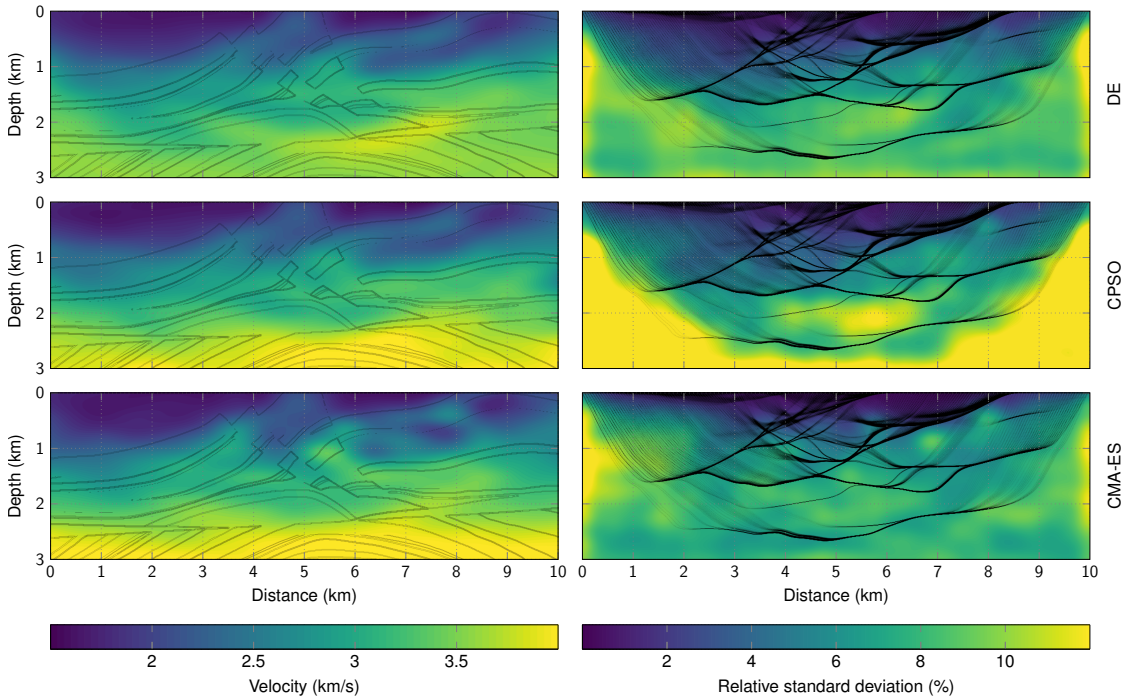

FIGURE 3.6 – A gauche : modèle de vitesse moyen, à droite : incertitudes associées pour l'évolution différentielle (en haut), la CPSO (au milieu) et la Covariance Matrix Adaptation-Evolution Strategy (en bas). D'après Luu et al. (2019).

3.4 Nouvelles paramétrisations parcimonieuses du modèle de vitesse

Dans cette partie, deux paramétrisations parcimonieuses du modèle de vitesse sont présentées : une paramétrisation basée sur la décomposition en ondelettes pour les modèles de vitesse 1 D

et une paramétrisation basée sur les cellules de Johnson Mehl pour les modèles de vitesse 2 D.

3.4.1 Paramétrisation basée sur la décomposition en ondelettes : application à des données réelles acquises dans le contexte du monitoring microsismique

Le premier exemple de paramétrisation parcimonieuse a été proposé dans le contexte du monitoring microsismique d'une exploitation par fracturation hydraulique. Dans ce type de projets, le modèle de vitesse utilisé pour localiser les événements sismiques induits par l'exploitation est généralement un modèle de vitesse à couches. Celui-ci est construit à partir d'un log sonique, puis est calibré par tomographie grâce à des tirs de perforation dont la position est connue (Eisner et al., 2009; Maxwell, 2010).

Le jeu de données réelles consiste ici en 15 tirs de calibration enregistrés à 80 capteurs déployés dans deux puits (Figure 3.7 gauche).

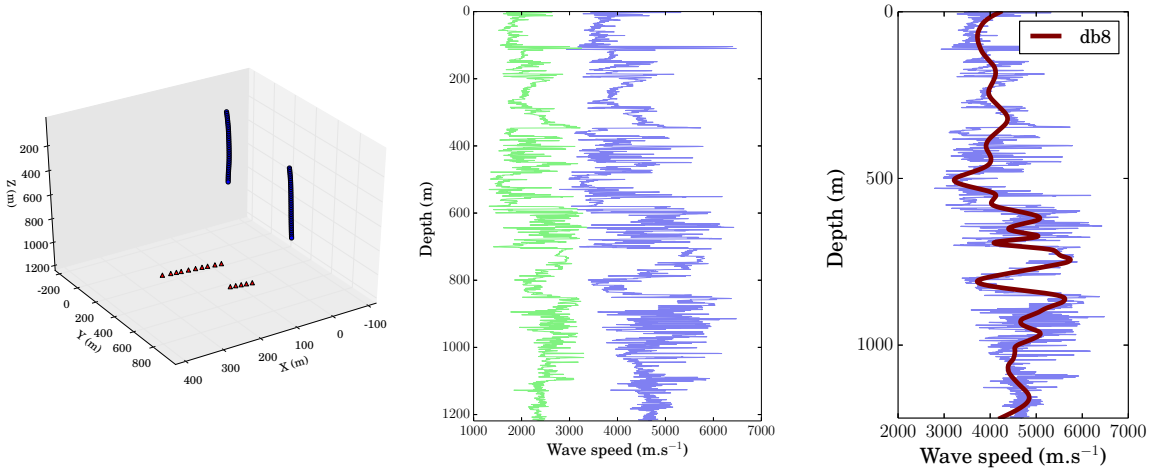

FIGURE 3.7 – Gauche : Géométrie d'acquisition correspondant à 15 tirs de calibration (triangles rouges) enregistrés à 80 capteurs déployés dans 2 puits (ronds bleus). Milieu : Logs soniques P (courbe bleue) et S (courbe verte). Droite : profil obtenu après décomposition de ce log sur une famille d'ondelettes (courbe rouge). D'après Bottero et al. (2016).

Des logs soniques P et S étaient également disponibles (Figure 3.7 milieu). Ces logs sont très haute fréquence, les ondes sismiques générées par les tirs de calibration n'ont pas le contenu fréquentiel nécessaire pour résoudre toutes ces hétérogénéités. De plus, paramétriser un tel profil de vitesse avec un modèle à couches n'est pas une tâche aisée car cela peut nécessiter un grand nombre N de couches (difficile à déterminer) et donc un trop grand nombre de paramètres à inverser ($3N - 1$ paramètres : V_p,V_s dans chaque couche et profondeurs des interfaces). Par exemple, les opérateurs avaient construit un modèle à 15 couches à partir de ces logs (Figure 3.8 gauche) mais ce modèle de référence n'était pas satisfaisant en termes de résidus entre temps observés et temps synthétiques. Nous avons donc proposé une paramétrisation parcimonieuse basée sur une décomposition sur une base d'ondelettes de ce

log sonique. En effet, le log $V(x_j)$ peut s'écrire :

$$V_M(x_j) = \sum_{i=1}^{M} b_i \phi_i(x_j), \tag{3.7}$$

où b_i sont les coefficients et $\phi_i(x_j)$ sont les ondelettes obtenues par dilatation et translation d'une ondelette analysante (type Haar, Ricker, Daubechie,...). Cette décomposition permet d'utiliser le log sonique comme information a priori et de décrire ce profil de vitesse complexe avec un faible nombre de paramètres. En effet, avec 15 coefficients seulement, un profil très satisfaisant est obtenu (courbe rouge de la Figure 3.7 droite) en décomposant le log sur une base d'ondelettes de Daubechie par exemple. L'intérêt de cette décomposition est de réduire le nombre de paramètres à inverser puisque seuls ces 15 coefficients seront à inférer par tomographie, permettant ainsi l'utilisation d'une approche probabiliste.

Les résultats de l'inversion obtenus avec l'algorithme IMCMC sont représentés sur la Figure 3.8 droite, qui corrrespondent ici au modèle moyen (en bleu), au meilleur modèle (vert), à l'écart type (pointillés) et aux density plots (niveaux de gris). Nous avons démontré que le meilleur modèle et le modèle moyen produisait des résidus de meilleure qualité que ceux obtenus dans un modèle de référence à 15 couches (Figure 3.8 gauche) utilisé par les opérateurs (Bottero et al., 2016).

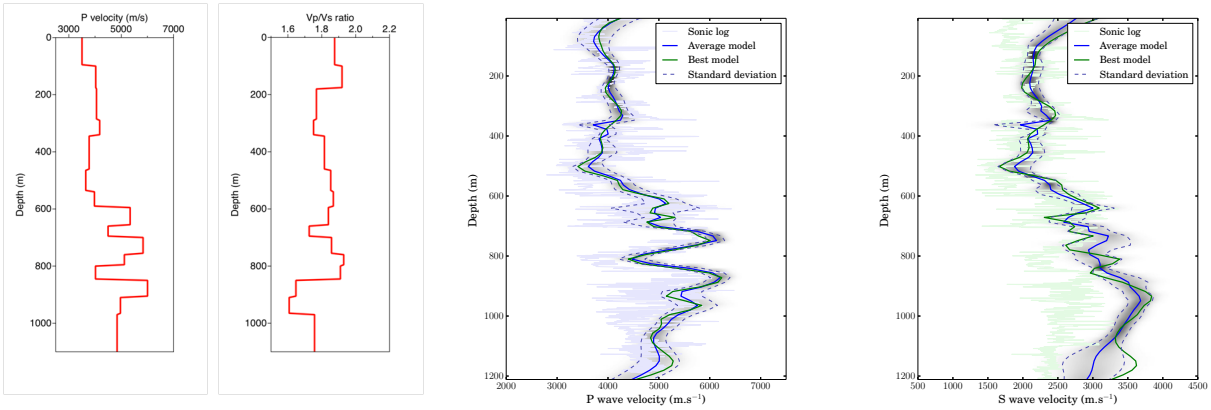

FIGURE 3.8 – Gauche : Modèles de référence P et S à 15 couches. Droite : Résultats P et S de la tomographie probabiliste en inversant les coefficients de la décomposition en ondelettes. D'après Bottero et al. (2016).

Cette paramétrisation originale a produit des résultats convaincants mais cette approche est limitée aux applications pour lesquelles des modèles de vitesse 1D sont suffisants pour caractériser la structure en profondeur, plutôt typiques de l'exploitation dans les bassins sédimentaires. Il est aussi utile de progresser dans l'estimation d'incertitudes dans des cas plus complexes tels que ceux rencontrés dans des expériences de sismique réfraction.

3.4.2 Paramétrisation basée sur les cellules de Johnson-Mehl : application à des données synthétiques de sismique réfraction 2D

Une des premières applications marquantes de la tomographie probabiliste en 2D a été obtenue par Bodin and Sambridge (2009). Les auteurs ont alors utilisé une paramétrisation du modèle de vitesse basée sur des cellules de Voronoi. Ce type de paramétrisation est maintenant très largement utilisé par la communauté scientifique. Généralement une inversion transdimensionnelle est alors utilisée, pour laquelle le nombre de paramètres à inférer, ici le nombre de cellules de Voronoï est un paramètre de l'inversion. Pour ce faire, un algorithme de reversible jump MCMC (Green, 1995), qui est une généralisation de l'algorithme classique de Metropolis Hastings, est utilisé.

Dans ce contexte de sismique $2D$, nous avons proposé une nouvelle paramétrisation basée sur les cellules de Johson Mehl, qui est une généralisation de la tesselation de Voronoi (Belhadj et al., 2018). Le nombre de noyaux est alors augmenté avec le temps. Toutes les cellules grandissent de manière isotrope avec une vitesse constante et la croissance des limites de cellules est stoppée lorsque les cellules se rencontrent (Figure 3.9). Contrairement à la tes-

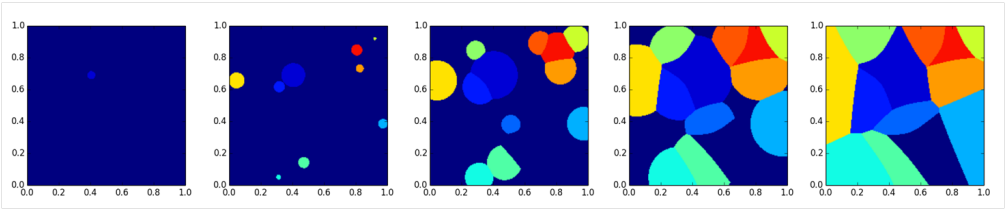

FIGURE 3.9 – Construction de la tesselation de Johson Mehl au cours du temps. D'après Belhadj et al. (2018).

selation de Voronoi, cette paramétrisation contient des cellules qui n'ont pas nécessairement des côtés droits. Les paramètres à inférer sont alors U, v, t, n où U représente la position du noyau, v la vitesse de la cellule, t le temps d'implantation du noyau et n le nombre de cellules. Le nombre de cellules étant un paramètre à inverser, l'algorithme rj-MCMC a été implémenté dans ce cas.

Le premier test de cette nouvelle paramétrisation est réalisé pour un modèle synthétique simple (Figure 3.10 gauche), proposé par Bodin and Sambridge (2009). Ce modèle est séparé en deux parties (vitesse plus rapide dans la partie supérieure gauche que dans la partie inférieure droite) par une interface diagonale, la partie supérieure gauche (resp. inférieure droite) contenant une anomalie à faible (resp. forte) vitesse. La géométrie d'acquisition consiste en 17 sources (carrés blancs) et 20 capteurs (triangles noirs) inégalement répartis.

Les résultats de l'inversion transdimensionnelle sont représentés pour une paramétrisation basée sur les cellules de Johson Mehl (Figure 3.10 milieu) et sur les cellules de Voronoi (Figure 3.10 droite). Ces illustrations montrent une amélioration de la qualité des résultats lorque la nouvelle tesselation est utilisée, en particulier au niveau de l'anomalie lente. En effet, sa forme ainsi que la valeur de sa vitesse sont mieux retrouvés. De plus, la majorité des rais sismiques ne traversent pas cette anomalie, une grande incertitude est donc attendue dans

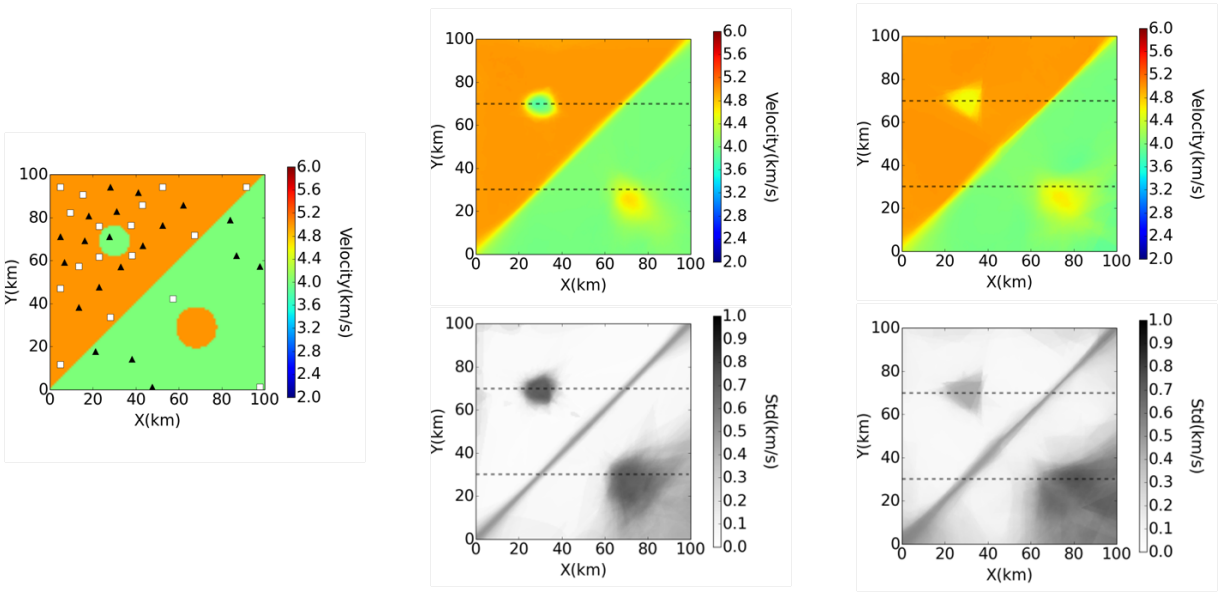

FIGURE 3.10 – À gauche, vrai modèle de vitesse et position des 17 sources (carrés blancs) et des 20 récepteurs (triangles noirs). Au milieu (resp. droite), résultats obtenus avec la paramétrisation de Johnson Mehl (resp. Voronoi) en termes de modèle moyen (en haut) et d'écart type (en bas). D'après Belhadj et al. (2018).

cette zone, résultat effectivement obtenu avec la paramétrisation basée sur des cellules de Johnson Mehl.

Nous avons également comparé la qualité des résultats obtenus avec les deux paramétrisations en termes d'efficacité et de convergence (Figure 3.11). Il apparaît que le misfit diminue plus

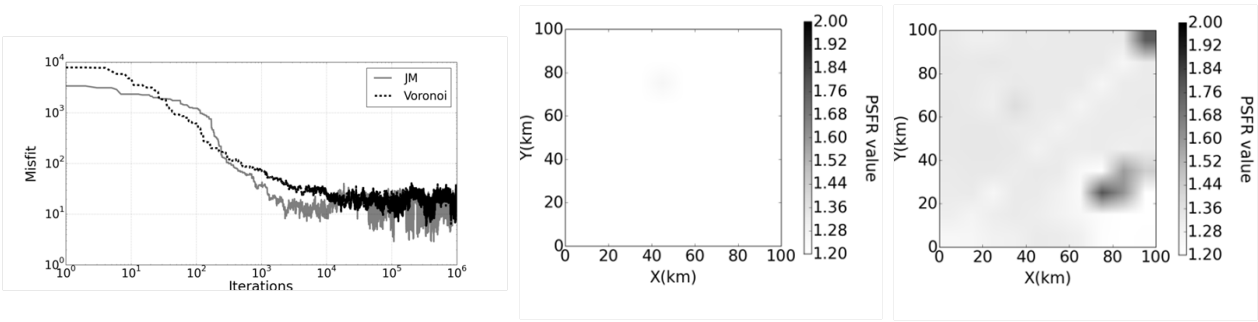

FIGURE 3.11 – A gauche, comparaison de l'évolution de la fonction coût en fonction de l'itération pour une paramétrisation basée sur les cellules de Johnson Mehl (resp. Voronoi) en gris (resp. en noir). Au milieu (resp. à droite) : diagnostic de Gelman-Rubin pour la paramétrisation de Johnson Mehl (resp. Voronoi). D'après Belhadj et al. (2018).

vite et atteint un niveau plus bas avec les cellules de Johnsn Mehl, illustrant une amélioration significative de l'efficacité. La convergence est estimée en utlisant le diagnostic de Gelman-Rubin qui compare la variance au sein de chaque chaîne à la variance entre plusieurs chaînes de Markov, qui sont censées être similaires et donc donner un ratio potential Scale Reduction Factor proche de 1. En pratique, un ratio inférieur à 1.2 indique que la chaîne a convergé vers

la distribution a posteriori. La figure 3.11 illustre qu'avec la paramétrisation de Voronoi, la stabilisation de la chaîne n'est pas encore atteinte puisque la majeure partie des valeurs sont supérieures à 1.2.

L'application de la nouvelle paramétrisation à un modèle plus réaliste est elle-aussi prometteuse (Belhadj et al., 2018). Le modèle synthétique, construit par l'Amoco Tulsa Research Lab, contient des variations dans les directions horizontales et verticales (Figure 3.12). Pour une géométrie d'acquisition consistant en 23 sources et 44 récepteurs déployés en surface, la paramétrisation de Johnson Mehl semble efficace. La forme des structures est retrouvée avec des valeurs de vitesse moyenne proche de la vraie, en témoigne les profils horizontaux représentés sur la Figure 3.9. L'incertitude, plus grande en profondeur, est cohérente avec la couverture des rais plus faible en profondeur. En conclusion, bien que la tesselation de Johson Mehl introduise un paramètre suppélementaire, la forme générale des cellules donne des meilleurs résultats et améliore l'efficacité de l'algorithme.

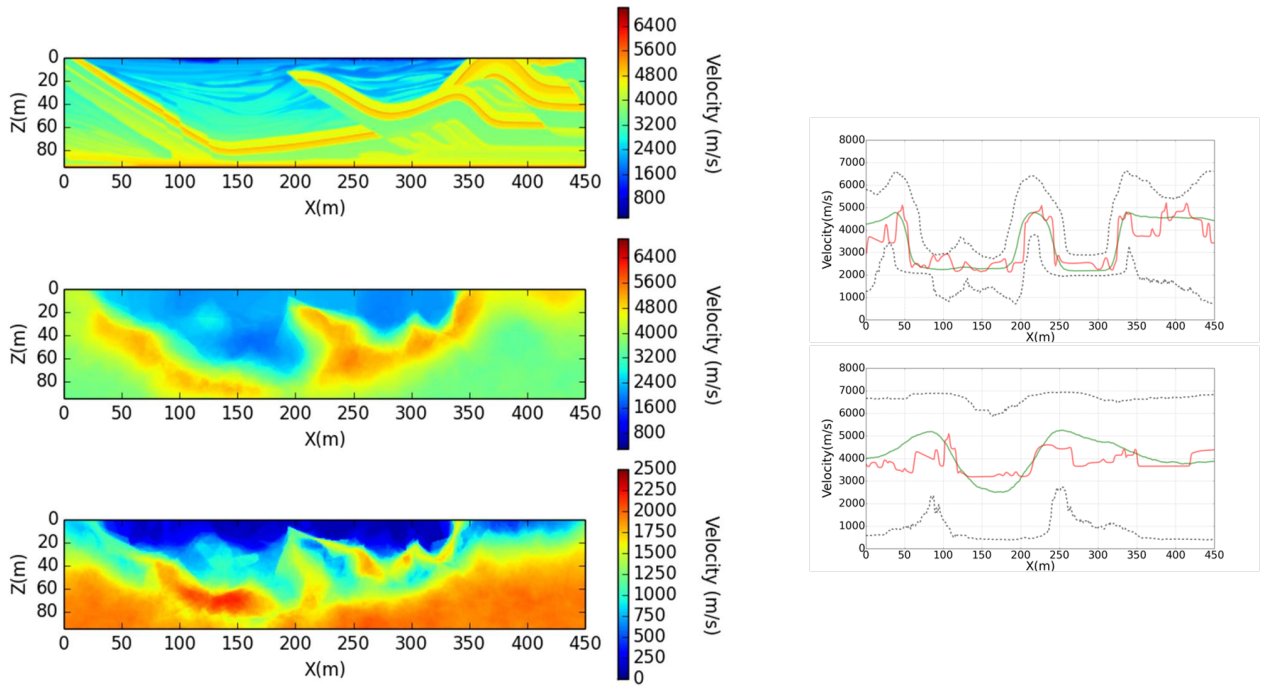

FIGURE 3.12 – A gauche, de haut en bas : modèle de vitesse exact, modèle moyen a posteriori, estimation d'incertitudes (écart type). A droite : profils horizontaux du modèle exact (rouge), du modèle moyen (vert) et l'intervalle de confiance 95% (noir). D'après Belhadj et al. (2018).

3.5 Conclusions

Les résultats de la paramétrisation en ondelettes ont été obtenus en recherchant le nombre de coefficients optimal pour la décomposition du log sonique avant l'étape d'inversion. En effet, des simulations pour différentes familles d'ondelettes et différents nombres de coefficients ont été réalisées afin de produire des temps de trajet proches des temps simulés pour le log sonique. Il serait intéressant d'introduire la transdimensionalité en utilisant un algorithme rj

MCMC, tel que celui utilisé dans le deuxième exemple de sismique réfraction. Ceci permettrait en effet d'inverser pour le nombre de coefficients d'ondelettes optimal, conditionné par les données observées, sans avoir à le fixer préalablement.

Malgré l'efficacité des algorithmes, le temps de calcul requis permet difficilement d'envisager des applications 3D, une piste afin d'évaluer plus rapidement le problème direct sera présentée dans la section 5.1.1 de Perspectives.

Le chapitre suivant est également dédié à l'inversion probabiliste mais cette fois appliquée à la localisation des événements sismiques.

Chapitre 4

Estimation d'incertitudes par localisation probabiliste

Ce chapitre présente également les principaux résultats de travaux liés à la thématique de géophysique stochastique mais cette fois dans le cadre de la localisation des événements sismiques, publiés dans trois articles (Gesret et al., 2015; Belayouni et al., 2015; Gaucher et al., 2017). Ces travaux ont été menés dans le cadre de collaborations avec l'équipe géostatistique du Centre de Géosciences, avec le Karlsruhe Institute of Technology et la société Magnitude-Baker Hughes, qui est spécialisée en monitoring microsismique.

4.1 Localisation probabiliste standard

Comme rappelé dans le chapitre 1, la localisation standard peut résulter en des solutions erronées et n'est pas fiable pour l'estimation d'incertitudes. Depuis les travaux de Tarantola and Valette (1982), la formulation probabiliste est souvent préférée (e.g., Moser et al., 1992; Wittlinger et al., 1993; Lomax et al., 2001; Husen et al., 2003) car elle permet de retrouver le minimum global de la fonction coût et d'estimer l'incertitude même pour une forme complexe de la fonction coût (Lomax et al., 2000; Husen and Smith, 2004). La solution finale n'est plus un seul point mais la fonction de densité de probabilité a posteriori (pdf) $\pi(\mathbf{l}|\mathbf{d}_s^{\text{obs}}, \mathbf{v})$ de la localisation $\mathbf{l} = (x, y, z, t_0)$ pour un modèle de vitesse $\mathbf{v}$ donné. Comme montré par Tarantola and Valette (1982), si l'information a priori sur le temps origine est considérée uniforme, cette pdf peut être intégrée analytiquement pour obtenir la pdf marginale de la localisation spatiale :

$$\pi(x, y, z|\mathbf{d}_s^{\text{obs}}, \mathbf{v}) \propto \pi(x, y, z) \exp[-\frac{1}{2}(\tilde{\mathbf{d}}_s^{\text{obs}} - \tilde{\mathbf{d}}_s^{\text{cal}})^t \Sigma_s^{-1} (\tilde{\mathbf{d}}_s^{\text{obs}} - \tilde{\mathbf{d}}_s^{\text{cal}})]. \tag{4.1}$$

Dans cette expression $\tilde{\mathbf{d}}_s^{\text{obs}}$ est le vecteur des temps observés $\mathbf{d}_s^{\text{obs}}$ moins leur moyenne pondérée, $\tilde{\mathbf{d}}_s^{\text{cal}}$ est le vecteur des temps théoriques $\mathbf{d}_s^{\text{cal}}$ moins leur moyenne pondérée, où les poids w_i sont donnés par $w_i = \sum_j w_{ij}$ et $w_{ij} = [\Sigma_s^{-1}]_{ij}$. Comme démontré par Moser et al. (1992), le temps d'origine le plus probable T_{ml} s'exprime

$$T_{ml}(x, y, z) = \frac{\sum_i \sum_j w_{ij}(d_{s,i}^{\text{obs}} - d_{s,i}^{\text{cal}})}{\sum_i \sum_j w_{ij}}. \tag{4.2}$$

En pratique la pdf marginale de la localisation spatiale $\pi(x, y, z|\mathbf{d}_s^{\text{obs}}, \mathbf{v})$ est estimée par "grid search" de l'espace des paramètres (x, y, z) comme implémentée par de nombreux auteurs tels que Moser et al. (1992); Wittlinger et al. (1993); Lomax et al. (2000).

Les solveurs de type Eikonal introduits dans la section 3.2 calculent les temps de trajet en tout point d'une grille pour une source donnée. Ces algorithmes sont donc particulièrement adaptés à la méthode de localisation par "grid search", qui recherche la meilleure localisation dans tout l'espace. En pratique, pour éviter de simuler la position de source en chaque point de l'espace, la réciprocité des temps de trajet est appliquée : les temps de trajets calculés depuis un récepteur sur la totalité de la grille correspondent aux temps de trajet issus de tous les points de grille vers ce même récepteur.

4.2 Nouvelle formulation prenant en compte l'erreur du modèle de vitesse

Même si la formulation probabiliste est plus fiable que les approches linéarisées, la qualité de l'hypocentre dépend essentiellement de la précision du modèle de vitesse utilisé (Husen and Hardebeck, 2010; Kinnaert et al., 2016). Classiquement un seul modèle de vitesse est supposé et les incertitudes du modèle sont intégrées dans l'incertitude sur le pointé. Une telle approche ne permet pas de reproduire l'impact réel de l'incertitude du modèle sur l'incertitude de localisation. Poliannikov et al. (2013) ont intégré les incertitudes du modèle de vitesse dans la formulation bayésienne mais en se basant sur une répartition équiprobable de modèles aléatoires autour d'un modèle de vitesse. Hauser et al. (2011) ont localisé un séisme dans un ensemble de réalisations de modèle de vitesse obtenu par une analyse bayésienne de données indépendantes ce qui lui permet d'estimer qualitativement les incertitudes de localisation qui résultent de l'incertitude du modèle de vitesse. Cependant l'incertitude finale associée à la localisation n'est pas calculée. Nous avons proposé dans Gesret et al. (2015) une nouvelle formulation probabiliste de la localisation qui prend en compte rigoureusement et l'incertitude du modèle de vitesse et l'incertitude sur le pointé dans le cas où des données indépendantes permettent d'estimer l'incertitude du modèle de vitesse.

Si un ensemble de modèles vitesses $v_1, \ldots, v_N$ distribué selon la distribution a posteriori $\pi(\mathbf{v}|\mathbf{d}_v)$ pour des données indépendantes $\mathbf{d}_v$ est disponible, la pdf a posteriori de la localisation peut être estimée par une intégrale de Monte-Carlo (Robert and Casella, 2013) :

$$\pi(\mathbf{l}|\mathbf{d}_v, \mathbf{d}_s^{\text{obs}}) \propto \frac{1}{N} \sum_{i=1}^{N} \pi(\mathbf{d}_s^{\text{obs}}|v_i, \mathbf{l}) P(\mathbf{l}). \tag{4.3}$$

Cette équation permet de propager les incertitudes du modèle de vitesse à la localisation. Comme pour la formulation standard, pour chaque réalisation v_i, le temps d'origine est intégré analytiquement et la pdf marginale spatiale est estimée par "grid search" de l'espace des paramètres (x, y, z). Cette étape est répétée pour chaque v_i et sommée sur les modèles de vitesse résultant en pdf a posteriori de la localisation qui prend en compte les incertitudes du modèle de vitesse.

Cette nouvelle formulation est ici illustrée pour des données synthétiques typiques du contexte de la fracturation hydraulique. La géométrie d'acquisition est la même que celle

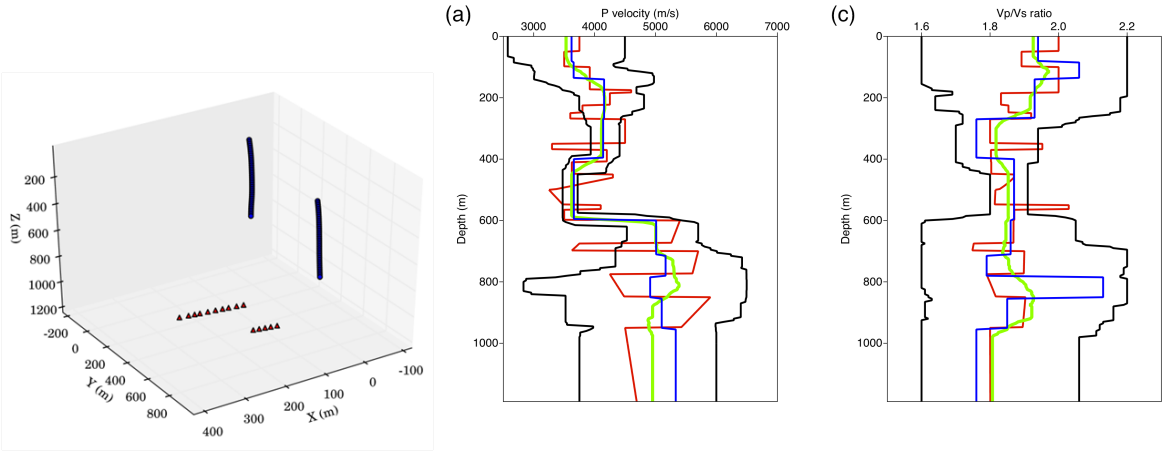

FIGURE 4.1 – Gauche : géométrie d'acquisition, milieu (resp. droite) : Profils verticaux V_p (resp. V_p/V_s) pour le vrai modèle (rouge), pour le modèle moyen (vert), pour le meilleur modèle (bleu) et pour les intervalles de confiance 95% basés sur les quantiles. D'après Gesret et al. (2015).

introduite dans la section 3.4.1 et le modèle de vitesse réaliste est constitué de fines couches et de zones à gradient (profils rouges sur la Figure 4.1). Les incertitudes du modèle de vitesse (profils noirs) sont estimées par tomographie probabiliste de 15 tirs de calibration avec un algorithme de Metropolis-Hastings classique en considérant un modèle à 15 couches (Figure 4.1). La figure 4.2 illustre la comparaison entre la localisation probabiliste standard dans le meilleur modèle (profil bleu de la Figure 4.1) et la nouvelle formulation prenant en compte l'incertitude du modèle de vitesse. Les incertitudes de localisation sont représentées par les intervalles de confiance 68% basés sur les pdf marginales pour XY (gauche), ZX (milieu) et ZY (droite). Pour le meilleur modèle de vitesse, la vraie position du séisme n'est pas incluse dans les intervalles de confiance. Classiquement, les incertitudes du modèle sont intégrées en augmentant artificiellement l'incertitude du pointé dans la matrice de covariance Σ_s considérée dans l'estimation de la distribution a posteriori (équation 4.1). Dans ce cas (Figure 4.2 milieu), les intervalles augmentent mais ils n'incluent toujours pas la position de l'hypocentre. En revanche, la nouvelle formulation donne des intervalles de confiance plus grands mais aussi de formes différentes (en particulier pour le plan ZX) permettant d'obtenir une localisation contenue dans les intervalles de confiance. Dans Gesret et al. (2015), nous avons également validé cette nouvelle formulation sur un jeu de données réelles.

4.3 Nouvelle formulation prenant en compte les ondes réfléchies

Si la formulation probabiliste résolue par une recherche exhaustive est plus fiable que les approches locales, de très grandes incertitudes sont parfois obtenues quand seuls les temps de première arrivée des ondes transmises sont utilisés. Ceci est particulièrement vrai si les premières arrivées sont des ondes réfractées car dans ce cas l'ouverture effective est faible. Zimmer (2010) a montré que lorsque les temps pointés contiennent des ondes réfractées et des ondes directes (selon la position du capteur), les incertitudes sont diminuées. Coffin et al.

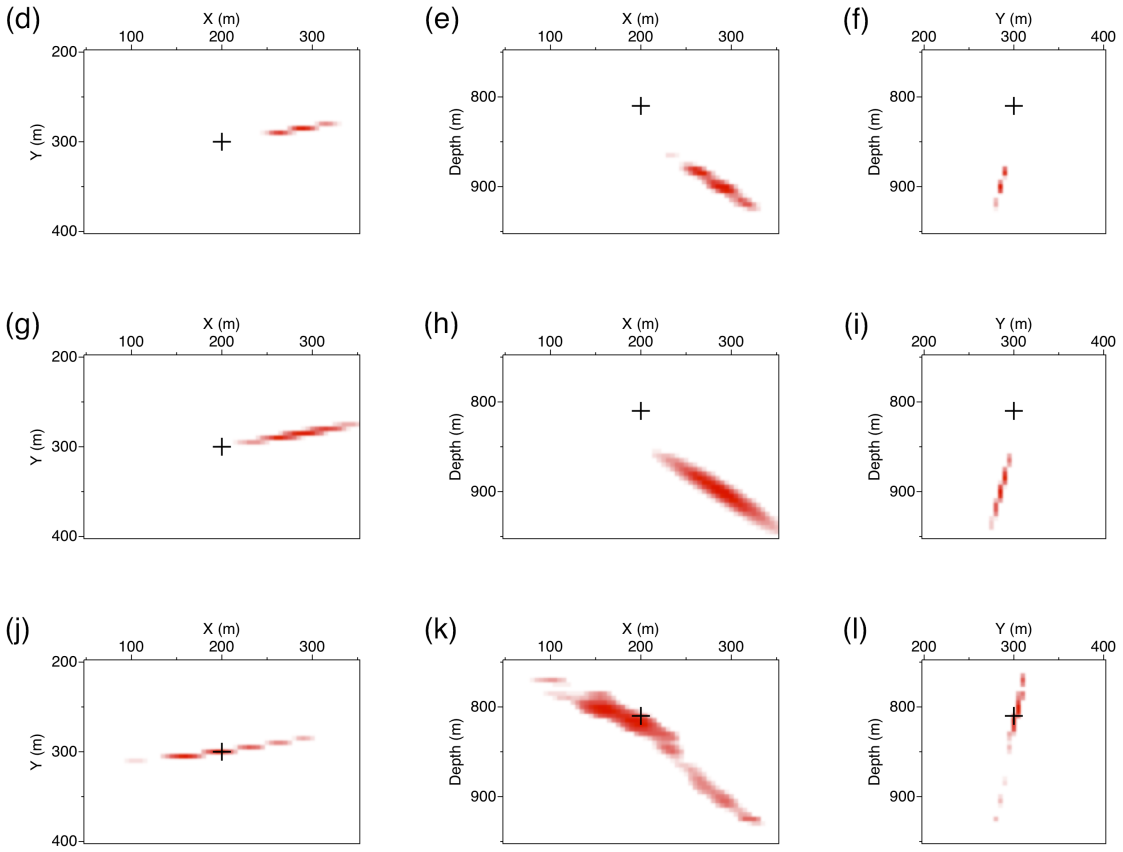

FIGURE 4.2 – Intervalles de confiance 68% basés sur les pdfs marginales pour les plans XY (gauche), ZX (milieu) et ZY (droite). La vraie position de l'hypocentre est indiquée par la croix. En haut : pdf standard pour le meilleur modèle. Au milieu : pdf standard pour le meilleur modèle lorsque les incertitudes de pointé considérées dans la matrice de variance Σ_s de la pdf a posteriori sont augmentées ($+0.001s$ pour les ondes P et $+0.002s$ pour les S). En bas : nouvelle pdf prenant en compte les incertitudes de pointés et de modèle de vitesse. D'après Gesret et al. (2015).

(2012) et Culver et al. (2012) ont démontré que les localisations sont améliorées lorsque les ondes réfractées et les ondes directes sont analysées.

Nous avons proposé d'ajouter les ondes réfléchies aux premières arrivées. En effet la formulation probabiliste est particulièrement adaptée pour intégrer différents types d'information. Dans ces travaux, nous avons considéré les temps de première arrivée $\mathbf{t}_f^{\text{obs}}$ (f pour first), leurs angles azimutaux ϕ_f^{obs} et les temps d'arrivée des ondes réfléchies $\mathbf{t}_r^{\text{obs}}$ (r pour reflected). En considérant ces trois types de données comme mesurées de manière indépendante, la vraisemblance peut s'écrire comme le produit des vraisemblances, c'est-à-dire la fonction coût peut alors s'écrire comme une simple somme :

$$L(\mathbf{l}) = \frac{1}{2}\Big[(\mathbf{t}_f^{\text{obs}} - \mathbf{t}_f^{\text{cal}})^t \Sigma_f^{-1} (\mathbf{t}_f^{\text{obs}} - \mathbf{t}_f^{\text{cal}}) \tag{4.4}$$

$$+(\phi_f^{\text{obs}} - \phi_f^{\text{cal}})^t \Sigma_\phi^{-1} (\phi_f^{\text{obs}} - \phi_f^{\text{cal}}) \tag{4.5}$$

$$+(\mathbf{t}_r^{\text{obs}} - \mathbf{t}_r^{\text{cal}})^t \Sigma_r^{-1} (\mathbf{t}_r^{\text{obs}} - \mathbf{t}_r^{\text{cal}})\Big]. \tag{4.6}$$

Dans cette équation, Σ_f (resp. Σ_ϕ, Σ_r) est la matrice de covariance des temps de première arrivée (resp. des angles azimutaux, des temps d'arrivée des ondes réfléchies). Les temps et angle synthétiques pour un ensemble de paramètres de localisation sont calculés grâce à un tracé de rais décrit dans Belayouni et al. (2015). Comme dans les sections précédentes, l'information a priori sur le temps d'origine est considérée uniforme, et le même formalisme d'intégration analytique sur le temps origine est appliqué pour ce cas multi-arrivées. La pdf marginale sur les paramètres de localisation spatiale se résume donc à :

$$\pi(x, y, z|\mathbf{d}^{\text{obs}}) \propto e^{-\frac{1}{2}(\phi_f^{\text{obs}} - \phi_f^{\text{cal}})^t \Sigma_\phi^{-1} (\phi_f^{\text{obs}} - \phi_f^{\text{cal}})} e^{-\frac{1}{2}(\tilde{\mathbf{t}}^{\text{obs}} - \tilde{\mathbf{t}}^{\text{cal}})^t \Sigma_t^{-1} (\tilde{\mathbf{t}}^{\text{obs}} - \tilde{\mathbf{t}}^{\text{cal}})} \tag{4.7}$$

Dans cette expression, $\tilde{\mathbf{t}}^{\text{obs}}$ est le vecteur des temps de première arrivée et des réfléchies observés moins leur moyenne pondérée, $\tilde{\mathbf{t}}^{\text{cal}}$ le vecteur des temps synthétiques moins leur moyenne pondérée et Σ_t la matrice de covariance des temps de première arrivée et des ondes réfléchies. En pratique, la pdf marginale $\pi(x, y, z|\mathbf{d}^{\text{obs}})$ est estimée par recherche exhaustive sur l'espace des paramètres spatiaux (x, y, z).

Nous avons montré sur des exemples synthétiques que l'ajout de temps d'arrivée des ondes réfléchies permet de diminuer l'incertitude sur la localisation. Ces tests ont été réalisés en générant des données "observées" avec un modeleur de formes d'ondes complètes et la robustesse de l'approche a été validée en ajoutant du bruit aux observations et également en perturbant le modèle de vitesse utilisé pour la localisation. Nous avons considéré une incertitude sur le pointé des ondes P (resp. S) de 5 ms (resp. de 7 ms) et une incertitude sur l'angle azimutal de 5°. Ces valeurs correspondent aux variances contenues dans les diagonales de Σ_t et de Σ_ϕ de l'équation 4.7. La Figure 4.3 représente les localisations avec leurs incertitudes associées lorque seules les premières arrivées (en haut), seules les ondes réfléchies (au milieu), les premières et les réfléchies (en bas) sont utilisées. Pour cet exemple, le modèle de vitesse est 20% plus rapide que le modèle vrai. Cette figure illustre que l'ajout des phases réfléchies résulte en une diminution d'environ 33% des incertitudes. Cela résulte également en une localisation bien plus précise puisque celle-ci se trouve à moins de 60 m de la vraie position de l'événement. Cet exemple montre également que l'addition des réfléchies permet de

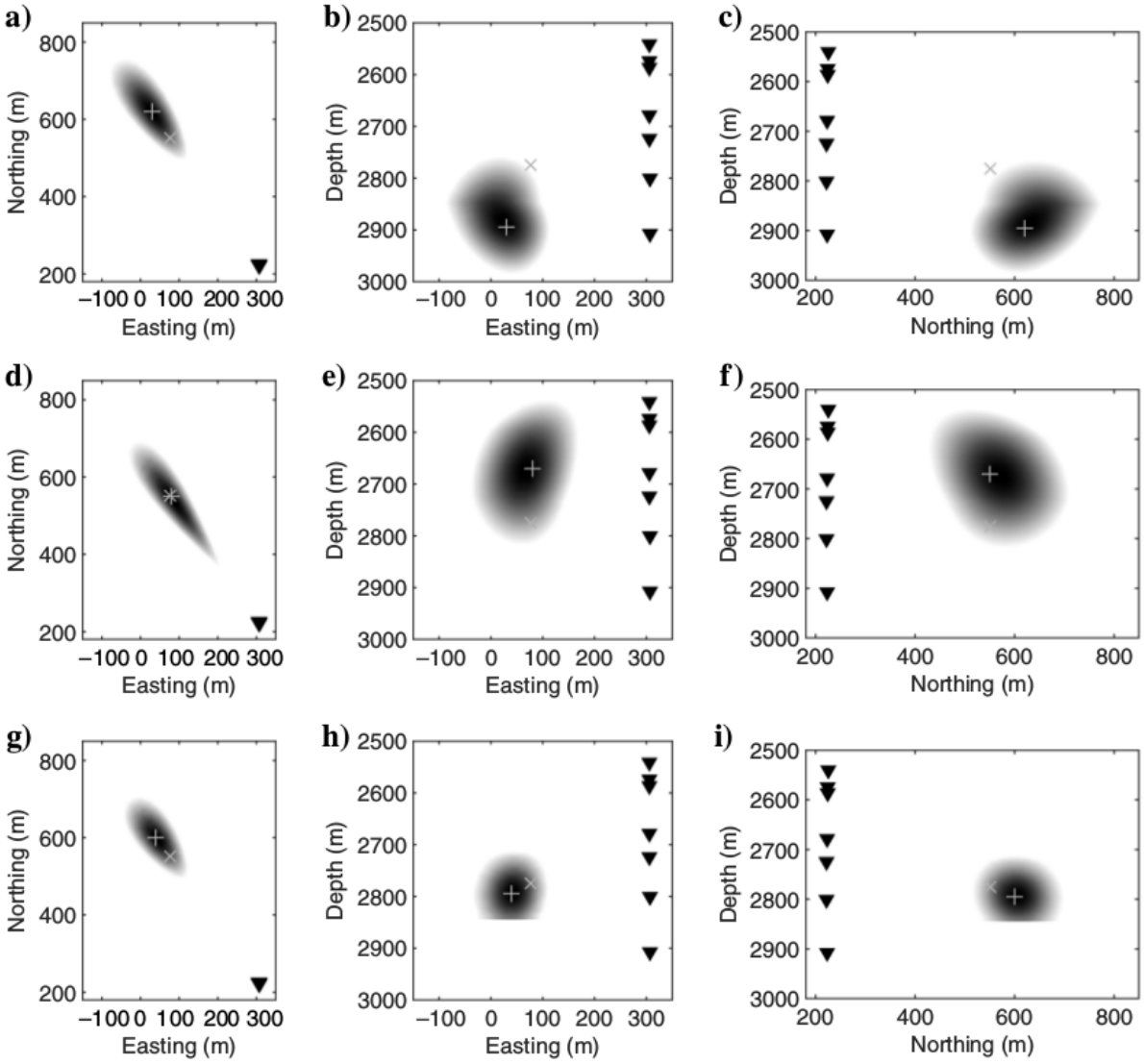

FIGURE 4.3 – Incertitudes associées à la localisation d'un événement microsimique. Intervalles de confiance 68% basés sur les pdf marginales pour les plans NE (gauche), ZE (milieu) et ZN (droite). En haut : pdf avec les premières arrivées seulement. Au milieu : pdf avec les réfléchies seulement. En bas : nouvelle pdf avec les arrivées premières et réfléchies. D'après Belayouni et al. (2015).

compenser l'erreur de localisation due au mauvais modèle de vitesse. Nous avons également illustré l'apport de cette nouvelle formulation sur un jeu de données réelles de Cotton Valley (Belayouni et al., 2015).

4.4 Nouvelle formulation prenant en compte la polarisation des ondes

Dans la section précédente, les erreurs sur les données sont considérées comme indépendantes puisque la vraisemblance s'exprime comme un simple produit des vraisemblances.

Dans le contexte du monitoring microsismique, les capteurs sont le plus souvent alignés verticalement dans un puits, ce qui laisse une incertitude sur l'azimut du séisme (angle entre le Nord et la direction séisme-puits). Afin de lever cette incertitude azimutale, la polarisation de l'onde est mesurée au capteur. C'est dans ce but que les capteurs 3 composantes, pourtant plus coûteux que les capteurs mono-composante, sont déployés dans les puits. La polarisation est alors utilisée soit directement pour donner l'azimut du séisme, soit incluse dans l'inversion, où l'écart entre les polarisations synthétiques et les polarisations observées sera minimisé conjointement. Le processus de localisation nécessite donc de modéliser les temps de trajet et les polarisations synthétiques entre une source et des récepteurs.

Les quelques travaux utilisant une approche probabiliste qui intègre l'information de polarisation considèrent une formulation gaussienne standard avec une fonction coût sur les valeurs angulaires telle qu'introduite dans la section précéndente pour l'azimuth uniquement ou en prenant en compte et l'azimuth et l'inclinaison (Kinscher et al., 2014). Dans ce cas, les erreurs de mesure entre azimuth et inclinaison sont considérées comme indépendantes et ces erreurs ne sont pas forcément très faciles à quantifier. Les angles d'azimuth et d'inclinaison sont déduits de l'analyse de la matrice de covariance. Nous avons proposé une nouvelle formulation qui utilise directement cette matrice de covariance et qui préserve ainsi toute l'information contenue dans cette matrice (Gaucher et al., 2017). Ceci est réalisé en considérant la matrice comme une distribution statistique de la direction d'arrivée de l'onde. En effet, d'après les travaux de Tyler (1987) et Mardia and Jupp (2000) sur les données sphériques, l'échantillon statistique 3D $\mathbf{u}$ représentant la direction d'arrivée instantanée de l'onde suit une distribution Gaussienne centrale angulaire $G(O, \mathbf{C})$ sur une sphère 3D et la probabilité d'observer la matrice de covariance pour une direction donnée $\mathbf{w}$ s'écrit alors :

$$P(\mathbf{C}|\mathbf{w}(\mathbf{X})) \propto |\mathbf{C}|^{-\frac{1}{2}}(\mathbf{w}\mathbf{C}^{-1}\mathbf{w}^t)^{-\frac{3}{2}} \tag{4.8}$$

La Figure 4.4 compare la nouvelle formulation Gausienne Centrale Angulaire (ACG) à la formulation standard pour une localisation avec un seul capteur et uniquement l'information de polarisation. Avec un seul capteur, l'information de polarisation ne permet pas de contraindre la distance au capteur, la plus grande probabilité a une densité constante le long du rai reliant la source à la station. La formulation ACG résulte en un domaine de localisation à 99.7% (surfaces rouges) qui couvre pratiquement l'ensemble du modèle 3D. Ce résultat est cohérent puisque la seule certitude avec cette seule information est que le séisme est localisé dans le modèle, les domaines d'incertitudes semblent trop optimistes avec la formulation standard. Le plus grand intérêt réside dans la prise en compte des corrélations d'erreurs entre azimuth

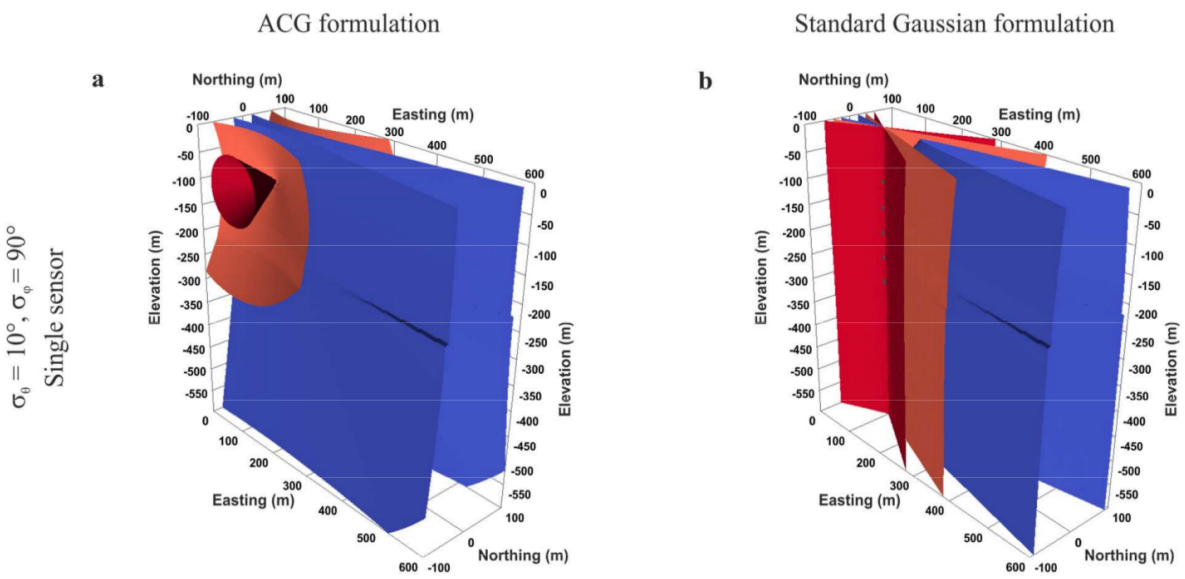

FIGURE 4.4 – Probabilité de localisation d'une source positionnée en $(400, -400)$ en utilisant la polarisation mesurée au capteur $(100, -100)$ avec des incertitudes angulaires considérées de $\sigma_\theta = 10°$, $\sigma_\phi = 90°$. Gauche : Résultat pour la nouvelle formulation ACG. Droite : Résultat pour la formulation standard.

et inclinaison qui mènent à des intervalles de confiance conique. L'utilisation de la formulation standard en considérant des erreurs non corrélées mènent à des surfaces verticales. Cette formulation permet donc de prendre en compte la corrélation des erreurs sans nécessiter de l'estimer.

4.5 Conclusions

La prise en compte de l'incertitude du modèle de vitesse dans la localisation des séismes semble pertinente mais elle est limitée au cas où des informations indépendantes sur le modèle de vitesse sont disponibles. Dans de nombreux contextes (géothermie, volcans, subduction en profondeur) il n'y a pas de tirs actifs. Il serait donc intéressant d'appliquer une tomographie des séismes locaux à quelques événements puis de propager l'incertitude aux autres événements, cet aspect est abordé dans la section 5.1.2. J'y introduis également d'autres applications de propagation d'incertitudes qu'il pourrait être intéressant d'explorer.

Chapitre 5

Perspectives

Dans cette dernière partie, un bref rappel des contributions qui me semblent les plus significatives me permet d'introduire des perspectives à la fois sur le plan méthodologique et sur les plan des applications à des données réelles.

5.1 Extension de la tomographie probabiliste des temps de trajet

Des avancées ont été réalisées par la communauté académique ces dernières années pour estimer les incertitudes de manière fiable, en particulier avec des approches MCMC. Concernant l'imagerie par sismique active, cette approche probabiliste est généralement limitée à la tomographie des temps de trajet car, dans ce cas, le problème direct est résolu de manière efficace. Je souhaiterais investir dans l'aspect méta-modèles et propagation d'incertitudes car ils pourraient constituer des compromis intéressants.

5.1.1 Méta-modèles

Le chapitre 3 a introduit des approches efficaces et parcimonieuses visant à estimer les incertitudes du modèle de vitesse à partir des temps de première arrivée. Dans le chapitre 4, les bénéfices d'ajouter d'autres informations telles que les temps d'arrivée des ondes réfléchies ou les polarisations aux capteurs sur la qualité des localisation des événements sismiques ont été illustrés. Il est dès lors naturel de souhaiter ajouter ce même type d'informations supplémentaires portées par les ondes dans le cas de la tomographie. La différence entre ces deux problèmes inverses réside dans le nombre de paramètres à inférer, seulement trois pour la localisation d'un événement. En effet, même si plusieurs séismes doivent être localisés, les cartes des temps de trajet ou angles ne sont calculées qu'une fois pour chacun des récepteurs puisqu'elles sont les mêmes pour l'ensemble de séismes, ce qui ne requiert pas un long temps de calcul. Les algorithmes d'inversion introduits sont efficaces, mais il semble difficilement envisageable d'ajouter d'autres observables telles que la polarisation en tomographie car le calcul du problème direct s'avère alors trop coûteux. Une piste qui me semble intéressante à envisager est de tester l'utilisation d'approximations statistiques pour remplacer le calcul du problème direct usuellement basé sur des solveurs de type Eikonal.

Les méta-modèles (aussi appelés surrogates) sont largement utilisés dans la quantification d'incertitudes de la sortie de modèles mathématiques de systèmes physiques dues à des paramètres d'entrée incertains (e.g., Sudret, 2007). Généralement, cela consiste en une caractérisation probabiliste des incertitudes sur les paramètres du modèle suivie d'une propagation de ces incertitudes à travers le modèle. Le principe des méta-modèles est de construire une approximation du modèle original qui reproduit la réponse du modèle à des changements dans les paramètres d'entrée incertains. La décomposition en chaos polynomial (Le Maître and Knio, 2010) est un exemple de construction de surrogate qui est particulièrement efficace quand les sorties du modèle varient de manière lisse par rapport aux entrées. Les coefficients de la décomposition en chaos polynomial sont obtenus par une série d'évaluations de la réponse déterministe du modèle, pour des jeux de paramètres d'entrée judicieusement choisis (grille creuse), qui sont ensuite validés sur un jeu de données indépendant.

Dans le cadre d'une collaboration récemment initiée avec Pierre Sochala du BRGM et Olivier Le Maître (Ecole Polytechnique), nous avons réalisé des premiers tests dans le cas de modèle de vitesse simple à 3 couches dans des contextes d'acquisition de sismique réfraction et de monitoring microsismique. Dans ce dernier cas, des tirs réalisés en profondeur sont enregistrés à des capteurs déployés dans un puits vertical (Figure 5.1 gauche). Nous avons testé une approximation basée sur la décomposition en polynômes de chaos pour différents niveaux de la grille qui correspondent à différents ordres des polynômes. Dans ce cas très simple d'un modèle à trois couches seulement, l'approximation est très performante, en témoigne l'évolution de l'erreur relative pour le jeu de validation (Figure 5.1 milieu). Cette approxima-

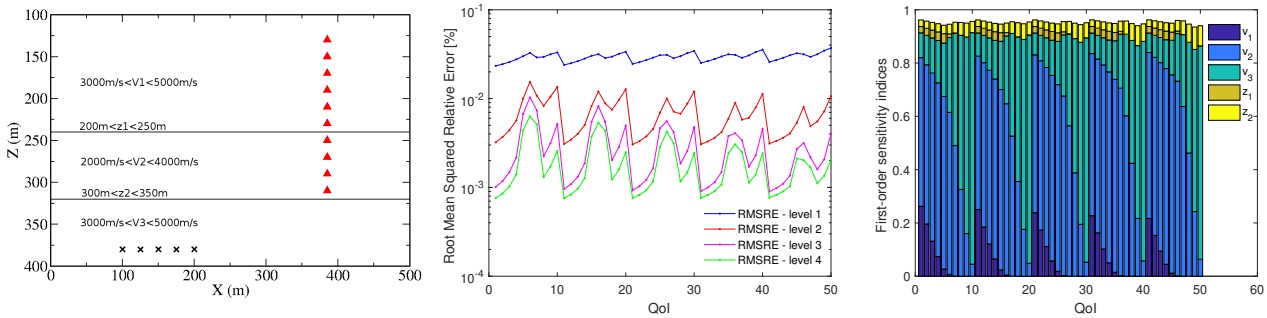

FIGURE 5.1 – Gauche : Géométrie d'acquisition (croix : sources, triangles : capteurs). Milieu : Erreurs relatives entre temps générés par l'Eikonal et ceux générés par le surrogate pour les 50 données et pour différents niveaux du polynôme de chaos. Indices de sensibilité du premier ordre pour les 50 données.

tion permet de mener une analyse de sensibilité basée sur l'estimation de la contribution de chaque paramètre d'entrée sur la variance de la quantité d'intérêt (Sobol, 1993; Homma and Saltelli, 1996), ici les temps d'arrivée. Cette analyse peut être menée de manière efficace en se basant sur les surrogates pour échantilloner l'espace des paramètres d'entrée. La variance totale peut se décomposer en termes d'indices de premier ordre dépendant d'un paramètre seulement plus des termes de variances dependant des interactions entre paramètres. Un paramètre d'entrée a de l'influence si son indice de premier ordre est important (proche de 1) alors qu'il a une influence faible si son indice total est proche de 0. De plus, la différence entre l'indice total et l'indice de premier ordre mesure l'interaction du paramètre. Les indices

de sensibilité de premier ordre sont représentés sur la figure 5.1 (droite). Les indices ont ici été directement calculés des expansions polynomiales (Crestaux et al., 2009). La somme des indices de premier ordre étant proche de 1 pour les 50 données implique une faible interaction entre les paramètres. Cette qualité du surrogate permet ainsi de réaliser très aisément une inversion stochastique puisque les temps sont calculés quasi instantanément.

Ces résultats prometteurs permettent d'envisager d'introduire d'autres observables que les temps de première arrivée dans la tomographie stochastique. C'est une thématique particulièrement importante ; en effet les polarisations et amplitudes des premières arrivées pourraient être ajoutées afin de diminuer les incertitudes sur le modèle de vitesse.

L'inconvénient de ce type d'approximation statistique est qu'elle est limitée au nombre de paramètres (une trentaine) et ne permet donc pas d'application directe à des modèles autres que ceux à couches typiques du monitoring microsismique. La piste que nous allons explorer se base sur une réduction du champ de vitesse via une décomposition Karhunen-Loeve (Le Maître and Knio, 2010) qui permettrait d'inférer ces coefficients du champ.

5.1.2 Propagation d'incertitudes

Dans le chapitre 4, les incertitudes du modèle de vitesse (obtenues par tomographie stochastique) ont été propagées aux incertitudes de localisation des événements sismiques. Cette approche est cependant actuellement limitée au cas où des tirs actifs sont disponibles (dans le contexte de la géophysique d'exploration) pour réaliser la tomographie. Dans de nombreux contextes tels qu'en géothermie, seule la sismicité naturelle ou induite est enregistrée. Dans les perspectives de recherche, je souhaiterais me focaliser sur le développement d'une approche de tomographie stochastique des séismes afin d'inverser conjointement le modèle de vitesse et la position des hypocentres. Agostinetti et al. (2015) ont récemment proposé une telle tomographie stochastique 3D des séismes mais celle-ci a nécessité un mois de temps de calcul pour 770 événements et une paramétrisation du modèle de vitesse avec 100 cellules de Voronoi. Haugmard (2016) ont inversé conjointement la localisation de 300 séismes et 30 paramètres structuraux. Une alternative pour inverser conjointement des modèles de vitesse 3D et des paramètres hypocentraux serait de développer une approche qui vise à estimer les incertitudes du modèle de vitesse en utilisant une sélection d'événements sismiques puis de propager les incertitudes de vitesse aux autres événements. Cela devrait permettre de réduire significativement le temps de calcul. Une question primordiale sera la sélection de l'ensemble de séismes utilisé par la tomographie. Pour être appliquée à des cas plus généraux que les modèles à couches souvent utilisés en fracturation hydraulique, une paramétrisation parcimonieuse du modèle de vitesse en 3D devra être utilisée, en étendant par exemple la paramétrisation basée sur des cellules de Johnson-Mehl de la 2D (section 3.4.2) à la 3D. La tomographie des séismes locaux permettra d'ouvrir un champ beaucoup plus large d'applications puisqu'elle s'affranchit des tirs actifs. J'espère que cela permettra alors d'appliquer l'approche probabiliste à des jeux de données réelles tels que ceux acquis dans le contexte minier ou en géothermie et aussi à une plus vaste échelle par les observatoires ou les déploiements temporaires financés dans le cadre de projets nationaux/internationaux.

La propagation d'incertitudes du modèle de vitesse à l'estimation de mécanisme au foyer devrait pouvoir être appliquée sans difficulte notoire. En effet des formulations probabilistes de l'estimation des mécanismes au foyer sont couramment utilisées mais ce à modèle de

vitesse fixé (e.g., Godano et al., 2009). La même démarche qu'introduite dans la section 4.2 devrait donc fonctionner si des données indépendantes de calibration du modèle de vitesse sont disponibles en ajoutant les paramètres de mécanisme aux paramètres hypocentraux dans la distribution des paramètres sachant les observations (équation 4.3).

La propagation d'incertitudes me semble également être une piste intéressante à tester dans des applications où les approches déterministes doivent être utilisées actuellement pour des raisons de temps de calcul et qui nécessitent un modèle de vitesse initial issu de la tomographie des temps de trajet.

L'estimation d'incertitudes est primordiale dans le domaine de la caractérisation de réservoirs, en particulier les estimations volumétriques et de profondeur doivent être fiables. En effet ces estimations peuvent être utilisées pour calculer des intervalles de confiance qui sont cruciaux dans la prise de décision en Exploration et Production, tels que la situation d'un nouveau puits ou dans la définition de la stratégie de production. La société Seisquare a développé des outils qui permettent de prendre en compte l'incertitude des données interprétées de sismique réflexion dans la caractérisation du réservoir, par exemple en matière d'estimations de toit ou base du réservoir ou en matière d'estimations volumétriques. Cependant, actuellement, les incertitudes d'entrée du workflow en termes d'incertitudes sur les temps/profondeurs des horizons pointés sur les images sismiques sont le plus souvent peu réalistes. Ces incertitudes sont difficiles à estimer puisque les profondeurs d'horizons sont issues de plusieurs étapes de traitement et interprétation des données de sismique réflexion. En effet un modèle de vitesse doit d'abord être estimé puis les données sont transformées en sections migrées sur lesquelles les horizons principaux doivent ensuite être pointés. L'interprétation structurale à partir des images sismiques n'étant elle-même pas unique. Il pourrait être intéressant de quantifier l'incertitude liée au modèle de vitesse issu de la tomographie puis de propager ces incertitudes du modèle de vitesse utilisé dans la migration à l'incertitude sur les temps d'arrivée/profondeur des horizons pointés. Cette approche sera testée dans le cadre d'une prochaine thèse, que je co-encadrerai, menée par un salarié de la société Seisquare.

Enfin il serait aussi intéressant d'intégrer la formulation bayésienne dans le cadre des approches qui prennent en compte plus de physique, en particulier les limites en fréquence des données, comme l'inversion des formes d'onde (Tarantola, 1986; Virieux and Operto, 2009) et ses extensions récentes (Chauris and Cocher, 2017). Les temps de calcul nécessaire à la résolution du problème direct et le nombre de paramètres étant encore trop grand pour envisager une inversion de formes d'onde stochastique, un premier pas serait de quantifier l'incertitude associée à l'incertitude du modèle de vitesse initial utilisé dans l'inversion de formes d'ondes. Ce modèle de vitesse initial "grande longueur d'onde" est issu de la tomographie des temps de trajet. L'incertitude de ce modèle de vitesse pourrait donc être quantifiée par tomographie probabiliste avec les outils existants (chapitre 3) puis propagée à l'inversion de forme d'onde en utilisant un ensemble de modèles initiaux distribués de manière proportionnelle à la distribution a posteriori estimée par tomographie stochastique.

5.2 Imagerie haute résolution du rift de Corinthe et quantification d'incertitudes

Cette dernière section introduit des perspectives proposant des approches méthodologiques afin de caractériser la structure fine des hétérogénéités sous le rift de Corinthe (Grèce). Ces travaux seront menés dans le cadre de collaborations avec Hélène Lyon-Caen de l'ENS, Mark Noble de MINES ParisTech ainsi que Christel Tiberi et Stéphanie Gautier de Géosciences Montpellier.

5.2.1 Contexte

La partie Ouest du golfe de Corinthe (Figure 5.2) est une région très active sismiquement qui présente un très grand taux de déformation (taux d'extension N-S du rift d'environ 1.5 cm/an) et l'activité microsismique la plus dense de la région Euro-Méditerranée (environ 10000 événements sismiques localisés chaque année). Cette région a également subi de

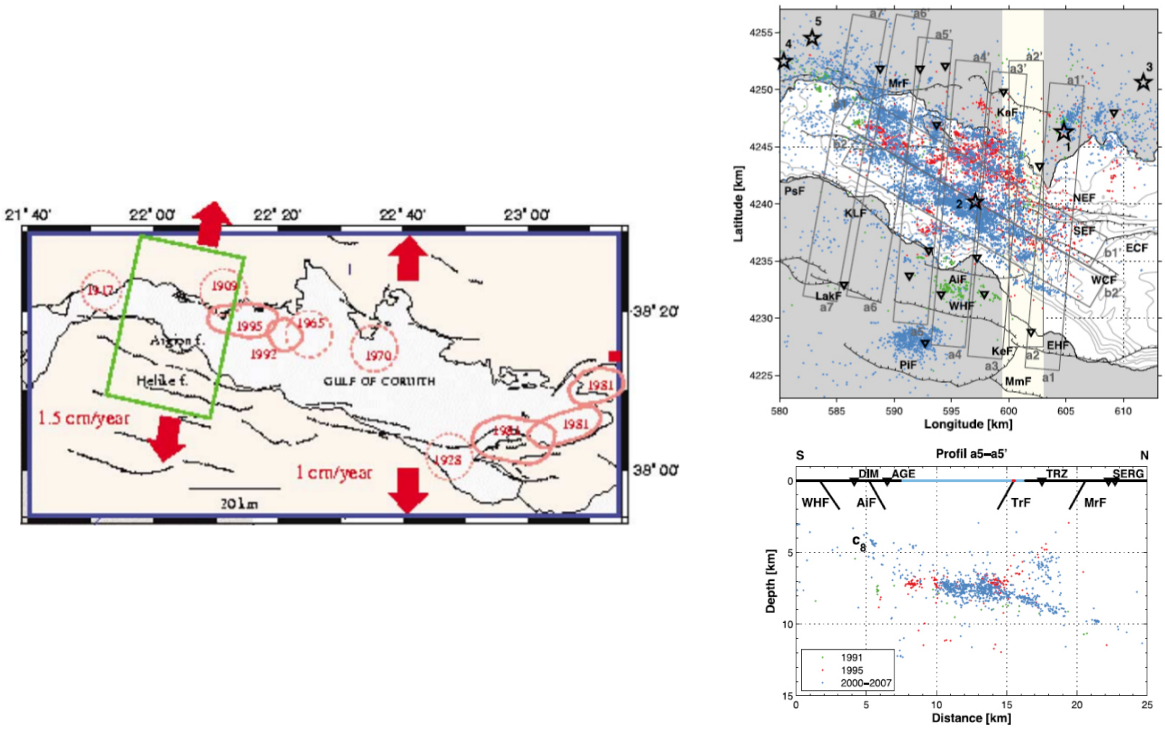

FIGURE 5.2 – Gauche : Carte du rift de Corinthe avec les zones de rupture des plus grands séismes historiques. Le rectangle vert indique la zone du CRL. D'après Cornet et al. (2004). Droite en haut : Carte de la sismicité relocalisée (bleu : 2000–2007, rouge : 1995 et vert : 1991). Les étoiles indiquent les séismes de magnitude supérieure à 5.5 et les triangles la position des stations de CRL. Droite en bas : Coupe verticale a5-a5' des multiplets relocalisés montrant la géométrie des failles normales de pendage $50 - 60°$ à la surface qui s'ancrent à $7 - 8$ km de profondeur sur une faille normale de pendage faible D'après Lambotte et al. (2014).

grand séismes historiques au cours des 18 et 19eme siècles. Plus récemment, deux séismes destructeurs ont eu lieu en 1992 ($M_W = 5.8$) et en 1995 ($M_W = 6.2$). Un ou plusieurs séimes

de magnitude supérieure à 6 sont attendus dans les prochaines décennies. Depuis 2000, un observatoire naturel multidisciplinaire (voir l'instrumentation du Laboratoire du Rift de Corinthe CRL, http ://crlab.eu) a été déployé visant, entre autres, à comprendre les mécanismes de fracturation et de nucléation des séismes dans le rift de Corinthe. Cet observatoire fait partie des zones sismiques les plus instrumentées mondialement et constitue une base de données exceptionnelles. Ce réseau a permis d'identifier de nombreux essaims sismiques dans la partie Ouest du rift de Corinthe qui montrent des pulsations d'activité sur différentes échelles spatiales et temporelles et qui sont localisés à $5 - 10$ km de profondeur à la racine des failles normales majeures (e.g., Rigo et al., 1996; Rietbrock et al., 1996). La migration temporelle observée suggère de la diffusion de pression de pores dans des roches perméables et fracturées (e.g., Bourouis and Cornet, 2009; Pacchiani and Lyon-Caen, 2010). Des analyses récentes d'identification de multiplets, de relocalisation d'événements et d'estimation des mécanismes au foyer (Lambotte et al., 2014; Godano et al., 2014) ont permis d'améliorer la cartographie de la structure en profondeur avec la présence d'une couche microsimique de $1 - 3$ km d'épaisseur de faible pendage vers le N entre 5 et 9 km de profondeur (Figure 5.2). L'analyse spatio-temporelle de multiplets d'un essaim sismique lié à l'activation de deux failles normales parallèles à pendage Nord a permis à Duverger et al. (2015) d'interpréter cette sismicité comme liée à la migration de pression de pores le long d'une couche perméable et fracturée contenue dans la couche microsismique à plus faible perméabilité. Une zone à fort V_p/V_s imagée par tomographie (Latorre et al., 2004; Gautier et al., 2006) à $8 - 9$ km de profondeur pourrait correspondre au réservoir ayant une pression de pores élevée.

De nombreuses études ont déjà mené à une meilleure compréhension de ces mécanismes mais une meilleure caractérisation de la structure en profondeur reste nécessaire afin d'améliorer la précision de localisation des séismes et de progresser dans l'interpétation mécanique de la sismicité. En effet, la croûte supérieure dans cette zone consiste en une superposition d'unités de composition et rhéologie différentes de quelques kilomètres d'épaisseur, dont une est associée à la sismicité localisée à $7 - 9$ km de profondeur. Cependant, ces unités n'ont pu être imagées avec précision. Il est donc pertinent de tester si une anlyse haute-résolution des RF permettrait de contraindre la position et la nature des interfaces associées à ces limites d'unités.

5.2.2 Résultats préliminaires

Dans le cadre du post-doctorat de Maxime Godano financé par un projet PSL entre MINES ParisTech et l'ENS et du stage de Master 1 d'Ibrahim Almarouni, un premier traitement des données aux stations du CRL a donné des résultats très prometteurs. L'automatisation des scripts de Seismic Handler a permis de traiter des milliers de téléséismes enregistrés aux 16 stations large-bande (Figure 5.3 gauche) sur la période $2010 - 2018$ en un temps très raisonnable. Par exemple, la figure 5.3 représente les RF Q (milieu) et T (droite) obtenus pour les meilleurs 67 téléséismes enregistrés à la station SERG.

Cette analyse permet d'identifier la signature du Moho Egéen (labellisé 3), du toit du slab Hellénique (labellisé 4) mais aussi la présence d'une couche superficielle (labellisée 1), d'une interface intracrustale et/ou de multiple (labellisée 2). Le temps d'enregistrement étant de plusieurs années, ces données s'adaptent tout à fait à la sommation de RF par station ayant un grand nombre des téléséismes de même origine (type Kuril ou Japon) afin d'améliorer le

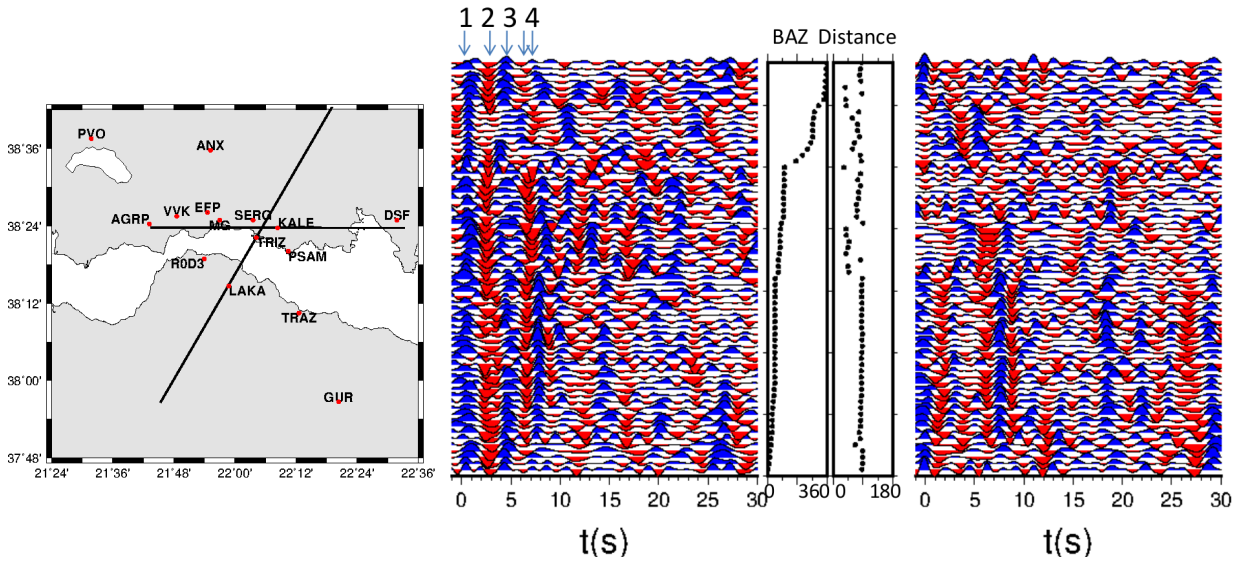

FIGURE 5.3 – Gauche : carte des stations large bande du CRL avec les 2 profils indiqués. RF Q (milieu) et T (droite) obtenues pour 67 téléséismes enregistrés à la station SERG, classées par ordre croissant de backazimut. Les labels 1 à 4 indiquent des conversions citées dans le texte.

rapport signal sur bruit puis de réaliser des profils (indiqués sur la figure 5.3 gauche) de cette sommation de RF, un dans la direction Ouest-Est et un dans la direction de pendage du slab (Figure 5.4).

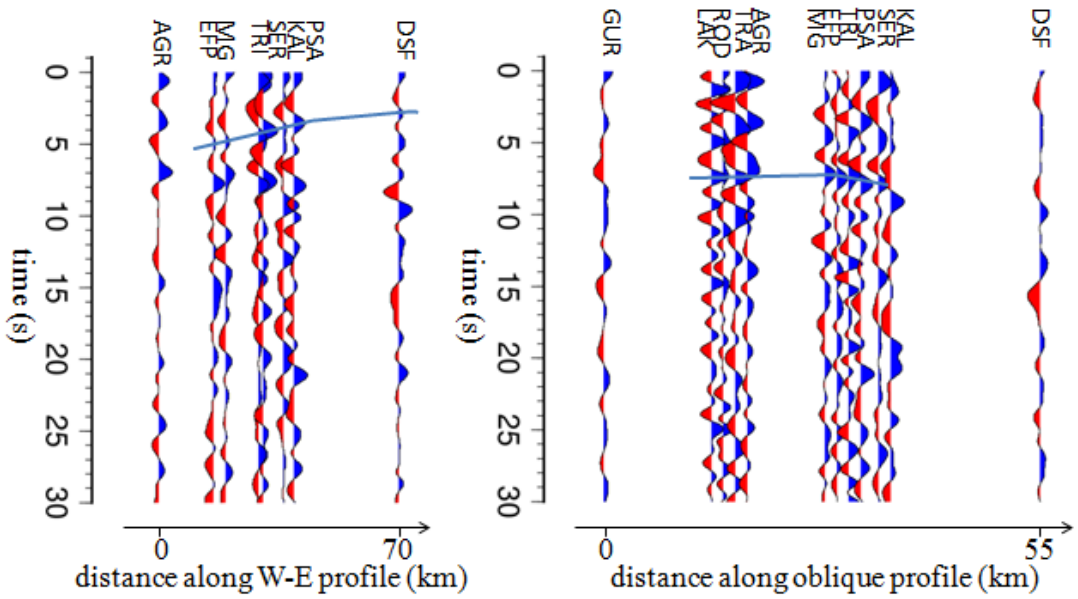

FIGURE 5.4 – Profils de RF sommées dans la direction Ouest-Est et dans la direction de pendage du slab Hellénique.

Le profil Ouest-Est illustre l'approfondissement du Moho Egéen d'environ 10 km vers l'Est, résultat cohérent avec Tiberi et al. (2001); Zelt et al. (2005); Sachpazi et al. (2007). Le profil NNE illustre lui un approfondissement du toit du slab d'environ 20 km. Ces résultats préliminaires donnent déjà des indications particulièrement intéressantes dans la zone du rift à une échelle globale mais surtout ils incitent à exploiter la richesse de ces données. En effet, la signature en conversion montre bien plus que la signature du Moho Egéen et du toit du slab tels que des signaux d'interfaces intracrustales, des variations de temps d'arrivée du Moho Egéen et du toit du slab fonction du backazimut et également du signal sur la composante tranverse. Dans la suite, je propose donc des méthodologies pour utiliser ces informations portées par les données.

5.2.3 Caractérisation des interfaces intracrustales

Il est clair qu'un signal positif vraisemblablement associé à une couche sédimentaire (labellisé 1 sur la figure 5.3) est présent mais un lobe négatif est systématiquement observé avant l'arrivée du Moho (labellisé 2). Ce négatif peut être la signature d'un multiple de la première interface ou une interface où la vitesse diminue ou l'interférence des deux. Pour statuer, il sera nécessaire d'améliorer la résolution et donc d'analyser le signal à plus haute fréquence (Figure 5.5). Une stratégie intéressante à tester sera de calculer les RF, non pas pour des téléséismes mais pour des séismes de profondeur intermédiaire, en effet le contenu haute fréquence de ce type de séismes permet d'améliorer la résolution (Calkins et al., 2006) et donc potentiellement d'imager par exemple la couche sismique d'environ 2 km d'épaisseur. L'analyse multi-échelle met ici en évidence plusieurs signaux de converties primaires et leurs

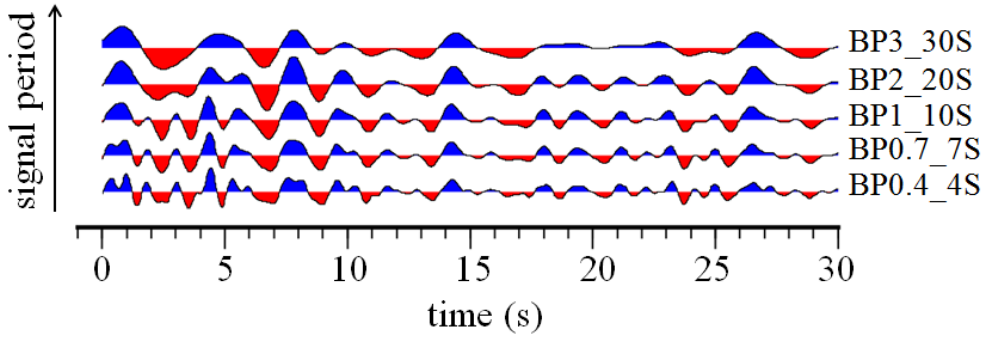

FIGURE 5.5 – Analyse multi-échelle de RF Q sommées sous la station SERG. Les filtres utilisés sont indiqués sur la droite.

multiples. Il semble pertinent de s'orienter vers la modélisation. Une fois le filtrage optimal déterminé par analyse multi-échelle, l'angle d'émergence $2f$ sera déterminé en recherchant l'angle qui annule la composante Q en $t = 0$ s ou en calculant la matrice de covariance. Cette information est rarement utilisée bien qu'elle porte une information importante sur la structure, en effet $p = \sin(f)/V_s(1)$ où p est le paramètre du rai qui dépend de la distance épicentrale et qui est connu et $V_s(1)$ la vitesse de propagatation des ondes S dans la première couche. Il est en effet primordial de commencer la modélisation par les interfaces les moins

profondes puisque toute modification d'une interface au-dessus modifie les temps d'arrivée des conversions suivantes. La difficulté réside dans la mesure, est-ce possible de trouver un filtrage qui permet de diminuer le bruit et d'éviter les interférences avec les ondes converties à des profondeurs très superficielles ?

L'approche multi-échelle a le potentiel pour caractériser la nature de la discontinuité. En effet dans le chapitre 2, j'ai illustré que l'évolution de l'amplitude en fonction de la période dominante révèle le dégré d'homogénéité de la singularité, c'est-à-dire, une pente de 1 correspond à un gradient (Figure 5.6 gauche) alors qu'une pente de 0 indique une fonction marche mais des singularités qui peuvent avoir un degré d'homogénéité différent d'un entier peuvent également être caractérisées par analyse en ondelettes. Ce type de fonctions auto-similaires a été proposé par Wapenaar (1998) pour paramétriser les réflecteurs en sismique réflexion :

$$V(z) = V_1 + (V_2 - V_1) \times \left(\frac{z - z_1}{z_2 - z_1} \right)^{\alpha} \tag{5.1}$$

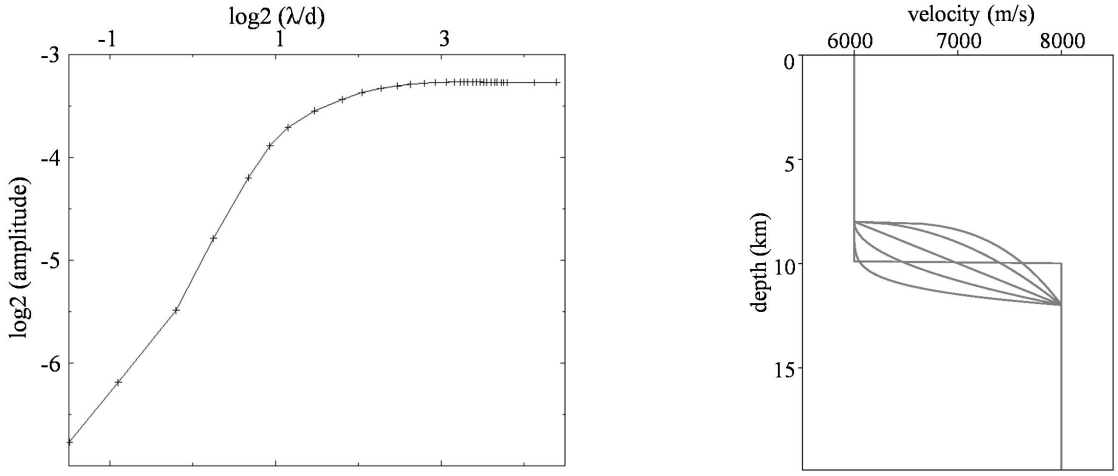

FIGURE 5.6 – Gauche : évolution de l'amplitude de la convertie en fonction de $\lambda/d = T_b/\tau$ pour une hétérogénité de type gradient (degré d'homogénéité $\alpha = 1$). Droite : profils de vitesse correspondant à différents degrés d'homogénéité.

Ce type de discontinuité (Figure 5.6) pourrait par exemple représenter une zone de variation graduelle de la vitesse due à la présence de fluide. J'ai jusqu'ici limité mes analyses multi-échelle de données réelles aux temps d'arrivée des ondes converties mais l'évolution de leurs amplitudes en fonction de la fréquence peut aussi se révéler très informative. La difficulté dans l'application à des données réelles réside dans le fait que lorsque différents filtres sont appliqués aux sismogrammes, les RF L obtenues ne constituent pas une vraie famille d'ondelettes due à des distorsions du signal. Ker et al. (2012) ont rencontré ce type de difficultés dans le contexte de la sismique réflexion et ont proposé une approche de correction de source qu'il me semble intéressant de tester dans le contexte des ondes converties.

Une avancée dans la caractérisation de la nature des hétérogénéités pourrait également s'appliquer à la caractérisation du Moho, aux limites de croûte océanique au toit des slab, par exemple présence de matériel serpentinisé où l'on peut attendre des évolutions graduelles de

la vitesse telles que représentées sur la Figure 5.6, et même à des discontinuités plus profondes en investiguant par exemple la nature de la limite Lithosphère-Asténosphère.

5.2.4 Inversion probabiliste des temps et polarités des converties

La mutualisation logique de l'ensemble des travaux présentés dans ce manuscrit est d'appliquer l'inversion probabiliste aux RF. Cette idée n'est pas nouvelle puisque le récent essor des approches stochastiques en géophysique a été en partie initié dans le cadre d'applications à ces ondes converties (e.g., Bodin et al., 012b) car la simplicité de la paramétrisation du profil de vitesse (modèles à couches) en fait un candidat adapté à l'inversion stochastique.

Moho Egéen : Estimation d'incertitudes d'épaisseur, de V_p et V_p/V_s

L'approche certainement la plus populaire pour caractériser la structure crustale est le stacking h-k (Zhu and Kanamori, 2000). Il est impossible de lister toutes les publications qui ont utilisé cette méthode pour estimer la profondeur du Moho et le V_p/V_s dans la couche au-dessus. Le principe repose sur la recherche des valeurs de h et V_p/V_s qui permettent de maximiser l'amplitude du stack des ondes converties Ps et de leurs multiples. Cette méthode présente l'avantage de ne pas nécessiter d'identifier les phases. Cependant, récemment Woelbern and Rümpker (2017) ont illustré la sensibilité des résultats aux paramètres d'entrée tels que le modèle de vitesse P ou la présence d'interfaces crustales. Dans le contexte de zone de subduction, une difficulté supplémentaire est due à la convertie de forte amplitude au Moho du slab qui peut être considérée comme un multiple du Moho de la plaque supérieure. Par exemple, pour des RF calculées à la station PSAM (Figure 5.7 gauche), la méthode h-k contraint une épaisseur de croûte de 20 km associée à un V_p/V_s de 2 (Figure 5.7 milieu) liée à une interprétation de multiple du Moho Egéen à 8 s, cette arrivée correspondant en réalité à la convertie au Moho du slab Hellénique.

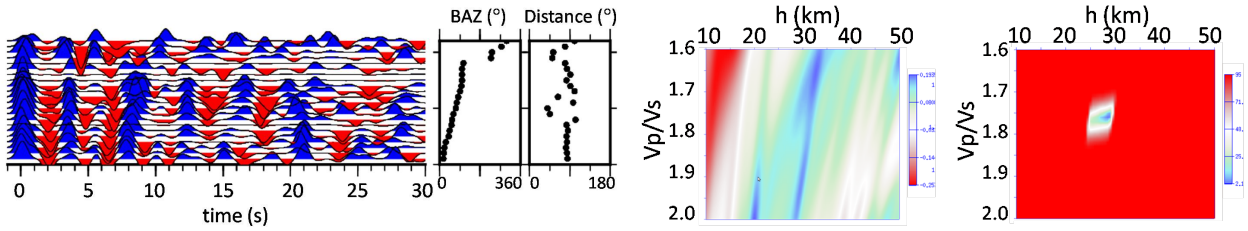

FIGURE 5.7 – Gauche : RF calculées à la station PSAM, classées par ordre croissant de backazimut. Résultats de la "grid search" avec la méthode h-k (milieu) de Zhu and Kanamori (2000) et avec la méthode proposée (droite).

Une méthode qui me semble plus pertinente est de pointer la primaire et son multiple, visible sur la figure à 3.5 s et 12.3 s, puis de réaliser une "grid search" sur h, V_p/V_s et V_p qui permet d'estimer une profondeur de 28 km pour un $V_p/V_s = 1.78$ (Figure 5.7 droite) correspondant à un misfit minimal entre temps d'arrivée observés et temps d'arrivée synthétiques. De plus cette approche permet de prendre en compte fidèlement l'incertitude sur l'observation, ici l'incertitude sur le pointé des converties Ps et Pps et de la transformer en incertitudes a posteriori sur les paramètres V_p, V_p/V_s et h. Dans l'approche classique type h-k, une seule

vitesse V_p est généralement considérée ou une méthode bootstrap est testée pour estimer l'incertitude (e.g., Plasman et al., 2017).

Dans beaucoup d'inversions transdimensionnelles des RF, seule la vitesse V_s est inversée, or le ratio V_p/V_s (ou V_p) choisi va fortement influencer les profondeurs d'interfaces retrouvées. Ces approches reposent sur l'inversion de la forme d'onde complète des RF et peuvent souffrir des mêmes limitations que l'approche de stacking h-k illustrées par Woelbern and Rümpker (2017) : l'influence du modèle de vitesse V_p considéré lorsque celui n'est pas inversé, erreurs dues à des amplitudes maximales de sommations de phases se convertissant à des interfaces différentes. Il me semble plus fiable de se concentrer sur les temps d'arrivée des ondes converties même si cela nécessite préalablement de les pointer.

Cet exemple démontre que, dans certains cas, un regard sur les données, même si cela peut paraître fastidieux, permet de diminuer le risque de mauvaise interprétation. Je souhaiterais donc appliquer cette inversion des temps d'arrrivée des Ps et Pps à chacune des stations du CRL.

Slab Hellénique : Estimation d'incertitudes d'épaisseur, de Vp et Vp/Vs et de pendage

Il est particulièrement intéressant de travailler sur cette zone puisqu'elle se trouve à l'aplomb de la zone de transition attendue entre la subduction continentale au Nord et la subduction océanique au Sud.

La grande base de données permet d'identifier clairement les converties Ps au toit du slab mais très certainement également les ondes multiples Pps et Pss converties au toit et à la base de l'inclusion au toit du slab. Ce jeu de données paraît donc idéal pour appliquer l'approche multi-échelle des ondes primaires et multiples introduite dans la section 2.2.3. En effet, l'approche multi-échelle permettra d'identifier le domaine de non-interaction et donc d'estimer de manière fiable le rapport V_p/V_s dans la croûte océanique en se plaçant dans un domaine de plus haute fréquence que celui classiquement utilisé dans le le traitement des téléséismes.

Le toit du slab est penté, dans la section 2.3, j'ai présenté une approche permettant de contraindre sa géométrie mais sans estimer les incertitudes. L'expérience acquise dans la géophysique stochastique me pousse à souhaiter incrémenter cette méthode en formulant ce problème inverse de manière Bayesienne. Le misfit des temps avait déjà été exprimé mais il serait intéressant de le combiner à un misfit des polarités sur la composante transverse. Pour ce faire, la formulation utilisée dans l'inversion des mécanismes au foyer me semble adaptée. En effet, la polarité du premier mouvement p_i est soit positive soit négative et une formulation probabiliste de la polarité a été proposée par Brillinger et al. (1980) puis utilsée par quelques auteurs tels que (Zollo and Bernard, 1991; Wéber, 2018).

$$\pi(\mathbf{p}|\mathbf{m}) = \prod_{i=1}^{N_p} \psi_i^{(1+p_i)/2}(1-\psi_i)^{(1-p_i)/2}, \tag{5.2}$$

où N_p correspond au nombre de polarités observées et ψ_i est donné par :

$$\psi_i = \gamma_i + (1-2\gamma_i)\Phi\left(\frac{A_i(\mathbf{m})}{\sigma_i}\right). \tag{5.3}$$

Ici $\Phi(.)$ est la fonction de distribution cumulée de la distribution normale et $A_i(\mathbf{m})$ l'amplitude théorique. γ_i définit la probabilité que la lecture de polarité est erronée, quant à σ_i, il décrit les erreurs de modélisation. Il suffira en effet de remplacer le calcul analytique 1D par un solveur 3D (par exemple "ray3d" de Owens ou avec la méthode de Frederiksen and Bostock (2000)). De plus la structure peu profonde obtenue par modélisation pourra aussi être prise en compte. Ceci me semble une avancée intéressante car une des difficultés rencontrées dans les différentes approches est la non prise en compte de la structure 3D que ce soit en inversion de formes d'onde ou en migration.

5.3 Conclusion

Pour conclure sur la partie scientifique de ce manuscrit, j'ai essentiellement dédié ces dernières années à des développements méthodologiques. Dans les prochaines années, je continuerai très certainement cette démarche avec toujours un souhait d'analyser des données réelles car, à mon sens, ces développements n'ont un sens que s'ils peuvent être appliqués à des données réelles. Le rift de Corinthe est une zone idéale pour tester les développements méthodologiques d'analyse d'incertitudes des RF. De plus son étendue géographique permet de combler la lacune entre l'échelle de la zone de subduction et l'échelle du réservoir. J'espère participer à une avancée dans l'imagerie haute résolution et la quantification d'incertitudes dans cette zone par analyse des RF mais aussi par tomographie des séismes locaux. Idéalement l'inversion conjointe devrait permettre de construire une image 3D très fine et donc de progresser dans la compréhension de la sismicité très particulière de cette région.

J'espère également appliquer les développemets proposés à des données recueillies à des stations sismologiques dans le cadre du projet HATARI (HAzard in TAnzanian Rift) porté par Géosciences Montpellier. Nous travaillons actuellement avec Christel Tiberi dans le but d'améliorer le protocole de traitement des RF en associant les avantages de Seismic Handler et de la déconvolution itérative dans le domaine temporel de Ligorria and Ammon (1999). Nous espérons améliorer la résolution de l'imagerie en profondeur des structures de la croûte et de la lithosphère pour mieux comprendre les relations entre sismicité et magmatisme et également investiguer l'influence de la présence de fluides.

Enfin je souhaiterais étendre la tomographie stochastique des temps de trajet en travaillant sur les méta-modèles qui pourraient permettre d'ajouter d'autres observations que les temps d'arrivée, cela constituerait un premier pas vers la simulation de la forme d'onde complète. La propagation d'incertitudes est également un sujet qui me semble intéressant pour quantifier l'incertitude due au modèle de vitesse initial dans la migration ou dans l'inversion de formes d'onde complète même si ces problèmes ne peuvent être actuellement résolus par des approches stochastiques. Une collaboration récemment initiée avec l'équipe Systèmes Hydrologiques et Réservoirs et l'UMR METIS (Sorbonne Université) devrait également me permettre de diversifier mes applications en travaillant sur l'inversion probabiliste des ondes de surface dans le but de caractériser des systèmes hydrologiques.

Bibliographie

Abers, G. A., 2000, Hydrated subducted crust at 100–250 km depth : Earth and Planetary Science Letters, **176**, 323–330.

Abers, G. A., J. Nakajima, P. E. van Keken, S. Kita, and B. R. Hacker, 2013, Thermal-petrological controls on the location of earthquakes within subducting plates : Earth and Planetary Science Letters, **369**, 178–187.

Afnimar and K. Koketsu, 2000, Finite difference traveltime calculation for head waves travelling along an irregular interface : Geophys. J. Int., **143**, 729–734.

Agostinetti, N., G. Giacomuzzi, and A. Malinverno, 2015, Local three-dimensional earthquake tomography by trans-dimensional monte carlo sampling : Geophysical Journal International, **201**, 1598–1617.

Alexandrescu, M., D. Gibert, G. Hulot, J.-L. Le Mouël, and G. Saracco, 1995, Detection of geomagnetic jerks using wavelet analysis : Journal of Geophysical Research : Solid Earth, **100**, 12557–12572.

Anderson, H. and J. Jackson, 1987, Active tectonics of the adriatic region. : Geophys. J. R. Astron. Soc., **91**, 937–983.

Andrieu, C., A. Jasra, A. Doucet, P. Del Moral, et al., 2011, On nonlinear markov chain monte carlo : Bernoulli, **17**, 987–1014.

Audet, P. and R. Burgmann, 2014, Possible control of subduction zone slow-earthquake periodicity by silica enrichment : Nature, **510**, 389–92.

Audet, P., M. G Bostock, N. I Christensen, and S. Peacock, 2009, Seismic evidence for overpressured subducted oceanic crust and megathrust fault sealing : Nature, **457**, 76–8.

Audet, P. and Y. Kim, 2016, Teleseismic constraints on the geological environment of deep episodic slow earthquakes in subduction zone forearcs : A review : Tectonophysics, **670**.

Audet, P. and S. Schwartz, 2013, Hydrologic control of forearc strength and seismicity in the costa rican subduction zone : Nature Geoscience, **6**, 852–855.

Baker, J. E., J. B. Minster, G. Zandt, and H. Gurrola, 1996, Constraints on crustal structure and complex moho topography beneath piñon flat, california, from teleseismic receiver functions. : Bull. Seismol. Soc. Am., **86**, 1830–1844.

Belayouni, N., 2013, Nouveaux algorithmes efficaces de modélisation 2d et 3d : Temps des premières arrivées, angles à la source et amplitudes : PhD thesis, Mines ParisTech.

Belayouni, N., A. Gesret, G. Daniel, and M. Noble, 2015, Microseismic event location using the first and reflected arrivals : GEOPHYSICS, **80**, WC133–WC143.

Belhadj, J., T. Romary, A. Gesret, M. Noble, and B. Figliuzzi, 2018, New parameterizations for bayesian seismic tomography : Inverse Problems, **34**, 065007.

Berkhout, A. J., 1977, Least-squares inverse filtering and wavelet deconvolution. : Geophysics,

42, 1369–1383.

Bijwaard, H. and W. Spakman, 1998, Closing the gap between regional and global travel time tomography. : J. Geophys. Res., **103**, 30,055–30,078.

Bocchini, G., A. Brüstle, D. Becker, T. Meier, P. van Keken, M. Ruscic, G. Papadopoulos, M. Rische, and W. Friederich, 2018, Tearing, segmentation, and backstepping of subduction in the aegean : New insights from seismicity : Tectonophysics, **734-735**, 96 – 118.

Bodin, T. and M. Sambridge, 2009, Seismic tomography with the reversible jump algorithm : Geophys. J. Int., **178**, 1411–1436.

Bodin, T., M. Sambridge, K. Gallagher, and N. Rawlinson, 2012b, Transdimensional inversion of receiver functions and surface wave dispersion : Journal of Geophysical Research : Solid Earth, **117**.

Bodin, T., M. Sambridge, N. Rawlinson, and P. Arroucau, 2012a, Transdimensional tomography with unknown data noise : Geophysical Journal International, **189**, 1536–1556.

Bodin, T., H. Yuan, and B. Romanowicz, 2014, Inversion of receiver functions without deconvolution-application to the indian craton : Geophysical Journal of the Royal Astronomical Society, **196**, 1025–1033.

Bottero, A., A. Gesret, T. Romary, M. Noble, and C. Maisons, 2016, Stochastic seismic tomography by interacting markov chains : Geophys. J. Int., **207**, 374–392.

Bourouis, S. and F. H. Cornet, 2009, Microseismic activity and fluid fault interactions : some results from the Corinth Rift Laboratory (CRL), Greece : Geophysical Journal International, **178**, 561–580.

Brillinger, D., A. Udias, and B. A Bolt, 1980, A probability model for regional focal mechanism solution : Bulletin of the Seismological Society of America, **70**, 149–170.

Calkins, J. A., G. Zandt, H. J. Gilbert, and S. L. Beck, 2006, Crustal images from san juan, argentina, obtained using high frequency local event receiver functions : Geophysical Research Letters, **33**.

Calo, M., C. Dorbath, F. H. Cornet, and N. Cuenot, 2011, Large scale aseismic motion identified through 4-d p-wave tomography. : Geophys. J. Int., **186**, 1295–1314.

Cassidy, J., 1992, Numerical experiments in broadband receiver function analysis. : Bull. Seismol. Soc. Am., **82**, 1453–1474.

Chauris, H. and E. Cocher, 2017, From migration to inversion velocity analysis : GEOPHYSICS, **82**, S207–S223.

Clément, C., A. Hirn, P. Charvis, M. Sachpazi, and F. Marnelis, 2000, Seismic structure and the active hellenic subduction in the ionian island. : Tectonophysics, **329**, 141–156.

Coffin, S., Y. Hur, J. S. Abel, B. Culver, R. Augsten, and A. Westlake, 2012, Beyond first arrivals : Improved microseismic event localization using both direct-path and head-wave arrivals : 82nd Annual International Meeting, SEG, Expanded Abstracts.

Cornet, F., P. Bernard, and I. Moretti, 2004, The corinth rift laboratory : Comptes Rendus Geoscience, **336**, 235–241.

Cornet, F., T. Bérard, and S. Bourouis, 2007, How close to failure is a granite rock mass at a 5 km depth ? : International Journal of Rock Mechanics and Mining Sciences and Geomechanics Abstracts, **44**, 47–66.

Crestaux, T., O. Le Maître, and J. M. Martinez, 2009, Polynomial chaos expansion for sensitivity analysis. : Reliab. Eng. Syst. Saf., **94**, 1161–1172.

Culver, B., R. Augsten, S. Coffin, Y. Hur, J. S. Abel, and A. Westlake, 2012, Interpretation of

multipath-analysis localizations of microseismic data : An alberta montney shale example : 82nd Annual International Meeting, SEG, Expanded Abstracts.

Day, A. J., C. Peirce, and M. C. Sinha, 2001, Three-dimensional crustal structure and magma chamber geometry at the intermediate spreading, back-arc valu fa ridge, lau basin-results of a wide-angle seismic tomographic inversion : Geophysical Journal International, **146**, 31–52.

Debski, W., 2010, Seismic tomography by monte carlo sampling : Pure and applied geophysics, **167**, 131–152.

Dettmer, J., S. E. Dosso, T. Bodin, J. Stipčević, and P. R. Cummins, 2015, Direct-seismogram inversion for receiver-side structure with uncertain source–time functions : Geophysical Journal International, **203**, 1373–1387.

Duverger, C., M. Godano, P. Bernard, H. Lyon-Caen, and S. Lambotte, 2015, The 2003–2004 seismic swarm in the western corinth rift : Evidence for a multiscale pore pressure diffusion process along a permeable fault system : Geophysical Research Letters, **42**, 7374–7382.

Eisner, L., P. M. Duncan, W. M. Heigl, and W. R. Keller, 2009, Uncertainties in passive seismic monitoring : The Leading Edge, **28**, 648–655.

Ellsworth, W. L., 2013, Injection-induced earthquakes : Science, **341**.

Flewelling, S. A., M. P. Tymchak, and N. Warpinski, 2013, Hydraulic fracture height limits and fault interactions in tight oil and gas formations : Geophysical Research Letters, **40**, 3602–3606.

Fomel, S., S. Luo, and H. Zhao, 2009, Fast sweeping method for the factored eikonal equation : Journal of Computational Physics, **228**, 6440–6455.

Frederiksen, A. W. and M. G. Bostock, 2000, Modelling teleseismic waves in dipping anisotropic structures : Geophysical Journal International, **141**, 401–412.

Gaucher, E., A. Gesret, and M. Noble, 2017, A New Probabilistic Formulation to Locate Seismic Events From P-Wave Polarization : 79th EAGE Conference and Exhibition, Expanded Abstracts.

Gautier, S., D. Latorre, J. Virieux, A. Deschamps, C. Skarpelos, A. Sotiriou, A. Serpetsidaki, and A. Tselentis, 2006, A new passive tomography of the aigion area (gulf of corinth, greece) from the 2002 data set : pure and applied geophysics, **163**, 431–453.

Gesret, A., N. Desassis, M. Noble, T. Romary, and C. Maisons, 2015, Propagation of the velocity model uncertainties to the seismic event location : Geophys. J. Int., **200(1)**, 52–66.

Gesret, A., A. Hirn, and M. Sachpazi, in prep., How resolving are teleseismic converted waves ?

Gesret, A., M. Laigle, J. Diaz, M. Sachpazi, M. Charalampakis, and A. Hirn, 2011, Slab top dips resolved by teleseismic converted waves in the hellenic subduction zone : Geophysical Research Letters, **38**, L20304.

Gesret, A., M. Laigle, J. Diaz, M. Sachpazi, and A. Hirn, 2010, The oceanic nature of the african slab subducted under peloponnesus : thin-layer resolution from multiscale analysis of teleseismic p-to-s converted waves : Geophysical Journal International, **183**, 833–849.

Geyer, C. J., 1991, Markov chain monte carlo maximum likelihood : E. D. Keramidas (Ed.), Computing Sciences and Statistics : Proceedings of the 23rd Symposium on the Interface, 156–163.

Godano, M., A. Deschamps, S. Lambotte, H. Lyon-Caen, P. Bernard, and F. Pacchiani,

2014, Focal mechanisms of earthquake multiplets in the western part of the Corinth Rift (Greece) : influence of the velocity model and constraints on the geometry of the active faults : Geophysical Journal International, **197**, 1660–1680.

Godano, M., M. Regnier, A. Deschamps, T. Bardainne, and E. Gaucher, 2009, Focal Mechanisms from Sparse Observations by Nonlinear Inversion of Amplitudes : Method and Tests on Synthetic and Real DataFocal Mechanisms from Sparse Observations by Nonlinear Inversion of Amplitudes : Bulletin of the Seismological Society of America, **99**, 2243–2264.

Goupillaud, P., A. Grossmann, and J. Morlet, 1984, Cycle-octave and related transforms in seismic signal analysis : Geoexploration, **23**, 85 – 102. Seismic Signal Analysis and Discrimination III.

Green, P. J., 1995, Reversible jump markov chain monte carlo computation and bayesian model determination : Biometrika, **82**, 711–732.

Hacker, B. R., S. M. Peacock, G. A. Abers, and S. D. Holloway, 2003, Subduction factory 2. are intermediate-depth earthquakes in subducting slabs linked to metamorphic dehydration reactions ? : Journal of Geophysical Research : Solid Earth, **108**.

Halpaap, F., S. Rondenay, and L. Ottemöller, 2018, Seismicity, deformation, and metamorphism in the western hellenic subduction zone : New constraints from tomography : Journal of Geophysical Research : Solid Earth, **123**, 3000–3026.

Hansen, N., S. D. Müller, and P. Koumoutsakos, 2003, Reducing the time complexity of the derandomized evolution strategy with covariance matrix adaptation (CMA-ES) : Evolutionary computation, **11**, 1–18.

Hastings, W. K., 1970, Monte carlo sampling methods using markov chains and their applications : Biometrika, **57**, 97–109.

Haugmard, M., 2016, Détermination non-linéaire des paramètres hypocentraux et structuraux : application à la sismicité intracontinentale du massif armoricain. : PhD thesis, Université de Nantes.

Hauser, J., K. M. Dyer, M. E. Pasyanos, H. Bungum, J. I. Faleide, S. A. Clark, and J. Schweitzer, 2011, A probabilistic seismic model for the european arctic : Journal of Geophysical Research : Solid Earth, **116**.

Hole, J. A. and B. C. Zelt, 1995, 3-D finite-difference reflection traveltimes : Geophys. J. Int., **121**, 427–434.

Homma, T. and A. Saltelli, 1996, Importance measures in global sensitivity analysis of nonlinear models. : Reliab. Eng. Syst. Saf., **52**, 1–17.

Husen, S. and J. Hardebeck, 2010, Earthquake Location Accuracy : Community Online Resource for Statistical Seismicity Analysis.

Husen, S., E. Kissling, N. Deichmann, S. Wiemer, D. Giardini, and M. Baer, 2003, Probabilistic earthquake location in complex three-dimensional velocity models : application to Switzerland : J. geophys. Res., **108(B2)**, 2077–2096.

Husen, S. and R. Smith, 2004, Probabilistic earthquake location in three-dimensional velocity models for the Yellowstone National Park region, Wyoming : Bull. seism. Soc. Am., **94(6)**, 880–896.

Kahle, H.-G., M. Cocard, Y. Peter, A. Geiger, R. Reilinger, A. Barka, and G. Veis, 2000, Gps-derived strain rate field within the boundary zones of the eurasian, african and arabian plates. : J. Geophys. Res., **105**, 23353–23370.

Kennedy, J. and R. Eberhart, 1995, Particle swarm optimization : Proceedings of ICNN'95 -

International Conference on Neural Networks, 1942–1948, IEEE.

Ker, S., Y. Le Gonidec, and D. Gibert, 2012, Multiscale seismic attributes : source-corrected wavelet response and application to high-resolution seismic data : Geophysical Journal International, **190**, 1746–1760.

Kim, Y., G. A. Abers, J. Li, D. Christensen, J. Calkins, and S. Rondenay, 2014, Alaska megathrust 2 : Imaging the megathrust zone and yakutat/pacific plate interface in the alaska subduction zone : Journal of Geophysical Research : Solid Earth, **119**, 1924–1941.

Kim, Y., R. W. Clayton, and J. M. Jackson, 2010, Geometry and seismic properties of the subducting cocos plate in central mexico : Journal of Geophysical Research : Solid Earth, **115**.

Kind, R., G. L. Kosarev, and N. V. Petersen, 1995, Receiver functions at the stations of the german regional seismic network. : Geophys. J. Int., **121**, 191–202.

Kinnaert, X., E. Gaucher, U. Achauer, and T. Kohl, 2016, Modelling earthquake location errors at a reservoir scale : A case study in the upper rhine graben. : Geophys. J. Int., **206**, 861–879.

Kinscher, J., P. Bernard, I. Contrucci, A. Mangeney, J. Piguet, and P. Bigarre, 2014, Location of microseismic swarms induced by salt solution mining : Geophysical Journal International, **200**, 337–362.

Kirkpatrick, S., C. D. Gelatt, M. P. Vecchi, et al., 1983, Optimization by simulated annealing : science, **220**, 671–680.

Kodaira, S., T. Iidaka, A. Kato, J.-O. Park, T. Iwasaki, and Y. Kaneda, 2004, High pore fluid pressure may cause silent slip in the nankai trough : Science, **304**, 1295–1298.

Koren, Z., K. Mosegaard, E. Landa, P. Thore, and A. Tarantola, 1991, Monte carlo estimation and resolution analysis of seismic background velocities : Journal of Geophysical Research : Solid Earth (1978–2012), **96**, 20289–20299.

Lahr, J., 1989, HYPOELLIPSE : A computer program for determining local earthquake hypocentral parameters, magnitude, and first motion pattern (Y2K compliant version) : U.S. Geol. Surv. Open-File Rep., 92pp.

———, 2002, User's Guide to HYPOINVERSE-2000 : a Fortran program to solve for earthquake locations and magnitudes : U.S. Geol. Surv. Open-File Rep., 123pp.

Laigle, M., M. Sachpazi, and A. Hirn, 2004, Variation of seismic coupling with slab detachement and upper plate structure along the western hellenic subduction zone. : Tectonophysics, **391**, 85–95.

Lambotte, S., H. Lyon-Caen, P. Bernard, A. Deschamps, G. Patau, A. Nercessian, F. Pacchiani, S. Bourouis, M. Drilleau, and P. Adamova, 2014, Reassessment of the rifting process in the Western Corinth Rift from relocated seismicity : Geophysical Journal International, **197**, 1822–1844.

Langston, A. C., 1977, The effect of planar dipping structure on source and receiver responses for constant ray parameter. : Bull. Seismol. Soc. Am., **67**, 1029–1050.

———, 1979, Structure under mount rainier, washington, inferred from teleseismic body waves. : J. Geophys. Res., **84**, 4749–4762.

Lapp, D. B., T. J. Owens, and R. S. Crosson, 1990, P-waveform analysis for local subduction geometry south of puget sound, washington. : Pure Appl. Geophys., **133**, 349–365.

Latorre, D., J. Virieux, T. Monfret, V. Monteiller, T. Vanorio, J.-L. Got, and H. Lyon-Caen, 2004, A new seismic tomography of aigion area (gulf of corinth, greece) from the 1991 data

set : Geophysical Journal International, **159**, 1013–1031.

Le Gonidec, Y., D. Gibert, and J. N. Proust, 2002, Multiscale analysis of waves reflected by complex interfaces : Basics principles and experiments. : J. Geophys. Res., **107**, 2184.

Le Maître, O. and O. M. Knio, 2010, Spectral methods for uncertainty quantification with applications to computational fluid dynamics. : Scientific Computation Springer.

Lee, W. and J. Lahr, 1975, HYPO71 (revised) : A computer program for determining hypocenter, magnitude, and first motion pattern of local earthquakes : U.S. Geol. Surv. Open-File Rep., 64pp.

Ligorria, J. P. and C. J. Ammon, 1999, Iterative deconvolution and receiver-function estimation. : Bull. Seismol. Soc. Am., **89**, 1395–1400.

Lomax, A., J. Virieux, P. Volant, and C. Berge-Thierry, 2000, Probabilistic earthquake location in 3D and layered models : Introduction of a Metropolis-Gibbs method and comparison with linear locations : Advances in Seismic Event Location, Thurber, C.H., and N. Rabinowitz (eds.), **228**, 101–134.

Lomax, A., A. Zollo, P. Capuano, and J. Virieux, 2001, Precise, absolute earthquake location under Somma-Vesuvius volcano using a new three-dimensional velocity model : Geophys. J. Int., **146**, 313–331.

Luu, K., M. Noble, A. Gesret, N. Belayouni, and P. F. Roux, 2018, A parallel competitive particle swarm optimization for non-linear first arrival traveltime tomography and uncertainty quantification : Computers and Geosciences, **113**, 81–93.

Luu, K., M. Noble, A. Gesret, and P. Thierry, 2019, Toward large scale stochastic refraction tomography : a comparison of three evolutionary algorithms : accepted in Geophysical Prospecting.

Mallat, S. and W. L. Hwang, 1992, Singularity detection and processing with wavelets. : IEEE Trans. Inf. Theory, **38**, 617–643.

Mardia, K. V. and P. E. Jupp, 2000, Directional statistics : Wiley.

Martin, S., A. Rietbrock, C. Haberland, and G. Asch, 2003, Guided waves propagating in subducted oceanic crust : Journal of Geophysical Research, **108**.

Maxwell, S., 2010, Microseismic : Growth born from success : The Leading Edge, **29**, 338–343.

Menke, W., 2012, Geophysical data analysis : discrete inverse theory : Academic press.

Metropolis, N., A. W. Rosenbluth, M. N. Rosenbluth, A. H. Teller, and E. Teller, 1953, Equation of state calculations by fast computing machines : The journal of chemical physics, **21**, 1087–1092.

Mosegaard, K. and A. Tarantola, 1995, Monte carlo sampling of solutions to inverse problems : J. geophys. Res., **100**, 12431–12447.

Moser, T., T. van Eck, and G. Nolet, 1992, Hypocenter determination in strongly heterogeneous earth models using the shortest path method : J. geophys. Res., **97**, 6563–6572.

Noble, M., A. Gesret, and N. Belayouni, 2014, Accurate 3-d finite difference computation of traveltimes in strongly heterogeneous media : Geophys. J. Int., **199**, 1572–1585.

Oleskevich, D. A., R. D. Hyndman, and K. B. Wang, 1999, The updip and downdip limits to great subduction earthquakes : Thermal and structural models of cascadia, south alaska, sw japan and chile. : J. Geophys. Res., **104**, 14,965–14,991.

Owens, T. J., R. S. Crosson, and M. A. Hendrickson, 1988, Constraints on the subduction geometry beneath western washington from broadband teleseismic waveform modeling. : Bull. Seismol. Soc. Am., **78**, 1319–1334.

Pacchiani, F. and H. Lyon-Caen, 2010, Geometry and spatio-temporal evolution of the 2001 Agios Ioanis earthquake swarm (Corinth Rift, Greece) : Geophysical Journal International, **180**, 59–72.

Pacheco, J. F. and L. R. Sykes, 1992, Seismic moment catalog of large shallow earthquakes, 1900 to 1989 : Bulletin of the Seismological Society of America, **82**, 1306–1349.

Papadopoulos, G. A., I. Baskoutas, and A. Fokaefs, 2014, Historical seismicity of the kyparissiakos gulf, western peloponnese, greece. : Bolletino di Geofisica Teorica ed Applicata, **55**, 389–404.

Papanikolaou, D. J. and L. H. Royden, 2007, Disruption of the hellenic arc : Late miocene extensional detachement faults and steep pliocene-quaternary normal faults–or what happened at corinth ?. : Tectonics, **26**, 5003.

Papazachos, B. C., V. G. Karakostas, C. B. Papazachos, and E. M. Scordilis, 2000, The geometry of the wadati-benioff zone and lithospheric kinematics in the hellenic arc. : Tectonophysics, **319**, 275–300.

Papazachos, C. and G. Nolet, 1997, P and s deep velocity structure of the hellenic area obtained by robust nonlinear inversion of travel times : Journal of Geophysical Research : Solid Earth, **102**, 8349–8367.

Peacock, S. M., 2001, Are the lower planes of double seismic zones caused by serpentine deydration in subducting oceanic mantle ?. : Geology, **9**, 1197–1211.

Pearce, F. D., S. Rondenay, M. Sachpazi, M. Charalampakis, and L. H. Royden, 2012, Seismic investigation of the transition from continental to oceanic subduction along the western hellenic subduction zone : Journal of Geophysical Research : Solid Earth, **117**.

Phillips, W. S., J. T. Rutledge, L. S. House, and M. C. Fehler, 2002, Induced microearthquake patterns in hydrocarbon and geothermal reservoirs : Six case studies, 345–369. Birkhäuser Basel.

Piromallo, C. and A. Morelli, 2003, P wave tomography of the mantle under the alpine-mediterranean area : Journal of Geophysical Research : Solid Earth, **108**.

Plasman, M., C. Tiberi, C. Ebinger, S. Gautier, J. Albaric, S. Peyrat, J. Déverchère, B. Le Gall, P. Tarits, S. Roecker, F. Wambura, A. Muzuka, G. Mulibo, K. Mtelela, M. Msabi, G. Kianji, S. Hautot, J. Perrot, and R. Gama, 2017, Lithospheric low-velocity zones associated with a magmatic segment of the tanzanian rift, east africa : Geophysical Journal International, **210**, 465–481.

Podvin, P. and I. Lecomte, 1991, Finite difference computation of traveltimes in very contrasted velocity models : a massively parallel approach and its associated tools : Geophys. J. Int., **105**, 271–284.

Poliannikov, O. V., M. Prange, A. Malcolm, and H. Djikpesse, 2013, A unified Bayesian framework for relative microseismic location : Geophys. J. Int., **194**, 557–571.

Rawlinson, N., A. Fichtner, M. Sambridge, and M. K. Young, 2014, Chapter one - seismic tomography and the assessment of uncertainty : Advances in Geophysics, **55**, 1–76.

Rawlinson, N., S. Pozgay, and S. Fishwick, 2010, Seismic tomography : A window into deep earth : Physics of the Earth and Planetary Interiors, **178**, 101 – 135.

Rawlinson, N. and M. Sambridge, 2004, Multiple reflection and transmission phases in complex layered media using multistage fast marching method : Geophysics, **69**, 1338–1350.

Reynard, B., J. Nakajima, and H. Kawakatsu, 2010, Earthquakes and plastic deformation of anhydrous slab mantle in double Wadati-Benioff zones : Geophysical Research Letters, **37**,

L24309.

Rietbrock, A., C. Tiberi, F. Scherbaum, and H. LyonCaen, 1996, Seismic slip on a low angle normal fault in the gulf of corinth : Evidence from high-resolution cluster analysis of microearthquakes : GEOPHYSICAL RESEARCH LETTERS, **23**, 1817–1820.

Rigo, A., H. Lyon-Caen, R. Armijo, A. Deschamps, D. Hatzfeld, K. Makropoulos, P. Papadimitriou, and I. Kassaras, 1996, A microseismic study in the western part of the gulf of corinth (greece) : implications for large-scale normal faulting mechanisms : Geophysical Journal International, **126**, 663–688.

Robert, C. and G. Casella, 2013, Monte carlo statistical methods : Springer Science & Business Media.

Romary, T., 2009, Integrating production data under uncertainty by parallel interacting markov chains on a reduced dimensional space : Computational Geosciences, **13**, 103–122.

Rutledge, J. T., W. Phillips, and B. K. Schuessler, 1998, Reservoir characterization using oil-production-induced microseismicity, clinton county, kentucky : Tectonophysics, **289**, 129 – 152.

Sachpazi, M., A. Galvé, M. Laigle, A. Hirn, E. Sokos, A. Serpetsidaki, J. M. Marthelot, J. M. Pi Alperin, B. Zelt, and B. Taylor, 2007, Moho topography under central greece and its compensation by pn time-terms for the accurate location of hypocenters : The example of the gulf of corinth 1995 aigion earthquake. : Tectonophysics, **440**, 53–65.

Sachpazi, M., M. Laigle, M. Charalampakis, J. Diaz, E. Kissling, A. Gesret, A. Becel, E. Flueh, P. Miles, and A. Hirn, 2016, Segmented hellenic slab rollback driving aegean deformation and seismicity : Geophysical Research Letters, **43**, 651–658.

Sambridge, M., 2014, A parallel tempering algorithm for probabilistic sampling and multimodal optimization : Geophysical Journal International, ggt342.

Sambridge, M. and K. Mosegaard, 2002, Monte carlo methods in geophysical inverse problems : Reviews of Geophysics, **40**, 3–1–3–29.

Sausse, J., C. Dezayes, L. Forbath, A. Genter, and J. Place, 2010, 3d model of fracture zones at soultz-sous-forêts based on geological data, image logs, induced microseismicity and vertical seismic profiles. : Comptes Rendus Geoscience, **342**, 531–545.

Sobol, I., 1993, Sensitivity estimates for nonlinear mathematical models. : Math. Model. Comput. Exp., **1**, 407–414.

Spakman, W., M. J. R. Wortel, and N. J. Vlaar, 1988, The hellenic subduction zone : A tomographic image and its geodynamic implications : Geophysical Research Letters, **15**, 60–63.

Stammler, K., 1993, Seismic handler-programmable multichannel data handler for interactive and automatic processing of seismological analyses. : Comput. and Geosci., **19**, 135–140.

Storn, R. and K. Price, 1997, Differential evolution – a simple and efficient heuristic for global optimization over continuous spaces : Journal of Global Optimization, **11**, 341–359.

Suckale, J., S. Rondenay, M. Sachpazi, M. Charalampakis, A. Hosa, and L. H. Royden, 2009, High-resolution seismic imaging of the western hellenic subduction zone using teleseismic scattered waves : Geophysical Journal International, **178**, 775–791.

Sudret, B., 2007, Uncertainty propagation and sensitivity analysis in mechanical models. contributions to structural reliability and stochastic spectral methods : PhD thesis, Habilitation à Diriger des Recherches.

Taillandier, C., M. Noble, H. Chauris, and H. Calandra, 2009, First-arrival traveltime tomo-

graphy based on the adjoint-state method : GEOPHYSICS, **74**, WCB1–WCB10.

Tarantola, A., 1986, A strategy for nonlinear elastic inversion of seismic reflection data : GEOPHYSICS, **51**, 1893–1903.

———, 2005, Inverse problem theory and methods for model parameter estimation : Society for Industrial and Applied Mathematics.

Tarantola, A. and B. Valette, 1982, Inverse problems - quest for information : J. Geophys., **50**, 159–170.

Tiberi, C., M. Diament, H. Lyon Caen, and T. King, 2001, Moho topography beneath the Corinth Rift area (Greece) from inversion of gravity data : Geophysical Journal International, **145**, 797–808.

Tyler, D. E., 1987, Statistical analysis for the angular central Gaussian distribution on the sphere : Biometrika, **74**, 579–589.

Vidale, J., 1988, Finite-difference calculation of travel times : Bull. seism. Soc. Am., **78**, 2062–2076.

———, 1990, Finite-difference calculation of travel times in three dimensions : Geophysics, **55**, 521–526.

Virieux, J. and S. Operto, 2009, An overview of full-waveform inversion in exploration geophysics : GEOPHYSICS, **74**, WCC1–WCC26.

Wapenaar, K., 1998, Seismic reflection and transmission coefficients of a self-similar interface. : Geophys. J. Int., **135**, 585–594.

White, D. J., 1989, Two-Dimensional Seismic Refraction Tomography : Geophysical Journal International, **97**, 223–245.

White, R. S., P. A. F. Christie, N. J. Kusnir, A. Roberts, A. Davies, N. Hurst, Z. Lunnon, C. J. Parkin, A. W. Roberts, L. K. Smith, R. Spitzer, A. Surendra, and V. Tymms, 2002, isimm pushes frontiers of marine seismic acquisition. : First Break, **20**, 782–786.

Widess, M. B., 1973, How thin is a thin bed ?. : Geophysics, **38**, 1176–1180.

Williams-Stroud, S., C. Ozgen, and R. L. Billingsley, 2013, Microseismicity-constrained discrete fracture network models for stimulated reservoir simulation : Geophysics, **78**, 37–B47.

Wittlinger, G., G. Herquel, and T. Nakache, 1993, Earthquake location in strongly heterogeneous media. : Geophys. J. Int., **115**, 759–777.

Woelbern, I. and G. Rümpker, 2017, Limitations of h-k stacking : ambiguous results caused by crustal layering : Journal of Seismology, **21**, 221–235.

Wortel, M. J. R. and W. Spakman, 2000, Subduction and slab detachement in the mediterranean-carpathian region. : Science, **290**, 1910–1917.

Wyss, M. and M. Baer, 1981, Earthquake hazard in the hellenic arc, 153–172. American Geophysical Union (AGU).

Wéber, Z., 2000, Seismic traveltime tomography : a simulated annealing approach : Physics of the Earth and Planetary Interiors, **119**, 149–159.

———, 2018, Probabilistic joint inversion of waveforms and polarity data for double-couple focal mechanisms of local earthquakes : Geophysical Journal International, **213**, 1586–1598.

Yuan, X., S. Sobolev, R. Kind, O. Oncken, G. Bock, G. Asch, B. Schurr, F. Graeber, A. Rudloff, W. Hanka, K. Wylegalla, R. Tibi, C. Haberland, A. Rietbrock, P. Giese, P. Wigger, P. Röwer, G. Zandt, S. Beck, T. Wallace, M. Pardo, and D. Comte, 2000, Subduction and collision processes in the central andes constrained by converted seismic phases : Nature, **408**, 958–961.

Zelt, B. C., B. Taylor, M. Sachpazi, and A. Hirn, 2005, Crustal velocity and moho structure beneath the gulf of corinth, greece : Geophysical Journal International, **162**, 257–268.

Zelt, C. A. and P. J. Barton, 1998, Three-dimensional seismic refraction tomography : A comparison of two methods applied to data from the faeroe basin : Journal of Geophysical Research : Solid Earth, **103**, 7187–7210.

Zhang, L., J. W. R. III, and G. M. Hoversten, 2005, Eikonal solver in the celerity domain : Geophys. J. Int., **162**, 1–8.

Zhao, H., 2005, A fast sweeping method for Eikonal equations : Math. Comp., **74**, 603–627.

Zhu, L. and H. Kanamori, 2000, Moho depth variation in southern california from teleseismic receiver functions : Journal of Geophysical Research : Solid Earth, **105**, 2969–2980.

Zimmer, U., 2010, Localization of microseismic events using head waves and direct waves : 80th Annual International Meeting, SEG, Expanded Abstracts, 2196–2200.

Zollo, A. and P. Bernard, 1991, Fault mechanisms from near-source data : joint inversion of S polarizations and P polarities : Geophysical Journal International, **104**, 441–451.

Chapitre 6

Annexes

6.1 Curriculum Vitae

Alexandrine Gesret
38 ans – 2 enfants

Maître assistant, MINES ParisTech
Centre de Géosciences – Equipe de Géophysique
35 rue Saint-honoré
77305 Fontainebleau, France
tel : +33 (0)1 64 69 49 25
e-mail : alexandrine.gesret@mines-paristech.fr

6.1.1 Expérience professionnelle

Depuis 2016 : Maître assistant – MINES ParisTech
2012-2016 : Chargée de Recherche – MINES ParisTech
2009-2011 : Assistante de Recherche – MINES ParisTech
2007-2008 : Assistant Temporaire d'Enseignement et de Recherche - IPGP
2004-2007 : Doctorante, bourse de thèse ministérielle - IPGP

6.1.2 Formation

2004-2008 : Thèse (meilleure mention) sous la direction d'Alfred Hirn - Equipe de Sismologie de l'Institut de Physique du Globe de Paris. *Résolution fine du toit de la subduction Hellénique par les ondes télésismiques converties.*
2003-2004 : DEA de géophysique interne, mention B, rang 3/24 - Institut de Physique du Globe de Paris.
2002-2003 : Maîtrise de physique, mention TB - Université de Rennes 1.
2001-2002 : Licence de physique, mention TB - Université de Malte (échange Socrates Erasmus).

6.1.3 Enseignements

Depuis 2011 : Stage de géophysique de la subsurface, Formation Ingénieurs civils 3A
Depuis 2009 : Stage de terrain de géologie, Formation Ingénieurs civils 1A, 3A-AST, Corps des Mines
Depuis 2012 : Tomographie stochastique, Master 2 GPX Mines/IPGP
Depuis 2012 : Sismologie, Formation Ingénieurs civils 3A
2009-2011 : Cours de statistiques, Master spécialisé CESECO

6.1.4 Encadremenent

Post-doctorant
2016 : M. Godano (co-encadrement 50%)

Doctorants
2010-2013 : N. Belayouni (co-encadrement 50%) - Nouveaux algorithmes efficaces de modélisation 2D et 3D : Temps des premières arrivées, angles à la source et amplitudes
2011-2014 : E. Vhi Nu Ba (co-encadrement 30%) - Détection des zones de failles par tomographie en transmission : application à la station expérimentale de Tournemire
2013-2016 : J. Belhadj (co-encadrement 30%) - Modèles paramétriques pour la tomographie sismique bayesienne
2015-2018 : K. Luu (co-encadrement 50%) - Optimisation numérique stochastique évolutionniste Application aux problèmes inverses de tomographie sismique
2018- : R. Abou Jaoude (co-encadrement 30%) - Evaluation des effets de sites d'origine géomorphologique et géologique de subsurface dans les pentes soumises à des sollicitations dynamiques : simulations numériques et validation sur le site de Byblos au Liban.

Stagiaires M2
P. Le Bouteiller (2010), A. Boterro (2013), N. Debellis Amaral (2016), B. Loubamono (2017)

Stagiaire M1
I. Almarouni (2018)

6.1.5 Principaux projets de recherche

- 2019 : Participation au projet GEODENERGIES - Développement d'Outils Numériques de Traitement et d'interprétation des Signaux géophysiques pour les réservoirs non conventionnels
- 2018 : Coordination de l'action CARNOT Mines (collaboration avec l'équipe géostatistique et Baker Hughes) - Apprentissage automatique en géophysique
- 2017-2018 : Participation au projet TelluS RIFT - Hazard in Tanzanian Rift
- 2015-2018 : Participation au projet GEODENERGIES - Utilisation de TEchniques de sisMiques Passives pour la mise en Exploitation, le suivi et l'évaluation du comportement dynamique du REservoir géotheRmique profond

— 2015-2017 : Coordination du projet structurant PSL (collaboration avec l'ENS) - Structural Imaging and Seismicity of COrinth

— 2016 : Coordination du projet entre Mines ParisTech et National Observatory of Athens (1 mois de chercheur invité) - Local earthquake tomography of OBS data

— 2014-2015 : Participation au projet CITEPH avec Magnitude financé par GDF et Total - Microsismicité induite-prise en compte de l'anisotropie

— 2011-2012 : Particpation au projet financé par Codelco (Chili) - 3D time-lapse tomography in mining context

— 2010 : Coordination de l'action CARNOT Mines (collaboration avec l'équipe géostatistique) - Géophysique stochastique

6.1.6 Autres implications

— Organisation d'un workshop sur les incertitudes lors de la conférence EAGE, 2019

— Séminaire invité à Nice-Sophia Antipolis (2010), à Centrale Supelec (2018), au BRGM (2018), à Géosciences Montpellier (2018)

— Organisation de séminaires : Maria Sachpazi (National Observatory of Athens, 2016) et Aurélien Nicolas (ENS Ulm, 2017)

— Membre du comité de sélection pour le recrutement d'un maître de conférences à l'ENSG, 2012

— Examinateur dans le jury de thèse de S. Ker, IPGP (2012) et de M. Irakarama, Nancy (2019)

— Reviewer pour les revues Geophysical Journal International, Geophysics, Journal of Applied Geophysics

— Membre de l'EAGE et de l'AGU

— Elue au conseil de laboratoire du Centre de Géosciences (2009-2011)

6.1.7 Publications

NB : Les auteurs soulignés indiquent des étudiants encadrés.

— **Gesret A.** and M. Sachpazi, How resolving are teleseismic converted waves ?, *in prep.*

— Sochala P., **Gesret A.** and O. Le Maître, Surrogate-based inversion for seismic traveltime tomography, *in prep.*

— Gaucher E., **Gesret A.** and M. Noble. A angular central gaussian likelihood formulation to locate earthquakes from body-wave polarization, *to be submitted to Geophysical Journal International*

— Luu, K., Noble M., **Gesret A.** and P. Thierry, Toward large scale stochastic tomography : a comparison of three evolutionnary algorithms, *accepted in Geophys. Prosp.*

— Belhadj, J., Romary T., **Gesret A.**, Noble M. and B. Figliuzzi, 2018, New parameterizations for bayesian seismic tomography, *Inverse Problems*, 34(6), 065007.

— Luu, K., Noble M., **Gesret A.**, Belayouni N. and P. F. Roux (2018), A parallel competitive particle swarm optimization for non-linear first arrival traveltime tomography and uncertainty quantification, *Computers and Geosciences*, 113, 81–93

— Bottero A., **Gesret A.**, Romary T., Noble M. and C. Maisons (2016), Stochastic seismic tomography by interacting Markov chains, *Geophys. J. Int*, 207(1), 374-392

— Belayouni N., **Gesret A.**, Daniel G. and M. Noble (2015), Microseismic event location using the first and reflected arrivals, *Geophysics*, 80(6), WC133-WC143

— Sachpazi M., Laigle M., Charalampakis M., Diaz J., Kissling E., **Gesret A.**, Becel A., Flueh E., Miles P. and A. Hirn (2015), Segmented Hellenic slab rollback driving Aegean deformation and seismicity, *Geophys. Res. Lett.*, 43, 651-658

— **Gesret A.**, Desassis N., Noble M., Romary T. and C. Maisons (2015), Propagation of the velocity model uncertainties to the seismic event location, *Geophys. J. Int.*, 200(1), 52-66

— Noble M., **Gesret A.** and N. Belayouni (2014), Accurate 3-D finite difference computation of traveltimes in strongly heterogeneous media, *Geophys. J. Int.*, 199(3), 1572-1585

— Laigle M., Hirn A., Sapin M., Bécel A., Charvis P., Flueh E., Diaz J., Lebrun J.-F., **Gesret A.**, Raffaele R. et al (2013), Seismic structure and activity of the north-central Lesser Antilles subduction zone from an integrated approach : Similarities with the Tohoku forearc. *Tectonophysics*, 603, 1-20

— **Gesret A.**, Laigle M., Diaz J., Sachpazi M., Charalampakis M. and A. Hirn (2011), Slab top dips resolved by teleseismic converted waves in the Hellenic subduction zone, *Geophys. Res. Lett.*, 38, L20304

— **Gesret A.**, Laigle M., Diaz J., Sachpazi M. and A. Hirn (2010), The oceanic nature of the African slab subducted under Peloponnesus : thin-layer resolution from multiscale analysis of teleseismic P-to-S converted waves, *Geophys. J. Int.*, 183(2), 833-849,

6.1.8 Conférences

Conférences invitées

— **A. Gesret**. Uncertainty estimation by probabilistc seismic tomography. Symposium on Uncertainty Quantification in Computational Geosciences, BRGM, Orléans, France, 2018.

— **A. Gesret**, Belhadj, T. Romary, M. Noble and N. Desassis. Uncertainty estimation by probabilistic first arrival time tomography using Markov Chain Monte Carlo sampling. In 79th EAGE Conference and Exhibition 2017, Paris, France, 2017.

Conférences avec acte et comité de lecture

— P. Sochala, **A. Gesret** and O. Le Maître, Surrogate-based inversion for first-arrival seismic tomography, UQOP 2019, Paris, France, 2019.

— E. Gaucher, **A. Gesret** and M. Noble. A New Probabilistic Formulation to locate seismic events from P-wave polarization. In 79th EAGE Conference and Exhibition 2017, Paris, France, 2017.

— K. Luu, M. Noble, **A. Gesret**, N. Belayouni and P.F. Roux. Propagation of Velocity Uncertainties to Microseismic Locations Using a Competitive Particle Swarm Optimizer. In 79th EAGE Conference and Exhibition 2017, Paris, France, 2017.

— E. Gaucher, **A. Gesret**, M. Noble, and T. Kohl. New Bayesian formulation to integrate body-wave polarization in non-linear earthquake location. In European Geothermal Congress, Strasbourg, France, 2016.

— K. Luu, M. Noble and **A. Gesret**. A competitive particle swarm optiimization for non linear first arrival traveltime tomography. In SEG Technical Program Expanded Abstracts 2016, Dallas, United States, 2016.

— N. Belayouni, M. Noble and **A. Gesret**. 3D VTI wave attribute modelling tools for microseismic monitoring processing : Traveltimes, amplitude and polarization. In 6th EAGE Workshop on Passive Seismic, Muscat, Oman, 2016.

— J. Belhadj, T. Romary, **A. Gesret**, and M. Noble. First Arrival Travel Time Tomography - Bayesian Approach. In Petroleum Geostatistics 2015, Biarritz, France, 2015.

— A. Benaichouche, M. Noble, and **A. Gesret**. First Arrival Traveltime Tomography Using the Fast Marching Method and the Adjoint State Technique. In 77th EAGE Conference and Exhibition 2015, Madrid, Spain, 2015.

— N. Belayouni and **A. Gesret**. Microseismic event location using first and reflected arrivals. In 1st SEG International workshop of Microseismic Technology, Asheville, United States, 2014.

— N. Belayouni, M. Noble, T. Bardainne, and **A. Gesret**. New 3D Wave Attribute Modelling Tools for Microseismic Monitoring Processing : Traveltimes, Amplitude and Polarization. In 4th EAGE Passive Seismic Workshop, Netherlands, 2013.

— **A. Gesret**, M. Noble, N. Desassis, and T. Romary. Microseismic Monitoring - Consequences of Velocity Model Uncertainties on Event Location Uncertainties. In 75th EAGE Conference and Exhibition incorporating SPE EUROPEC 2013, United Kingdom, 2013.

— N. Belayouni, M. Noble, **A. Gesret**, and T. Bardainne. A New Method for First Arrival Travel Times and Amplitude Computation in High Contrast Velocity Models. In Near Surface Geoscience 2012 - 18th European Meeting of Environmental and Engineering Geophysics, France, September 2012.

— M. Noble, **A. Gesret**, and N. Belayouni. A New 3D Eikonal Solver for Accurate Traveltimes, Takeoff Angles and Amplitudes. In 74th EAGE Conference and Exhibition incorporating SPE EUROPEC 2012, Denmark, June 2012.

— **A. Gesret**, M. Noble, N. Desassis, and T. Romary. Microseismic Monitoring : Consequences of Velocity Model Uncertainties on Location Uncertainties. In Third Passive Seismic Workshop, Eur. Ass. of Geoscientists and Engineers, Athens – Greece, 2011.

— N. Belayouni, M. Noble, T. Bardainne, H. Chauris, and **A. Gesret**. Fast Method for Amplitude Computation on High Contrast Velocity Models. In 73rd EAGE Conference and Technical Exhibition, Eur. Ass. of Geoscientists and Engineers, Vienna, Austria, 2011.

Conférences sans comité de lecture

- J. Belhadj, T. Romary, **A. Gesret** and M. Noble. Bayesian seismic tomography as a velocity anomaly detection tool. In Geostats 2016, Valencia, Spain, 2016.
- E. Gaucher, **A. Gesret**, M. Noble, and T. Kohl. A new Bayesian formulation to locate earthquakes from body-wave direction of arrival. In AGU Fall Meeting, San Francisco, United States, 2016.
- **A. Gesret**, J. Belhadj, T. Romary, M. Noble, E. Gaucher and N. Belayouni. Microseismic monitoring : Hierarchical transdimensional tomography and propagation ofvelocity model uncertainties to seismic event locations. In AGU Fall Meeting, San Francisco, United States, 2016.
- M. Godano, **A. Gesret**, M. Noble, H. Lyon-Caen, S. Gautier, and A. Deschamps. 3D imaging of the Corinth rift from a new passive seismic tomography and receiver function analysis. In AGU Fall Meeting, San Francisco, United States, 2016.
- M. Godano, **A. Gesret**, M. Noble, H. Lyon-Caen, S. Gautier, and A. Deschamps. 3D imaging of the Corinth rift from a new passive seismic tomography and receiver function analysis. In EGU general assembly 2016, Vienne, Austria, 2016.
- E. Gaucher, **A. Gesret**, M. Noble, and T. Kohl. A new Bayesian formulation to integrate body-wave polarisation in non-linear probabilistic earthquake location. In EGU general assembly 2016, Vienne, Austria, 2016.
- T. Romary, A. Bottero, **A. Gesret**, N. Desassis and M. Noble. Bayesian first arrival travel time tomography by interacting MCMC. In geoENV 2014, Paris, France, July 2014.
- **A. Gesret**, A. Bottero, T. Romary, M. Noble, and N. Desassis. Bayesian seismic tomography by parallel interacting Markov chains. In EGU General Assembly 2014, Austria, 2014.
- T. Romary, A. Bottero, **A. Gesret**, N. Desassis, and M. Noble. Bayesian first arrival travel time tomography by interacting MCMC. In 15th Annual Conference of the International Association for Mathematical Geosciences, Madrid, Spain, September 2013.
- M. Noble and **A. Gesret**. A new 3D Eikonal solver for accurate traveltimes, takeoff angles and amplitudes. In EGU General Assembly 2013, Austria, 2013.
- E. Vi Nhu Ba, M.. Noble, C. Gelis, **A. Gesret**, and J.Cabrera. Geophysical imaging of near subsurface layers to detect fault and fractured zones in the Tournemire experimental Platform, France. In EGU General Assembly 2013, Austria, 2013.
- **A. Gesret**, M. Noble, N. Desassis, and T. Romary. A new Bayesian approach of tomography and seismic event location dedicated to the estimation of the true uncertainties. In EGU General Assembly 2013, Austria, 2013.
- A. Hirn, M. Laigle, M. Sachpazi, P. Charvis, E. Flueh, A. Becel, J. Diaz, **A. Gesret**, A. Galve, M. Sapin, M. Charalampakis, J-F. Lebrun, M. Evain, M. Ruiz, H. Kopp, Y. Hello, J. Gallart, E. Kissling, R. Nicolich, and R. Raffaele. New features revealed by multi-method seismic imaging of the seismic structure and activity of the Lesser Antilles and Hellenic subduction zones, and their comparison with Tohoku. In 2012 AGU Fall Meeting, United States, December 2012.

— **A. Gesret**, M. Noble, N. Desassis, and T. Romary. Estimation of the velocity model uncertainties and of the associated uncertainties on microseismic event locations by a Bayesian approach. In AGU 2012 Fall Meeting, United States, December 2012.

— M. Sachpazi, **A. Gesret**, M. Charalampakis, M. Laigle, J.Diaz, and A.Hirn. High-resolution imaging of the subduction thrust location, properties and geometry, from teleseismic converted waves in the Western Hellenic and Lesser Antilles subduction zones. In 2012 AGU Fall Meeting, United States, December 2012.

— M. Laigle, A. Hirn, M. Sapin, A. Becel, P. Charvis, E. Flueh, J. Diaz, J-F. Lebrun, **A. Gesret**, R. Rafaele, A. Galve, M. Evain, M. Ruiz, H. Kopp, G. Bayrakci, W. Weinzierl, Y. Hello, J-C Lepine, J-P. Viode, M. Sachpazi, J. Gallart, E. Kissling, and R. Nicolich. Seismic structure and activity of the north-central Lesser Antilles subduction zone from an integrated approach : similarities with the Tohoku forearc. In 2012 AGU Fall Meeting, United States, December 2012.

— **A. Gesret**, M. Noble, T. Romary, and N. Desassis. Microseismic monitoring : new accurate estimate of velocity model uncertainties and consequences on location uncertainties. In EGU General Assembly 2011, Austria, April 2011.

— N. Desassis, T. Romary, **A. Gesret**, and Mark S. Noble. Inversion sismique dans un milieu aleatoire. In 42e Journees de Statistique, Tunisia, 2011.

— M. Noble, **A. Gesret**, N. Desassis, and T. Romary. Passive Seismic Monitoring- understanding and reducing event location uncertainties. In ESC 2010 European Seismological Commission 32nd General Assembly, Montpellier, France, September 2010.

— **A. Gesret**, M. Laigle, J. Diaz, M. Sachpazi, and A. Hirn. Thin-layer resolution from multiscale analysis of teleseismic P-to-S converted waves : the oceanic nature of the African slab subducted under Peloponnesus. In EGU General Assembly 2010, Austria, 2010.

— **A. Gesret**, M. Laigle, J. Diaz, M. Sachpazi, and A. Hirn. High-resolution approach to the top of the African slab under Eastern Peloponnesus : its nature and depth from teleseismic receiver-functions along a tight array. In ESC 2010 Montpellier, France, 2010.

— M. Sachpazi, M. Laigle, J. Diaz, **A. Gesret**, M. Charalampakis, E. Kissling, and A. Hirn. Along-strike slab segmentation under Greece from a 500 km long teleseismic receiver function swath profile : control on large earthquakes, upper plate motion, and surface morphology. In AGU 2010 Fall Meeting, United States, 2010.

— M. Sachpazi, M. Laigle, M. Charalampakis, J. Diaz, **A. Gesret**, E. Sokos, P. Petrou, E. Flueh, R. Nicolich, and A. Hirn. Hellenic subduction earthquake locations including OBS, ocean bottom seismometers and hints at shallow slab structure from teleseismic conversions : A pilot experiment. In EGU General Assembly 2010, Austria, 2010.

6.2 Sélection d'articles

Les cinq publications choisies sont les suivantes :

— **Gesret A.**, Laigle M., Diaz J., Sachpazi M. and A. Hirn (2010), The oceanic nature of the African slab subducted under Peloponnesus : thin-layer resolution from multiscale analysis of teleseismic P-to-S converted waves, *Geophys. J. Int.*, 183(2), 833-849

— **Gesret A.**, Laigle M., Diaz J., Sachpazi M., Charalampakis M. and A. Hirn (2011), Slab top dips resolved by teleseismic converted waves in the Hellenic subduction zone, *Geophys. Res. Lett.*, 38, L20304

— **Gesret A.**, Desassis N., Noble M., Romary T. and C. Maisons (2015), Propagation of the velocity model uncertainties to the seismic event location, *Geophys. J. Int.*, 200(1), 52-66

— Belayouni N., **Gesret A.**, Daniel G. and M. Noble (2015), Microseismic event location using the first and reflected arrivals, *Geophysics*, 80(6), WC133-WC143

— Bottero A., **Gesret A.**, Romary T., Noble M. and C. Maisons (2016), Stochastic seismic tomography by interacting Markov chains, *Geophys. J. Int*, 207(1), 374-392

Geophysical Journal International

Geophys. J. Int. (2010) **183,** 833–849 doi: 10.1111/j.1365-246X.2010.04738.x

The oceanic nature of the African slab subducted under Peloponnesus: thin-layer resolution from multiscale analysis of teleseismic *P*-to-*S* converted waves

A. Gesret,[1,2] M. Laigle,[1] J. Diaz,[3] M. Sachpazi[4] and A. Hirn[1]

[1]*Sismologie, Institut de Physique du Globe de Paris, UMR* 7514 *CNRS,* 4 *place Jussieu,* 75 *Paris, France. E-mail: alexandrine.gesret@mines-paristech.fr*
[2]*Mines ParisTech, Centre de Géosciences,* 77 *Fontainebleau, France*
[3]*Consejo Superior de Investigaciones Cientificas, Instituto Jaume Almera, c/Sole i Sabaris, Barcelona, Spain*
[4]*National Observatory of Athens, Geodynamical Institute Lofos Nymfon, Athens, Greece*

Accepted 2010 July 15. Received 2010 July 2; in original form 2009 September 7

SUMMARY

In the Hellenic subduction zone, the lithospheric slab may comprise continental and oceanic units juxtaposed downdip and along strike. For stations along eastern Peloponnesus, teleseismic *P*-wave receiver-function (RF) processing in the standard frequency band produces an image of a low-velocity layer (LVL) at the top of the slab apparently twice thicker than for an oceanic crust. To assess if this could come from a lack of resolution of the standard processing, we develop a multiscale approach with the RFs based on the wavelet-response of the medium, akin to the wavelet-transform of the velocity–depth function. The synthetic response in conversion is obtained for a multiscale singularity formed by two opposite velocity-steps at the boundaries of a crust embedded in mantle material. This indicates that only wavelet periods shorter than about 0.8 s will allow to identify clearly a 7 km thin oceanic crust. Going to longer periods leads to underestimate or overestimate the time-thickness of the LVL, due to interference phenomena. The analysis of the response in conversion from full waveform synthetic seismograms in a dipping slab model validates a multiresolution approach to real observations. With earthquakes of broad-enough spectrum towards high frequencies, yielding energy to provide wavelet periods significantly shorter than 1 s, the *P*-to-*S* conversions obtained allow us to resolve for the first time a standard oceanic crust at the slab top beneath the eastern coast of Peloponnesus. This documents the subduction of a purely oceanic slab of most reduced buoyancy since 4–5 Myr under the rapidly southwestward extending upper plate continental material.

Key words: Wavelet transform; Body waves; Subduction zone processes; Dynamics of lithosphere and mantle; Africa; Europe.

1 INTRODUCTION

Under Greece, oceanic and continental lithospheric segments have been subducted in succession, or lateral juxtaposition along the Hellenic subduction zone (Fig. 1), according to geological evidence (e.g. van Hinsbergen *et al.* 2005). In accordance to their nature, the subducted plate segments differ by their crustal thickness, superficial structure and buoyancy as expressed in the depth under water of their top before entering subduction (e.g. Royden 1993). These differences induce corresponding variations in the geometry and the nature of the interaction between the subducting material and the medium above the slab. Slab buoyancy variations likely control transients like trench retreat or slab rollback when oceanic lithosphere of strongest negative buoyancy enters subduction. Such variations may induce different behaviours in space and time at the subduction zone that have major significance for the geodynamic processes (Royden & Husson 2006) and also for the seismic coupling of the seismogenic part of the interplate (Laigle *et al*. 2002). This subduction zone is indeed prone to *M* 8 earthquakes, such as occurred for example at the turn of the 19th–20th century (e.g. Wyss & Baer 1981), or even greater ones as the 365 AD Gortyn earthquake (Laigle *et al.* 2004).

In the specific case of the Aegean domain, past or presently active deformation of the upper plate is rather complex in time and space and may not be fully understood if the only forces considered are those applied at the plate boundaries seen at the surface. Indeed the slab present underneath may also control the evolution, especially if its structure and behaviour are heterogeneous.

The characteristics of the crust at the top of the slab are diagnostic of the nature of the slab, with the oceanic case of strongest negative buoyancy corresponding to the smallest thickness, of only 7 km, of low density crust (White *et al.* 1992). However, the depth resolution

© 2010 The Authors
Journal compilation © 2010 RAS

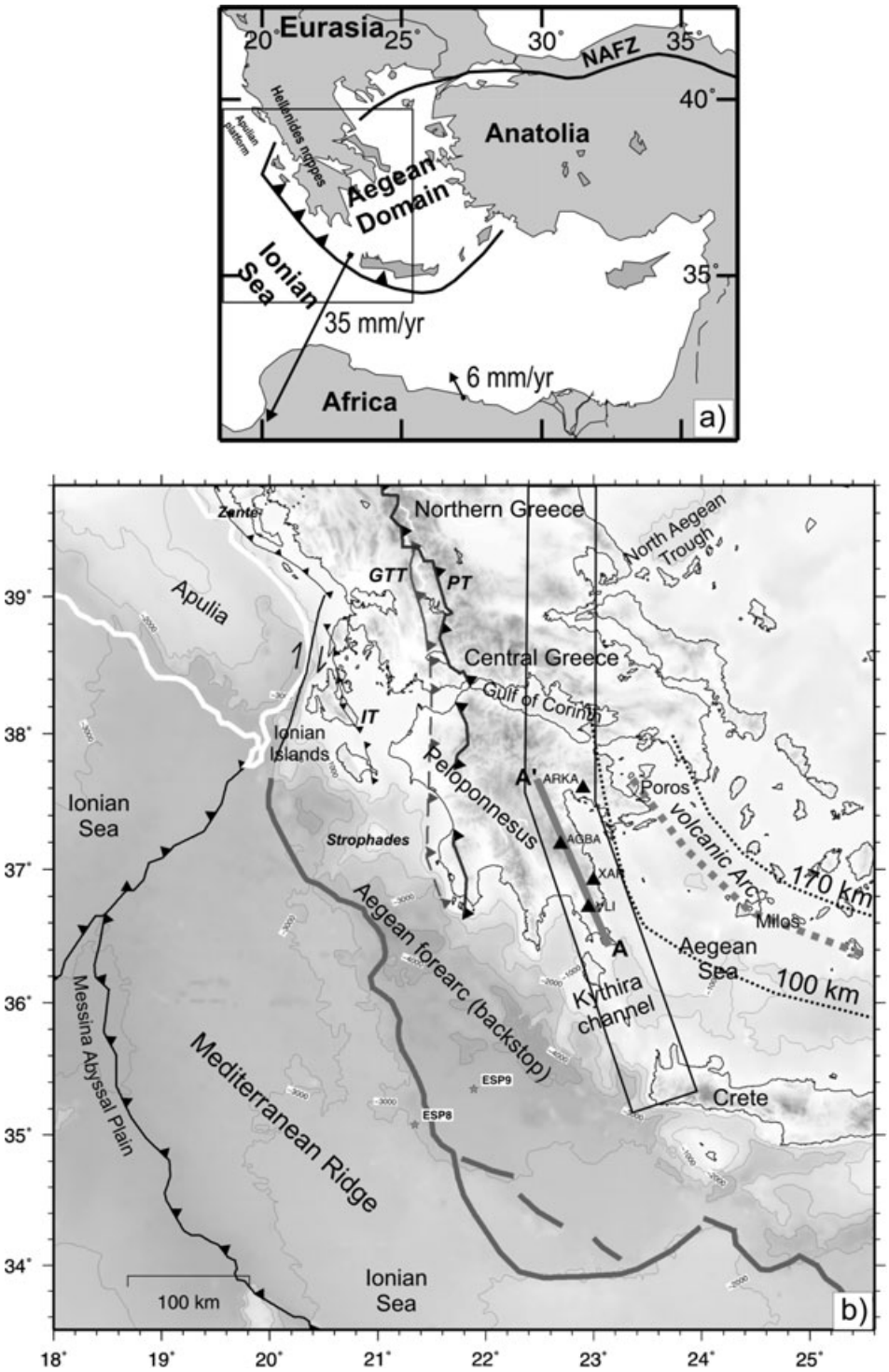

Figure 1. (a) Sketch of the Hellenic subduction zone in the wider context, with the vectors of instantaneous velocity of the SW Aegean domain and the African continent derived from GPS (after Kahle *et al*. 2000). (b) Map of the Hellenic subduction region with black triangles indicating the particular position of seismometers for which data are shown (Figs 9 and 10) and the 150 km segment AA' of the image section of 300 receiver-functions over eight stations in Fig. 2, within the swath of stations deployed in the 'THALES WAS RIGHT' project. Main tectonic elements related to the convergence are sketched: from SW to NE. Full barbed line: External limit, deformation front at the frontal thrust of the Mediterranean ridge accretionary wedge over the deep oceanic basin of the Messina Abyssal plain in the Ionian Sea, that is the northern margin of the African Plate. Grey bold line offshore: limit (generally a local backthrust in its shallow part, e.g. Chamot-Rooke *et al.* 2005) between the accretionary wedge of the Mediterranean Ridge and the backstop that is the Aegean forearc. CF indicated west of the Ionian Islands in northward continuation of the two previous lines is the presently active Cephalonia fault, strike-slip limit at surface with the Apulian continuation of Africa and linking northward with compressional structures where collision has followed the end of subduction in the Dinarides. Barbed lines further inland mark frontal thrusts of Hellenic nappe, labelled IT for the Ionian thrust of the Ionian Zone on the Pre-Apulian, active from 13 Ma, and GTT for the Gavrovo-Tripolis and PT for the Pindos thrust active earlier. Dotted lines labelled 100 and 170 km are proposed isobath for the Wadati-Benioff earthquakes (Papazachos *et al.* 2000) that encompass the volcanic Arc marked by line with big grey squares.

© 2010 The Authors, *GJI*, **183,** 833–849
Journal compilation © 2010 RAS

of the top of this slab obtained by regional or global traveltime tomography is no better than tens of kilometres (e.g. Spakman 1986; Spakman *et al.* 1993). On the other hand, active source seismics with combined multichannel seismic imaging and wide-angle refraction and reflection modelling have the required resolution, but their penetration seems limited to depths shallower than 25 km in the Hellenic subduction zone. The precise location and nature of the slab top cannot either be well resolved by the intermediate depth earthquakes of the Wadati-Benioff zone. Their hypocentres are not constrained to better than tens of kilometres, since their magnitudes are generally too low for a good worldwide recording.

In order to evaluate the specific behaviour of this particular subduction zone, we need a specific seismic approach that resolves the nature of the slab segments at depth, which may vary from continental to oceanic.

Incoming teleseismic body waves, recorded by seismometers located above the target at the Earth's surface, undergo forward scattering by mode conversion. The first arriving *P* wave is thus followed by the *S* converted from it at singularities in the velocity–depth function, of which the simplest is the step function at interfaces between layers. The receiver function (RF) method applied on the recordings allows us to retrieve these mode-converted waves. For the case of the crust on top of a slab that is already subducted deeper than the upper plate Moho, and thus forms a low-velocity layer (LVL) between the mantle material of the upper plate and that of the slab, two opposite polarity *S* arrivals converted from *P* are expected in the first seconds of the *P* coda. Their time interval or spacing is hence a measure of the thickness of the slab crust, with their amplitudes being a function of the contrast at conversion boundaries, mainly of the *S* velocity. Recently, RF or scattered wave analyses across subduction zones and related new imaging techniques could be used to resolve the crust at the top of the slab and the domain of interaction with the overlying mantle (Ferris *et al*. 2003; Rondenay *et al.* 2008). However, these studies reported apparently much thicker LVL at the slab top than expected for an oceanic crust, and discussed the far-reaching implications of such results.

We present a new approach to resolve the fine nature of heterogeneities encountered at depth and to image the LVL located at the top of the subducting slab. We adapted a multiresolution approach by wavelet-analysis to the case of converted waves and applied it to the conventional RF processing approach, which uses forward-scattered *S* waves converted from teleseismic *P* waves. Single-station analysis is necessary as a first step to avoid blurring the accuracy and resolution. The multiresolution analysis will demonstrate that interactions between the signal wavelength and the LVL thickness may prevent an accurate determination of the nature of the heterogeneity. This analysis thus reveals that for such a thin inclusion, special attention is required to check that forward-scattered teleseismic body waves can provide us with the necessary signal wavelength.

We also present the first results of the multiresolution approach as applied to examples of the data set collected with the objective of better constraining the structural control of the large subduction-earthquakes segmentation. This data set and study is part of an ongoing project along the Western Hellenic Arc that includes support in the frame of the 'THALES WAS RIGHT' project of the European Commission FP6 NEST-INSIGHT programme. The receivers have been installed in a swath from western Crete to central Greece, in particular along the eastern coast of Peloponnesus. In this region, the question of the nature of the slab top LVL with respect to the presence of an oceanic crust can be specifically addressed and results used to track its spatial variation, which is indeed crucial to discuss the models of the geodynamic evolution of the region.

The strike-line swath profile in our project contributes to the general coverage of the region in connection with the NSF MEDUSA project in Greece. Their dip-line runs from the middle of the western coast of Peloponnesus, onshore at the latitude of the Strophades islands (Fig. 1) through the isthmus east of the Gulf of Corinth. From their multimode imaging comprising the *P*-to-*S* converted waves and in addition the surface-backscattered and converted waves, Suckale *et al.* (2009) suggest at the top of the slab an LVL with relatively constant thickness of 15–22 km and dip of 21° towards east. They report along-strike slab variations close to their dip-line, from observed variations of results with backazimuths.

The first observations we report here are obtained south of such a dip-line from Strophades to Corinth, up to 100 km along the strike of the structural trend at the surface along eastern Peloponnesus. This is the subducted lithospheric panel downdip the largest well documented earthquake from the subduction zone for which the location and extent of the rupture zone have been inferred, the *M* 7.9, 1903 so-called Kithira earthquake (e.g. Wyss & Baer 1981).

2 GEODYNAMIC, STRUCTURAL AND SEISMOLOGICAL CONTEXT

2.1 Upper plate tectonics and structure

Between the two large plates, Europe and Africa (Fig. 1), that converge slowly at less than 10 mm yr^{-1} and the Anatolia subplate that rotates in-between (e.g. Le Pichon *et al.* 1995), the Aegean domain does not appear as a regular plate, since it does not meet the criterion of a rigid body limited by plate-boundary faults. The South-Aegean domain, which has undergone extension in rather recent times, does not deform internally any more at present, while it travels southward four times faster than the large plates converge. The present internal deformation shown by GPS is in a rather broad region along the northeastern and northwestern transitions of this Aegean domain, respectively to Anatolia on one side, and to Europe (i.e. Northern Greece) on the other side (e.g. McClusky *et al.* 2000; Nyst & Thatcher 2004; Hollenstein *et al.* 2008). These rather broad surroundings of the Aegean domain are furthermore the places of highest seismic activity of Europe and the Mediterranean domain.

This Aegean upper plate, and its ill-defined northwestern boundary also appear characterized by strong variations in crustal thickness that may be related to processes deeper in the lithosphere and asthenosphere. From the Pn traveltime anomalies of a major local earthquake recorded by a dense array, Sachpazi *et al.* (2007) document a line striking SW–NE from the western Gulf of Corinth towards the North Aegean Trough as being a contact between thinned crust in the southeastern area and thicker crust in the northwestern one.

These limits thus happen to coincide with structures of Late-Miocene to Early Pliocene deformation, such as the Parnon trench-parallel extensional detachment running SSE through Eastern Peloponnesus, as they have been derived from surface geology by Papanikolaou & Royden (2007). The independently reached findings of the limits of the high in the Moho-depth map of Sachpazi *et al.* (2007) and of the tectonic identification of a CHSZ, Central Hellenic Shear zone by Papanikolaou & Royden (2007) clearly concur to defining a region of thinned crust with two limits. One is running from the middle of the Gulf of Corinth towards ENE as the

© 2010 The Authors, *GJI*, **183,** 833–849
Journal compilation © 2010 RAS

northern limit of the CHSZ, and the other towards SSE to south-eastern Peloponnesus.

2.2 Top of the subducting plate at shallow depth

The depth variation of the top of the African slab under the region, and thus the values of dip and azimuth of the subducted slab are not tightly constrained from previous studies. There is a variation along the arc of both the strike of the sea-bottom trace of the frontal thrust at the tip of the accretionary wedge (Fig. 1b, barbed line) and of the strike of its inner boundary with the backstop (Fig. 1b, full grey line). In addition, the difference among these strikes is variable along the arc in relation with the variation of slip partitioning and deformation in the wedge (e.g. Le Pichon *et al.* 1995). However, for the particular segment offshore SW Peloponnesus, their strikes are the same, about N120°E. At the greater depth of 100 km, the slab depth contour (Fig. 1b, dotted lines) inferred from seismicity (Papazachos *et al.* 2000) is almost N–S along eastern Peloponnesus,whereas the volcanic arc, supposedly above an isobath of the deeper slab, is again striking N120°E between Poros and Milos volcano islands.

The direction and magnitude of slab dip may thus not be constant and whether they may vary smoothly or abruptly, such as by juxtaposing segments of slab along strike, is not documented. In case of such a geometrical segmentation of the slab, this may affect that of the interplate thrust. Indeed, a geometrical segmentation may result in variations of the seismic coupling along the seismogenic part of this interplate boundary at the top of the slab and therefore be of relevance to the question of major earthquakes.

The interplate boundary has been evidenced and imaged by a few dedicated marine seismic projects that pushed the active source marine seismics exploration methods from surface to largest depth, with the aim to learn more on this seismogenic part.

In the Ionian Islands region, marine multichannel reflection seismic (MCS) profiling between Cephalonia and Zante (Hirn *et al.* 1996; Clément *et al.* 2000) imaged a reflector, dipping landward from around 13 to 15 km depth. Since this level happened to correspond to a limit between microearthquakes of different mechanisms (Sachpazi *et al.* 2000) and to the location of the major instrumentally located earthquakes, it was suggested to mark the locked interplate boundary that could be the source of the earthquakes of magnitude above 7 that occur once or twice a century (Laigle *et al.* 2002). Offshore western Crete, flat thrust earthquakes relocated at 40 km depth (Taymaz *et al.* 1990) may indicate the depth to the top of the subducting plate there. None of those data has provided a clear clue on the nature of the medium beneath the interplate boundary and on the upper part of the lower plate before subduction, in this zone close to the termination of the subduction against the Cephalonia fault.

Beginning on the lower plate before it enters subduction, a more complete section across the subduction has been obtained since then, in the southwestern offshore of southern Peloponnesus. In the long and narrow Messina abyssal plain where the top of the Ionian oceanic lithosphere is at 4000 m water depth, several MCS profiles across the deformation front reveal a 3–4 km thick sedimentary cover above the oceanic basement top (Reston *et al.* 2002; Polonia *et al.* 2002). There, the offscraping process of the sediments of the Ionian subducting lithosphere and their accretion against the Aegean backstop results in the huge deforming accretionary wedge of the Mediterranean Ridge above the interplate décollement. The seismic images show that at the deformation front, the interplate beneath which the subducting lithosphere is underthrusting, generally lies at the base of the Messinian evaporites. There is evidence that it may even step further down into deeper levels of the sedimentary cover at short distance of the deformation front. At the landward deformation front of the accretionary wedge against the backstop 200 km further East, reinterpretation of ESP profiles (ESP 9 in Fig. 1) and OBH wide-angle and refraction modelling have identified the interplate boundary at 14 km depth. The top of the subducting plate is interpreted as comprising sediments of only 1–2 km thickness, remaining above the igneous oceanic crust (de Voogd *et al.* 1992; Truffert *et al.* 1993; Jones *et al.* 2002). This suggests that the slab subduction may not entrain an important thickness of sediments on top the igneous oceanic crust. In this case, there is no reason for the LVL between the slab mantle and the overlying mantle to be significantly thicker than a standard oceanic crust.

2.3 Nature of the subducting plate

In the northwestern Hellenides of northern Greece (Fig. 1) and the Dinarides further north, it is widely accepted that the subduction has halted and turned into collision, since there is no further oceanic lithosphere to consume.

Based on seismic tomographic images (e.g. Spakman *et al.* 1993), Wortel & Spakman (2000) have suggested that there, the slab would have been broken off from above, thus causing a segmentation at large scale of the subduction zone. In the northernmost, now continental-collision part, the deeper part of the slab, already detached from above, would have remained attached laterally to its southern prolongation (Wortel & Spakman 2000). The lateral overweight thus exerted at depth on that part of the slab which is still attached and in continuity with the Ionian basin lithosphere from the surface, might influence the trench retreat, the seismic coupling and the motion and deformation of the upper plate, and modulate them from the Dinarides to Crete (Laigle *et al.* 2002, 2004).

Global and regional seismic tomographic images do not distinguish internal heterogeneity within the large volume of subducted lithosphere under the Aegean. However, there is geological evidence in the recent evolution for successive consumption of three oceanic basins and docking of two continental blocks (e.g. van Hinsbergen *et al.* 2005) that are now in the shallow part of the tomographic anomaly that reaches 1400 km deep. Such subduction of a succession of different lithospheric segments has been inferred from the recent orogenic evolution of the Hellenides. This has been described as a foreland-propagating fold and thrust belt (e.g. Underhill 1989). Its front jumped in middle Miocene 13 Ma from a position at the Pindos thrust over the Gavrovo-Tripolis zone to a position west of the Ionian zone (Fig. 1). There, the corresponding Ionian Thrust over the Paxos or Pre-Apulian zone outcrops on the Ionian Islands where at present it is not anymore the active subduction boundary. In the Ionian Islands segment, the frontal thrust is considered to have jumped 4–5 Ma ago further to the west of the southern island of Zante and the Strophades islets. In this region, the southern part of the pre-Apulian continental domain now actively overthrusts the deep Ionian basin lithosphere with its oceanic crust.

The pre-Apulian continental domain does not outcrop at present further south than the Ionian Islands along the Hellenic Arc, and there is no evidence that it would have extended further south. This is of particular relevance for our study of the subducted slab, since it suggests that the underthrusting and subduction of the lithosphere of the deep Ionian basin sea could indeed have occurred earlier

© 2010 The Authors, *GJI*, **183,** 833–849
Journal compilation © 2010 RAS

under southern Peloponnesus and the Kythira channel than it did in the Ionian Islands.

3 OBJECTIVE OF THE STUDY, TARGET AND DESIGN OF THE SURVEY

3.1 Objective of the RF slab imaging study

A major support to a model in which the present regime corresponds to fastest trench retreat and slab rollback occurring in the southern part of the Western Hellenic subduction, would be that the corresponding slab has the largest negative buoyancy. This is the case for a slab segment of purely oceanic lithosphere.

Such fast trench retreat due to an oceanic slab could have been occurring since at least 4 Ma ago, in relation with the migration or jump of the subduction front. The latter migrated from its position as the Ionian Thrust of the Ionian Zone over the pre-Apulian domain that was not of oceanic lithosphere and is now outcropping through the Ionian Islands, to a position of this subduction thrust that would be now in the marine domain to the west of these islands. If the present rate of convergence of 30–40 mm yr^{-1} across the subduction boundary between Africa and the south Aegean domain (not Europe as a whole) applied since 4 Ma, the slab crust subducted then would be now at a 120–160 km distance northeast of the present subduction backstop tip offshore southwestern Peloponnesus. This corresponds to the eastern coast of Peloponnesus. We hence deployed there several stations of our seismic array in order to investigate this possible oceanic nature of the slab by testing specifically its crust. We are also carrying on observations both towards north and south in order to detect along-strike variations.

Oceanic lithosphere is characterized by the thinnest crust at its top. Whether, when subducted to large depths, a resulting LVL as thin as its 7 km can be identified is a major question in seismic imaging. Indeed, a much larger thickness of low-velocity zones at the slab top region appears in images obtained recently from the supposedly most resolving approach with body waves that are forward converted or scattered from incoming teleseismic *P* waves. This is the case in Alaska (Ferris *et al.* 2003, Rondenay *et al.* 2008), in the Cascadia subduction of Oregon (Bostock *et al.* 2002) and in Vancouver (Nicholson *et al.* 2005). We will similarly use body waves from distant earthquakes that are mode-converted at the top of the slab, but will present here a new method to reach in a quantifiable way the high-resolution required.

3.2 Design of the survey and data set

Current teleseismic sources at adequate distances of the study region are located in Kuriles, Kamchatka, Japan, western Pacific and Indonesian subduction zones and thus confined to northeastern backazimuths, ranging from N10°E to N100°E. For a slab dipping grossly to Northeast as expected here, a single line of receivers in this direction is then aligned along dip and with the earthquakes, and most adequate for the purpose of investigating the slab attitude and variation with depth. Instead, in order to search for variations in the slab attitude along the subduction zone, such as tears and segmentation of the slab, observations are needed along a NW–SE strike-line.

We concentrate here on the fine analysis of the *S* converted forward-scattered from *P* at the slab top that arrive shortly after *P*. This phase is free from the interference with the response of the deeper structure. This is not the case for the much later arriving so-called multiples from the slab top that could be used also, since in addition they have interacted with the heterogeneity near the surface from which they are backscattered. For the slab depths expected here, on the order of 60 km, the response in *P*-to-*S* conversion of the slab crust will also be earlier than, and thus non-interfering with the multiples of the upper plate crust conversions that can be so strong that they have been used to constrain further parameters such as V_P/V_S of that crust (e.g. Lombardi *et al.* 2008).

A profile of 500 km has been deployed from Crete to Central Greece (Fig. 1), with N150°E direction South of the Gulf of Corinth, and veering direction to the North further north. This could be done within the EU 'THALES WAS RIGHT' project beginning in mid 2006, with different pools of seismological stations comprising Hathor, Reftek, Marslite and Titan dataloggers equipped with 5, 20, 40 or 120 s Lennartz, Güralp and Streckeisen sensors. The instrument number has fluctuated over time between 20 and 40. We have redeployed them several times in different sites in order to improve spatial coverage or to better constrain some localised complex regions identified in the preliminary results. They are still in operation at the time of writing, in order to complete the survey.

The Z-N-E three-component waveforms of recorded teleseismic events are projected into the local *P–Sv–Sh* (L–Q–T) ray-based coordinate system thus isolating the *P* waves on the L component along the impinging first arrival, and the *S* waves converted from *P* at horizontal interfaces on the Q, or Sv component. (To obtain the RF, the *Sv* component is then deconvolved by the *P* component signal.) We use the methods implemented in Seismic Handler (Stammler 1993; Kind *et al.* 1995) to obtain from observed seismograms the wavelet of the *P* and by deconvolution, the wavelet of the *Sv* converted from *P*, that is the receiver function, RF and also to generate synthetics.

4 ANALYSIS OF REAL OBSERVATIONS AND WAVELET ANALYSIS APPROACH

4.1 Evidence for the slab top from standard RF processing

Interpretations of RF and scattered waves studies are often based on images resulting from migration of RF amplitude into a time- or depth-section along a profile. For about 300 RF data of 8 stations along a 150 km long line (Fig. 1), we applied such a migration with the same processing as Yuan *et al.* (2000) who reported a 10-km-thick low-velocity zone at the top of the Pacific oceanic slab under the Andes. Here in Fig. 2, we have chosen a symmetrical colour scale for positive and negative variations of velocity with depth, as Li *et al.* (2000) for the Japan subduction, in order to clearly identify the velocity contrast with increasing depth at the slab crust top as well as at its base, by their respective blue negative, and red positive.

On this densely documented profile of Fig. 2, apart from the positive polarity converted waves at the Agean Moho at around 3 s, the clearest feature is the positive of the conversion at the lithospheric slab Moho arriving between 6.5 and 8.5 s. About 2 s earlier, an almost equally strong negative polarity can thus be associated with the top of the slab crust under the overlying upper plate mantle. With these two opposite polarity signals we obtain quantitative data for a discussion of the slab crust and thus its nature.

The migrated image of Fig. 2 is obtained from data filtered with a 0.5 Hz high-frequency cut-off. Commonly, the high-frequency cut-off is even 0.3 Hz hence neglecting signal periods shorter than 3 s (e.g. Nicholson *et al.* 2005; Rondenay *et al.* 2008). The latter filter is applied in the example of the RF in the figure, of a $M_w = 6.6$

© 2010 The Authors, *GJI*, **183,** 833–849
Journal compilation © 2010 RAS

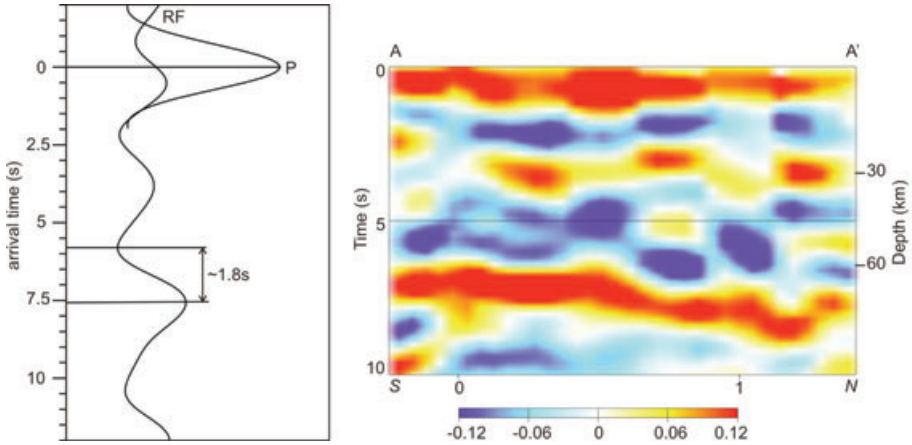

Figure 2. On the left is the receiver-function obtained by deconvolution of the *Sv* wave on the Q by the *P* wave on the L component. Trace noted RF is indeed that of *S* waves converted from the incoming teleseismic *P*, of which the deconvolved zero-phase wavelet is shown as trace noted *P*. Traces for a $M_w \sim 6.6$ Kuril earthquake (2006 September 30, backazimuth 32°, distance 86°) recorded at the VLI (Fig. 1) station obtained after application to the seismograms of a commonly used filter of passband 3–20 s. On the right, migrated image of 300 RF of eight stations from south to north along the 150 km line AA' shown in Fig. 1. Time-section, the corresponding depth is also indicated on the right-hand scale (crust at $V_P = 6.3$ km s^{-1} from 0 to 30 km depth, mantle at $V_P = 8$ km s^{-1}). VLI is at the southern third of the line.

Kuril earthquake (2006 September 30 17h50m23s) recorded at the VLI permanent seismological station of the National Observatory of Athens (see Fig. 1) equipped with a seismometer with flat velocity response up to 20 s period (this has been replaced since by a standard 60 s period broad-band sensor Güralp 3ESPC/60 used for instance in Fig. 10, that confirms the analyses made in this study). The resulting RF shows a clear signature of the top of the Hellenic slab arriving around 6 s later than the first arrival *P*, that is a conversion from about 50 km depth (Fig. 2). It marks as a negative, a trough, followed by a positive, a peak. This is typical of a LVL, as expected for the crust at the top of the lithospheric slab underneath the Aegean mantle. The RF amplitude with respect to *P* wavelet, that is the amplitude of the *Sv* converted from *P* is larger than for the mere velocity contrast of upper plate crust on slab mantle material. This is expected because of the updip incidence on the inclined slab from the northeastern backazimuths of most data. However, the time difference between the trough and peak, expected to be proportional to the thickness of the LVL, is measured as 1.8 s on this example of standard processing. Using typical *P* and *S* velocities for the oceanic crust, this measure would result in a 14 km thickness of the LVL at the top of the slab. This is twice the 7 km thickness expected for a standard oceanic crust (White *et al.* 1992).

Whether the large slab crust thickness thus inferred from standard processing is real or may be due to a resolution problem for thin layers deserves further attention. The phenomenon of wave interaction with LVL inclusion has been identified and taken into account earlier in reflection–refraction investigations of the crust (Fuchs 1969) and uppermost mantle (Hirn *et al.* 1973; Kennett 1980). The strong dependence of the resulting signal on the scale of fine structure, such as thin LVL embedded in a medium, has indeed been used to identify and quantify such layers. In that case, the source signal was narrow band, but the incidence angles, and thus the apparent thickness sensed by the waves, could be varied by recording reflections at variable offset from the source to large distances. In a simpler way, in the present teleseismic *P*-to-*S* conversion, or RF approach, the signal from an earthquake source has a much broader spectrum. It provides us with a broad range of signal periods or wavelengths that we may thus use in order to identify and quantify the embedded LVL by the variation of its response with frequency. We also take advantage of the more recent development of the wavelet transform (e.g. Mallat & Hwang 1992) that has the property of identifying singularities at various scales and thus quantify the resolution, here in the velocity–depth function.

4.2 Wavelet response analysis

We proceed to localize and identify the singularities of interest in the frame of the wavelet transform approach (e.g. Mallat & Hwang 1992; Holschneider 1995). In order to remotely probe the structure of singularities in the velocity–depth function, Le Gonidec *et al.* (2002) and Le Gonidec & Gibert (2007) studied the reflection of acoustic waves from a medium with velocity–depth variations in laboratory experiments. They verified that the 'wavelet-response' of a velocity–depth function, which they obtained experimentally by propagating a wavelet family through a medium, follows the properties of the classic wavelet transform of that function. In this case, we use the *S* waves generated by conversions of the *P* teleseismic body waves on their upward propagation through the velocity–depth structure beneath the receivers. This allows thus to approach singularities in the velocity–depth structure by the variation of the response with period, that is across scales.

In theory, the wavelet-transform of a signal, for example a velocity–depth function, is defined as the result of the convolution of this signal by a wavelet family whose elements have same shape but varied periods and amplitudes since they are derived by successive dilatation *a* of one analysing wavelet. For convenience, traces obtained for different values of dilatation of the wavelet transform or response are commonly assembled side by side in a scalogram as a function of the wavelet period. For our problem of a crustal layer embedded in the mantle, as an illustration anticipating on the next section, a typical wavelet response in *P*-to-*S* conversion is represented on a scalogram in Fig. 4. The velocity–depth function does not have a single singularity but two successive steps with opposite polarities. In the scalogram in this Fig. 4, the analysis following Mallat & Hwang (1992) leads to identify the response of these velocity steps in the traces at the largest dilatation or period and then

follow them through the scalogram to the shortest periods as the amplitude extrema of the wavelet response along two ridge-functions correlated as dashed lines. Taken separately each of these velocity steps is well known from seismological theory to have a response that is constant with respect to the incoming signal whatever period, but their cluster shows in fact a response varying as a function of scale. If the evolutions of the amplitude of the extrema are represented as a function of wavelet periods such as in the usual diagram of $\log_2$ amplitude–$\log_2$ period, then the slope will show variations. This allows to identify a multiscale singularity, whose signature changes with the observation scale.

When singularities in the velocity–depth function are far enough from one another to appear as isolated, the evolution across wavelet periods of the amplitude of the extremum along the ridge function can also resolve their nature, such as velocity steps, spikes or gradients. As shown by Mallat & Hwang (1992), and verified experimentally in acoustic wave propagation by Le Gonidec *et al.* (2002), the amplitude variation is a straight line in a diagram $\log_2$ amplitude–$\log_2$ period, with a slope $\alpha = 0$ for the Heaviside function, that is, velocity step between layers. A negative slope $\alpha = -1$ corresponds to the velocity spike or Dirac function for the case of a thin-layer embedded in a medium, and a positive slope $\alpha = 1$ corresponds to the onset of a ramp function, like at the boundary between a constant velocity layer and one with a velocity gradient with depth. This is because such singularities can be parametrized by a self-similar mathematical function which is solution of the homogeneity equation $s(kt) = k^{\alpha}\, s(t)$ (e.g. Holschneider 1995). They thus can be identified by their power-law exponent that is the slope of their bi-logarithmic variation of amplitude versus period.

For seismic observations with limited bandwidth, wavelet response analyses have been applied in a version that uses instead of a suite of wavelet of different dilatations or scales, the set of derivatives of a single wavelet on a fixed scale support, such as in reflection seismics for the characterization of seismic facies (Herrmann *et al.* 2001), or for studying deep upper-mantle transition zones with *S* converted from teleseismic *P* (Herrmann & Bernabé 2004). RF stacks of such deep upper-mantle transitions have also been processed by the wavelet transform using a Morlet wavelet (Castillo *et al.* 2001). We choose here to make use of the full extent of the frequency spectrum of the source of each particular earthquake, since the teleseismic *P* signal is often found to extend over more than three octaves. Furthermore, we use the specific suite of wavelets derived from filtering and deconvolving the particular signature of each earthquake, in order to perform a multiresolution analysis.

The RF processing is indeed a deconvolution of the *Sv* component by the *P* component to get rid of the source time-function for such reasons as for instance that it may be longer than the time interval between the impinging *P* and its conversions of interest. In practice, we use the procedure implemented by Stammler (1993), in which the inverse filtering of Berkhout (1977) is used. The parameters of the inverse filter adapt to concentrate into a zero-phase wavelet the whole *P* signal on the L component. Deconvolution is obtained by applying the corresponding filter parameters to the original *Sv* on the Q-component. The result is the response in conversion to the corresponding *P* zero-phase wavelet. Since we normalize the wavelets to a same unit amplitude it is the wavelet response of Le Gonidec & Gibert (2007). This is hence the wavelet transform, to an amplitude factor proportional to scale that is wavelet dilatation (Holschneider 1995). This renders this specific RF estimation procedure akin to the study of the wavelet-response in reflection seismics, whereas the source used there is better known since generated in a controlled way as part of the survey.

As an example of the wavelet analysis in *P*-to-*S* conversion, the RF response on the *Sv* component as a function of the *P* wavelet period is computed. In practice, we apply a wide range of different bandpass filters to the original seismogram and we construct the scalogram with the suite of RF resulting from deconvolution, as for example in Fig. 3 for the same Kuril earthquake at VLI as in Fig. 2.

This procedure allows an unprecedented identification of the main feature observed on the figure, composed of a trough followed by a peak and corresponding to the top and bottom of the LVL at the top of the slab in the Hellenic subduction. This feature can be followed with high amplitudes through all periods or scales along the ridge functions in the classical wavelet-transform. Since each ridge function is seen to vary both in arrival time and amplitude across scales, this evidences that the LVL at the slab top has a response in conversion that depends on the period or scale. This illustrates that the interpretation of structure in terms of the LVL depth, thickness and velocity contrast, inferred from RF conversion arrival-times and amplitudes would greatly change depending on the period.

The RF highlighted as bold in Fig. 3 is the same as in Fig. 2, with the commonly used high-frequency cut-off at 0.3 Hz. As mentioned earlier, this standard processing would result in a 1.8 s trough to peak time interval, yielding 14 km thickness for a crustal LVL at the top of the slab. It is made obvious from this scalogram that this

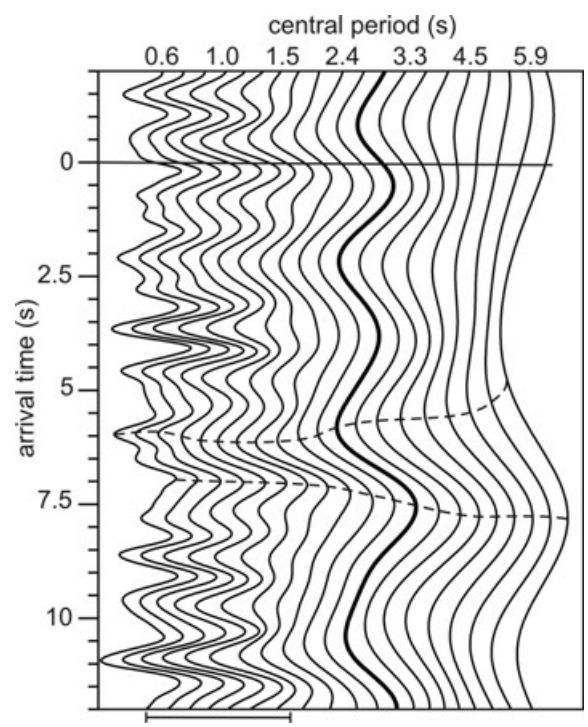

Figure 3. Scalogram of RF, showing the wavelet-response in *P*-to-*S* conversion of the structure beneath the VLI station. (The segment below the figure gives the amplitude of the corresponding *P*.) Traces for different central periods are obtained by application of filters with different bandpass to the original seismograms of the $M_w \sim 6.6$ Kuril earthquake, followed by the deconvolution step. The amplitude extrema of the wavelet response of the LVL at the Hellenic slab top are followed along ridge functions (dashed lines). Bold highlighted trace corresponds to the RF of Fig. 2.

© 2010 The Authors, *GJI*, **183,** 833–849
Journal compilation © 2010 RAS

estimate has to be greatly decreased by up to nearly half this value, when considering the *P* analysing wavelet to shorter periods.

In the next part, we develop the theoretical wavelet response in conversion and define resolution criteria for the case of low-velocity inclusions such as typical oceanic crust by computing synthetic RF. We will also validate the whole approach of multiresolution analysis on synthetic seismograms obtained for the case of a dipping slab.

5 MULTIRESOLUTION ANALYSIS OF THE LOW VELOCITY ZONE RESPONSE IN CONVERSION: SYNTHETIC EXAMPLES

5.1 Wavelet response of a low-velocity layer

We first consider the simplest horizontally layered velocity–depth model of an oceanic crust on top of the slab under the overlying mantle. The wavelet response in conversion (Fig. 4) of a 7-km-thick LVL with $V_P = 6.5$ km s^{-1} and $V_P/V_S = 1.8$, embedded in a mantle-velocity medium at 50 km depth, is computed for the case of teleseismic incidence, using the forward modelling of Kind *et al.* (1995) and Stammler (1993). The theoretical delay time between the wave converted at the top and the wave converted at the base of the LVL, which is also between a path in *P* and in *S* in this LVL, is

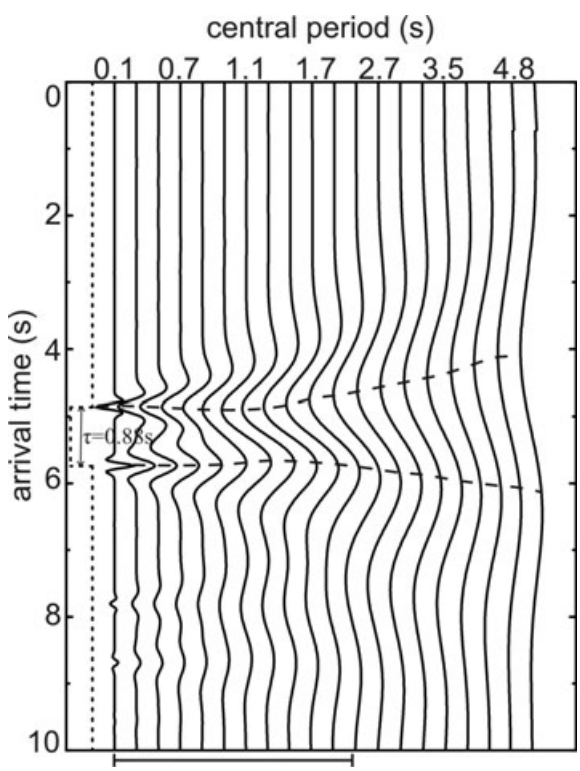

Figure 4. Scalogram showing wavelet response of synthetic RF, computed for a model of an oceanic crust 7 km thick at slab top (i.e. having a LVL of V_P 6.5 km s^{-1} at 50 km depth, equivalent to a theoretical time delay of $\tau = 0.88$ s as sketched in time as a dotted line on the left) embedded in a medium of $V_P = 8$ km s^{-1}, and with $V_P/V_S = 1.8$ throughout. Synthetic RF sorted according to the *P* wavelet central period T_c (note that this is not the nominal or peak period T_p commonly used in the identification of the Ricker wavelets, but according to their equation $T_c \sim 0.67T_p$). Amplitude extrema are followed along ridge functions (dashed lines). (The segment below the figure gives the amplitude of the corresponding *P* wavelet.)

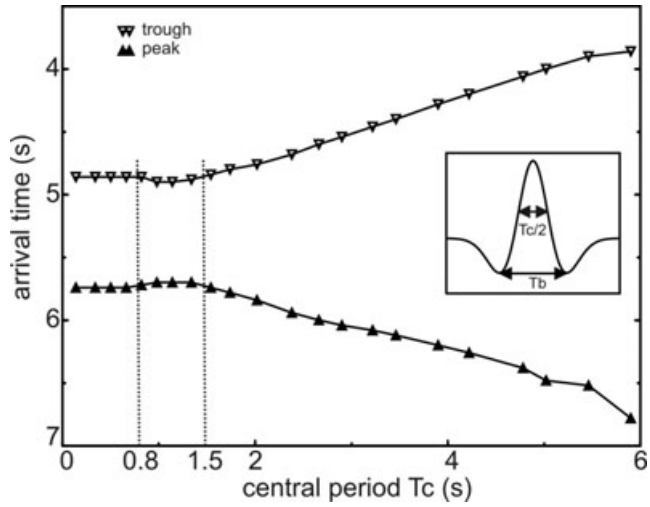

Figure 5. Time attributes of the synthetic RF of the simple model of Fig. 4, with arrival times of the trough as open inverted triangles and those of the peak as full triangles, as a function of the central period of the Ricker wavelet used. Insert: Illustration for a Ricker wavelet of the two definitions of period used in the study: the central period T_c and the dominant period T_b.

equal to 0.88 s (Fig. 4). The computation of the synthetic RF is done using for *P* a Ricker wavelet family of varying period but constant amplitude. Two measures of period are commonly used for zero-phase wavelets (Fig. 5, insert). Following Widess (1973), the central period T_c is defined as twice the time separation between inflection points on the central peak, and the dominant period T_b also called wavelet breadth is defined as the time separation between the two side lobes of the wavelet (Fig. 5, insert). For the Ricker wavelet used in the examples, these two periods can be measured to be, respectively, about the two-thirds and three-quarters of the peak period, which is commonly used to characterize the Ricker, as can also be derived formally from the wavelet being described by a known equation in this particular case.

It is obvious that the response of the modelled subducting oceanic crust, here at about 5 s time (Fig. 4), changes with the frequency of the incoming signal in terms of arrival times and amplitude of the converted waves. These are the main attributes commonly used to characterize the inclusion: the velocity contrasts at its boundaries are deduced from the amplitudes, its depth is deduced from the arrival time of the trough and its thickness from the spacing between the trough and peak. For this synthetic example, the picked arrival times of the trough and peak are represented with respect to the Ricker wavelet central period. As shown by their significant variation through the scalogram in Fig. 5, they cannot be related in a simple way to the depths of the two boundaries of the inclusion. Only for wavelet periods shorter than about 0.8 s, is the measured spacing between the trough and peak (called Δt hereafter) equal to the theoretical time delay (called τ hereafter). Thus, the true depths and the thickness can be univocally retrieved only in this short-period domain, whereas with wavelet periods longer than $T_c = 1.5$ s the layer time-thickness gets increasingly overestimated.

Previous studies of thin-layer response in reflection seismics established that the parameter which better characterizes the response of an inclusion is the ratio λ/d (*e.g.* Widess 1973) where $\lambda = TV_P$ is the wavelength of the signal and d the thickness of the inclusion. A variation of this parameter can be obtained by a variation of the layer thickness as considered by de Voogd & den Roijen (1983) or by a variation of the wavelet period as we consider here. In conversion

upon transmission, the characteristic wavelength λ in the inclusion depends on the dominant period T_b of the wavelet and on both P and S layer velocities, by the relation $\lambda = T_b/(1/V_S - 1/V_P)$ (when corrected for the incidence angle). The parameter controlling the response then expresses as $\lambda/d = T_b/[d(1/V_S - 1/V_P)]$ being also equal to $\lambda/d = T_b/\tau$. The main characters of the wavelet response of the multiscale singularity can be summarized by the study of two signal attributes for varying λ/d: the amplitudes of the two converted waves (trough and peak) and the spacing between them.

5.1.1 Amplitude

In order to compare our study to the wavelet response of a window function in the acoustic case (Le Gonidec *et al.* 2002), the amplitude evolution is represented in a $\log_2$–$\log_2$ diagram (Fig. 6a) with respect to the dominant period T_b and to the ratio λ/d. This representation allows to discuss the geometry of singularities in the velocity–depth function, since the slope of the curve indicates the homogeneity degree of the singularity as recalled earlier (Mallat & Hwang 1992). Slope variations are observed on the diagram and indicate that the LVL representing an oceanic crust appears not as an isolated singularity but as a multiscale singularity, which is differently seen depending on the signal frequency. Three domains of different evolution of the response with period can be defined according to their slope. Their boundaries correspond to particular values of the ratio λ/d. For the inclusion of a standard oceanic crust considered here, the domain 'A' of no-interaction between the wave converted at the top and the one converted at the base from a same incoming wave is defined by $\lambda/d < 1$ that is $T_b <$ 0.88 s. The domain 'B' of interference is defined by $1 < \lambda/d < 4$, that is for 0.88 s $< T_b <$ 3.52 s. The thin-layer domain 'C', is for $\lambda/d > 4$, that is for $T_b >$ 3.52 s.

In the no-interaction domain A, the amplitude is constant with period and corresponds to the true velocity contrast, (here the same at the top and at the base of the LVL), which can thus be directly deduced. The slope is equal to $\alpha = 0$, the characteristic value for the step function, and the signal distinguishes each of the two interfaces which form the boundaries of the LVL. For intermediate periods of the B domain, the amplitude varies due to interferences between the converted waves at the top and at the base of the inclusion, reaching a maximum for $T_b \approx 1.76$ s, corresponding to constructive interferences that is to the resonance condition $\lambda/d = 2$. This is similar to reflection seismics for which the resonance condition corresponds to $\lambda/d = 4$ (Widess 1973) where $\lambda = TV_P$ because there is a two-way path in the inclusion. In this domain, the velocity contrast cannot any more be deduced from the amplitude.

This amplitude is much increased from its value in the non-interaction domain, by a quantity as much as 40 per cent depending on details of the wavelet, as tested with different Morlet, Ricker and sinc wavelets. For example, for a dominant period of 1.8 s, the S velocity inferred for the LVL of crust between mantle material would be of 3.4 km s^{-1} instead of the true 3.8 km s^{-1}. This results in the LVL appearing with a velocity that, as a function of the signal period considered, can be either of upper or lower crustal value if embedded in a normal mantle, so that amplitude considerations can be misleading when not based on a detailed analysis. Towards longer periods beyond this resonance, in the domain C, the trough-to-peak amplitude decreases with a slope equal to $\alpha = -1$, the value characteristic of a Dirac distribution that corresponds to the thin-layer case, as was previously noted in the reflection case (Widess 1973).

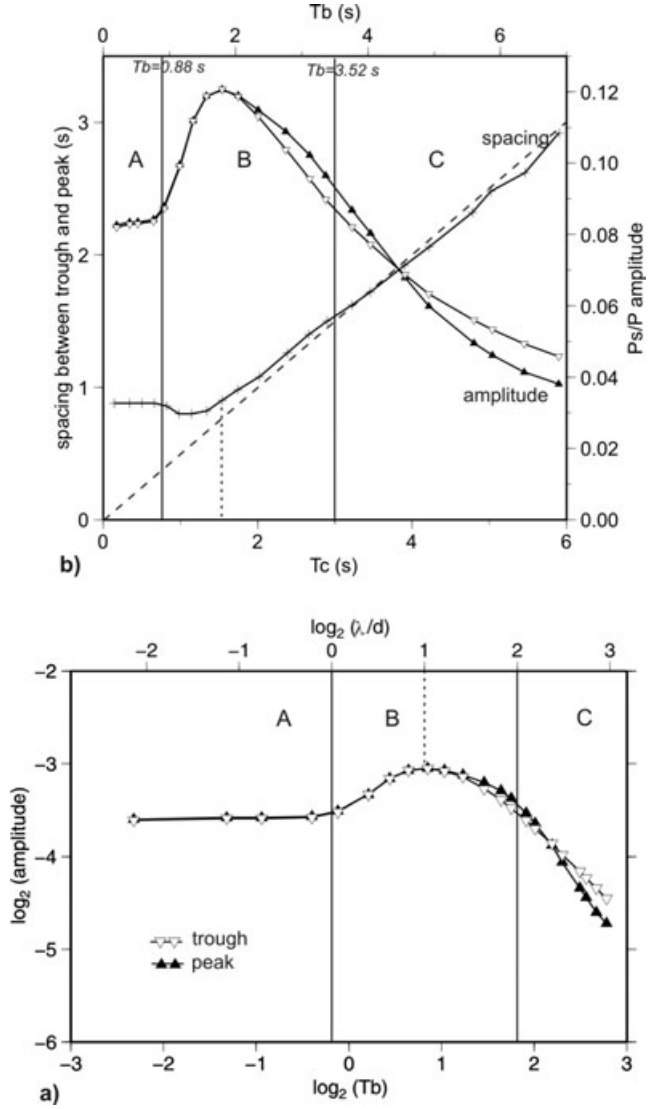

Figure 6. Other attributes of the synthetic RF of the simple model of Fig. 4. (a) Amplitude versus dominant period in a $\log_2$–$\log_2$ diagram of the trough (open inverted triangles) and of the peak (full triangles), with respect to the dominant period T_b, (lower axis). Upper axis is the ratio λ/d (with λ the characteristic wavelength and d the thickness of the LVL), with $\log_2$ λ/d values of 0 and 2 bounding the three domains corresponding to the non-interaction (A), the interference-resonance domain (B), and the thin-layer domain (C). The dotted vertical line indicates $\lambda/d = 2$ for which conversion amplitude is maximum (resonance). (b) Time-spacing (scale on the left) between the trough and peak as a function of the central period T_c (lower axis). The dashed line represents the Ricker criterion of limit of resolvability of a thin bed $\Delta t = T_c/2$. Curves for amplitudes (scale on the right) of the trough (open inverted triangles) and of the peak (full triangles), as a function to the dominant period T_b (upper axis), with resonance for $\lambda/d = 2$.

5.1.2 Arrival times

Following the variation of the spacing between the trough and peak with respect to the central period (Fig. 6b) allows to analyse more easily the evolution of the apparent thickness of the LVL. In the no-interaction A domain, this spacing is constant and equal to the theoretical time delay $\tau = 0.88$ s in the LVL. In the interference B domain, this spacing between trough and peak decreases slightly and then increases strongly with increasing period. The amount of decrease varies with the type of wavelet as tested with several

© 2010 The Authors, *GJI*, **183,** 833–849
Journal compilation © 2010 RAS

Morlet, Ricker and sinc wavelets. This may induce a decrease as large as 25 per cent of the spacing between the trough and the peak, with respect to the non-interference value at shortest periods. In the part of this domain B where this spacing increases again, its value equals the theoretical time delay of the no-interaction domain, for the particular value of $T_b = 1.76$ s (i.e. $\Delta t = \tau = T_b/2$ or $\lambda/d = 2$). This value of period is where amplitudes are also most increased by resonance, with respect to the no-interaction domain. This condition corresponds to the Rayleigh criterion which states that the resolution limit between two source objects occurs when the maxima of their two diffraction patterns are separated by half the distance between the minima of the two side lobes of one diffraction pattern (e.g. Widess 1973). This condition also corresponds to the tuning thickness in reflection seismics (Kallweit & Wood 1982) where apparent thickness is the same as true thickness.

In the thin-layer domain C for $T_b > 3.52$ s, for which the LVL corresponds to a spike in the velocity–depth function with respect to the period of the incoming wavelet, the response has the shape of the derivative of the *P* wavelet, that is with one more extremum, as described by Widess (1973) in reflection seismics. Indeed this means that the LVL, when seen as a spike by a long period wavelet has still a response with a trough and peak because the orders of homogeneity of the velocity step and spike differ by one. Obtaining the trough and peak signature is thus not diagnostic of the LVL thickness being resolved or not. The limit of resolvability of a thin-bed according to the Ricker criterion (Widess 1973) occurs when two zero-phase wavelets are separated by an interval equal to the time separation between the inflection points on their central peak. For longer wavelet periods, the trough to peak spacing in the RF caused by the LVL that is seen as a spike, increases then linearly with the incoming *P* wavelet period and is simply equal to $\Delta t = T_c/2$. For incoming *P* wavelet periods longer than $T_b = 1.76$ s, which is over twice the no-interference value of the trough-to-peak spacing of the RF, the trough-to-peak values observed have lost any relation with the characteristics of the LVL, which conversely cannot be deduced from the observed spacing.

In summary the normal 7-km-thick oceanic crust can be only measured directly by the trough–peak spacing and amplitudes for wavelets with a central period shorter than about 0.8 s, this upper limit slightly depending on the type of wavelet. For the typical oceanic crust and for a signal period of $T_c = 3$ s ($T_b = 3.5$ s) resulting from commonly used filtering with 0.3 Hz low-pass filter, Fig. 6(b) illustrates that a trough to peak time of 1.5 s would be found that is a thickness of 12 km would be inferred, which is almost twice the true thickness of the oceanic crust in the model.

5.2 Analysis of numerical simulation of propagation and conversion in realistic model in section of dipping slab

The previous example on the synthetic RF response shows that multiresolution analysis in conversion can characterize inclusions at depth such as a LVL at the slab top. In order to validate and refine the strategy to be applied in the analysis of real data, we need to check two aspects.

First, we have to estimate the effect, with respect to the forward modelling with a wavelet family to obtain the scalogram as in Fig. 4, of the RF processing which we apply to really observed seismograms to obtain a scalogram for observed signals, as in Fig. 3. In order to do this check, we will compute full waveform synthetic seismograms resulting from the propagation through a known model for a source with a broad but still limited frequency band, and apply to them the same RF processing as for real data.

Second, we have to check the effect of a structural dip, such as is likely for the slab top, with respect to the synthetic responses for a 1-D velocity–depth function considered before. Therefore we introduce such a dipping slab crust into the 2-D velocity–depth model.

In order to check these aspects over a wide band of periods, we use two sources each of 3 octaves-broad spectrum with dominant periods respectively $T_b = 0.64$ s ($T_c = 0.6$ s) and $T_b = 1.68$ s ($T_c = 1.55$ s). A set of synthetic seismograms is obtained by a full waveform simulation implemented and run by D. Rousset at Pau University using finite differences (Virieux 1986). The *P* wavefront, with the incidence from beneath of a teleseismic wave, is propagating updip in the 2-D-section of a model containing a 45° dipping, 10-km-thick oceanic crust. This is embedded between a forearc mantle and a slab mantle given the same velocity. The value of the dip, stronger than expected for the Hellenic slab, is chosen to make any effect more obvious. The thickness of the layer corresponds to the upper limit of that expected for an oceanic crust. The wavelet analysis is performed in exactly the same way as on real data. The original multicomponent seismograms are filtered with different bandpass and from each output the RF is computed by the procedure of Stammler (1993), obtaining for *P* a zero-phase wavelet. From the three octaves-broad signal, RF can be stably derived by variable bandpass filtering for central periods covering an octave, here $T_c = 1.3$–2.7 s, around the dominant period. The resulting scalogram, as seen in Fig. 7 for the source with dominant period at $T_b = 1.68$ s, allows to follow the evolution of waves converted at the top and bottom of the slab crust along the ridge functions (dotted lines) across scales. It appears notably that for the two shortest periods or smallest scales, the sidelobes of the two opposite polarity wavelets associated to the limits of the LVL are still distinguishable whereas for the longer periods they merge by interference. The spacing between the trough and peak is represented with respect to central period (in black in Fig. 8a) for the two sources. Its behaviour can be compared with that in the previous simple 1-D model direct computation of the RF for the Ricker wavelets (Fig. 6b). Very similarly, there is here a domain A of constant spacing for shorter periods giving the real theoretical time delay in the dipping LVL, then the spacing first decreases then increases again, passing over the value at the shortest periods for $\lambda/d = 2$, and continuing to increase for longer periods. The amplitude of the relative decrease of the spacing in the domain B with respect to A had been already seen in the case of horizontal structure to have different magnitudes with the different specific wavelets used, here it is as much as 20 per cent.

In order to take into account the effect of the possibly variable shapes of the *P* wavelet obtained by filtering of the signal, we use a simple procedure. We compute synthetic RF through a 1-D model but we use as input the suite of the *P* wavelets derived from the different filter settings on the synthetic seismograms obtained by propagation through the 2-D model. In the 1-D model the LVL is given a 11.8 km instead of 10 km thickness to compensate for the effect that propagation is now not anymore updip. The resulting green curve of the spacing between trough and peak on Fig. 8(a) retrieves almost exactly the black curve obtained from processing the seismograms of the propagation in the 2-D model. Hence the evolution of spacing appears not to be affected by the dip, when using the apparent LVL thickness compensated for it.

The coincidence in detail of the two spacing–period curves illustrates also another important aspect. It shows that when taking as

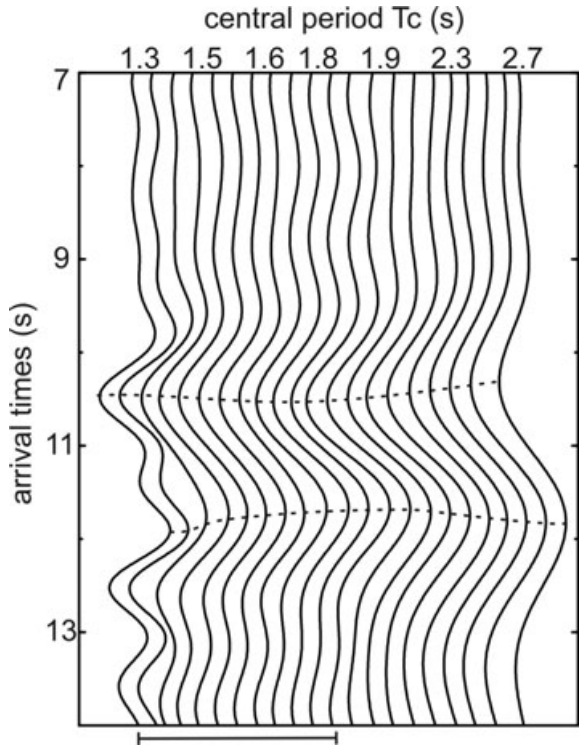

Figure 7. Scalogram analysis of RF processed from a full-waveform multicomponent seismogram obtained numerically from propagation in a realistic model of a 2-D section of a slab having a 45° dipping 10-km-thick LVL embedded in a medium of mantle-like velocity with updip incidence from below. Source signal has 1.55 s central period and three octaves bandwidth. RF, represented here for arrival times between 7 and 13 s, are obtained as for observed data by application of filters with different bandpass to the full waveform synthetics, followed by the deconvolution step. Dotted lines represent the ridge functions. (The segment below the figure gives the amplitude of the corresponding *P* wavelet.)

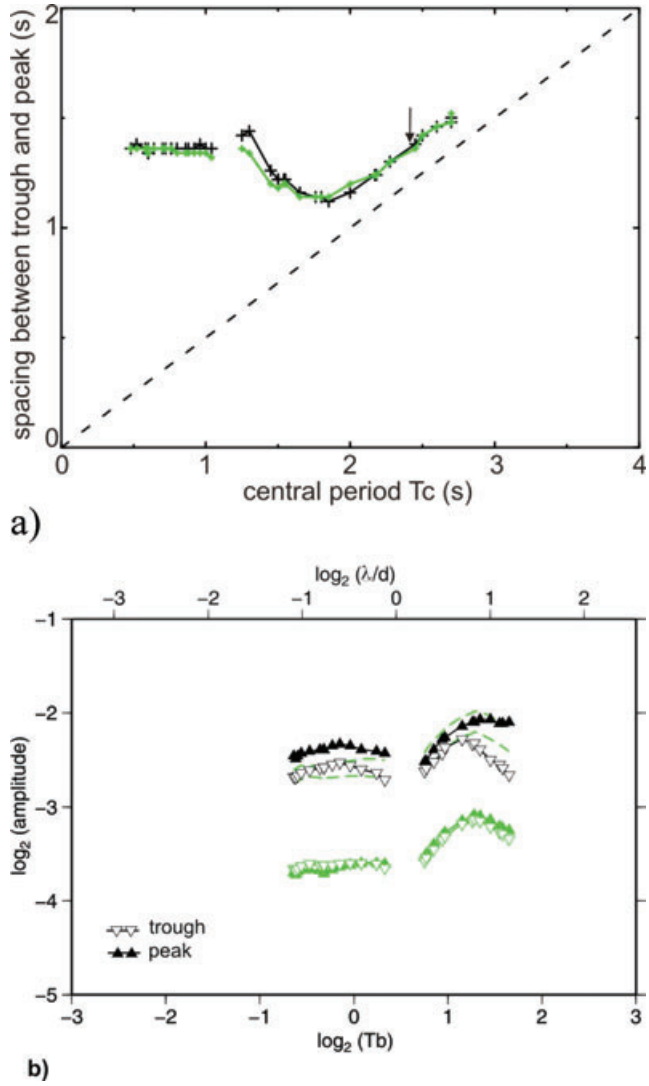

Figure 8. Analysis of the scalogram of Fig. 7 of RF resulting from processing of full-waveform synthetics in the dipping slab, for sources of 1.55 s and of 0.6 s central periods. In black, spacing between trough and peak (a) and their amplitudes (b) with respect to the signal period. In green, spacing and amplitudes of synthetic RF in a horizontally layered model using as an input the *P* wavelet obtained after each bandpass filtering and deconvolution of the full waveform synthetic seismograms. For the amplitudes in (b) the green dotted lines are derived from the full lines by taking into account the theoretical amplitude increase due to the updip propagation with respect to the slab. The arrow on (a) indicates the point for which $\lambda/d = 2$ where the spacing between trough and peak is equal to the real time delay in the dipping layer as expected.

input to the 1-D synthetics the *P* wavelets that do not have strictly the same shapes, as a result of filtering the signal, a very fine agreement is obtained with the RF processing of the result of the real propagation of the bandlimited signal. The effects which could be due to their deviation from strict similarity in shape can thus be obviated in practice.

The amplitudes of trough and peak are represented with respect to dominant periods (in black in Fig. 8b). The no-interaction domain is seen through the range of wavelets extracted from the source signal with shorter dominant period by their rather constant amplitude response, with a zero slope in the $\log_2$ amplitude–$\log_2$ period diagram. The interference domain is seen through the range of wavelets extracted from the longer period source, which shows an amplitude maximum that has its slope varying from positive to negative around resonance. With respect to these variations, the amplitude level itself is dominated by the effect of dip. The amplitudes measured from the propagation in the medium accounting for the slab dip (in black in Fig. 8b) are clearly higher, twice the value computed for a horizontal slab (green symbols in Fig. 8b). Shifting amplitude up by taking the theoretical effect of dip on them into account (green dotted lines) then reproduces quite well the amplitude evolution of the RF of synthetic seismograms. Apart this amplitude level, the clearest difference with respect to the direct RF synthetics computed in the previous section with horizontal layering and Ricker wavelets is a small variation of the relative amplitudes of the trough and of the peak. This can be attributed to the dip, as a consequence of the incidence angle of the *P* wave on the interfaces being different below the LVL and after propagating through it, at its top. The maximum of the peak is found as expected at $\lambda/d = 2$.

Principal characteristics expected for a LVL are retrieved from the analysis of the wavelet response applied to full waveform synthetic seismograms and validate this approach for the case of real data. Applying filters of different bandpass to seismograms prior to the deconvolution step permits conducting a multiresolution analysis and identifying the characteristics of a LVL at depth such as a slab crust.

© 2010 The Authors, *GJI*, **183,** 833–849
Journal compilation © 2010 RAS

6 WAVELET ANALYSIS OF REAL DATA: OCEANIC SLAB, 180 km INBOARD THE SUBDUCTION BACKSTOP

6.1 Avoiding an underestimation of the thickness: earthquake source dependant effects

At the same location, with the same system of seismometer and recorder, and seen through the same bandpass filter, the incoming signals of different earthquakes do not produce the same *P* wavelet shape in detail, not even with the same central and dominant periods. This is even true for neighbouring earthquakes, for which propagation occurs along the same path. There is thus clearly an effect of the particular spectrum of each different source.

We have searched the database for examples illustrating the reported phenomena, and that would allow to discuss and to constrain the real structure.

For larger earthquakes the higher overall amplitude level might correspondingly keep signal above noise down to the shortest periods. This appears to be the case of the example of the VLI record of Fig. 3 obtained in the quieter site of a permanent observatory station. Indeed this particular earthquake has been chosen among several Kuriles earthquakes of about same hypocentral region because significant signal could be recovered down to the bandpass of 0.1 to 1 s, giving a *P* wavelet with a 0.6 s central period.

Here, the trough-to-peak spacing of the LVL conversion decreases for the *P* central period decreasing from $T_c = 6$ s to 1.25 s, but as it can be followed to a *P* period as short as $T_c = 0.6$ s, it is seen to increase again slightly, then stabilize. This behaviour is similar to the variation obtained in the synthetics of Fig. 6 that have allowed the discussion of the domains of interference A, B and C. Indeed this spacing decreases from long periods and its reversal for the shortest allows to define when the non-interfering value of time-thickness is reached.

We applied the wavelet analysis to the AGBA station located about 50 km to the North of the VLI station. The wavelet response (Fig. 9) of a Honshu earthquake (2008 July 19, $M = 6.9$, backazimuth 44°, distance 87°) shows again variations. A wide spacing of about 1.7 s between the trough and peak is again obtained with the commonly used 0.3 Hz high-frequency cut-off, giving here a corresponding central period of $T_c = 3.1$ s. This would suggest a thickness as large as 15 km for the crust of the slab. This thickness estimate can be shown as inadequate since the trough to peak delay can be greatly reduced when decreasing signal periods. Interestingly, an even very thin signature is evidenced at the shortest period obtained for this event (here $T_c = 0.8$ s), $\Delta t = 0.75$ s which would correspond to less than 6 km of oceanic crust. The shortening of the signature to values smaller than the time delay in the LVL is predicted by the synthetic seismograms modelling (Section 5.2, or Fig. 8a).

These examples show that if the interference effects due to the frequency are not taken into account, two opposite types of wrong interpretations can be reached. A standard processing with a 0.3 Hz high-frequency cut-off will largely overestimate the LVL thickness, such as by a factor 2. On the other hand, a higher frequency processing may lead to an underestimation of the thickness, if the shortest period available from the particular earthquake would remain in the interference domain. Hence, very high frequency signals are necessary to capture the change from the interference domain, where the spacing underestimates the inclusion layer thickness, to the non-interference domain of the converted waves, and then propose a documented reliable structural interpretation.

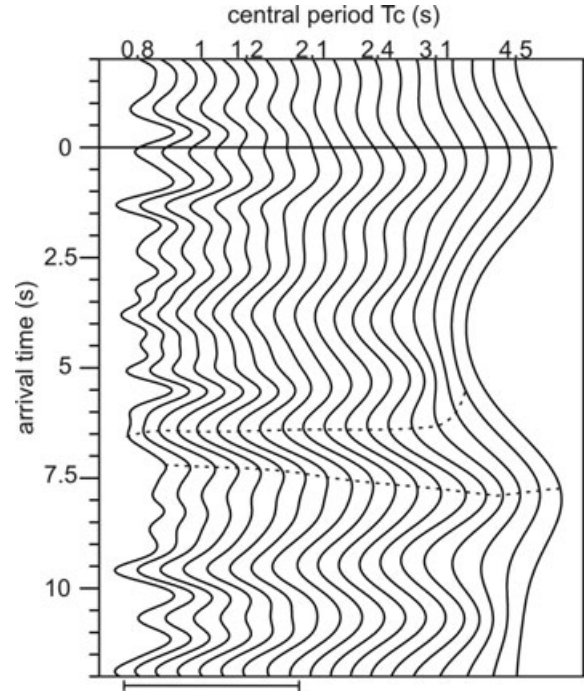

Figure 9. Scalogram of RF, or wavelet response in conversion, of the structure beneath the AGBA station (Fig. 1) obtained after application of filters with different bandpass to the original seismograms of a Honshu earthquake (2008 July 19, backazimuth 44°, distance 87°). Amplitude extrema of the wavelet response of the LVL at Hellenic slab top are followed along ridge functions (dotted lines). (The segment below the figure gives the amplitude of the corresponding *P* wavelet.)

Deployment since 3 yr of a number of stations allows, with respect to more current shorter deployments or time spans analysed, to compare the results obtained from different source signals and increase the chances of recording unusual events.

Several major earthquakes that could be recorded from each of such source regions as Sumatra, Honshu or Kuriles have provided data, the standard processing of which resulted in RF that on closer analysis showed differences among them for a same propagation path. Hence, diverse interpretations could have been reached in the case only one or few would be available, or if they would have been stacked such as to reduce noise, instead of their differences being analysed and understood. Indeed it appears that with a same standard filter, different earthquakes from neighbouring source locations may result in *P* wavelets that may differ in diverse aspects, even by over 20 per cent in their resulting wavelet periods. Then, different spacings of the RF trough and peak may result, and thus apparently different values for the LVL thickness sampled at a same location, that will be averaged out to the largest if stacked together.

Having thus established the need for shortest period signal, we searched for very deep sources with a large magnitude. They produce a rich spectrum at short period due to the large depth confinement, and their high amplitude may overcome the effect of attenuation and thus be recorded far away. Over the last 10 yr, only 4 earthquakes deeper than 300 km had magnitudes over 7.5. The major important magnitude $M \sim 7.7$ earthquake at the very large depth of 615 km under the Sea of Okhotsk on the 2008 July 5 is thus an exceptional event captured in our 3 yr deployment. As illustrated by the RF of the seismograms recorded for instance at the AGBA station (Fig. 10c) the LVL at the slab top has a clear signal to the

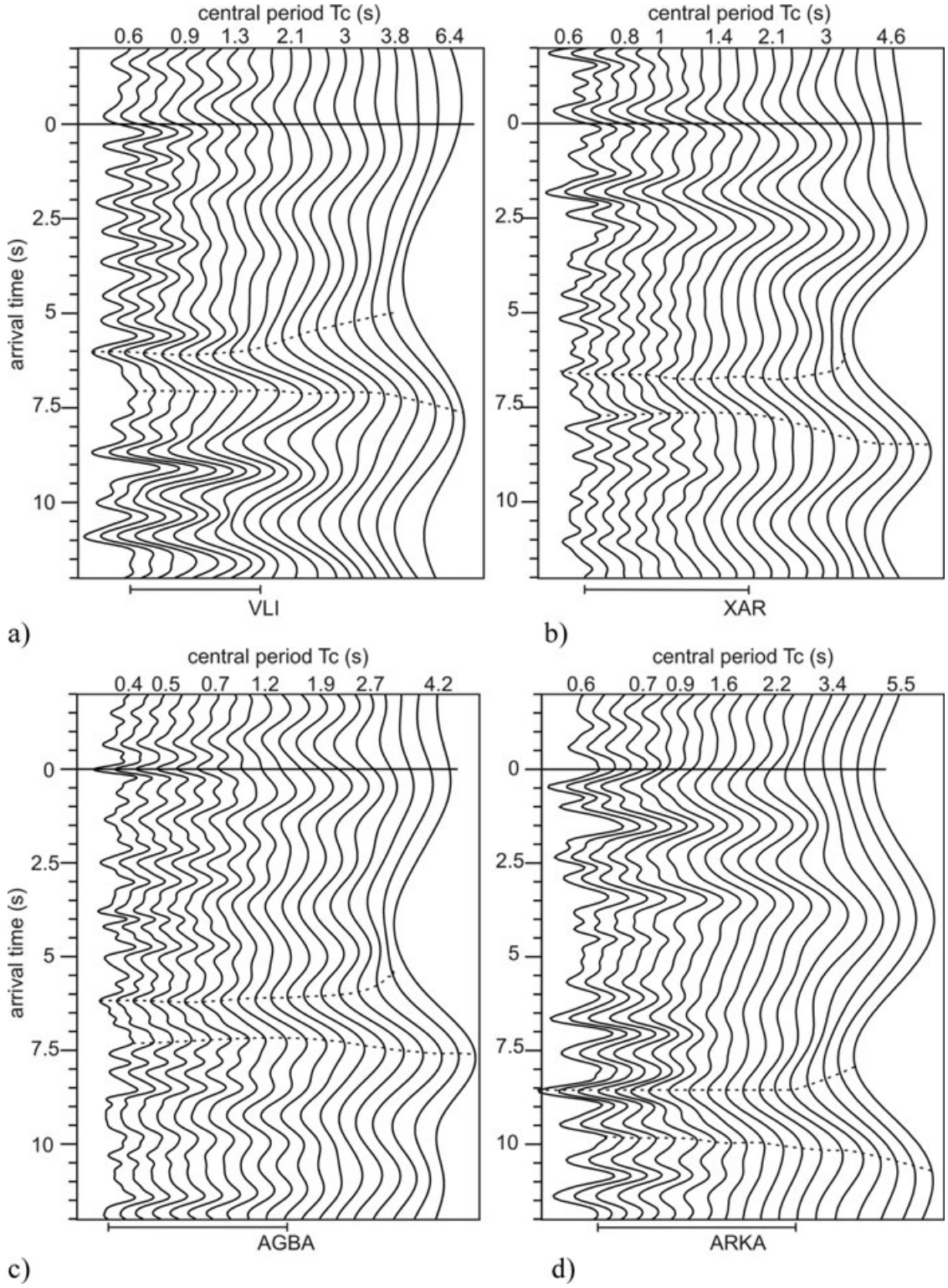

Figure 10. Scalogram of RF, or wavelet response in conversion of the structure beneath stations VLI, XAR, AGBA and ARKA obtained for the original seismograms of the major, over 600 km deep hence high-frequency earthquake of the Sea of Okhotsk (2008 July 5, $M \sim 7.7$, backazimuth 27°, distance 80°). Amplitude extrema are followed along ridge functions (dotted lines). (The segment below the figure gives the amplitude of the corresponding *P* wavelet.)

trace of shortest central period, which is here as short as $T_c = 0.42$ s. The corresponding dominant period of $T_b = 0.6$ s implies that this earthquake can resolve LVL as thin as 5.5 km ($\lambda/d < 1$). This occurrence is then a great opportunity to approach the real thickness of the LVL at the top of the Hellenic slab.

6.2 Wavelet response in southeastern Peloponnesus: an oceanic slab crust

The wavelet responses derived for the high frequency, large depth and large magnitude Okhotsk earthquake show a clear signature of

© 2010 The Authors, *GJI*, **183,** 833–849
Journal compilation © 2010 RAS

the Hellenic slab top as shown beneath southern Peloponnesus by four stations from south to north along the eastern coast displayed in Fig. 10: VLI, XAR, AGBA and ARKA. The cone-like shape of the variation of the trough and peak pair of extrema in the scalograms indicate strong and wide responses at longer periods. Following the pair of extrema in continuity to short period illustrates the narrowing of their spacing in time and depth, thus more accurately and correctly localizing the slab top. Note that the amplitude levels at short period in Fig. 11(b) of the observed seismograms of Fig. 10 are comparable although scattered, on the order of $\log_2$ amplitude $= -3$, that is 1/8 of the P amplitude. They are thus significantly higher than for the short-period response of a typical oceanic crust without dip in the synthetics of Figs. 6(a) or 8(b) (green) but smaller than the amplitude obtained by the processing of the seismograms propagated through the model with a 45° dip in Fig. 8(b) (black). Amplitudes are thus in agreement to first order with a normal oceanic crust on top of a slab with an intermediate dip on the order of 25°. The dip is certainly less than 45°, and close to 20°, when taking the ratio between the slab depth and the distance from the subduction front or also measuring dip from the azimuthal arrival time variation of the converted waves (Gesret 2008). For the longer periods, these observed amplitudes do not decay as strongly as for the synthetic case of a model containing only a LVL (Fig. 6a). This may be because in the observed data, at the corresponding T_b of 4 s, such a great length of the seismogram is involved that it contains not only the signature of the LVL by itself but the real velocity structure in tens of kilometres of depth around it.

The trough-to-peak spacing value obtained in these observations (Fig. 11a), hardly larger than 1 s is then consistent to better than 1 km with a standard 7-km-thick oceanic crust with a 25° dip. This is when compared to the 0.9 s value for the trough to peak spacing for a horizontal inclusion of a normal oceanic crust in Section 5.1 and the 20 per cent increase in apparent thickness due to updip propagation for a 45° dipping slab described in Section 5.2. We have thus constrained both the velocity contrast and thickness as typical of the oceanic crust of the dipping slab, in the 60–80 km depth range, 150 km inboard of the subduction backstop boundary. This oceanic value for the thickness of the crust of the slab deduced from the spacing between the trough and peak is an upper limit. This is because, with respect to the normal oceanic crustal velocities used for this estimate, only higher value of V_P/V_S could have to be considered for geological reasons, such as in the case of hydration in the LVL, but then an even thinner layer estimate would result from this spacing. The wavelet response we developed shows here unambiguously for the first time that the slab presently underlying southeastern Peloponnesus is made of lithosphere with a typically oceanic nature. The arrival time of the trough gives a first order indication on the depth of the top of the LVL at the slab top and its variation, which are consistent through the station network. Indeed the converted wave at the upper boundary of the crustal inclusion that is at the slab top, arrives at 6 s at VLI (Fig. 10a), at 6.2 s at AGBA (Fig. 10c), at 6.6 s at XAR (Fig. 10b) and at 8.6 s at ARKA (Fig. 10d). This deepening from about 55 to 80 km is in accordance with a slab dipping in-between to northeast.

Previous studies with the RF method (Li *et al.* 2003; Sodoudi *et al.* 2006) report converted waves they detect after that of the Aegean Moho under the station as being generally a single positive pulse, which they interpret as the Moho of the subducted African slab. We obtain instead a waveform that is clearly diagnostic of the top of the slab, with a negative pulse followed in the next second or so by a positive one, hence unmistakably corresponding to the interplate boundary or top of the crust of the slab lithosphere and respectively

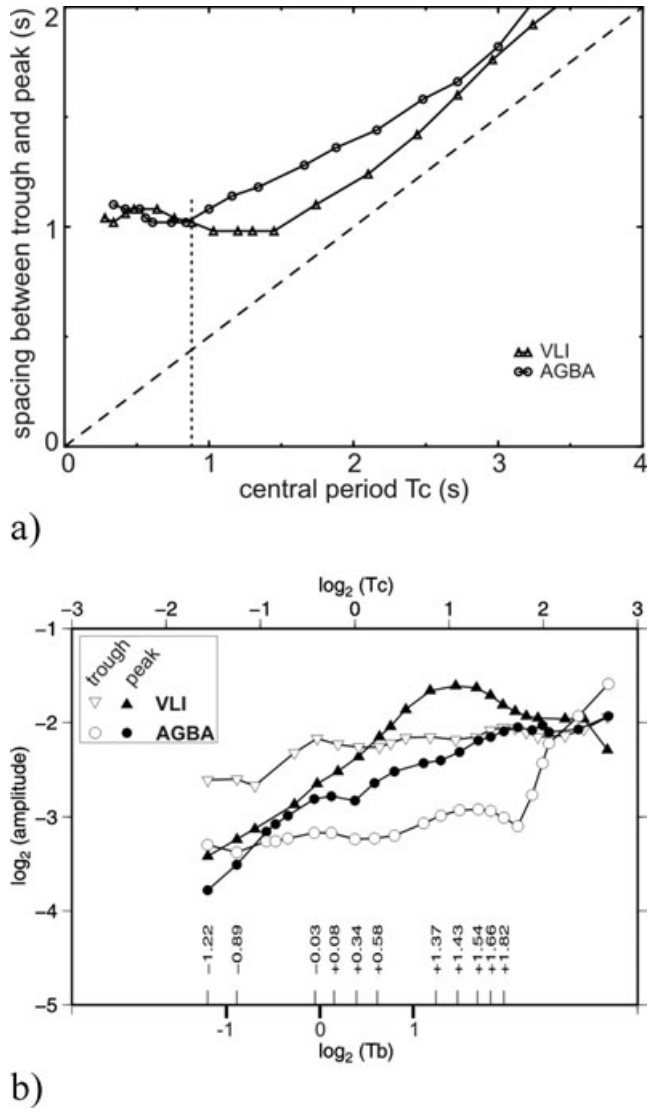

Figure 11. Examples of variation of the spacing and amplitude attributes of the RF of the observed data of the Okhotsk earthquake for station VLI (triangles) of Fig. 10(a) and for station AGBA (circles) of Fig. 10(c), (a) Time-spacing between the trough and peak of the RF with respect to the central period of the P wavelet. The dashed line represents the Ricker's criterion of limit of resolvability of a thin bed $\Delta t = T_c/2$. The dotted line indicates the period ($T_c \sim 0.9$ s) above which the spacing varies and cannot be used anymore to determine the thickness of the LVL at the slab top. (b) Amplitude as a function of period for the trough (open symbols) and the peak (full symbols) in a $\log_2$–$\log_2$ diagram. Central period T_c, on the upper horizontal axis and on the lower one, corresponding values of the dominant period T_b when they could be measured from unambiguous sidelobe separation. This allows comparison with other such diagrams in Figs 6(a) and 8(b).

to the base of this slab crust less than 10 km deeper. We have conspicuously identified a very strong negative pulse, documenting the subduction interplate boundary. With these two opposite polarity signals we thus obtained quantitative data for a discussion of the slab crust and nature.

Whether the lack of resolution of normally thin oceanic crust in several studies could be due to low frequencies classically used is an open question. Indeed, signals are most often not considered at short period since they are filtered to suppress high-frequency

noise. From the examples shown here, it appears that the standard processing of the observed data likely leads to see the LVL only in the interference, that is thin-layer, domain, where the trough-peak spacing has lost the relation with the LVL thickness. For studies that use instead *P* converted from *S* waves, the situation is even more extreme. The converted *P* being of the same low-frequency as the *S* they are converted from, the signal has much lower frequency than *P* propagated from the earthquake because of both the source radiation and propagation attenuation that are shaping *S* to long period. Whereas they are useful to map gradational velocity changes at large scale to which they are more sensitive, they are even much worse than *P*-to-*S* conversions for resolving velocity interfaces in a layered medium. This effect degrades the resolution power of *P* converted from *S* with respect to *S* converted from *P* in a layered medium, such that they may be blind to the thin LVL inclusion of the lower plate crust between the mantle of the lower plate and the mantle above.

7 SUMMARY AND CONCLUSIONS

In the Hellenic subduction zone, the lithospheric slab may comprise continental and oceanic units juxtaposed downdip and along strike, as evidenced from the diversity in the nature of their covers that have been accreted to form the Hellenic nappes at outcrop. Present fast trench retreat, attested by the southwestward fast motion of the edge of the Aegean upper plate domain documented from GPS, would be consistent with the subduction of a purely oceanic slab of most reduced buoyancy of the Ionian sea basin. If this occurred indeed since 4–5 Ma, the slab underlying now eastern Peloponnesus to about 180 km from the backstop tip should show correspondingly a thin oceanic crust at its top under the overlying mantle, which our objective is to test.

RF processing of teleseismic *P* waves in the standard frequency band, for stations along eastern Peloponnesus, results in the image of a LVL at the top of the slab twice thicker than expected for the crust of an oceanic slab. Such a large thickness for the LVL between the slab mantle and the overlying mantle has been found in other scattered or converted wave studies, and led to developing new hypotheses on the nature or evolution of subducting slabs.

In such studies elsewhere that found a thick LVL at the top of the slab, this has been considered as an evidence of either one among the three following cases. The first case is that of the subduction of a lithosphere with a thick crust, such as part of a continental crust, an oceanic plateau or an exotic terrane, as in Alaska (Ferris *et al.* 2003; Rondenay *et al.* 2008). The second case is the presence of serpentinized mantle exhibiting crust-like velocity beneath the subducted oceanic crust and therefore adding to it for an apparently thicker LVL. This serpentinization might have occurred in its early history, or when the plate enters subduction due to its bending-faulting and hydration from the top (Ranero *et al.* 2003). The third case is that of an additional thickness of low-velocity material above the slab. This would be progressively generated by the dehydration of the slab on its way to depth and the related upward fluid migration that would cause progressive serpentinization of the mantle wedge (Kawakatsu & Watada 2007).

Finding a thick LVL would exclude a strong negative buoyancy of the slab only in the two first cases, since the slab will have in its upper part a thick crust with low-density material, or a mantle with lowered density. In the third case, finding a thick LVL would appear to be inconclusive in disproving an oceanic slab of strong negative buoyancy since the material with lower density is above the slab top. This third hypothesis may however not need to be considered. Indeed, antigorite which is the particular serpentinite produced at large depth has recently been reported to keep a normal mantle-like high velocity and low V_P/V_S up to a high serpentinization degree (Reynard *et al.* 2007; Christensen 2004). If this were so, even if an alteration of part of the forearc mantle is present above the slab top, it could thus hardly contribute to thicken the LVL. Hence, finding a thick LVL could only correspond to the first two cases, and thus exclude a negative buoyancy of the slab.

It follows from this discussion that the thick LVL apparently found with standard processing, like in several cases elsewhere, would not be consistent with a subducting slab having strong negative buoyancy, that is of oceanic nature, under Peloponnesus.

In order to assess if this result could be due to a lack of resolution of the standard processing, we developed a multiscale approach with the RFs. It is based on the wavelet-response of the medium, akin to the wavelet-transform of the velocity–depth function. The synthetic response in conversion of a multiscale singularity formed by two opposite velocity-steps at the boundaries of a crust embedded in mantle material leads to quantify the domain of non-interaction between the signal wavelength and the heterogeneity thickness. Only at the shortest periods can the slab crust LVL between upper plate and slab mantle be simply characterized in term of thickness and velocity contrast at its boundaries. For a 7-km-thick oceanic crust LVL, only wavelet periods shorter than about 0.8 s will allow to identify clearly a thin oceanic crust. Going to longer periods will first lead to underestimate the time-thickness of the LVL, then to overestimate it increasingly above twice this period. For a bandpass commonly used in data processing, the LVL will thus appear twice thicker than it is. The amplitudes also vary, increasing from the short period, non-interaction domain where their values only depend on the velocity contrast, to the resonance period, and then decreasing. Inferences on the velocity contrast, as well as using it for the transformation of the time to thickness for this layer will be in error if the domain with respect to resonance is not identified.

The analysis of the response in conversion, then carried out from full waveform synthetic seismograms in a dipping slab model, allows to test and validate a multiresolution approach to real observations. This approach involves building the wavelet response of the slab top as the scalogram of RFs for *P* wavelets of different scales extracted from observations through application of bandpass filters to the seismograms.

With earthquakes providing wavelet periods shorter than 1 s, the multiscale analysis developed here allows for the first time to constrain the top of the slab at 60–70 km depth under Eastern Peloponnesus to have a crust of 7–8 km thickness, hence the slab segment to be of typical oceanic nature. This is found at 180 km inboard the subduction backstop. This supports a model of the subduction of purely oceanic lithosphere since 4–5 Myr, overridden at the present fast rate by its backstop of southwestward fastly extending upper plate continental material.

ACKNOWLEDGMENTS

This research is supported by the European Union FP6 NEST (New and Emerging Science and Technology)-INSIGHT programme, under project 'THALES WAS RIGHT' no. 029080, as well as national funding of participating institutions that provided also their instruments: IPGParis, CSIC Barcelona, National Observatory of Athens, Univ. Trieste, ETH Zürich, as well as that from national pools such

as CNRS-INSU (pools Refraction, Lithoscope and RLBM). IPG Paris contribution IPGP3064.

REFERENCES

Berkhout, A.J., 1977. Least-squares inverse filtering and wavelet deconvolution, *Geophysics,* **42,** 1369–1383.

Bostock, M.G., Hyndmann, R.D., Rondenay, S. & Peacock, S.M., 2002. An inverted continental Moho and serpentinization of the forearc mantle, *Nature,* **417,** 536–538.

Castillo, J., Mocquet, A. & Saracco, G., 2001. Wavelet transform: a tool for the interpretation of upper mantle converted phases at high frequency, *Geophys. Res. Lett.,* **28,** 4327–4330.

Chamot-Rooke, N., Rangin, C., Le Pichon, X. & Dotmed Working Group, 2005. DOTMED: a synthesis of deep marine data in eastern Mediterranean, *Mém. Soc. Géol. France,* **177,** 64p., 9pl.

Christensen, N.I., 2004. Serpentine, peridotites and seismology, *Int. Geol. Rev.,* **46,** 795–816.

Clément Ch., Hirn, A., Charvis, Ph., Sachpazi, M. & Marnelis, F., 2000. Seismic structure and the active Hellenic subduction in the Ionian Islands, *Tectonophysics,* **329,** 141–156.

de Voogd, N. & den Roijen, H., 1983. Thin-layer response and spectral bandwidth, *Geophysics,* **48,** 12–18.

de Voogd, B., Truffert, C., Chamot-Rooke, N., Huchon, P., Lallemant, S. & Le Pichon, X., 1992. Two-ship deep seismic sounding in the basins of the eastern Mediterranean Sea (Pasiphae Cruise), *Geophys. J. Int.,* **109,** 536–552.

Ferris, A., Abers, G.A., Christensen, D.H. & Veenstra, E., 2003. High resolution image of the subducted Pacific (?) plate beneath central Alaska, 50–150 km depth, *Earth planet. Sci. Lett.,* **214,** 575–588.

Fuchs, K., 1969. On the properties of deep crustal reflectors, *Z. Geophys.,* **35,** 133–149.

Gesret, A., 2008. Résolution fine du toit de la subduction Héllénique par les ondes télésismiques converties, *Thesis*, Institut de Physique du Globe de Paris, pp. 146.

Herrmann, F.J., & Bernabé, Y., 2004. Seismic singularities at upper-mantle phase transitions: a site percolation model, *Geophys. J. Int.,* **159,** 949–960.

Herrmann, F.J., Lyons, W.J. & Stark, C.P., 2001. Seismic facies characterization by monoscale analysis, *Geophys. Res. Lett.,* **28,** 3781–3784.

Hirn, A., Steinmetz, L., Kind, R., & Fuchs, K., 1973. Long-range profiles in Western Europe: II. Fine structure of the lower lithosphere in France (southern Bretagne), *Z. Geophys.,* **39,** 363–384.

Hirn, A., Sachpazi, M., Siliqi, R., Mc Bride, J., Marnelis, M. & the STREAMERS/PROFILES Group, 1996. A traverse of the Ionian Islands front with coincident normal incidence and wide-angle seismics, *Tectonophysics,* **264,** 35–49.

Hollenstein, Ch., Müller, M.D., Geiger, A. & Kahle, H.-G., 2008. Crustal motion and deformation in Greece from a decade of GPS measurements, 1993–2003, *Tectonophysics,* **449,** 17–40.

Holschneider, M., 1995. *Wavelets: An Analysis Tool,* Clarendon, Oxford, England, pp. 423.

Jones, K.A., Warner, M., Le Meur, D., Pascal, G., Tay, P.L. & the IMERSE Working Group, 2002. Wide-angle images of the Mediterranean backstop structure, *Mar. Geol.,* **186,** 145–166.

Kahle, H.-G., Cocard, M., Peter, Y., Geiger, A., Reilinger, R., Barka, A. & Veis, G., 2000. GPS-derived strain rate field within the boundary zones of the Eurasian, African, and Arabian plates, *J. geophys. Res.,* **105,** 23 353–23 370.

Kallweit, R.S. & Wood, L.C., 1982. The limits of resolution of zero-phase wavelets, *Geophysics,* **47,** 1035–1046.

Kawakatsu, H. & Watada, S., 2007 Seismic evidence for deep-water transportation in the mantle, *Science,* **316,** 1468–1471.

Kennet, B.L.N., 1980. Seismic waves in a stratified medium. II. Theoretical seismograms, *Geophys. J. R. astr. Soc.,* **57,** 557–583.

Kind, R., Kosarev, G.L. & Petersen, N.V., 1995. Receiver functions at the stations of the German Regional Seismic network (GRSN), *Geophys. J. Int.,* **121,** 191–202.

Laigle, M., Hirn, A., Sachpazi, M. & Clément, C., 2002. Seismic coupling and structure of the Hellenic subduction in the Ionian islands region, *Earth planet. Sci. Lett.,* **200,** 243–253.

Laigle, M., Sachpazi, M. & Hirn, A., 2004. Variation of seismic coupling with slab detachment and upper plate structure along the Hellenic subduction, *Tectonophysics,* **391,** 97–108.

Le Gonidec, Y. & Gibert, D., 2007. Multiscale analysis of waves reflected by granular media: acoustic experiments on glass beads and effective medium theories, *J. geophys. Res.,* **112,** B05103, doi:10.1029/2006JB004518.

Le Gonidec, Y., Gibert, D., & Proust, J., 2002. Multiscale analysis of waves reflected by complex interfaces: basic principles and experiments, *J. geophys. Res.,* **107**(B9), 2184, doi:10.1029/2001JB000558.

Le Pichon, X., Chamot-Rooke, N., Lallemant, S., Noomen, R. & Veis, G., 1995. Geodetic determination of the kinematics of central Greece with respect to Europe: implications for eastern Mediterranean tectonics, *J. geophys. Res.,* **100,** 12 675–12 690.

Li, X., Sobolev, S.V., Kind, R., Yuan, X. & Estabrook, C., 2000. A detailed receiver function image of the upper mantle discontinuities in the Japan subduction zone, *Earth planet. Sci. Lett.,* **183,** 527–541.

Li, X. *et al*., 2003. Receiver function study of the Hellenic subduction zone: imaging crustal thickness variations and the oceanic Moho of the descending African lithosphere, *Geophys. J. Int.,* **155,** 733–748.

Lombardi, D., Braunmiller, J., Kissling E. & Giardini, D., 2008. Moho depth and Poisson's ration in the Western-Central Alps from receiver functions, *Geophys. J. Int.,* **173,** 249–264.

Mallat, S. & Hwang, W.L., 1992. Singularity detection and processing with wavelets, *IEEE Trans. Inform. Theory,* **38,** 617–643.

McClusky, S. *et al*., 2000. Global Positioning System constraints on plate kinematics and dynamics in the eastern Mediterranean and Caucasus, *J. geophys. Res.,* **105,** 5695–5719.

Nicholson, T., Bostock, M. & Cassidy, J.F., 2005. New constraints on subduction structure in northern Cascadia, *Geophys. J. Int.,* **161,** 849–859.

Nyst, M. & Thatcher, W., 2004. New constraints on the active tectonic deformation of the Aegean, *J. geophys. Res.,* **109,** B11406.

Papanikolaou, D. & Royden, L.H., 2007. Disruption of the Hellenic arc: late Miocene extensional detachment faults and steep Pliocene-Quaternary normal faults—or what happened at Corinth? *Tectonics,* **26,** TC5003, doi: 10.1029/2006TC002007.

Papazachos, B.C., Karakostas, V.G., Papazachos, C.B. & Scordilis, E.M., 2000. The geometry of the Wadati-Benioff zone and lithospheric kinematics in the Hellenic arc, *Tectonophysics,* **319,** 275–230.

Polonia, A., Camerlenghi, A., Davey, F. & Sorti, F., 2002. Accretion, structural style and syn-continental sedimentation in the Eastern Mediterranean Sea, *Mar. Geol.,* **186,** 127–144.

Ranero, C., Morgan, J.P., McIntosh, K., & Reichert, C. 2003. Bending-related faulting and mantle serpentinization at the Middle America trench, *Nature,* **425,** 367–373.

Reston, T.J., von Huene, R., Dickmann, T., Klaeschen, D. & Kopp, H., 2002. Frontal accretion along the western Mediterranean Ridge: the effect of Messinian evaporites on the wedge mechanics and structural style, *Mar. Geol.,* **186,** 59–82.

Reynard, B., Hilairet, N., Balan, E. & Lazzeri, M., 2007. Elasticity of serpentines and extensive serpentinization in subduction zones, *Geophys. Res. Lett.,* **34,** L13307, doi:10.1029/2007GL030176.

Rondenay, S., Abers, G.A. & van Keken, P., 2008. Seismic imaging of subduction zone metamorphism, *Geology,* **36,** 275–278.

Royden, L. H., 1993. Evolution of retreating subduction boundaries formed during continental collision, *Tectonics,* **12,** 629–638.

Royden, L.H. & Husson, L., 2006. Trench motion, slab geometry and viscous stresses in subduction systems, *Geophys. J. Int.,* **167,** 881–905.

Sachpazi, M., *et al*., 2000. Western Hellenic subduction and Cephalonia transform: local earthquakes and plate transport and strain, *Tectonophysics,* **319,** 301–319.

Sachpazi, M. *et al*., 2007. Moho topography under central Greece and its compensation by Pn time-terms for the accurate location of hypocenters:

the example of the Gulf of Corinth 1995 Aigion earthquake, *Tectonophysics,* **440,** 53–65.

Sodoudi, S. *et al*., 2006. Lithospheric structure of the Aegean obtained from P and S receiver functions, *J. geophys. Res.,* **111,** B12307, doi: 10.1029/2005JB003932.

Spakman, W., 1986. Subduction beneath Eurasia in connection with the Mesozoic Tethys, *Geologie en Mijnbouw,* **65,** 145–153.

Spakman, W., Van Der Lee, S. & Van Der Hilst, R., 1993. Travel-time tomography of the European-Mediterranean mantle down to 1400 km, *Phys. Earth planet. Int.,* **79,** 3–74.

Stammler, K., 1993. Seismic Handler-Programmable multichannel data handler for interactive and automatic processing of seismological analyses, *Comput. Geosci.,* **19,** 135–140.

Suckale, J., Rondenay, S., Sachpazi, M., Charalampakis, M., Hosa, A. & Royden, L.H., 2009. High-resolution seismic imaging of the western Hellenic subduction zone using teleseismic scattered waves, *Geophys. J. Int.,* doi:10.1111/j.1365–246X.2009.04170x.

Taymaz, T., Jackson, J. & Westaway, R., 1990. Earthquake mechanisms in the Hellenic Trench near Crete, *Geophys. J. Int.,* **102,** 695–731.

Truffert, C., Chamot-Rooke, N., Lallemant, S., de Voogd, B., Huchon, P. & Le Pichon, X., 1993. The crust of the western Mediterranean Ridge from deep seismic data and application to field data from the northern Rio Grande Rift, *Geophys. J. Int.,* **125,** 443–458.

Underhill, J., R., 1989. Late Cenozoic deformation of the Hellenides foreland, western Greece, *Geol. Soc. Am. Bull.,* **101,** 613–634.

van Hinsbergen, D.J.J., Hafkenscheid, E., Spakman, W., Meulenkamp, J.E. & Wortel, R., 2005. Nappe stacking resulting from subduction of oceanic and continental lithosphere below Greece, *Geology,* **33,** 325–328.

Virieux, J., 1986. P-SV wave propagation in heterogeneous media: velocity-stress finite-difference method, *Geophysics,* **51,** 889–899.

White, R.S., McKenzie, D. & O'Nions, R.K., 1992. Oceanic crustal thickness from seismic measurements and rare Earth element inversions, *J. geophys. Res.,* **97,** 19 683–19 715.

Widess, M.B., 1973. How thin is a thin bed?, *Geophysics,* **38,** 1176–1180.

Wortel, M.J.R. & Spakman, W., 2000. Subduction and slab detachement in the Mediterranean-Carpathian region, *Science,* **290,** 1910–1917.

Wyss, M. & Baer, M., 1981. Earthquake hazard in the Hellenic arc, in *Earthquake Prediction: An international Review*, Vol. **4**, pp. 153–172, eds Simpson, D.W. & Richards, P.G., AGU Maurice Ewing Series, Am. geophys. Union, Washington, D.C.

Yuan, X. *et al*., 2000. Subduction and collision processes in the Central Andes constrained by converted seismic phases, *Nature,* **408,** 958–961.

© 2010 The Authors, *GJI*, **183,** 833–849
Journal compilation © 2010 RAS

Slab top dips resolved by teleseismic converted waves in the Hellenic subduction zone

A. Gesret,[1,2] M. Laigle,[2] J. Diaz,[3] M. Sachpazi,[4] M. Charalampakis,[4] and A. Hirn[2]

Received 21 July 2011; revised 19 September 2011; accepted 22 September 2011; published 22 October 2011.

[1] The variations of the arrival times and polarities with backazimuth and distance of teleseismic P-to-S converted waves at interfaces bounding the slab crust under the upper plate mantle are used to constrain the depth, dip angle and azimuth of the slab of the Hellenic subduction zone. A grid search is designed to estimate the model parameters. Dip values of 16–18°, with an azimuth of 20° to 40°, are thus derived at 3 sites aligned over 50 km along the eastern coast of Peloponnesus. They are consistent with the variation from 54 to 61 km of the slab top depths constrained below each receiver. North of the Gulfs of Corinth and Evvia, a similar depth for the top of the slab is found at a distance from the subduction at least 100 km larger. This suggests flatter subduction of a different slab segment. Such a variation in slab attitude at depth across the region from south of the eastern Gulf of Corinth to north of Evvia is a candidate for the control of the recent or active localized crustal thinning of the upper plate we documented in earlier work, and of the surface deformation. **Citation:** Gesret, A., M. Laigle, J. Diaz, M. Sachpazi, M. Charalampakis, and A. Hirn (2011), Slab top dips resolved by teleseismic converted waves in the Hellenic subduction zone, *Geophys. Res. Lett.*, *38*, L20304, doi:10.1029/2011GL048996.

1. Introduction

[2] In the Hellenic subduction region (Figure 1), the geometry of the slab top has remained only loosely constrained by the spatial distribution of seismicity [e.g., *Papazachos et al.*, 2000] or travel time tomography [e.g., *Bijwaard et al.*, 1998], with a spread or resolution of tens of kilometers with respect to a dipping plane. The size of the seismic velocity anomaly shown by seismic tomography is huge for a slab, but because its internal structure is not resolved, it has been considered as resulting from a single subduction having been active throughout most of the Mesozoic and the entire Cenozoic [e.g., *Jolivet and Brun*, 2010]. However slab detachments and tears have been considered [e.g., *Wortel and Spakman*, 2000], among which the evidence for the one suggested to be associated to the Kefalonia fault has remained elusive.

[3] A better resolution may be reached with the receiver-function (RF) method at an array of temporary seismometers, since the dipping slab may be sampled at the spacing of the receivers deployed. From teleseismic P-to-S converted waves at interfaces with sharp velocity contrasts, the slab top and Moho, can be identified and located. We have illustrated that such interfaces with less than 10 km separation in depth can be resolved, and we have constrained consistently over several receivers in Peloponnesus such a thin low-velocity layer (LVL) between the upper plate mantle and the slab mantle [*Gesret et al.*, 2010]. This is the typical thickness of oceanic crust and hence for the first time we documented that the slab under Peloponnesus is unambiguously made of oceanic lithosphere.

[4] The dip angle and the dip azimuth of the slab top were not precisely known yet in this region though it has been approached early on by teleseismic converted waves studies [*van der Meijde et al.*, 2003; *Li et al.*, 2003]. The slab dip under Peloponnesus could not be resolved by the sparse receiver coverage of the broad scale study of *Sodoudi et al.* [2006]. From a profile of receivers aligned along the N 60° E azimuth through Peloponnesus to the Corinth Isthmus, *Suckale et al.* [2009] have derived a 15–20 km thick LVL with a constant dip of 22° from about 30 to 90 km depth by an advanced method of 2D inversion of the primary converted waves and of the multiples, i.e., backscattered waves at the free surface [*Rondenay et al.*, 2001]. Their preferred interpretation of this thick LVL, which is twice that of an oceanic crust, is that there is also serpentinization of an additional mantle domain above or below the slab crust. Since the position of the slab top inside this thick LVL is not precisely defined, neither is the value of the slab dip angle. Nor can the slab dip azimuth, that is the true dip direction.

[5] In the present study, we nevertheless will constrain the geometry of the slab under the receivers taking advantage of the clearly recorded signals we obtained. We resolve the slab top depth, dip value and dip azimuth by an analysis of the variation of converted wave times and polarities among earthquakes with different azimuths and distances. Such a resolution can be obtained only from processing high-quality data up to higher frequencies than in the usually considered broad band range. This is because the times of the successive negative and positive peaks from the top and base of the slab crust lose their relation to the depth of the interfaces for longer period signals, since in this domain of the thin-layer response, the spacing and amplitude of the peaks become a function of the period of the incoming P signal itself [*Gesret et al.*, 2010].

[6] We use high-frequency and resolution P to S converted signals at those of the several tens of receivers in the swath from SE Peloponnesus through central Greece in Figure 1, which have recorded earthquakes with a good

[1]Centre de Géosciences, Mines ParisTech, Fontainebleau, France.
[2]Sismologie, Institut de Physique du Globe de Paris, UMR 7514, CNRS, Paris, France.
[3]Instituto Jaume Almera, Consejo Superior de Investigaciones Científicas, Barcelona, Spain.
[4]Institute of Geodynamics, National Observatory of Athens, Athens, Greece.

Copyright 2011 by the American Geophysical Union.
0094-8276/11/2011GL048996

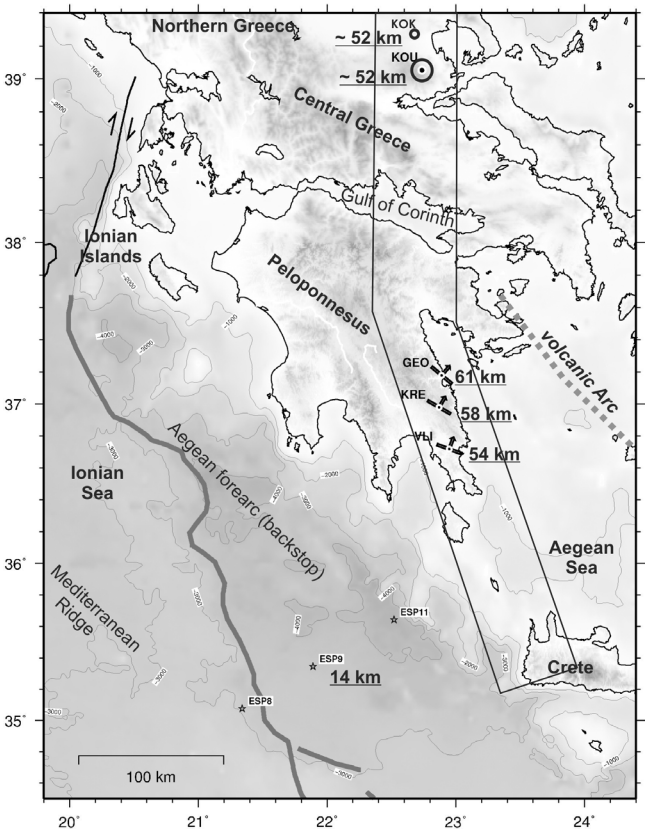

Figure 1. Location map of seismometer stations labelled VLI, KRE, GEO in the south and KOU, KOK in the North discussed in text, within swath indicated of temporary deployment of seismometers. At each of these station sites the slab top depth is indicated in kilometres and its direction of dip is indicated by an arrow, except at KOU in the North where the dip is too small to be resolved. The grey bold line offshore is the limit of the Aegean forearc, upper plate backstop, that is the plate boundary at sea-bottom. Its northward continuation as the active Cephalonia strike-slip fault is indicated.

azimuthal distribution, in order to place quantitative constraints on the depth, dip angle and dip azimuth of the slab top.

2. Data and Processing

[7] In the framework of the 'THALES WAS RIGHT' project, several tens of temporary seismometers have been deployed in a swath along Eastern Peloponnesus and northward across the Gulf of Corinth (Figure 1). A standard receiver-function, RF, processing has been applied to the 3-component seismograms of teleseismic body waves [e.g., *Stammler*, 1993; *Kind et al.*, 1995; *Galvé et al.*, 2002]. The vertical and the two horizontal components are first rotated into the local P, SV, SH ray-based coordinate system hereafter also called L-, Q-, and T-components. After deconvolution of the Q- and T-components by the P signal on the L-component, we obtain the SV or Q-RF containing the SV converted from P on the normal to it in its vertical plane of incidence, and the SH or T-RF on the normal to this vertical plane of incidence, which is null except for dipping or anisotropic layers beneath the receiver. Since we aim at detecting dipping interfaces, we also consider the T-RF as they generate signal on this component. The P to S converted waves at the top and bottom of the LVL at the Hellenic slab top at station VLI (Figure 1) in this SE Peloponnesus study region, appear on the SV-RF as a trough followed by a peak at about ~6–7 s after the P arrival. This is the signal from opposite polarity converters at about 60 and 70 km depth in a standard regional velocity model of a 30 km thick crust with Vp = 6.5 km/s on top of a normal velocity mantle. The robustness and success of the deconvolution can be illustrated (Figures S1a and S1b in the auxiliary material) for the M 9.3 Sumatra megathrust earthquake with its very complex and long source time and space function.[1]

[8] Some of the temporary seismometers have been deployed long enough to obtain an adequate coverage in terms of backazimuth and epicentral distance. The comparison of RF retrieved for earthquakes in very different azimuths show clear variations in terms of polarities and arrival times of the converted waves at the slab top. In the subsequent analysis, we use these variations to search for the depth, dip value and azimuth parameters of a dipping interface, as it is expected in this subduction zone context.

[9] With the advent of portable broadband seismometers, deployment of several of them along a line has been used to interpret topography of interfaces along vertical cross-sections from RF teleseismic data by stacking and imaging techniques [e.g., *Kosarev et al.*, 1999; *Galvé et al.*, 2002]. In these approaches, converted wave amplitudes are first back-propagated along their ray path to their conversion points, then projected and stacked as a depth-section along the line of receivers.

[10] This imaging is justified only if the real structure is 1D-layered. Indeed if there is a dipping structure, the converted ray does not remain in the azimuth of the incoming P wave and the incidence is considered, according to Snell's law with respect to the normal of the dipping interface and not anymore with respect to the vertical axis. Hence the converted S azimuth, incidence angle and travel time are different from the case of a horizontal interface. Nevertheless the transmitted P does not undergo the same complexity in the case of the slab crust between upper plate mantle and slab mantle, since a LVL behaves like a thin inclusion between parallel boundaries in optics. The arrival time delay of the converted S with respect to the first arriving P corresponds to the sampling of the conversion interface at a point that is different from the case of a horizontal interface. For instance, for a LVL at 60 km depth, with a 20° dip angle, the assumption of horizontal layering would induce errors in piercing point positions reaching 10 km in the updip direction (Figure S2a), and underestimation in depths reaching 2 km, as well as underestimation of 1° of the dip value.

[11] With respect to the isotropic horizontally layered case, the effects of a dipping converter is to generate signal also on the SH and not only SV RF, and to cause a variation of lag time with backazimuth, with both having specific patterns with respect to the dip direction and value. Significant SH amplitudes are indeed found, and their variation

[1]Auxiliary materials are available in the HTML. doi:10.1029/2011GL048996.

with backazimuth documented (Figure S6). Concerning the variation of lag time with azimuth, a range of only 0.5 s is expected for 15° dip. However, as we illustrated from synthetics and observations [*Gesret et al.*, 2010], there can be an effect on the picked times of the deformation of the waveforms by the resonance or thin layer effect that depend on signal spectrum with respect to LVL parameters. This is illustrated for two earthquakes from a same location and similar magnitudes for which the time lags picked for the top of the converting LVL differ by 0.3 s because of different signal spectra (Figure S1b), which is very significant with respect to resolving variations with azimuth of 0.5 s due to dip.

3. Grid Search for Slab Depth, Dip Angle and Dip Direction

[12] P to S converted waves at dipping interfaces are known to show also amplitude on the SH or T-RF, polarity reversals on the Q RF and/or T RF and variation of converted waves arrival times. These observations depend all on the backazimuth and incidence of the incoming P wave with respect to the dip direction and on the value of the incidence angle compared to the dip value. Opposite polarities for SH-RF are documented here between NNW and ESE backazimuths, indicating a SSW-NNE dip direction (Figure S6). Alternatively such two-lobed symmetry could be due to a horizontal converter with anisotropy in the overburden, but only in the special case of a strongly dipping axis of symmetry. A case has been reported for the Cascadia slab [e.g., *Park et al.*, 2004] where the wave pattern indicated an axis of symmetry along the strike, whereas it would be along dip in the dipping converter model and absence of anisotropy. We will check that here a dipping converter is the cause of the wave pattern by using several receivers on a line instead of only a single station analysis. The dip value and azimuth derived at each receiver for itself in the hypothesis of a dipping converter should then be consistent with the different depths of the converter under each receiver along the line.

[13] We explore the constraints that can be placed on the geometry of the interface under a receiver, by a grid search among its depth and dip parameters for the fit of polarities and arrival times of synthetics with the observations. To illustrate our approach, we use the VLI station, in Eastern Peloponnesus (Figure 1) of the permanent network of the National Observatory of Athens. For this station that sampled the whole range of azimuths (Figure S2b), we selected 44 earthquakes for the SV-RF polarity and arrival time and the clearest 25 among them showing amplitude on the SH-RF for its polarity. We compute the synthetic polarities and arrival times of the converted waves [*Owens et al.*, 1988] at the slab top and the corresponding receiver functions [*Ammon*, 1991]. The same procedure applied to the negative peak of the top of the slab crust has also been applied to the positive peak of its Moho, with consistent results for the dip and a difference in depth of 7 to 10 km. The following description and figures are for the case of the negative signal peak from the slab top.

[14] Polarities are not dependent on the depth of the conversion interface. Hence in a first step we explore the model parameter space for the dip angle value and dip direction azimuth which minimize the SV- and SH-RF polarity misfit between observations and synthetics. The SV-RF polarities (Figure 2a) allow us to constrain unambiguously the dip angle to lie between 0 and 20°. For the dip direction, a rather broad range from N to N 90°E azimuth, satisfies the 44 observed polarities The SH-RF polarities (Figure 2b) allow to reduce the range of dip values, constraining them to be above 12°, with a minimum misfit at 16°. For the dip azimuth, the value is then considerably reduced to a range between N20°E and N50°E, with the minimum at N 35° E. This azimuth of the minimum misfit indeed satisfies the 20 clearest among the 25 data. A dipping slab top model is thus comforted to account for the SH-RF.

[15] The arrival time observations on the SV-RF are then used (Figures 2f and 2g) in order to explore the depth versus the dip angle parameter in the range defined above, in a method inspired by *Baker et al.* [1996]. The absolute values of the residuals, observed-predicted time in the standard velocity-depth model mentioned (Figure 2f) and their algebraic values (Figure 2g) are then summed for each model. The intersection of the area of the minimum of the former by the zero line of the latter defines the depth for the slab top under the receiver as 54 km within a kilometer for the dip values from 0 to 18°, within which admissible values from polarities are contained.

[16] The arrival times for the slab top depth of 54 km can then also be used to further refine the dip angle value and dip direction azimuth values independently from the polarity misfit analysis that needs data from critical backazimuths. For these two model parameters, the mean of the absolute values of time residuals are contoured in Figure 2c and the mean of their algebraic values in Figure 2d. Finally, Figure 2e shows the intersection of acceptable domains from polarities (under the blue curve for radial and inside the magenta curve for transverse) and times (inside the green curve for the minimum of the mean of absolute values of time residuals and on the zero curve of the algebraic value of time residuals in stippled red). The intersection allows to restrict the dip angle value between 15° and 18° and the dip direction azimuth between N20°E and N30°E. In the best fit model the slab top depth is sampled to range from 49 to 56 km over about 20 km along dip (Figure S3a), with a random distribution of residuals with azimuth and incidence angle (Figure S3b)

[17] In order to check the consistency of the slab dip angle and direction at the scale of several tens of kilometers, our approach has been applied to other sites as well. However, very clear RF are required to resolve time picking on high-frequency signals, and due to the low level of seismicity in certain azimuths, only few sites have acquired sufficient data. This is the case for two other stations KRE and GEO located 25 and 50 km NNE from VLI. Beneath KRE, the slab top is at 58 km, its Moho at 65 km, and is dipping by about 16° in the N 30°E direction. Under GEO (Figure S4) the slab top is found to be at 61 km, and the base of its crust at 70 km, with a dip angle value of about 18° in the N 40°E azimuth. The regional depth variation computed from a mean dip of 16° in the N 30°E direction is consistent with the depths given by our grid search, to within a kilometer.

[18] In order to check the variation of the slab top at the scale of a hundred kilometers, we analyzed with the same approach the slab top beneath KOU located in central Greece to the North of the Corinth and Evvia gulfs (Figure 1). Minimization of the residuals gives a slab top depth of 52 km

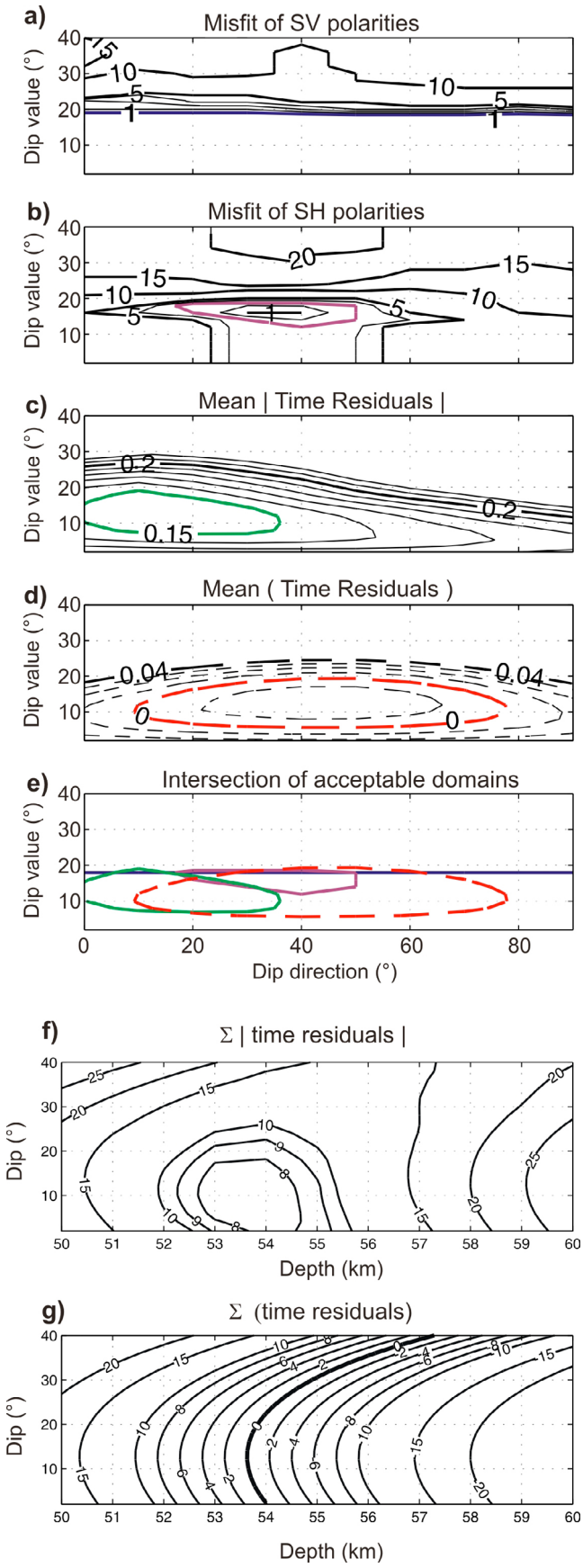

(Figure S5). This is about the same depth as for the three stations in SE Peloponnesus, whereas the station is located at a much larger distance from the subduction boundary at the outer limit of the forearc west of Cephalonia. Hence, to the north the average dip appears much smaller. This may explain that we could not resolve here locally from the 20 km aperture spanned by single station data neither a value for the dip angle significantly different from zero for the dip angle, nor an estimate of dip azimuth.

4. Conclusions and Discussion

[19] From the analysis of the variation with azimuth and angle of incidence of the arrival times of P-to-S converted waves and their polarities we constrain under SE Peloponnesus a slab dipping with an angle of 16–18° in a direction of azimuth N 20°E to N 40°E. This estimation of slab dip value and azimuth is consistent with the variation of the slab depth constrained simultaneously under each receiver. This increases northwards from 54 to 61 km under three receivers aligned over 50 km along the eastern coast of Peloponnesus (Figure 1).

[20] These dip directions of N 20–40° E appear to have more northerly azimuth values than the N 60°E azimuth perpendicular to the general strike of the subduction zone. North of the Gulfs of Corinth and Evvia, for instance at station KOU and KOK (Figures S1d and S1e), a similar depth of 52 km is found for a clear LVL which we interpret similarly as being the slab crust. The slab top thus documented is much shallower than the 160 km deep slab top inferred there by *Sodoudi et al.* [2006] mainly from S-to-P conversion. The shallow slab segment sampled at 52 km depth north of the Gulf of Corinth and Evvia by our observations is obviously not in continuity with the slab under Peloponnesus. The northward prolongation of that one, with its dip measured, and from its depth under Peloponnesus would lie much deeper. We note that the two observations would not be contradictory if the huge volume of the seismic tomography velocity anomaly, that is much thicker than

Figure 2. Station VLI. Grid search of model space for depth, dip angle value and dip direction azimuth of the slab top to minimize differences between model synthetics and observations of conversion times and polarities. Horizontal axis is dip direction azimuths from N to N 90°E and vertical axis is dip angle values from 0 to 40°. (a) Number of polarity misfits of 44 data of converted S on the SV, i.e., Q-RF. (b) Number of polarity misfits of 25 data of converted S on the SH, i.e., T-RF. (c and d) Mean of absolute values, respectively of algebraic values in seconds of time residuals, observed-synthetics, computed for a 54 km depth to the top of the slab derived from our analysis in Figure 2e and 2f. (e) The preferred dip azimuth on horizontal axis and dip angle on vertical axis are defined by the intersection of curves enclosing minima of acceptable domains of Figure 2a in blue, Figure 2b in magenta, Figure 2c in green, and their intersection by the dotted red curve of Figure 2c. (f and g) Horizontal axis is slab top depths from 50 to 60 km and vertical axis is dip angles value from 0 to 40° for respectively minimizing the mean of absolute and zeroing the sum of algebraic values in seconds of residuals of observed-synthetic times.

expected for a regular slab, would be made of superposed slab segments that seismic tomography cannot resolve.

[21] The depth of the slab top we define in the North is about the same as under receivers in SE Peloponnesus, but the distance of KOU and KOK from the subduction plate boundary is much larger, by at least 100 km along the normal to the forearc limit to up to 180 km when taken along the plate convergence vector. The average dip from under the backstop edge thus appears much smaller in this northern region. This may explain that a dip value and direction could not be resolved here locally from the 20 km aperture spanned by single station data (Figure S5) suggesting that it is underlain by a different segment of the slab. Also, the multiscale analysis of KOU and KOK did not succeed to constrain a layer as thin as an oceanic crust with respect to sites in Peloponnesus, since the negative to positive peak interval does not get that narrow even towards the higher frequencies (Figures S1d and S1e). A possibly larger thickness of the slab top LVL would be consistent with a continental or continental margin nature of the slab to the North. A corresponding larger buoyancy would also account for its shallower position and flatter dip, with respect to the domain south of the Gulf of Corinth where we have shown the oceanic nature of the slab by resolving its thin crust [*Gesret et al.*, 2010].

[22] The seismic observations hence suggest a slab tear or major warping in-between the south of the Gulf of Corinth and the north of the Gulf of Evvia. Across this region comprising the eastern Gulf of Corinth, a broad region of complex thinning of the crust of the upper plate was revealed by the Moho map derived from artificial source and natural earthquake refraction-reflection seismics [*Sachpazi et al.*, 2007]. This is also the region of surface deformation described as the Central Hellenic Shear Zone by *Papanikolaou and Royden* [2007]. The region of major variation of upper plate crustal thickness and the related region of surface deformation appear from the present study to be underlain by a domain of variation in attitude and possibly nature of slab segments, which may have exerted the primary control on the tectonic evolution through the plate above. From the recognition of such possibly sharp variations in slab depth early during the field experiment, receivers have been moved to achieve a denser and more 2D sampling over a broad swath, rather than remain along the initial line of receivers, in order to reveal the details of how the slab varies in-between (M. Sachpazi et al., manuscript in preparation, 2011).

[23] **Acknowledgments.** This research has been supported by the European Union FP6 NEST_INSIGHT programme, under project THALES WAS RIGHT.

[24] The Editor wishes to thank Laurent Jolivet and Frederik Tilmann for their assistance evaluating this paper.

References

Ammon, C. J. (1991), The isolation of receiver effects from teleseismic P waveforms, *Bull. Seismol. Soc. Am.*, *81*, 2504–2510.

Baker, J. E., J. B. Minster, G. Zandt, and H. Gurrola (1996), Constraints on crustal structure and complex Moho topography beneath Pinon flat, California, from teleseismic receiver-function, *Bull. Seismol. Soc. Am.*, *86*, 1830–1844.

Bijwaard, H., W. Spakman, and E. R. Engdahl (1998), Closing the gap between regional and global travel time tomography, *J. Geophys. Res.*, *103*, 30,055–30,078, doi:10.1029/98JB02467.

Galvé, A., M. Sapin, A. Hirn, J. Diaz, J.-C. Lépine, M. Laigle, J. Gallart, and M. Jiang (2002), Complex images of Moho and variation of Vp/Vs across the Himalaya and South Tibet, from a joint receiver-function and wide-angle-reflection approach, *Geophys. Res. Lett.*, *29*(24), 2182, doi:10.1029/2002GL015611.

Gesret, A., M. Laigle, J. Diaz, M. Sachpazi, and A. Hirn (2010), The oceanic nature of the African slab subducted under Peloponnesus: Thin-layer resolution from multiscale analysis of teleseismic P-to-S converted waves, *Geophys. J. Int.*, *183*, 833–849, doi:10.1111/j.1365-246X.2010.04738.x.

Jolivet, L., and J.-P. Brun (2010), Cenozoic geodynamic evolution of the Aegean, *Int. J. Earth Sci.*, *99*, 109–138, doi:10.1007/s00531-008-0366-4.

Kind, R., G. L. Kosarev, and N. V. Petersen (1995), Receiver-functions at the stations of the German Regional Seismic network (GRSN), *Geophys. J. Int.*, *121*, 191–202, doi:10.1111/j.1365-246X.1995.tb03520.x.

Kosarev, G., R. Kind, S. V. Sobolev, X. Yuan, W. Hanka, and S. Oreshin (1999), Seismic evidence for a detached Indian lithospheric mantle beneath Tibet, *Science*, *283*, 1306–1309, doi:10.1126/science.283.5406.1306.

Li, X., G. Bock, A. Vafidis, R. Kind, H.-P. Harjes, W. Hanka, K. Wylegalla, M. Van Der Meijde, and X. Yuan (2003), Receiver function study of the Hellenic subduction zone: Imaging crustal thickness variations and the oceanic Moho of the descending African lithosphere, *Geophys. J. Int.*, *155*, 733–748, doi:10.1046/j.1365-246X.2003.02100.x.

Owens, T. J., R. S. Crosson, and M. A. Hendrickson (1988), Constraints on the subduction geometry beneath western Washington from broadband teleseismic waveform modeling, *Bull. Seismol. Soc. Am.*, *78*, 1319–1334.

Papanikolaou, D. J., and L. H. Royden (2007), Disruption of the Hellenic arc: Late Miocene extensional detachment faults and steep Pliocene-Quaternary normal faults—Or what happened at Corinth?, *Tectonics*, *26*, TC5003, doi:10.1029/2006TC002007.

Papazachos, B. C., V. G. Karakostas, C. B. Papazachos, and E. M. Scordilis (2000), The geometry of the Wadati-Benioff zone and lithospheric kinematics in the Hellenic arc, *Tectonophysics*, *319*, 275–300, doi:10.1016/S0040-1951(99)00299-1.

Park, J., H. Yuan, and V. Levin (2004), Subduction-zone anisotropy under Corvallis, Oregon: A serpentinite skidmark of trench-parallel terrane migration?, *J. Geophys. Res.*, *109*, B10306, doi:10.1029/2003JB002718.

Rondenay, S., M. G. Bostock, and J. Shragge (2001), Multiparameter two-dimensional inversion of scattered teleseismic body waves: 3. Application to the Cascadia 1993 data set, *J. Geophys. Res.*, *106*, 30,795–30,807, doi:10.1029/2000JB000039.

Sachpazi, M., A. Galvé, M. Laigle, A. Hirn, E. Sokos, A. Serpetsidaki, J.-M. Marthelot, J. M. Pi Alperin, B. Zelt, and B. Taylor (2007), Moho topography under central Greece and its compensation by Pn time-terms for the accurate location of hypocenters: The example of the Gulf of Corinth 1995 Aigion earthquake, *Tectonophysics*, *440*, 53–65, doi:10.1016/j.tecto.2007.01.009.

Sodoudi, S., R. Kind, D. Hatzfeld, K. Priestley, W. Hanka, K. Wylegalla, G. Stavrakakis, A. Vafidis, H.-P. Harjes, and M. Bohnhoff (2006), Lithospheric structure of the Aegean obtained from P and S receiver functions, *J. Geophys. Res.*, *111*, B12307, doi:10.1029/2005JB003932.

Stammler, K. (1993), Seismichandler—Programmable multichannel data handler for interactive and automatic processing of seismological analyses, *Comput. Geosci.*, *19*, 135–140, doi:10.1016/0098-3004(93)90110-Q.

Suckale, J., S. Rondenay, M. Sachpazi, M. Charalampakis, A. Hosa, and L. H. Royden (2009), High-resolution seismic imaging of the western Hellenic subduction zone using teleseismic scattered waves, *Geophys. J. Int.*, *178*, 775–791, doi:10.1111/j.1365-246X.2009.04170.x.

van der Meijde, M., S. van der Lee, and D. Giardini (2003), Crustal structure beneath broad-band seismic stations in the Mediterranean region, *Geophys. J. Int.*, *152*, 729–739, doi:10.1046/j.1365-246X.2003.01871.x.

Wortel, M. J. R., and W. Spakman (2000), Subduction and slab detachment in the Mediterranean-Carpathian region, *Science*, *290*, 1910–1917, doi:10.1126/science.290.5498.1910.

M. Charalampakis and M. Sachpazi, Institute of Geodynamics, National Observatory of Athens, Lofos Nymfon, GR-11810 Athens, Greece. (cmarinos@noa.gr; m.sachp@.noa.gr)

J. Diaz, Instituto Jaume Almera, Consejo Superior de Investigaciones Científicas, C/Sole i Sabaris s/n, E-08028 Barcelona, Spain. (jdiaz@ija.csic.es)

A. Gesret, Centre de Géosciences, Mines ParisTech, 35 rue Saint-Honoré, F-77305 Fontainebleau CEDEX, France. (alexandrine.gesret@mines-paristech.fr)

A. Hirn and M. Laigle, Sismologie, Institut de Physique du Globe de Paris, UMR 7514, CNRS, 4 place Jussieu, F-75238 Paris CEDEX 05, France. (hirn@ipgp.fr; laigle@ipgp.fr)

Geophysical Journal International

Geophys. J. Int. (2015) **200,** 52–66
GJI Seismology

doi: 10.1093/gji/ggu374

Propagation of the velocity model uncertainties to the seismic event location

A. Gesret,[1] N. Desassis,[1] M. Noble,[1] T. Romary[1] and C. Maisons[2]

[1]*MINES ParisTech, PSL Research University, Centre de géosciences,* 35 *rue St Honoré, F-*77300 *Fontainebleau, France.*
E-mail: alexandrine.gesret@mines-paristech.fr
[2]*Magnitude SAS; Centre Regain, Route de Marseille, F-*04220 *Sainte-Tulle, France*

Accepted 2014 September 24. Received 2014 September 23; in original form 2014 February 28

SUMMARY

Earthquake hypocentre locations are crucial in many domains of application (academic and industrial) as seismic event location maps are commonly used to delineate faults or fractures. The interpretation of these maps depends on location accuracy and on the reliability of the associated uncertainties. The largest contribution to location and uncertainty errors is due to the fact that the velocity model errors are usually not correctly taken into account. We propose a new Bayesian formulation that integrates properly the knowledge on the velocity model into the formulation of the probabilistic earthquake location. In this work, the velocity model uncertainties are first estimated with a Bayesian tomography of active shot data. We implement a sampling Monte Carlo type algorithm to generate velocity models distributed according to the posterior distribution. In a second step, we propagate the velocity model uncertainties to the seismic event location in a probabilistic framework. This enables to obtain more reliable hypocentre locations as well as their associated uncertainties accounting for picking and velocity model uncertainties. We illustrate the tomography results and the gain in accuracy of earthquake location for two synthetic examples and one real data case study in the context of induced microseismicity.

Key words: Inverse theory; Probability distribution; Seismic tomography; Theoretical seismology.

1 INTRODUCTION

Earthquake hypocentre locations are central in seismogenic and tectonic interpretation. Indeed visual inspection of earthquake location maps is commonly used to delineate faults or fractures and mislocation can lead to an incorrect model of the Earth structure. For example, diffuse patterns that are sometimes observed can be due to unmapped or hidden faults but can also arise due to location inaccuracy. A precise location is particularly important in the microseismic context where the seismicity induced by mine or reservoir exploitation is often the only available tool to follow the fracturation. In addition, the spatial distribution of the uncertainties associated to the hypocentre location should also be estimated to interpret the results quantitatively. It is thus of primary importance to have accurate seismic event locations and their true associated uncertainties to obtain reliable interpretations.

The location of earthquake hypocentre is a typical inverse problem that can be solved with iterative linearized inversion approaches such as implemented in widely used softwares (e.g. Lee & Lahr 1975; Lahr 1989, 2002). These algorithms aim to retrieve the maximum likelihood solution that corresponds to the minimum of the misfit function between observed and computed *P* and *S* traveltimes. The major drawback of such local optimization methods is to give only a unique solution that can be inaccurate. Indeed as this problem is non-linear, its solution can be multimodal and the algorithm can be stuck in a local minimum that does not correspond to the true hypocentre location. The shape of the misfit surface will be especially irregular for a poor network coverage and for a heterogeneous medium (with velocity gradients and/or interfaces). Very often the uncertainties are estimated at the final hypocentre location under the Gaussian assumption, for example by scaling the partial derivatives of traveltime with respect to the hypocentre coordinates by the time residuals (Flinn 1965) or by prior estimates for picking and traveltime errors (Evernden 1969; Jordan & Sverdrup 1981). These approaches lead to confidence regions of elliptical shape that can be erroneous due to the strong assumption that the misfit function has a single optimum and a Gaussian shape. Since the work of Tarantola & Valette (1982), the probabilistic Bayesian formulation is often preferred (e.g. Moser *et al.* 1992; Wittlinger *et al.* 1993; Lomax *et al.* 2001; Husen *et al.* 2003) as it allows to retrieve the global minimum of the misfit function even for a non-linear/multimodal solution. With this Bayesian approach, the final solution is not a single point anymore but the complete posterior probability density function (pdf) of the event location. This formulation allows for

© The Authors 2014. Published by Oxford University Press on behalf of The Royal Astronomical Society.

Downloaded from http://gji.oxfordjournals.org/ by guest on November 27, 2014

uncertainty estimation even for a complex shape of the misfit function (Lomax *et al.* 2000; Husen & Smith 2004).

Even if a probabilistic earthquake location is more reliable, the quality of the estimated hypocentre location depends essentially on the velocity model accuracy (Husen & Hardebeck 2010, and references therein). As the velocity model used to locate events is always an approximation of reality, the locations and the associated uncertainties can be wrong if the velocity model uncertainties are not taken into account. Usually a unique velocity model is used to locate events and the velocity model uncertainties are integrated in the formulation of the pdf by adding a term to the traveltime picking uncertainties. Such an approach does not always allow reproduction of the real impact of the velocity model uncertainties on the shape of the pdf of the event location. Myers *et al.* (2007) account for velocity model errors in their Bayesian formulation of event location by estimating a joint posterior probability distribution that includes a term of correction to the traveltime curve predictions. Poliannikov *et al.* (2013) integrate velocity model uncertainties in a Bayesian formulation, based on random pertubations around a given velocity model; their approach is based on an equiprobability assumption of the random models. Gesret *et al.* (2011) and Hauser *et al.* (2011) took into account velocity model uncertainties by locating a seismic event in the ensemble of velocity model realizations obtained by a Bayesian analysis of independent data. The resulting cloud of possible locations allows them to estimate qualitatively the event location uncertainties that results from velocity model uncertainties. However, in these works, the final uncertainties associated to the location are not computed. Here, we propose a new rigorous formulation of the probabilistic event location that takes into account the picking uncertainties and the true uncertainties associated to the velocity model in the case where we have independent data that give us information on the velocity model.

In this work, the velocity model uncertainties are first estimated with a sampling approach of the Bayesian tomography of active shot data. We implement a Monte Carlo type algorithm to generate a large number of samples of statistically near-independent velocity models distributed according to the posterior distribution (Koren *et al.* 1991; Mosegaard & Tarantola 1995). The sampling of the whole posterior distribution allows for an unbiased estimation of the velocity model uncertainties (Debski 2010). In a second step, we propagate these velocity model uncertainties to the seismic event location uncertainties in a probabilistic framework. This enables to obtain more reliable hypocentre locations as well as their associated uncertainties accounting for velocity model uncertainties.

We illustrate our methodology in the context of induced microseismicity. Our approach is indeed particularly adapted to this case, where active and passive seismic data are available. For example, the routine microseismic monitoring of hydraulic fracturing projects often uses a laterally homogeneous layered velocity model constructed from a sonic log, which is then usually calibrated with perforation shots from known locations (Eisner *et al.* 2009; Maxwell 2010). These active sources can thus be used to estimate the velocity model uncertainties.

The paper is organized as follows. We first recall the standard formalism of the Bayesian earthquake location before introducing the new formalism that accounts for velocity model uncertainties. We then give a brief presentation of the Bayesian seismic tomography methodology and of the sampling algorithm developed to estimate the velocity model uncertainties. Finally, we illustrate on synthetic and real examples the results of our Bayesian tomography and the gain on accuracy of earthquake location obtained with our new approach.

2 PROBABILISTIC INVERSION: PRINCIPLE AND ALGORITHMS

2.1 Standard Bayesian earthquake location

The aim of seismic event location is to infer the hypocentre (x, y, z) and the origin time t_0 from a data set $\mathbf{d}_s^{\text{obs}}$ of observed traveltimes, where the subscript s stands for seismic event data. The corresponding forward problem that predicts the observations from the set of model parameters $\mathbf{l} = (x, y, z, t_0)$ in a given velocity field $\mathbf{v}$ writes

$$\mathbf{d}_s^{\text{obs}} = g_s(\mathbf{l}, \mathbf{v}) + \varepsilon_s = \mathbf{d}_s^{\text{cal}} + \varepsilon_s, \tag{1}$$

where g_s is the function that computes the traveltimes $\mathbf{d}_s^{\text{cal}}$ at the receivers for given $\mathbf{l}$ and $\mathbf{v}$, and where ε_s is a random error vector. In this work, the deterministic part of the forward problem $g_s(\mathbf{l}, \mathbf{v})$ is modelled with a new Eikonal solver (Noble *et al.* 2012, 2014) that generates accurate theoretical first arrival traveltimes with a finite-difference scheme (Vidale 1988; Podvin & Lecomte 1991).

To solve the inverse problem, we work in the Bayesian paradigm. In this framework, all the information of the problem is formulated in terms of pdf. The prior knowledge on the parameters is summarized by a prior pdf $\pi(\mathbf{l})$. The data are modelled by the pdf $\pi(\mathbf{d}_s^{\text{obs}}|\mathbf{l}, \mathbf{v})$, the likelihood, that links the data and the unknown parameters. More precisely, we suppose that ε_s follows a Gaussian probability distribution: $\varepsilon_s \sim \mathcal{G}(\mathbf{0}, \Sigma_s)$, where $\mathcal{G}(\mu, \Sigma)$ stands for the multi-Gaussian distribution with mean vector μ and variance matrix Σ. Note that both measurement errors and modelling errors are accounted for by Σ_s. Within this formalism, the variances of the measurement errors (contained in the diagonal of Σ_s) can vary as for instance when traveltime picks are made by different operators. As a result $\mathbf{d}_s^{\text{obs}} \sim \mathcal{G}(g_s(\mathbf{l}, \mathbf{v}), \Sigma_s)$ and the associated likelihood writes

$$\pi\left(\mathbf{d}_s^{\text{obs}}|\mathbf{l}, \mathbf{v}\right) = \mathrm{e}^{-L_s(\mathbf{l})}, \tag{2}$$

where

$$L_s(\mathbf{l}) = \frac{1}{2}\left(\mathbf{d}_s^{\text{obs}} - \mathbf{d}_s^{\text{cal}}\right)^t \Sigma_s^{-1}\left(\mathbf{d}_s^{\text{obs}} - \mathbf{d}_s^{\text{cal}}\right) \tag{3}$$

is a misfit function. The Bayes formula allows updating the prior knowledge on the model parameters by computing the posterior pdf of event location

$$\pi\left(\mathbf{l}|\mathbf{d}_s^{\text{obs}}, \mathbf{v}\right) = \frac{\pi\left(\mathbf{d}_s^{\text{obs}}|\mathbf{l}, \mathbf{v}\right)\pi(\mathbf{l})}{\int \pi\left(\mathbf{d}_s^{\text{obs}}|\mathbf{l}, \mathbf{v}\right)\pi(\mathbf{l})\mathrm{d}\mathbf{l}}. \tag{4}$$

Note that this computation involves an integral over the model space that can be regarded as a constant since it is not function of any particular model (Tarantola 2005). Therefore, the posterior is considered known up to a constant and can be written

$$\pi\left(\mathbf{l}|\mathbf{d}_s^{\text{obs}}, \mathbf{v}\right) \propto \pi\left(\mathbf{d}_s^{\text{obs}}|\mathbf{l}, \mathbf{v}\right)\pi(\mathbf{l}). \tag{5}$$

This posterior distribution summarizes how the information brought by the traveltime data improves the knowledge on the hypocentre coordinates and origin time. This formulation is especially useful for ill-posed inverse problem, when the solution is not unique as it allows for a complete understanding of all possible solutions. As shown by Tarantola & Valette (1982), if the prior information on the origin time T is taken as uniform, then it is possible to integrate analytically the pdf over T to obtain the marginal pdf for the spatial location parameters $\pi(x, y, z|\mathbf{d}_s^{\text{obs}}, \mathbf{v})$. This marginal pdf reduces to

$$\pi\left(x, y, z|\mathbf{d}_s^{\text{obs}}, \mathbf{v}\right) \propto \pi(x, y, z)\mathrm{e}^{-L_s(x,y,z)}, \tag{6}$$

Downloaded from http://gji.oxfordjournals.org/ by guest on November 27, 2014

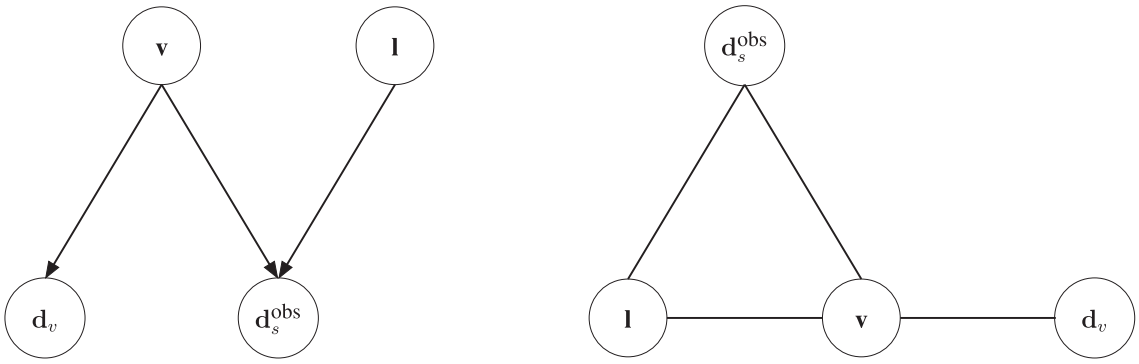

Figure 1. Left-hand panel: directed acyclic graph (DAG). Right-hand panel: moral graph.

where

$$L_s(x, y, z) = \frac{1}{2}\left(\tilde{\mathbf{d}}_s^{\mathrm{obs}} - \tilde{\mathbf{d}}_s^{\mathrm{cal}}\right)^t \Sigma_s^{-1}\left(\tilde{\mathbf{d}}_s^{\mathrm{obs}} - \tilde{\mathbf{d}}_s^{\mathrm{cal}}\right). \tag{7}$$

In this expression $\tilde{\mathbf{d}}_s^{\mathrm{obs}}$ is the vector of observed arrival times $\mathbf{d}_s^{\mathrm{obs}}$ minus their weighted mean, $\tilde{\mathbf{d}}_s^{\mathrm{cal}}$ is the vector of theoretical traveltimes $\mathbf{d}_s^{\mathrm{cal}}$ minus their weighted mean, where the weights w_i are given by $w_i = \sum_j w_{ij}$ and $w_{ij} = [\Sigma_s^{-1}]_{ij}$. As shown by Moser *et al.* (1992), the corresponding maximum likelihood origin time is given by

$$T_{ml}(x, y, z) = \frac{\sum_i \sum_j w_{ij}\left(d_{s,i}^{\mathrm{obs}} - d_{s,i}^{\mathrm{cal}}\right)}{\sum_i \sum_j w_{ij}}. \tag{8}$$

In practice the marginal pdf for the spatial location $\pi(x, y, z|\mathbf{d}_s^{\mathrm{obs}}, \mathbf{v})$ is estimated by applying an exhaustive grid search of the parameter space (x, y, z) as implemented by many authors such as Moser *et al.* (1992), Wittlinger *et al.* (1993) and Lomax *et al.* (2000).

2.2 Integrating several sources of information

In practice, the velocity field $\mathbf{v}$ is never perfectly known. It is generally derived from calibration data $\mathbf{d}_v$ and prior knowledge modelled by the distribution $\pi(\mathbf{v})$. As described in Section 2.3, the posterior distribution $\pi(\mathbf{v}|\mathbf{d}_v)$ of $\mathbf{v}$ knowing the data $\mathbf{d}_v$ can be obtained through the Bayes formula

$$\pi(\mathbf{v}|\mathbf{d}_v) \propto \pi(\mathbf{d}_v|\mathbf{v})\pi(\mathbf{v}). \tag{9}$$

Since the location depends on the velocity model (see eq. 5), we would like to incorporate in the event location the information brought by $\pi(\mathbf{v}|\mathbf{d}_v)$. The Bayesian paradigm provides a consistent framework to the situation where several sources of information are available. Indeed, it allows the propagation of the uncertainties on $\mathbf{v}$ to the earthquake location $\mathbf{l}$, as shown below. In a Bayesian perspective, the problem is to compute $\pi(\mathbf{l}|\mathbf{d}_s^{\mathrm{obs}}, \mathbf{d}_v)$ the posterior pdf of the event location knowing all the available data. For this purpose, we can write the pdf $\pi(\mathbf{l}|\mathbf{d}_s^{\mathrm{obs}}, \mathbf{d}_v)$ as the marginal of the joint pdf $\pi(\mathbf{v}, \mathbf{l}|\mathbf{d}_v, \mathbf{d}_s^{\mathrm{obs}})$

$$\pi\left(\mathbf{l}|\mathbf{d}_v, \mathbf{d}_s^{\mathrm{obs}}\right) = \int \pi\left(\mathbf{v}, \mathbf{l}|\mathbf{d}_v, \mathbf{d}_s^{\mathrm{obs}}\right) \mathrm{d}\mathbf{v}. \tag{10}$$

Using the Bayes formula, we have

$$\pi\left(\mathbf{v}, \mathbf{l}|\mathbf{d}_v, \mathbf{d}_s^{\mathrm{obs}}\right) \propto \pi\left(\mathbf{d}_v, \mathbf{d}_s^{\mathrm{obs}}|\mathbf{v}, \mathbf{l}\right)\pi(\mathbf{v}, \mathbf{l}). \tag{11}$$

We can reasonably assume that $\mathbf{l}$ and $\mathbf{v}$ are independent *a priori*

$$\pi(\mathbf{v}, \mathbf{l}) = \pi(\mathbf{v})\pi(\mathbf{l}). \tag{12}$$

For the other term of (11), we have the following equalities

$$\begin{aligned}\pi\left(\mathbf{d}_v, \mathbf{d}_s^{\mathrm{obs}}|\mathbf{v}, \mathbf{l}\right) &= \pi\left(\mathbf{d}_s^{\mathrm{obs}}|\mathbf{v}, \mathbf{l}\right)\pi(\mathbf{d}_v|\mathbf{v}, \mathbf{l}) \\ &= \pi\left(\mathbf{d}_s^{\mathrm{obs}}|\mathbf{v}, \mathbf{l}\right)\pi(\mathbf{d}_v|\mathbf{v}).\end{aligned} \tag{13}$$

Indeed, for fixed $\mathbf{v}$ and $\mathbf{l}$, $\mathbf{d}_v$ and $\mathbf{d}_s^{\mathrm{obs}}$ are independent. Moreover, $\mathbf{d}_v$ only depends on $\mathbf{v}$. Finally, integrating (11)–(13) in (10) we obtain

$$\pi\left(\mathbf{l}|\mathbf{d}_v, \mathbf{d}_s^{\mathrm{obs}}\right) \propto \int \pi(\mathbf{d}_v|\mathbf{v})\pi(\mathbf{v})\pi\left(\mathbf{d}_s^{\mathrm{obs}}|\mathbf{v}, \mathbf{l}\right)\pi(\mathbf{l})\mathrm{d}\mathbf{v}, \tag{14}$$

and, using (9),

$$\pi\left(\mathbf{l}|\mathbf{d}_v, \mathbf{d}_s^{\mathrm{obs}}\right) \propto \int \pi(\mathbf{v}|\mathbf{d}_v)\pi\left(\mathbf{d}_s^{\mathrm{obs}}|\mathbf{v}, \mathbf{l}\right)\pi(\mathbf{l})\mathrm{d}\mathbf{v}. \tag{15}$$

If we have a sample of velocity models $v_1, \ldots, v_N$ distributed according to the posterior distribution $\pi(\mathbf{v}|\mathbf{d}_v)$, the integral (15) can be estimated by Monte Carlo integration (Robert & Casella 2004) as follows:

$$\pi\left(\mathbf{l}|\mathbf{d}_v, \mathbf{d}_s^{\mathrm{obs}}\right) \propto \frac{1}{N}\sum_{i=1}^{N} \pi\left(\mathbf{d}_s^{\mathrm{obs}}|v_i, \mathbf{l}\right)\pi(\mathbf{l}). \tag{16}$$

This last equation allows the propagation of velocity model uncertainties to the seismic event location. As for the standard formulation, for each velocity model realization v_i, we integrate the origin time analytically and estimate the marginal pdf for the spatial location by applying an exhaustive grid search of the parameter space (x, y, z). This step is repeated for each v_i and the sum over the velocity models finally gives the posterior pdf that accounts for the true velocity model uncertainties.

The set of hypothesis and the links between the data and the parameters is a Bayesian network that can be represented with two graphs (Fig. 1). The first one is the Directed Acyclic Graph which summarizes the causal structure of the problem. The second graph is the moral graph which is obtained from the previous one by connecting nodes that have a common child and making all edges undirected. This graph allows us to read the conditional independence relationships. For instance, $\mathbf{d}_v$ is independent of $\mathbf{d}_s^{\mathrm{obs}}$ and $\mathbf{l}$ knowing $\mathbf{v}$ since there is no link between $\mathbf{d}_v$ and $(\mathbf{d}_s^{\mathrm{obs}}, \mathbf{l})$ if we suppress $\mathbf{v}$.

2.3 Bayesian tomography

In the previous section, we derived the general framework for propagating the velocity model uncertainties to earthquake location without any assumption about the data used for the calibration of the velocity model. From now on, we suppose that the estimation of $\mathbf{v}$ is performed by a first arrival traveltime tomography of active

Downloaded from http://gji.oxfordjournals.org/ by guest on November 27, 2014

shot data $\mathbf{d}_v$. The forward problem relates the velocity field $\mathbf{v}$ to the observed traveltimes $\mathbf{d}_v$ measured with a random noise ε_c

$$\mathbf{d}_v = g_c(\mathbf{v}) + \varepsilon_c, \tag{17}$$

where g_c is the function that gives the traveltimes and ε_c is a random error term. Similarly to the earthquake location problem, the traveltimes are computed with the Eikonal solver and we consider that $\varepsilon_c \sim \mathcal{G}(\mathbf{0}, \Sigma_c)$. We can then write the likelihood

$$\pi(\mathbf{d}_v|\mathbf{v}) = \mathrm{e}^{-L_v(\mathbf{v})}, \tag{18}$$

where

$$L_v(\mathbf{v}) = \frac{1}{2}[\mathbf{d}_v - \mathbf{g}_c(\mathbf{v})]^t \Sigma_c^{-1}[\mathbf{d}_v - \mathbf{g}_c(\mathbf{v})] \tag{19}$$

is the misfit function for the tomography. The Bayesian model is fully described by specifying $\pi(\mathbf{v})$ the prior pdf for $\mathbf{v}$ which reflects our knowledge on $\mathbf{v}$. Using the Bayes formula, we can write the posterior pdf for $\mathbf{v}$ that is considered known up to a constant

$$\pi(\mathbf{v}|\mathbf{d}_v) \propto \pi(\mathbf{d}_v|\mathbf{v})\pi(\mathbf{v}). \tag{20}$$

Several methods have been proposed in the literature for solving inverse problems in the Bayesian framework: mainly the Kitanidis–Oliver algorithm (Kitadinis 1995, 1996), developed for petroleum engineering applications and the neighbourhood algorithm (Sambridge 1999a,b), developed for geophysical inverse problems. We will sample the posterior distribution with a Markov Chain Monte Carlo (MCMC) algorithm which only requires to know the posterior pdf up to a multiplicative constant. To sample the velocity models according to the posterior distribution, we use a classical Metropolis–Hastings algorithm. This algorithm is known to converge towards the true posterior distribution (Robert & Casella 2004). However, the convergence can be quite slow. To overcome this drawback, during the first iterations of the algorithm (namely the burn-in period), the posterior $\pi(\mathbf{v}|\mathbf{d}_v)$ is replaced by a tempered distribution

$$\pi_T(\mathbf{v}|\mathbf{d}_v) \propto \mathrm{e}^{\frac{-L_v(\mathbf{v})}{T}}, \tag{21}$$

where T is a temperature. This mimics the simulated annealing algorithm which is commonly used in an optimization prospect where the final best velocity model is reached when the annealing temperature is close to zero (e.g. Weber 2000). Opposite to this classical optimization approach, our simulated annealing sampling algorithm aims to sample the posterior distribution in a similar way as proposed by Koren *et al.* (1991). We thus stop decreasing the annealing temperature when it is equal to one, for which $\pi_T(\mathbf{v}|\mathbf{d}_v) = \pi(\mathbf{v}|\mathbf{d}_v)$. With this fixed temperature, the accepted models sample the posterior distribution, in other words, their frequency of occurrence approximates the posterior pdf. All these models are consistent with both prior information (uniform in this case) and data (here the picking uncertainties). With this final set of accepted solutions, the statistical estimators such as means, variances or quantiles can be computed (Bodin & Sambridge 2009; Debski 2010). We will illustrate on two numerical examples that sampling the posterior is much more reliable and informative than selecting only one final velocity model, for the tomography but also for the subsequent event location.

3 EXAMPLES

In this section, we present the results obtained with the Bayesian sampling tomography that enables to obtain velocity model uncertainties and the gain in accuracy provided when they are taken into account in the probabilistic earthquake location formulation. We illustrate our approach on two synthetic examples, the first model with four layers is fairly simple, the second one inspired from a real acquisition is more complex. We finally apply our methodology to a real data set recorded in the context of hydraulic fracturing.

3.1 Numerical example 1

The model and the acquisition geometry are represented in Fig. 2. This four layer velocity model spans 600 m in depth, the third layer is slightly dipping (Fig. 2b). P velocities range from 3500 to 6000 m s^{-1} (Fig. 2c) and the V_P/V_S ratio varies from 1.6 to 1.95 (Fig. 2d). This velocity model is quite similar to those typically encountered in hydraulic fracturing projects. 8 calibration shots (black circles in Fig. 2a) are located in the bottom layer and 32 receivers (red triangles in Fig. 2a) are deployed in two boreholes. In this 3-D reference velocity model, we generated the P and S traveltime data with an Eikonal solver. To reproduce realistic picking errors we added a Gaussian noise (ε_c in equation 17) of respectively 2 and 4 ms standard deviation to the P- and S-wave arrival times. We end up with a set of 512 P and S 'observed' data $\mathbf{d}_v$.

With these observed data the first step is to apply the Bayesian tomography algorithm to retrieve the velocity model and, most important of all, the uncertainties. In other words the posterior pdf of the model parameters. For this example the velocity model is

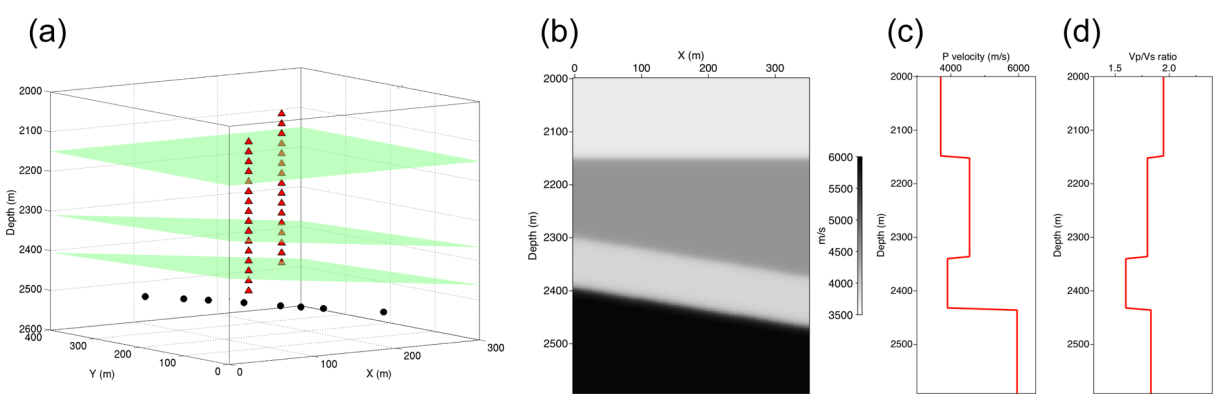

Figure 2. (a) 3-D acquisition geometry for the first example with calibration shot locations (black circles), receiver locations (red triangles) and positions of layer interfaces (green planes). (b) Vertical section of the reference V_P velocity model at $y = 200$ m. (c) V_P and (d) V_P/V_S vertical profiles of the reference velocity model at $y = 200$ m and $x = 150$ m.

Downloaded from http://gji.oxfordjournals.org/ by guest on November 27, 2014

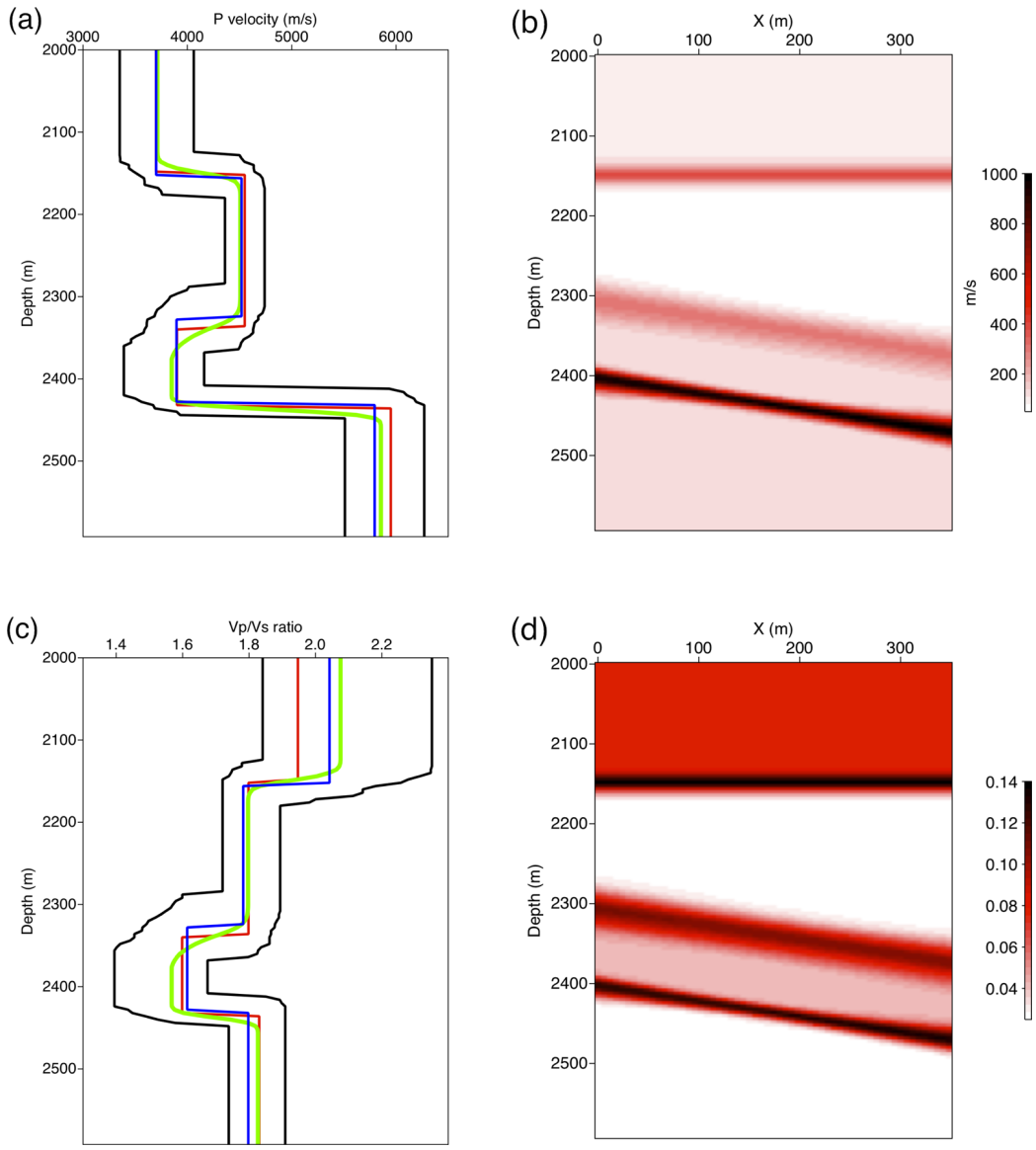

Figure 3. Results of the Bayesian tomography for the first example. (a) V_P vertical profiles at $y = 200$ m and $x = 150$ m for the true model (red line), the average model (green line), the maximum likelihood model (blue line) and the 95 per cent confidence interval based on the empirical quantiles (black lines). (b) Vertical section of the standard deviation with respect to the average model at $y = 200$ m. (c) and (d) Same representation as, respectively, (a) and (b) for the V_P/V_S ratio.

described by 13 parameters, the V_P and V_S velocities for each layer, the three interface depths and the two angles defining the azimuth and the dip value of the third layer. It must be mentioned that for this inversion step we are using exactly the same parametrization as used to build the reference model and to generate the observed data. The results obtained after running the simulated annealing sampling algorithm are summarized in Fig. 3. Top figures correspond to P velocity information and bottom figures to V_P/V_S ratio. Fig. 3(a) represents a vertical profile at $x = 150$ m and $y = 200$ m. The average P velocity profile (green line) is very close to and appears as a smooth version of the true P velocity model (red line). At first sight the maximum likelihood model (blue line) seems also satisfying. We also display the 2.5 and 97.5 per cent quantiles (black lines) associated to the marginal posterior pdf of V_P velocity. These quantify the uncertainties about the velocity model. A vertical section at $y = 200$ m of the standard deviation with respect to the average model is displayed in Fig. 3(b). This representation emphasizes the large uncertainties located at the interfaces. The same representation has been used for the V_P/V_S ratio (Figs 3c and d).

To estimate the influence of the velocity model accuracy on seismic event location, we generated observed traveltime data $\mathbf{d}_s^{\text{obs}}$ in the reference velocity model for one seismic event. As for the calibration data we added a Gaussian noise of, respectively 2 and 4 ms standard deviation to the P- and S-wave arrival times. We then relocate this event in a subset of 170 accepted velocity models resulting from the simulated annealing sampling tomography algorithm. We use the standard probabilistic approach to solve the inverse problem of the event location, whose formalism is recalled in Section 2.1. For the sake of clarity we only represent on Fig. 4 the hypocentres corresponding to the maximum of the pdf. At this stage it must be emphasized that all these 170 velocity models are not randomly generated around a given model but are all consistent with both the prior information and the data uncertainties considered in the tomography step. Despite this strong constraint, the resulting

Downloaded from http://gji.oxfordjournals.org/ by guest on November 27, 2014

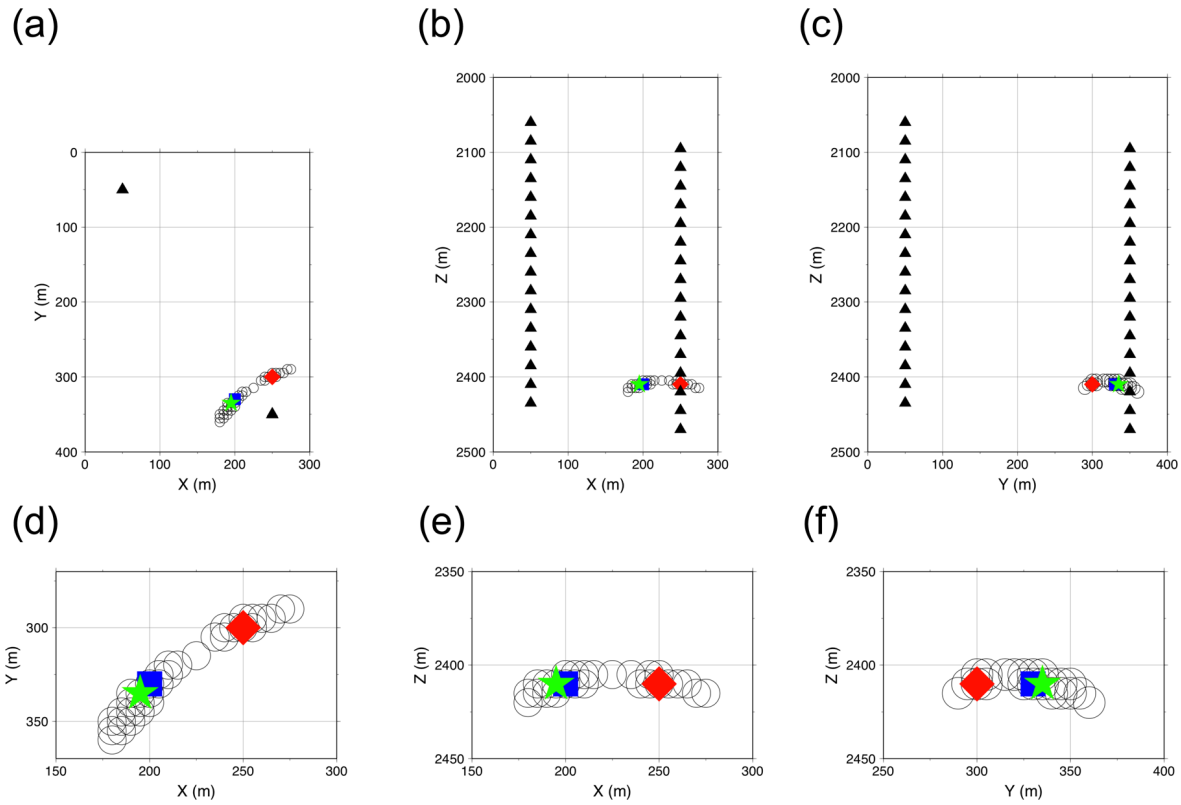

Figure 4. Influence of the velocity model on event location represented for the (a) XY, (b) ZX and (c) ZY planes. The black triangles indicate the receiver positions and the red diamond indicates the true location of the seismic event. The estimated hypocentres are represented for 170 velocity models resulting of the Bayesian tomography (open circles), for the average model (green star) and for the maximum likelihood model (blue square). (d)–(f) Locations of the event at a larger scale.

hypocentre distribution (black open circles) is very diffuse spreading up to 100 m in the X direction, 70 m in the Y direction, only the depth is relatively well constrained. In addition, the hypocentres obtained with the maximum likelihood velocity model (blue square in Fig. 4) and with the average model (green star in Fig. 4) are more than 50 m away from the true location (red diamond in Fig. 4). Both these statistical estimators (maximum likelihood and average models) can lead to a wrong event location as illustrated on this very simple four layer model. This example shows that considering only one velocity model in the location process can produce either a correct or a wrong event location with no mean to check the reliability of the result. On this example our formulation of the probabilistic event location (Section 2.2) can overcome this issue as illustrated below.

To quantify the contribution of our new pdf formulation that integrates both the picking and velocity model uncertainties, we compare it to the standard formulation for the seismic event that we generated previously. Fig. 5 displays the 68 per cent confidence intervals built from the marginal pdfs for the XY, ZX and ZY planes. Figs 5(a)–(c) represent the standard marginal pdf for the average velocity model. For this model that appears to be very close to the reference model (Fig. 3a), the 68 per cent confidence intervals for these three sections do not even include the true position of the event, indicated by the cross. In particular for the ZX plane, the true location is about 50 m away from the confidence interval. The standard pdf estimated in the maximum likelihood model (Figs 5d–f) gives similar results as computed for the average model. We can notice for this model that a weak second mode of the posterior pdf very close to the true location has emerged. This second mode is better identified (Figs 5g–i) when we increase the traveltime picking uncertainties (+0.001 s for P and +0.002 s for the S traveltimes) in the variance matrix Σ_s of the posterior pdf of event location (eq. 7). We inflated the picking uncertainties to reproduce the standard Bayesian approach where velocity model errors are accounted for by adding artificially a term to the measurement errors in the pdf. Even if it is very close, the confidence interval does not include the true location. With the new approach accounting for both picking and velocity model uncertainties, the results are much more convincing as the confidence envelope now includes the true position (Figs 5j–l). Note that for this latter case, we considered the true picking uncertainties (without inflating them) that are 0.002 s for P and 0.004 s for S traveltimes. This formulation allows, for the first time to our knowledge, to handle properly the propagation of the velocity model uncertainties to the uncertainties on event location.

Even on this simple four layer velocity model we have shown that inversion results should be cautiously interpreted. In the next section, we illustrate our approach on a more realistic model.

3.2 Numerical example 2

The second example is inspired from a real acquisition. The model and the acquisition geometry are represented in Fig. 6. P velocities range from 3200 to 6000 m s^{-1} (Fig. 6b) and the V_P/V_S ratio varies from 1.75 to 2.05 (Fig. 6c). This 23 layer model includes velocity gradients and very thin beds. 10 calibration shots (black circles in Fig. 6a) are located at a depth of 1035 m and 60 receivers (red

Downloaded from http://gji.oxfordjournals.org/ by guest on November 27, 2014

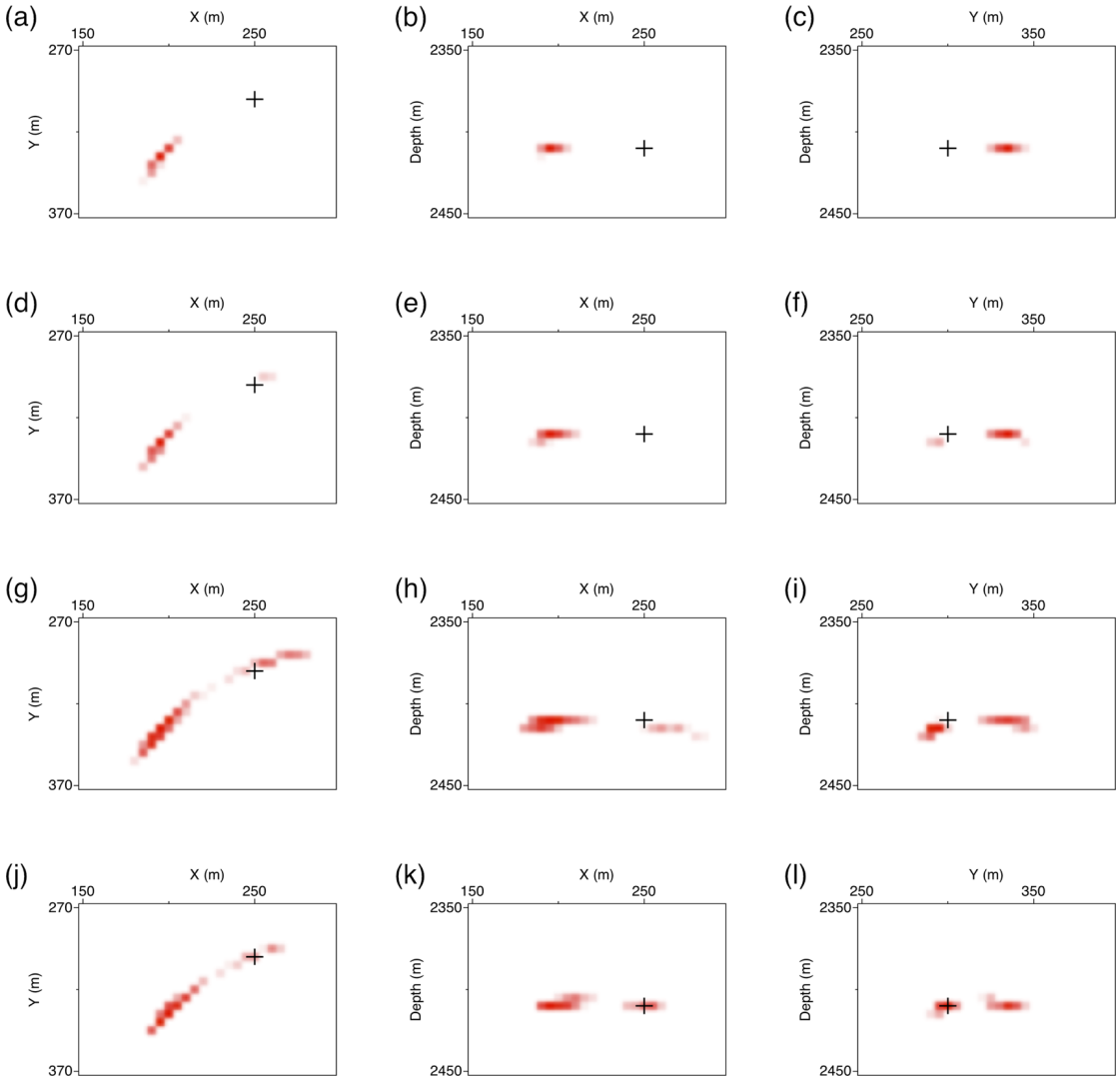

Figure 5. 68 per cent confidence intervals built from the marginal pdfs for the XY (left-hand figures), ZX (middle figures) and ZY (right-hand figures) planes. The true hypocentre location is indicated by the cross. (a)–(c) Standard pdf for the average model. (d)–(f) Standard pdf for the maximum likelihood model. (g)–(i) Standard pdf for the maximum likelihood model when traveltime picking uncertainties of the variance matrix Σ_s in the posterior pdf of event location are increased (+0.001 s for *P* and +0.002 s for the *S* traveltimes). (j)–(l) New pdf accounting for both picking and velocity model uncertainties without artificially inflating picking uncertainties.

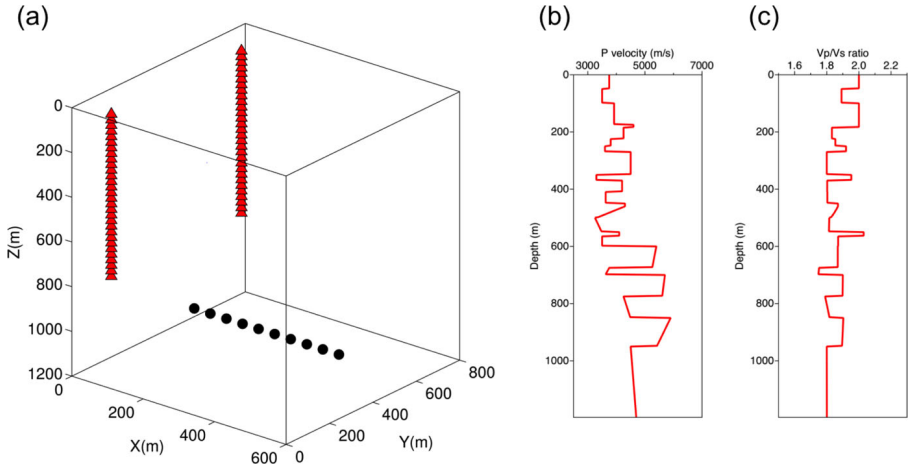

Figure 6. (a) Acquisition geometry for the second example inspired from a real acquisition with calibration shot positions (black circles) and receiver positions (red triangles). (b) V_P and (c) V_P/V_S vertical profiles of the 1-D reference velocity model.

Downloaded from http://gji.oxfordjournals.org/ by guest on November 27, 2014

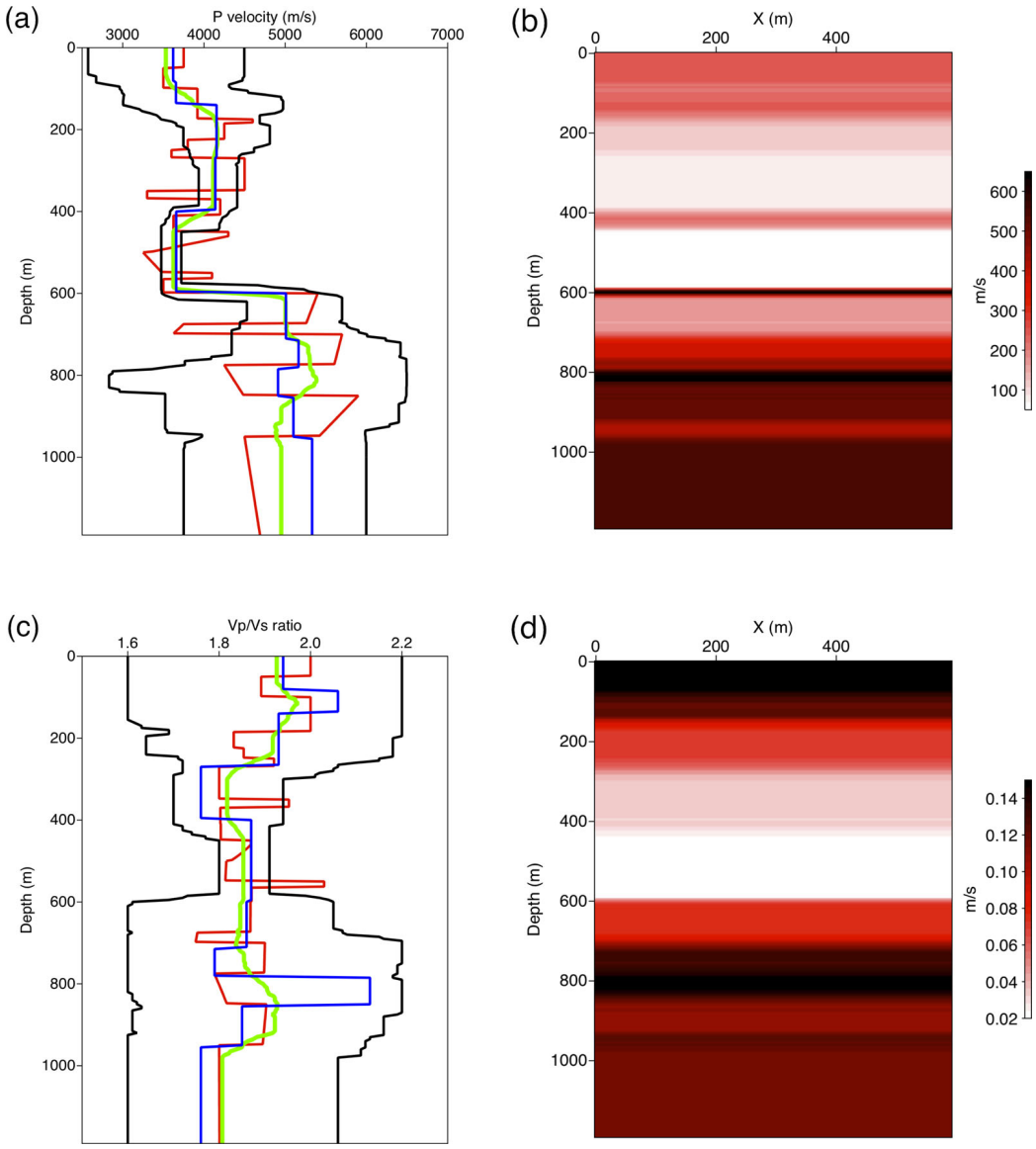

Figure 7. Results of the Bayesian tomography for the second example (V_P: top figures and V_P/V_S ratio: bottom figures). Information is plotted in the same way as Fig. 3.

triangles in Fig. 6a) are deployed in two boreholes. As for the previous example we generated the P and S traveltime data and added to them a gaussian noise of, respectively, 2 and 4 ms standard deviation. In addition to these 1200 data $\mathbf{d}_v$, we also generated the observed data $\mathbf{d}_s^{\text{obs}}$ for one seismic event.

The results of the Bayesian tomography algorithm are displayed in Figs 7(a)–(d). The average, the maximum likelihood models, the quantiles and the standard deviation are represented for the V_P velocity and the V_P/V_S ratio. As in a real situation we chose for the inversion a sparser parametrization (10 layers) that does not take into account all the complexity of the true model (thin layers and gradient within layers). The average P velocity and V_P/V_S profiles (green lines) appear as a smooth version of the true models (red lines) and seem to compensate for the sparse parametrization. At first sight, the maximum likelihood V_P/V_S model (blue line) is quite far from the reference model. It must be mentioned that as the true model (red lines) is included in the 95 per cent confidence intervals (black lines) except for very thin layers, this validates the tomography results. In spite of this positive criteria, it is not straightforward to estimate the quality of such a tomography; only the relocation of a seismic event will allow us to assess its reliability.

As for the first example, we compare our pdf formulation to the standard formulation for one seismic event. The confidence intervals built from the marginal pdfs for the XY, ZX and ZY planes are displayed in Fig. 8. The confidence intervals for the average velocity model (Figs 8a–c) are very close to the true location (cross), this assesses the relative quality of the average velocity model. The confidence intervals estimated for the maximum likelihood model (Figs 8d–f) are more than 50 m away from the true location. When the traveltime picking uncertainties are increased (+0.001 s for P and +0.002 s for the S traveltimes), the confidence intervals are wider but they do not contain the true location (Figs 8g–i). The common approach of artificially inflating the picking uncertainties in the posterior pdf of event location to account for velocity model errors does not work. The new formulation accounting for both picking and velocity model uncertainties allows a great improvement of the results since the confidence intervals now include the true location (Figs 8j–l). Although these intervals are spread over

Downloaded from http://gji.oxfordjournals.org/ by guest on November 27, 2014

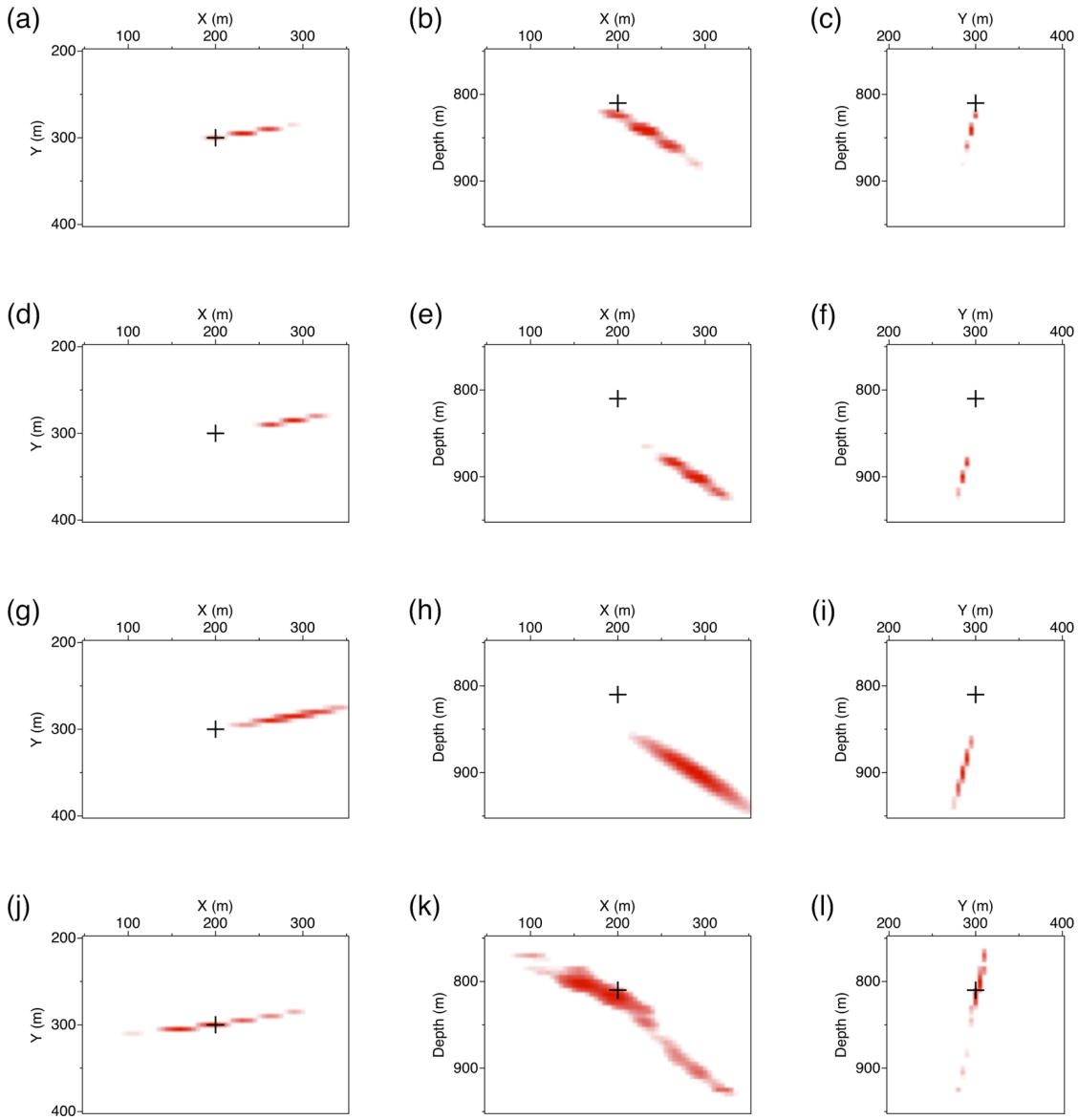

Figure 8. 68 per cent confidence intervals built from the marginal pdfs for the second example. Information is plotted in the same way as Fig. 5.

200 m in the X direction, the true hypocentre position is well located in the zone of higher probability (darker red). It should be noticed that the widening of the confidence intervals is due to the propagation of velocity model uncertainties as we considered the true picking uncertainties (0.002 s for *P* and 0.004 s for *S* waves) in our new formulation.

3.3 Real data case study

In this last section, we present the results of our approach that was applied to real data recorded in the context of hydraulic fracturing. The acquisition geometry is represented in Fig. 9 in a relative Cartesian coordinate system. The monitoring network consisted of two wireline arrays of twenty 3C-receivers that were deployed in two different vertical wells (red triangles in Fig. 9a). For both arrays, the top sensor is at the same depth and the receiver spacing is 30 m.

The initial velocity model consisted of a blocky horizontal model with fifteen layers (see Figs 9b and c). This model was derived from *a priori* geological information (sub-horizontal layers) and from compressive and shear velocity logs. The velocity variations observed on the logs have been taken into and resulted in building a fifteen layers model. *P* velocities range from 3500 to 6000 m s^{-1} and V_P/V_S ratio varies from 1.6 to 1.95.

Ten perforation shots performed along a horizontal well (black circles in Fig. 9a) at a depth of 1050 m (relative to the top sensor) have been considered. An illustration of a typical three component seismogram associated to a perforation shot is shown in Fig. 10. The seismograms, recorded with a sampling rate of 0.5 ms, have been rotated into the local (L-Q-T) ray-based coordinate system and have been normalized. In this case, the *S* waves are clearly identifiable even if their amplitudes appear to be fairly low. The *S* waves are not systematically observed as the perforation shots are basically isotropic explosive source that should not radiate *S*-wave energy. However, *S* waves are assumed to be induced at the well bore when the charges penetrate the formation through the casing of the well and therefore are assumed to be generated at the same origin time (Bardainne & Gaucher 2010). For each of the ten perforation shots, almost all 40 first *P* wave and approximately 20 *S* wave arrivals could be picked. For high signal to noise ratio, the uncertainties on

Downloaded from http://gji.oxfordjournals.org/ by guest on November 27, 2014

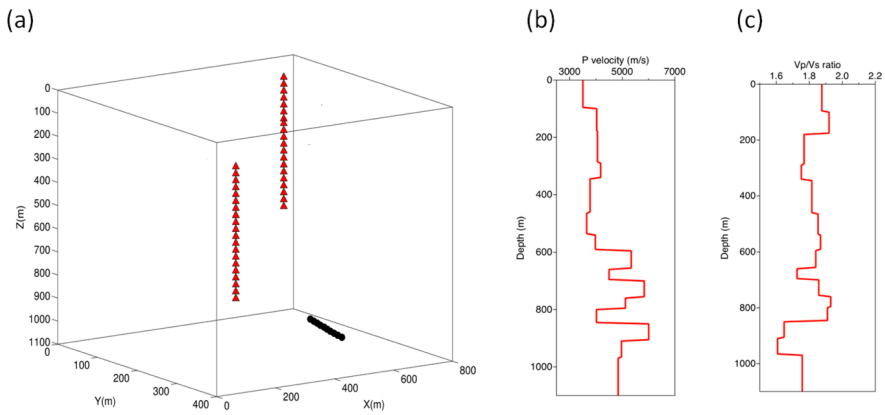

Figure 9. (a) Acquisition geometry for the real data example with calibration shot positions (black circles) and receiver positions (red triangles). (b) V_P and (c) V_P/V_S vertical profiles of the 1-D initial calibrated velocity model.

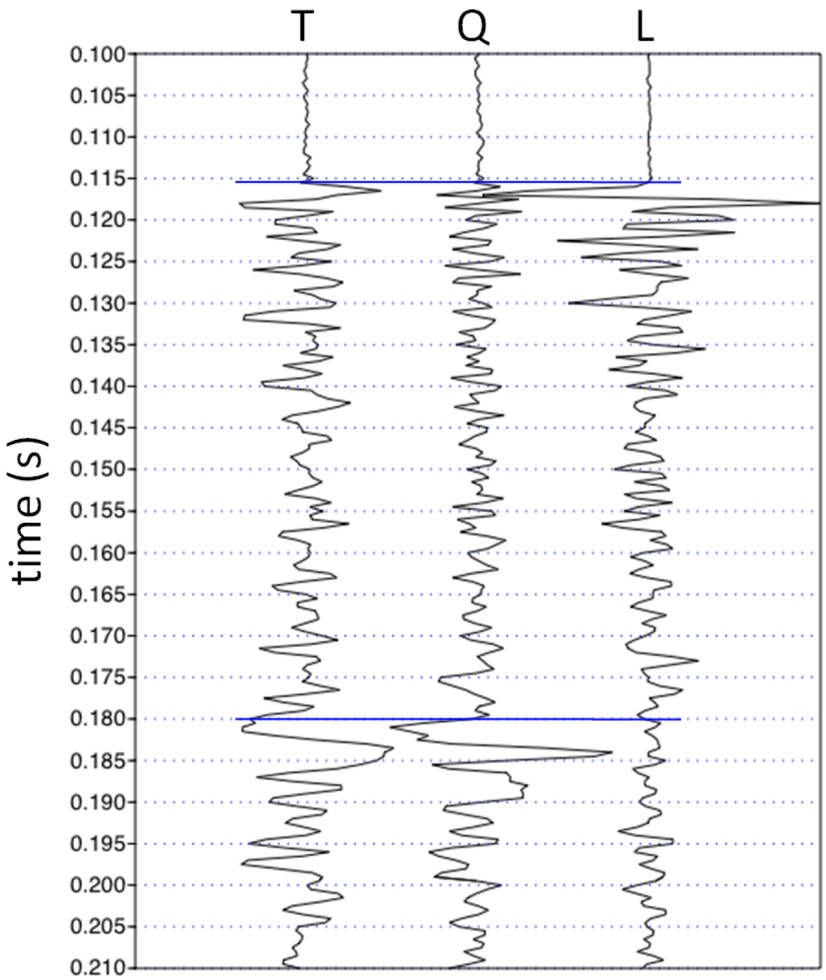

Figure 10. Example of a good quality 3-C seismograms recorded with a sampling rate of 0.5 ms, after rotation into the local (L-Q-T) ray-based coordinate system and normalization. Blue lines indicate the *P*- and *S*-wave picked arrival times with associated uncertainties not greater than, respectively, 1 and 2 ms for this case.

the picked arrival times are not greater than 1 ms for the *P* wave and 2 ms for the *S* wave. Over the entire data set we estimate the average *P*- and *S*-wave picking uncertainties to be around 2.5 and 5 ms, respectively.

The results of the Bayesian tomography algorithm are displayed in Figs 11(a)–(d). We started the inversion from the 15 layer parametrization of the initial velocity model (red lines). The model parameters to retrieve were the V_P and V_S velocities for each layer and the 14 interface depths. The average (green lines) and the maximum likelihood (blue lines) models are represented for the V_P velocity and the V_P/V_S ratio. The 2.5 per cent and 97.5 per cent quantiles (black lines) are displayed in order to quantify rigorously the uncertainties associated to the velocity model. A vertical section of the standard deviation is also represented.

Downloaded from http://gji.oxfordjournals.org/ by guest on November 27, 2014

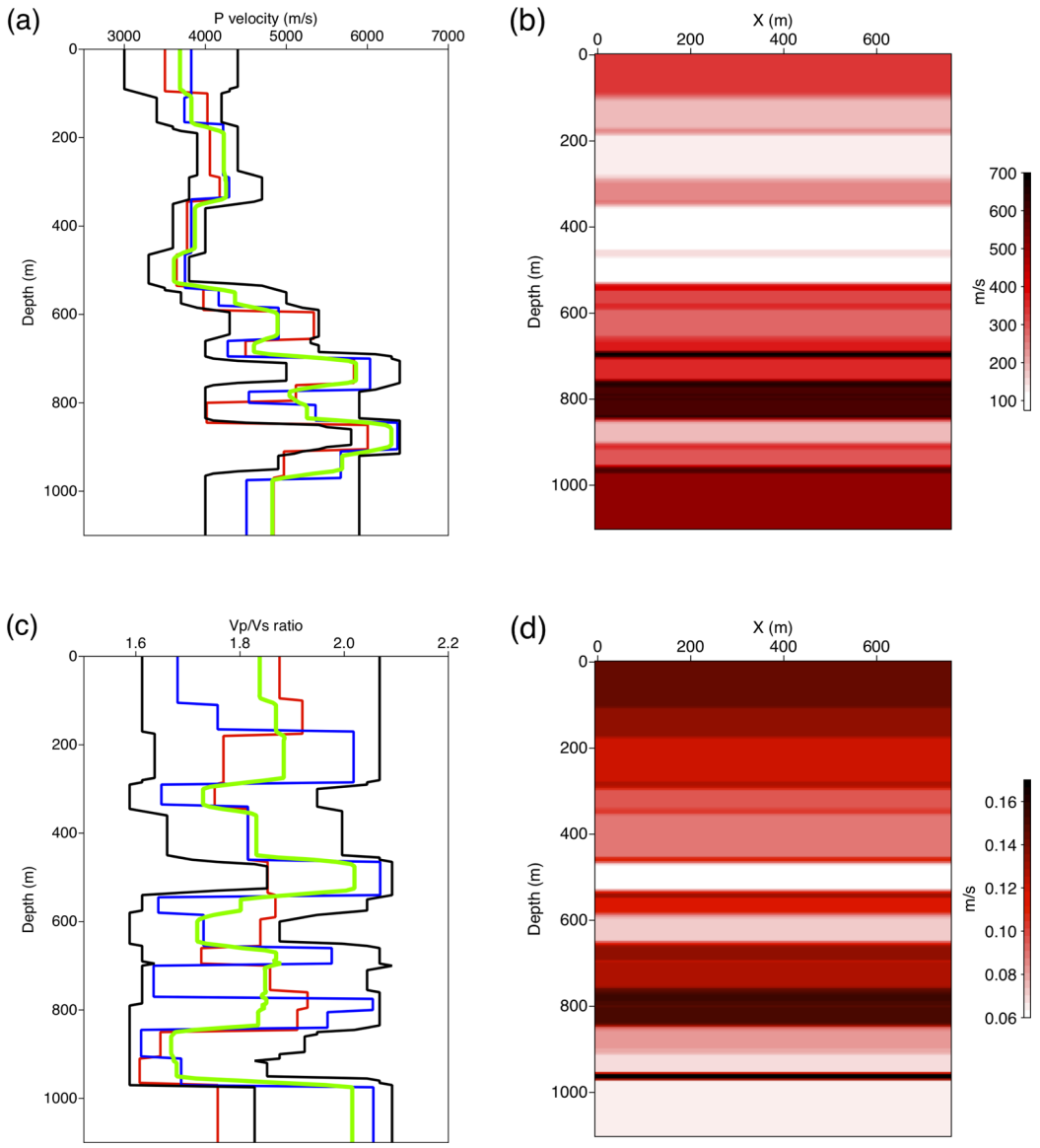

Figure 11. Results of the Bayesian tomography for the real data example. (a) V_P vertical profiles for the initial calibrated model (red line), the average model (green line), the maximum likelihood model (blue line) and the 95 per cent confidence interval based on the empirical quantiles (black lines). (b) Vertical section of the standard deviation with respect to the average model at $y = 200$ m. (c) and (d) Same representation as, respectively, (a) and (b) for the V_P/V_S ratio.

We compare our new pdf formulation (accounting for both picking uncertainties and velocity model uncertainties) to the standard formulation (just accounting for picking uncertainties) for five calibration shots. This comparison allows validation of our approach on real data as the locations of such perforation shots are known. Fig. 12(a)–(o) represent the standard marginal pdf for the initial velocity model estimated for the the five shots. Even if the location uncertainty (pdf) and the location errors (true location indicated by the cross) are relatively small, the confidence intervals for this initial velocity model do not include the true locations of calibration shots. Thus, we can consider that this initial velocity model would not be perfectly adapted to locate seismic events induced by operation. With the new formulation accounting for velocity model uncertainties, the true locations of the perforation shots are systematically included in the confidence intervals (Figs 13a–o). It should be mentioned that the picking uncertainties considered in the shot relocations are the same for both the standard and the new formulation. The approach allows thus us to propagate reliably the velocity model uncertainties and the picking uncertainties to the seismic event location.

4 DISCUSSION AND CONCLUSIONS

The accuracy of seismic event locations and the reliability of their associated uncertainties are crucial for many scientific and industrial applications. The largest contribution to location and uncertainty errors is due to the fact that the velocity model errors are usually not correctly taken into account. To overcome this issue, we proposed an approach that integrates properly the knowledge on the velocity model into the formulation of the probabilistic earthquake location.

In this paper, the information on the velocity model was provided by a tomography of first arrival traveltimes. Whatever the tomography method (local or global optimization or sampling) used to retrieve the velocity model, if the output is only a single velocity model (maximum likelihood or average), the subsequent event

Downloaded from http://gji.oxfordjournals.org/ by guest on November 27, 2014

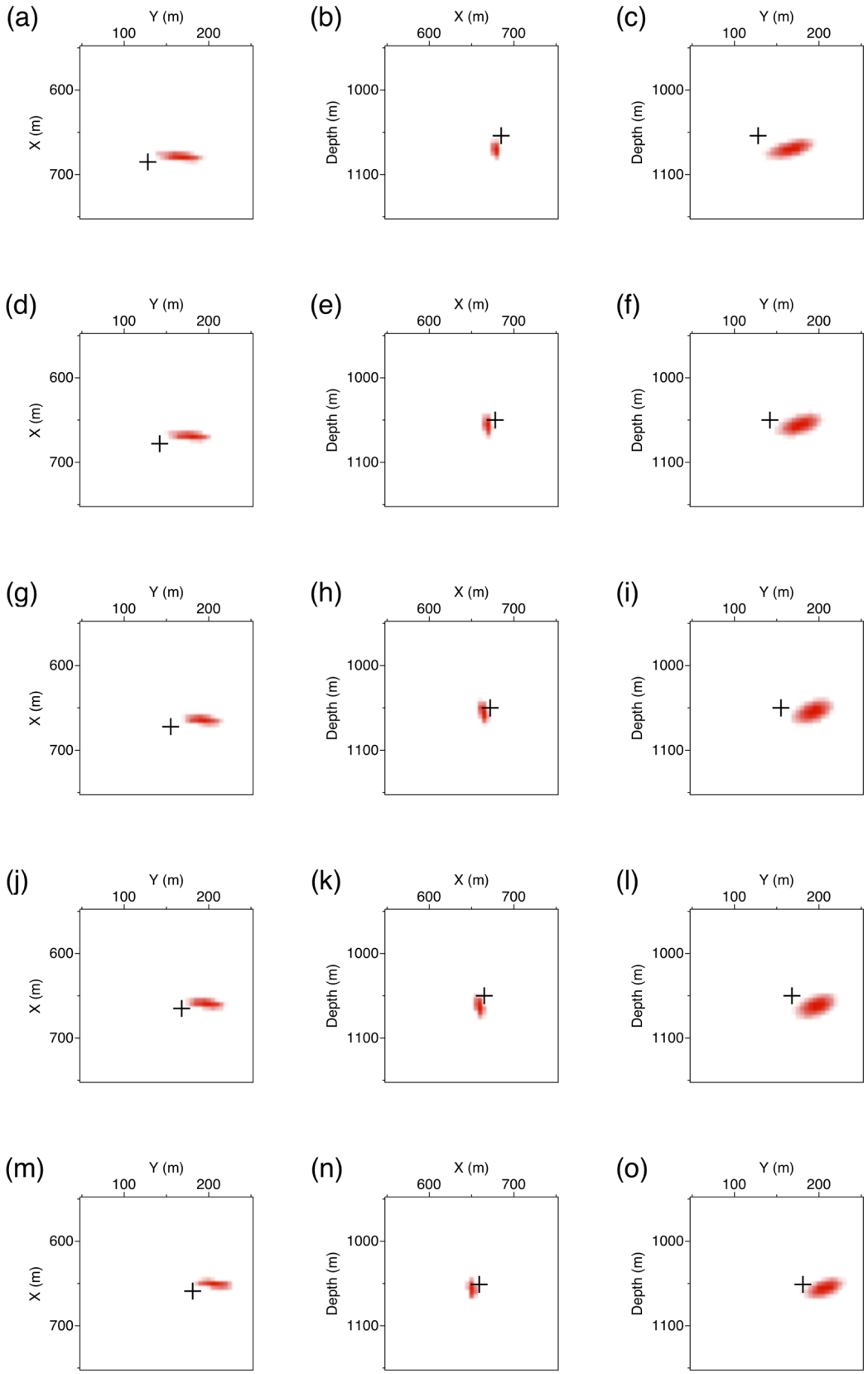

Figure 12. Standard pdf for the initial calibrated velocity model for the first (a–c), second (d–f), third (g–i), forth (j–l) and the fifth (m–o) calibration shot. 68 per cent confidence intervals built from the marginal pdfs for the XY (left-hand figures), ZX (middle figures) and ZY (right-hand figures) planes. The true calibration shot location is indicated by the cross.

Downloaded from http://gji.oxfordjournals.org/ by guest on November 27, 2014

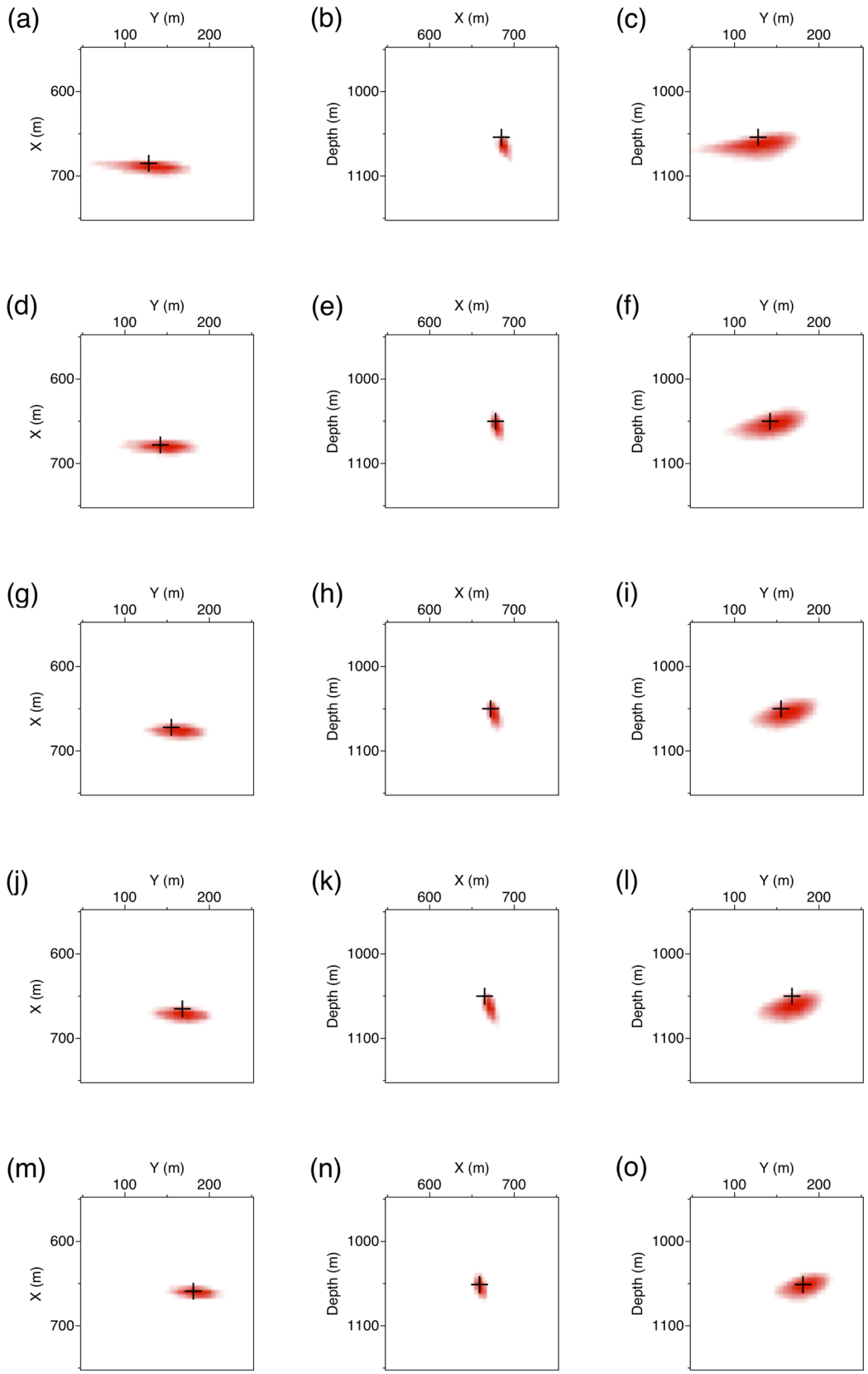

Figure 13. New pdf accounting for velocity model uncertainties for the first (a–c), second (d–f), third (g–i), forth (j–l) and the fifth (m–o) calibration shot. 68 per cent confidence intervals built from the marginal pdfs for the XY (left-hand figures), ZX (middle figures) and ZY (right-hand figures) planes. The true calibration shot location is indicated by the cross.

Downloaded from http://gji.oxfordjournals.org/ by guest on November 27, 2014

location can be inaccurate. For example standard linearized tomographic approaches aim to retrieve the maximum likelihood velocity model. We have shown that this estimator should be avoided for further computations of seismic event location. Indeed if the posterior pdf of the velocity model has an irregular shape (multimodal for example), neither the average nor the maximum likelihood model have a meaning. A more exhaustive analysis is required by estimating the whole posterior pdf of with a sampling approach. With these velocity model samples, the posterior pdf of seismic event location accounting for picking and velocity model uncertainties can then be properly estimated.

For the three examples we presented, the confidence intervals of the event location computed with the new formulation of the pdf include the true location of the event. We used for the tomography step a fairly simple sampling simulated annealing algorithm. Such a code can be stuck in a local mode of the posterior pdf if it is multimodal. More sophisticated algorithms that run several chains at different temperatures could be used to sample the pdf in a more reliable way (Romary 2010; Sambridge 2014). These algorithms could allow a gain in computation time with a shorter burn-in period. With efficient algorithms, it may then become possible to develop an approach of probabilistic passive tomography where both the hypocentre parameters and the velocity model parameters will be simultaneously inverted. Such a joint inversion would allow a characterization of the structure in a larger volume than that bounded by calibration shots.

Finally, in this paper, we illustrated our methodology in the context of induced microseismicity. Our approach is particularly adapted to the case where active data are available to calibrate the velocity model and obtain the related uncertainties. It could be worthwhile investigating if this new approach could be applied in a more general seismological context such as subduction zones or any other region that induce seismicity and where independent data are available to constrain the velocity model. For example, some authors (e.g. Cassidy & Waldhauser 2003; Robertson Maurice *et al.* 2003; Laigle *et al.* 2013) locate subduction zone events in velocity models obtained by seismic refraction profile analyses, by receiver function analyses or by surface wave tomography. Besides stochastic velocity inversions have recently been applied to such reflection/refraction traveltime data (e.g. Clark *et al.* 2013), to receiver functions of teleseismic data (e.g. Bodin *et al.* 2014) and to surface wave dispersion measurements (e.g. Young *et al.* 2013). These probabilistic approaches provide samples of velocity model that could thus be used to test the propagation of the velocity model uncertainties to the seismic event locations.

ACKNOWLEDGEMENTS

This project was funded by the Carnot M.I.N.E.S. Institute. The authors would like to thank the two anonymous reviewers for their valuable comments and suggestions for the improvement of the manuscript.

REFERENCES

Bardainne, T. & Gaucher, E., 2010. Constrained tomography of realistic velocity models in microseismic monitoring using calibration shots, *Geophys. Prospect.,* **58,** 739–753.

Bodin, T. & Sambridge, M., 2009. Seismic tomography with the reversible jump algorithm, *Geophys. J. Int.,* **178,** 1411–1436.

Bodin, T., Yuan, H. & Romanowicz, B., 2014. Inversion of receiver functions without deconvolution-application to the Indian craton, *Geophys. J. Int.,* **196,** 1025–1033.

Cassidy, J.F. & Waldhauser, F., 2003. Evidence for both crustal and mantle earthquakes in the subducting Juan de Fuca plate, *Geophys. Res. Lett.,* **30**(2), 1095, doi:10.1029/2002GL015511.

Clark, S.A., Faleide, J.I., Hauser, J., Ritzmann, O., Mjelde, R., Ebbing, J., Thybo, H. & Flueh, E., 2013. Stochastic velocity inversion of seismic reflection/refraction traveltime data for rift structure of the southwest Barents Sea, *Tectonophysics,* **593,** 135–150.

Debski, W., 2010. Seismic tomography by Monte Carlo Sampling, *Pure appl. Geophys.,* **167,** 131–152.

Eisner, L., Duncan, P.M., Heigl, W.M. & Keller, W.R., 2009. Uncertainties in passive seismic monitoring, *Leading Edge,* **28**(6), 648–655.

Evernden, J.F., 1969. Precision of epicenters obtained by small numbers of world-wide stations, *Bull. seism. Soc. Am.,* **59,** 1365–1398.

Flinn, E.A., 1965. Confidence regions and error determinations for seismic event location, *Rev. Geophys.,* **3,** 157–185.

Gesret, A., Noble, M., Desassis, N. & Romary, T., 2011. Microseismic monitoring: consequences of velocity model uncertainties on location uncertainties, in *Proceedings of the 3rd EAGE Passive Seismic Workshop,* PAS31, Athens, Greece, 27–30 March.

Hauser, J., Dyer, K.M., Pasyanos, M.E., Bungum, H., Faleide, J.I., Clark, S.A. & Schweitzer, J., 2011. A probabilistic seismic model for the European Arctic, *J. geophys. Res.,* **116**, B01303, doi:10.1029/2010JB007889.

Husen, S. & Hardebeck, J., 2010. *Earthquake Location Accuracy,* Community Online Resource for Statistical Seismicity Analysis, doi:10.5078/corssa-55815573.

Husen, S. & Smith, R., 2004. Probabilistic earthquake location in three-dimensional velocity models for the Yellowstone National Park region, Wyoming, *Bull. seism. Soc. Am.,* **94**(6), 880–896.

Husen, S., Kissling, E., Deichmann, N., Wiemer, S., Giardini, D. & Baer, M., 2003. Probabilistic earthquake location in complex three-dimensional velocity models: application to Switzerland, *J. geophys. Res.,* **108**(B2), 2077–2096.

Jordan, T.H. & Sverdrup, K.A., 1981. Teleseismic location techniques and their applications to earthquake clusters in the south-central Pacific, *Bull. seism. Soc. Am.,* **71,** 1105–1130.

Kitadinis, P.K., 1995. Quasi-linear geostatistical theory for inversing, *Water Resour. Res.,* **31,** 2411–2419.

Kitadinis, P.K., 1996. On conditional simulation to inaccurate data, *Math. Geol.,* **28,** 811–817.

Koren, Z., Mosegaard, K., Landa, E., Thore, P. & Tarantola, A., 1991. Monte Carlo estimation and resolution analysis of seismic background velocities, *J. geophys. Res.,* **96,** 20 289–20 299.

Lahr, J., 1989. HYPOELLIPSE: a computer program for determining local earthquake hypocentral parameters, magnitude, and first motion pattern (Y2K compliant version), *U.S. Geol. Surv. Open-File Rep.,* p. 92.

Lahr, J., 2002. User's Guide to HYPOINVERSE-2000: a Fortran program to solve for earthquake locations and magnitudes, *U.S. Geol. Surv. Open-File Rep.,* p. 123 pp.

Laigle, M. *et al.*, 2013. Seismic structure and activity of the north-central Lesser Antilles subduction zone from an integrated approach: similarities with the Tohoku forearc, *Tectonophysics,* **603,** 1–20.

Lee, W. & Lahr, J., 1975. HYPO71 (revised): a computer program for determining hypocenter, magnitude, and first motion pattern of local earthquakes, *U.S. Geol. Surv. Open-File Rep.,* p. 64.

Lomax, A., Virieux, J., Volant, P. & Berge-Thierry, C., 2000. Probabilistic earthquake location in 3D and layered models: introduction of a Metropolis-Gibbs method and comparison with linear locations, in *Advances in Seismic Event Location,* Vol. 228, pp. 101–134, eds Thurber, C.H. & Rabinowitz, N., Kluwer.

Lomax, A., Zollo, A., Capuano, P. & Virieux, J., 2001. Precise, absolute earthquake location under Somma-Vesuvius volcano using a new three-dimensional velocity model, *Geophys. J. Int.,* **146,** 313–331.

Maxwell, S., 2010. Microseismic: growth born from success, *Leading Edge,* **29**(3), 338–343.

Mosegaard, K. & Tarantola, A., 1995. Monte Carlo sampling of solutions to inverse problems, *J. geophys. Res.,* **100,** 12 431–12 447.

Downloaded from http://gji.oxfordjournals.org/ by guest on November 27, 2014

Moser, T., van Eck, T. & Nolet, G., 1992. Hypocenter determination in strongly heterogeneous earth models using the shortest path method, *J. geophys. Res.,* **97,** 6563–6572.

Myers, S.C., Johannesson, G. & Hanley, W., 2007. A Bayesian hierarchical method for multiple-event seismic location, *Geophys. J. Int.,* **171,** 1049–1063.

Noble, M., Gesret, A. & Belayouni, N., 2012. A new 3D Eikonal solver for accurate traveltimes, takeoff angles and amplitudes, in *Proceedings of the 74th EAGE Conference & Exhibition,* P283, Copenhagen, Denmark, 4–7 June.

Noble, M., Gesret, A. & Belayouni, N., 2014. Accurate 3-D finite difference computation of traveltimes in strongly heterogeneous media, *Geophys. J. Int.,* **199**(3) 1572–1585.

Podvin, P. & Lecomte, I., 1991. Finite difference computation of traveltimes in very contrasted velocity models: a massively parallel approach and its associated tools, *Geophys. J. Int.,* **105,** 271–284.

Poliannikov, O.V., Prange, M., Malcolm, A. & Djikpesse, H., 2013. A unified Bayesian framework for relative microseismic location, *Geophys. J. Int.,* **194,** 557–571.

Robert, C. & Casella, G., 2004. *Monte-Carlo Statistical Methods,* 2nd edn, Springer-Verlag.

Robertson, Maurice S.D., Wiens, D.A., Shore, P.J., Vera, E. & Dorman, L.M., 2003. Seismicity and tectonics of the South Shetland Islands and Bransfield Strait from a regional broadband seismograph deployment, *J. geophys. Res.,* **108,** 2461, doi:10.1029/2003JB002416.

Romary, T., 2010. Bayesian inversion by parallel interacting markov chains, *Inverse Problems Sci. Eng.,* **18**(1), 111–130.

Sambridge, M., 1999a. Geophysical inversion with a neighbourhood algorithm: I. searching a parameter space, *Geophys. J. Int.,* **138,** 479–494.

Sambridge, M., 1999b. Geophysical inversion with a neighbourhood algorithm: II. Appraising the ensemble, *Geophys. J. Int.,* **138,** 727–746.

Sambridge, M., 2014. A Parallel Tempering algorithm for probabilistic sampling and multi-modal optimization, *Geophys. J. Int.,* **196,** 357–374.

Tarantola, A., 2005. *Inverse Problem Theory and Model Parameter Estimation,* SIAM.

Tarantola, A. & Valette, B., 1982. Inverse problems – quest for information, *J. Geophys.,* **50,** 159–170.

Vidale, J., 1988. Finite-difference calculation of travel times, *Bull. seism. Soc. Am.,* **78,** 2062–2076.

Weber, Z., 2000. Seismic traveltime tomography: a simulated annealing approach, *Phys. Earth planet. Inter.,* **119,** 149–159.

Wittlinger, G., Herquel, G. & Nakache, T., 1993. Earthquake location in strongly heterogeneous media, *Geophys. J. Int.,* **115,** 759–777.

Young, M.K., Rawlinson, N. & Bodin, T., 2013. Transdimensional inversion of ambient seismic noise for 3D shear velocity structure of the Tasmanian crust, *Geophysics,* **78**(3), WB49–WB62.

Downloaded from http://gji.oxfordjournals.org/ by guest on November 27, 2014

GEOPHYSICS, VOL. 80, NO. 6 (NOVEMBER-DECEMBER 2015); P. WC133–WC143, 12 FIGS.
10.1190/GEO2015-0068.1

Downloaded 03/30/16 to 93.3.150.44. Redistribution subject to SEG license or copyright; see Terms of Use at http://library.seg.org/

Microseismic event location using the first and reflected arrivals

Nidhal Belayouni[1], Alexandrine Gesret[2], Guillaume Daniel[1], and Mark Noble[2]

ABSTRACT

Locating microseismic events accurately is essential to characterizing hydrofracked reservoirs. Several location approaches have been developed to solve this problem. We have developed a global grid search method based on the Bayesian probabilistic approach. In addition to retrieving the global minimum of the cost function, it enabled the computation of the uncertainty that was essential to quantify the quality of the results. The location uncertainty was tightly related to the amount and the quality of observed data used to perform the location. Using multiple arrivals increased the quantity of information collected in a cost-effective manner (no additional receivers were required). In this location algorithm, we have used the first and reflected arrivals to constrain the locations. To locate the events, it was essential to model the first and reflected arrivals given a velocity model and acquisition geometry. We have developed a ray-tracing algorithm capable of computing traveltimes and polarization of direct, refracted, and reflected waves in layered velocity models. We have applied this methodology for several examples. The synthetic data set was generated using full-waveform finite-difference modeling and recorded in a single vertical well. The first and reflected traveltimes were picked using the 3C seismograms. In the last example, we used the Cotton Valley real data set in which reflections could be seen for strong events due to the high velocity contrasts. The applications revealed that the location uncertainty was significantly reduced when using both arrivals compared with the case when only first arrivals were used. Combining the first and reflected arrivals even allowed us to improve the location accuracy when the velocity model was inaccurate.

INTRODUCTION

Human activities in the context of conventional or unconventional hydrocarbon reservoirs, mining areas, water reservoirs, or geothermal sites induce microseismicity that carries information on the fracturing process. In the particular case of hydraulic fracture stimulation, microseismic monitoring has the potential to reveal the fracture geometry (e.g., Phillips et al., 2002) indicating the extent and growth of fractures and to investigate the progress of fluid fronts during production (Maxwell and Urbancic, 2001). Seismic monitoring is thus important to optimize production and to avoid fracking-induced hazards. Most of the information extracted from microseismic data is based on the hypocenter source locations. Knowledge about event location accuracy and meaningful estimation of the associated uncertainties are consequently of primary importance to allow a reliable interpretation of microseismicity in terms of geomechanics and also seismic hazard related to hydraulic fracturing.

The location of an earthquake hypocenter is a typical inverse problem that can be solved with iterative linearized inversion approaches as implemented in widely used software (e.g., Lee and Lahr, 1975; Lahr, 1989, 2002). These algorithms aim to retrieve the maximum likelihood solution that corresponds to the minimum of the misfit function between the observed and computed P and S traveltimes. Because this problem is nonlinear, its solution can be multimodal and such local optimization methods can be stuck in a local minimum that does not correspond to the true hypocenter location. Very often, the uncertainties are estimated at the final hypocenter location under the Gaussian assumption (e.g., Flinn, 1965; Evernden, 1969; Jordan and Sverdrup, 1981). These approaches lead to confidence regions of elliptical shape that can be erroneous due to the strong assumption that the misfit function has a single optimum and a Gaussian shape.

Since the work of Tarantola and Valette (1982), the probabilistic Bayesian formulation, in which the final solution is not a single

Manuscript received by the Editor 30 January 2015; revised manuscript received 7 August 2015; published online 15 October 2015.
[1]Magnitude SAS, Centre Regain, Sainte-Tulle, France. E-mail: nidhal.belayouni@gmail.com; guillaume.daniel@bakerhughes.com.
[2]PSL Research University, MINES ParisTech, Centre de Géosciences, Fontainebleau, France. E-mail: alexandrine.gesret@mines-paristech.fr; mark.noble@mines-paristech.fr.
© 2015 Society of Exploration Geophysicists. All rights reserved.

Downloaded 03/30/16 to 93.3.150.44. Redistribution subject to SEG license or copyright; see Terms of Use at http://library.seg.org/

point anymore but the complete posterior probability density function (pdf) of the event location, is often preferred (e.g., Moser et al., 1992; Wittlinger et al., 1993; Lomax et al., 2001; Husen et al., 2003). Estimating this complete posterior pdf with a global grid search allows retrieval of the global minimum of the misfit function and estimation of uncertainty even for a complex shape of the misfit function (Lomax et al., 2000; Husen and Smith, 2004; Poliannikov et al., 2013; Gesret et al., 2015).

This probabilistic location solved with an exhaustive grid search is much more reliable than local approaches, but it can lead to very large uncertainties when only first-arrival traveltimes are considered. This is especially true if the first arrivals are head waves because the effective aperture is small. Adding arrivals from either reflected or head waves results in a longer effective array that could improve the resolution (Eisner et al., 2010). Zimmer et al. (2010) show that when the picked traveltime arrivals include head waves and direct waves depending on the sensor location, the uncertainties associated with these event locations are decreased. Coffin et al. (2012) and Culver et al. (2012) demonstrate that analyzing head waves in addition to direct arrivals can greatly improve the microseismic event localizations with the location procedure originally described in Abel et al. (2011). The objective of the article is to go a step forward by accounting for the reflected arrivals in addition to the first arrivals to reduce the event location uncertainties.

The posterior pdf of the event location is derived from the estimation, at each point (x, y, z) of the space, of the misfit function between the observed and computed P and S traveltimes. Most of the time, eikonal solvers (e.g., Vidale, 1990; Podvin and Lecomte, 1991; Lecomte, 1993; Noble et al., 2014) are used to efficiently compute the synthetic traveltimes at each point of a spatial grid. However, this finite-difference computation is especially adapted to estimate the first arrivals. To incorporate supplementary arrivals, we have implemented a new ray tracer that produces arrival times of several kinds of waves at each point of a spatial grid. The ray tracer also computes the polarization angles (azimuth and inclination) of these various arrivals because this information is needed when only a single well of geophones is available. The Bayesian formulation is particularly well suited to simultaneously handle different kinds of information. Thus, we can formulate the new posterior pdf of event location that takes into account the P and S traveltimes and the polarization of several arrivals.

The article is organized as follows: In the "Methods" section, we describe the 1D modeler that we have developed to compute arrival times and polarizations of direct arrivals, head waves, and the reflected and converted arrivals. We also derive the new formulation of the probabilistic location when several kinds of waves are taken into account. Synthetic examples are then presented to illustrate the decrease of uncertainty associated with the event location when considering the first and reflected arrivals. We finally show an application on some real data recorded in the Carthage Cotton Valley gas field.

METHODS

Traveltime calculation of the first and reflected arrivals

The probabilistic location of a seismic event needs to solve the forward problem, which consists in computing the P and S traveltimes from the potential source to the receivers and eventually the associated polarization angles (azimuth and/or inclination). Here, we are interested in modeling the first (direct and head waves) and the reflected arrivals that follow different paths.

This modeling problem has been widely studied, and many approaches are used to compute traveltimes. For example, Belayouni (2013) and Noble et al. (2014) develop an efficient and accurate eikonal solver that computes refracted and direct arrivals for highly contrasted velocity models, but this algorithm does not generate reflected arrivals. Other algorithms based on 3D ray tracing techniques (e.g., Červený, 2000) can generate multiple arrivals in smooth velocity models but often fail in the case of highly contrasted velocity models. In this paper, we introduce a two-point ray tracing method in horizontally layered velocity models that has a rapid and accurate convergence (Yue and Xiao-Fei, 2005; Pei et al., 2009). Even though the method is limited to flat 1D models, it is adapted to the routine microseismic monitoring of hydraulic fracturing projects. Indeed, this kind of monitoring often uses a laterally homogeneous layered velocity model constructed from a sonic log and calibrated with perforation shots from known locations (Eisner et al., 2009a; Maxwell, 2010).

The objective of our method is first to compute the raypath of the direct wave given the velocity model and the positions of the source and receiver. For the sake of simplicity, here we describe the approach for a 2D acquisition geometry (zx vertical plane) but our algorithm is developed for 3D acquisition geometry. For an N-layer model in which the source is located at (x_S, z_S) and the receiver is at (x_R, z_R), the traveltime along a ray defined by the ray parameter p is

$$t(S,R) = \sum_{i=0}^{N} \frac{h_i}{V_i\sqrt{1-p^2V_i^2}}, \tag{1}$$

where V_i and h_i are the velocity and the vertical distance of the ray in the layer i, respectively. The ray parameter p represents the horizontal slowness of the propagating wave and is constant along the ray. We can write it as follows:

$$p = \frac{\sin\theta_0}{V_0}, \tag{2}$$

where θ_0 is the takeoff angle and V_0 is the velocity in the layer containing the source. Following Fermat's principle, we minimize equation 1 with respect to the p to obtain the traveltime of the direct ray between the source S and the receiver R under the constraint $g(S,R) = |x_R - x_S|$, where g is the sum of the horizontal distances of the ray in each layer and is shown as follows:

$$g(S,R) = \sum_{i=0}^{N} \frac{pV_i}{\sqrt{1-p^2V_i^2}} h_i. \tag{3}$$

This method finds the geometric ray starting from S and reaching R with the minimum traveltime.

The minimization of the traveltime with respect to the ray parameter has severe limitations and fails when the angle is close to critical incidence. Indeed, a small change in the ray parameter could result in a huge variation of the traveltime leading to numerical instabilities. To avoid this pitfall, we introduce a new variable d_0, which represents the horizontal distance of the ray in the first layer. Inserting d_0 into equation 2, we obtain

Downloaded 03/30/16 to 93.3.150.44. Redistribution subject to SEG license or copyright; see Terms of Use at http://library.seg.org/

$$p = \frac{d_0}{V_0\sqrt{h_0^2 + d_0^2}}. \tag{4}$$

After replacing p in equations 1 and 3 by its expression in equation 4, we minimize the traveltime with respect to the new variable d_0 with the golden-section search method (Brent, 1973). Unlike the Newton method, the golden-section search does not evaluate the derivative of the function to be minimized and thus converges faster. Figure 1a shows a schematic example of a direct ray (bold line) that result from the minimization of equation 1 for a five-layer model.

The second step of our approach consists in estimating the traveltime of the refracted waves. These head waves appear at critical incidence. In this case, the takeoff angle is defined, and the computation of the ray is straightforward. The ray parameter has the following expression:

$$p = \frac{1}{V_{\max}}, \tag{5}$$

where $V_{\max}$ is the velocity of the refracting layer. We decompose the ray into three parts: the incident part from the source to the interface, the horizontal part that corresponds to the propagation along the refracting interface, and the emitted part from the interface to the receiver (bold dashed-dotted in Figure 1a). The advantage of this formulation is that the ray traveltime and path have an explicit expression. The minimization step is avoided, and the algorithm is consequently much faster. To obtain the first arrival, we choose the minimum traveltime between the direct and refracted waves.

The last step of our method consists of estimating the reflected ray. We follow the same approach as described above. However, we use an alternative velocity model and source/receiver positions to transform the reflection problem into a transmission problem. The associated velocity model is shown in Figure 1b. The lower part is a symmetry of the upper part with respect to the reflecting interface. Then, we apply the same algorithm as for the direct ray. Figure 1a shows an example of a reflected ray (bold dashed line) that corresponds to a direct ray in the associated velocity model (bold dashed line in Figure 1b).

Probabilistic event location with the first and reflected arrivals

The aim of the seismic event location is to infer the hypocenter (x, y, z) and the origin time T from a data set $\mathbf{d}^{\text{obs}}$ of observations. To solve this inverse problem, we work in the Bayesian paradigm. In this framework, all the information of the problem is formulated in terms of the pdf. The prior knowledge on the set of model parameters $\mathbf{l} = (x, y, z, T)$ is summarized by a prior pdf $\pi(\mathbf{l})$. The data are modeled by the pdf $\pi(\mathbf{d}^{\text{obs}}|\mathbf{l})$, the likelihood that links the data and the unknown parameters. The Bayes' formula allows updating the prior knowledge on the model parameters by computing the posterior pdf of the event location:

$$\pi(\mathbf{l}|\mathbf{d}^{\text{obs}}) = \frac{\pi(\mathbf{d}^{\text{obs}}|\mathbf{l})\pi(\mathbf{l})}{\int \pi(\mathbf{d}^{\text{obs}}|\mathbf{l})\pi(\mathbf{l})d\mathbf{l}}. \tag{6}$$

This computation involves an integral over the model space that can be regarded as a constant because it is not a function of any particular model (Tarantola, 2005). Therefore, the posterior is considered known up to a constant and can be written as follows:

$$\pi(\mathbf{l}|\mathbf{d}^{\text{obs}}) \propto \pi(\mathbf{d}^{\text{obs}}|\mathbf{l})\pi(\mathbf{l}). \tag{7}$$

This posterior distribution summarizes how the information brought by the observed data improves the knowledge on the hypocenter coordinates and origin time. This formulation is especially useful for an ill-posed inverse problem when the solution is not unique because it allows for a complete understanding of all possible solutions. We assume that the measurement errors and modeling errors follow a Gaussian probability distribution: $\varepsilon \sim \mathcal{G}(\mathbf{0}, \Sigma_d)$, where $\mathcal{G}(\mu, \Sigma)$ stands for the multi-Gaussian distribution with mean vector μ and variance matrix Σ. Within this formalism, the variances of the measurement errors (contained in the diagonal of Σ_d) can vary such as, for instance, when traveltime picks are made by different operators. As a result, the associated likelihood is shown as

$$\pi(\mathbf{d}^{\text{obs}}|\mathbf{l}) = e^{-L(\mathbf{l})}, \tag{8}$$

where

$$L(\mathbf{l}) = \frac{1}{2}(\mathbf{d}^{\text{obs}} - \mathbf{d}^{\text{cal}})^t \Sigma_d^{-1}(\mathbf{d}^{\text{obs}} - \mathbf{d}^{\text{cal}}) \tag{9}$$

is a misfit function. The estimation of this misfit function needs to solve the forward problem to compute the predicted data $\mathbf{d}^{\text{cal}}$ for a set of model parameters $\mathbf{l}$.

The Bayesian framework is particularly adapted to consider several kinds of observed data because the vector $\mathbf{d}^{\text{obs}}$ can contain various parameters. Here, we consider that this vector is composed of the first-arrival traveltimes $\mathbf{t}_f^{\text{obs}}$, the azimuth angles of these first arrivals ϕ_f^{obs}, and the reflected traveltimes $\mathbf{t}_r^{\text{obs}}$. Assuming independence between these three types of data parameters, we can rewrite the misfit function (equation 9) as a sum of the following terms:

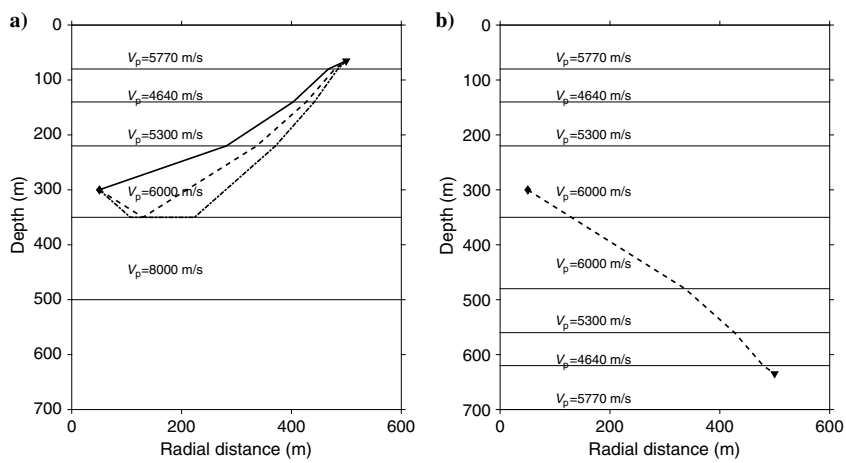

Figure 1. Ray geometry: (a) raypaths of direct, refracted, and reflected arrivals in a five-layer model with variable velocity and (b) raypath of the direct wave in the associated velocity model that corresponds to the reflected ray in the five-layer model.

$$L(\mathbf{l}) = \frac{1}{2}[(\mathbf{t}_f^{\text{obs}} - \mathbf{t}_f^{\text{cal}})^t \Sigma_f^{-1} (\mathbf{t}_f^{\text{obs}} - \mathbf{t}_f^{\text{cal}}) + (\phi_f^{\text{obs}} - \phi_f^{\text{cal}})^t \Sigma_\phi^{-1} (\phi_f^{\text{obs}} - \phi_f^{\text{cal}}) + (\mathbf{t}_r^{\text{obs}} - \mathbf{t}_r^{\text{cal}})^t \Sigma_r^{-1} (\mathbf{t}_r^{\text{obs}} - \mathbf{t}_r^{\text{cal}})]. \quad (10)$$

In this equation, Σ_f (respectively, Σ_ϕ and Σ_r) is the variance matrix of the first-arrival traveltimes (respectively, the azimuth angles and reflected traveltimes). The predicted traveltimes and azimuth angles $\mathbf{t}_f^{\text{cal}}$, ϕ_f^{cal}, and $\mathbf{t}_r^{\text{cal}}$ are computed for a set of model parameters $\mathbf{l}$ with the new ray tracer described in the previous section. If the prior information on the origin time T is taken as uniform, we can apply for this multiarrival case the same formalism as do Tarantola and Valette (1982) to integrate analytically the pdf over T. We obtain the marginal pdf for the spatial location parameters:

$$\pi(x, y, z|\mathbf{d}^{\text{obs}}) \propto e^{-\frac{1}{2}(\phi_f^{\text{obs}} - \phi_f^{\text{cal}})^t \Sigma_\phi^{-1} (\phi_f^{\text{obs}} - \phi_f^{\text{cal}})} e^{-\frac{1}{2}(\tilde{\mathbf{t}}^{\text{obs}} - \tilde{\mathbf{t}}^{\text{cal}})^t \Sigma_t^{-1} (\tilde{\mathbf{t}}^{\text{obs}} - \tilde{\mathbf{t}}^{\text{cal}})}. \quad (11)$$

In this expression, $\tilde{\mathbf{t}}^{\text{obs}}$ is the vector of the observed first and reflected arrival times minus their weighted mean, $\tilde{\mathbf{t}}^{\text{cal}}$ is the vector of theoretical traveltimes minus their weighted mean, and Σ_t is the variance matrix of the first and reflected traveltimes. In practice, the marginal pdf $\pi(x, y, z|\mathbf{d}^{\text{obs}})$ is estimated by applying an exhaustive grid search of the parameter space (x, y, z) as implemented by many authors, such as Moser et al. (1992), Wittlinger et al. (1993), and Lomax et al. (2000).

In this section, we assumed the independency between the observed azimuthal angles and the observed traveltimes. Considering this dependency would complicate the equations, and, to our best knowledge, the formalism has not been developed yet. The derivation of the equations is beyond the scope of this article because this assumption is not critical for our results. In complex 3D models, the calculated azimuths and traveltimes are also dependent. These parameters are, however, independent in most of the microseismic applications because the velocity models are described by horizontal layers and the acquisition geometries by linear sensor arrays.

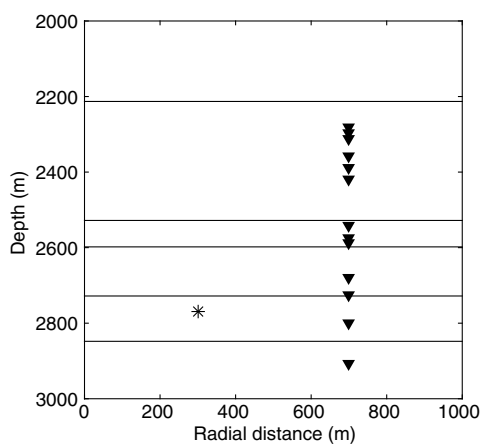

Figure 2. Acquisition geometry of the Cotton Valley real data example that is also used in the synthetic examples.

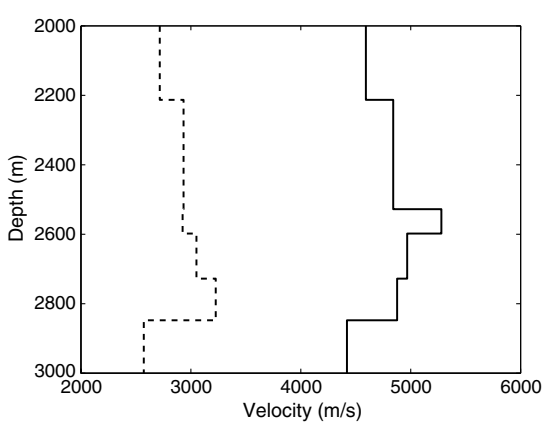

Figure 3. Velocity model used for the Cotton Valley real data example and also used in the synthetic examples (solid line, P-wave velocity; dashed line, S-wave velocity).

RESULTS

In this section, we introduce the results obtained when accounting for the first and reflected arrivals in the probabilistic earthquake location formulation and the gain in accuracy provided by this approach. We first illustrate our methodology on several realistic synthetic examples. The observed data are generated with a full-waveform modeler, and we demonstrate the robustness of the methodology by adding noise to the observations and by perturbing the velocity model. We finally apply our methodology to a real data set recorded in the context of hydraulic fracturing.

Numerical examples

We based our numerical examples on a real data set recorded in the Cotton Valley field. We use the same velocity model and receiver positions as Rutledge and Phillips (2003). The acquisition geometry consists of a single vertical array containing 13 receivers with depth ranging from 2280 to 2908 m, and the average east and north positions are 307 and 224 m, respectively (Figure 2). The six-layer model is represented in Figure 3 with P velocities ranging from 4420 to 5280 m/s and S velocities varying from 2570 to 3220 m/s. More details on the Cotton Valley experiment are given in the next section, which is dedicated to the application of our approach to a real data set.

We computed the synthetic observed data set using finite-difference full-waveform modeling software that generates the three velocity components. The horizontal force source time function is a 100-Hz Ricker wavelet. Figure 4 shows the vertical component of the seismograms recorded at 13 receivers for a source at (east, north, z) = (77, 550, 2770 m). This position will be used in the next three synthetic examples. The P- and S-wave direct arrivals have strong amplitude and are separated by approximately 70 ms. To be sure we are associating the reflection to the correct interface, a preliminary study is needed. We assume that the depths of the reflectors are generally well constrained with sonic logs, and we compare seismograms to theoretical traveltimes for the different interfaces. For this example, we superimpose on the seismograms some theoretical traveltimes computed with our new ray-tracing algorithm. This allows a reliable identification of the different arrivals that are present on the seismograms, such as arrivals corresponding to reflections occurring at the bottom interfaces. For example, a first S-S reflection is clearly visible right after the direct S-wave arrival. It corresponds to the reflections on the deeper interface (2848-m

Downloaded 03/30/16 to 93.3.150.44. Redistribution subject to SEG license or copyright; see Terms of Use at http://library.seg.org/

Downloaded 03/30/16 to 93.3.150.44. Redistribution subject to SEG license or copyright; see Terms of Use at http://library.seg.org/

depth). We can also identify a later arrival (between 250 and 400 ms) that corresponds to the reflections of the S wave at 2213-m depth. Even though their amplitudes are significantly weaker than the amplitudes of the direct waves, they can still be identified for strong events.

In the following examples 1–3, to locate the synthetic event, we picked the seismograms the P and S traveltimes of the first arrivals and the PP and SS traveltimes of the reflected waves at the deepest interface (2848-m depth). We use the observed azimuthal angles for the first P-wave arrivals only. When analyzing real data, the azimuths of the reflected phases are difficult to estimate because they have a worse signal-to-noise ratio (S/N) than direct waves. We set the picking uncertainty of the observed data to 5 ms for the P waves and 7 ms for the S waves and the uncertainties of the azimuthal angles to 5°. Even though the azimuthal uncertainty seems small compared to some studies (e.g., Eisner et al., 2009b), the traveltime uncertainty values seem pessimistic for synthetic data but we use them to be consistent with the real data application. These values correspond to the variances contained in the diagonal of Σ_t in equation 11.

Example 1

We use the probabilistic approach to solve the inverse problem of the event location, the predicted traveltimes and azimuthal angles being estimated with our ray-tracing algorithm. In Figure 5, we reveal the resulting uncertainty associated with the location of the event using the first arrivals only, the reflected arrivals only, and using the first and the reflected arrivals. Figure 5a–5c displays the 68% confidence intervals built from the marginal pdfs for the NE, ZE, and ZN when only first arrivals are considered. For this case, the maximum of the posterior pdf (plus symbol) corresponds to the true position of the event (multiplication symbol). This was expected because the velocity model considered for the location is the exact one, and there is no noise in the observations. Even though the true location of the event is retrieved correctly, the 68% confidence intervals for the three sections are spread over more than 170 m in the east direction and more than 200 m in the north direction, and the depth uncertainty is approximately 200 m. In addition, the confidence interval is spread over two different layers. This situation leads to difficulties when interpreting the location results in real case studies. We represent the marginal pdf when only the reflected arrivals are considered in Figure 5d–5f. In this case, the maximum of the posterior pdf is approximately 30-m away from the true position of the event, and the 68% confidence intervals have a similar range as for first arrivals with a slightly different shape. We finally compute the marginal pdf when the first and reflected arrivals are included in the probabilistic location (Figure 5g–5i). The maximum of the posterior pdf corresponds to the true event location. The uncertainties associated with the location are greatly decreased because the 68% confidence intervals are now spread over only 110 m in the east direction, 150 m in the north direction, and 130 m in depth. The uncertainty on the depth of the event is now fully included in only

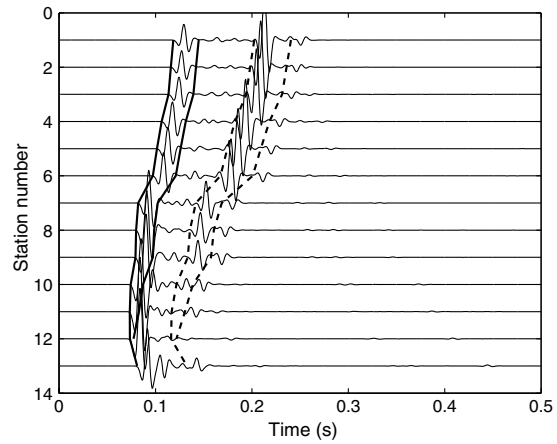

Figure 4. Synthetic wavefield for an event located at (east, north, z) = (77, 550, 2770 m). Some theoretical arrival times computed with our new ray-tracing algorithm are superimposed on the seismograms. The solid and the dashed lines represent the theoretical traveltimes of the first and reflected arrivals of P and S waves, respectively, computed using the velocity model of Figure 3.

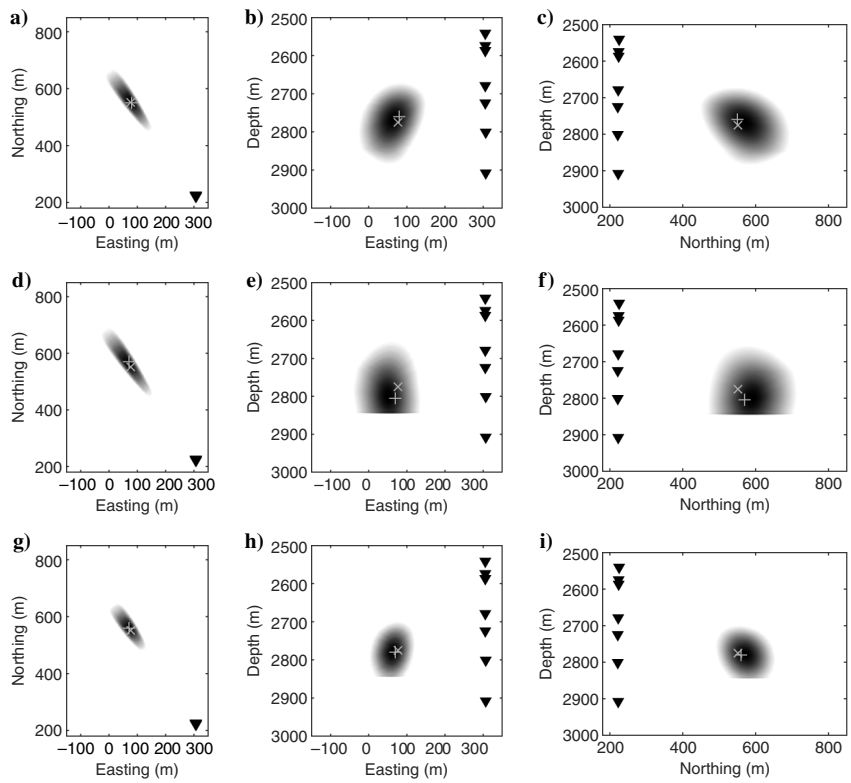

Figure 5. Uncertainties associated with the location of a synthetic microseismic event. There is a 68% confidence interval built from the marginal pdfs for the NE (left figures), ZE (middle figures), and ZN (right figures) planes. The multiplication symbol indicates the true location, the plus symbol indicates the estimated location (maximum of the posterior pdf), and the black triangles indicate the positions of the receivers. (a-c) The pdf using first arrivals only, (d-f) pdf using reflected arrivals only, and (g-i) new pdf using the first and reflected arrivals.

one layer. The reduction of uncertainty is due to the combination of the pdf because the lower figures are somewhat equivalent to the multiplication of the upper figures with the middle figures. The 68% contour of this multiplication is expected to be smaller than the 68% confidence interval of only one type of arrival. This example shows that accounting for the first and reflected arrivals allows us to greatly decrease (approximately 33%) the uncertainties associated with the event location compared to the standard case when only first arrivals are considered.

Example 2

In this example, we added noise to the observations that are the picked arrival times and the azimuthal angles. We considered a Gaussian noise of, respectively, 5 ms, 7 ms, and 5° standard deviation for the P-wave arrival times, S-wave arrival times, and P azimuthal angles. We show in Figure 6 the uncertainties of the event location obtained with our probabilistic approach. The results are similar to the case without noise even if the confidence intervals are more wide here, in particular in the *xy*-plane. Locating the event with first arrivals only results in 68% confidence intervals that are spread over approximately 180 m in the east direction, approximately 250 m in the north direction, and approximately 200 m in depth (Figure 6a–6c). As for the previous example, the uncertainties are decreased by approximately 33% when integrating reflected arrivals in the probabilistic location (Figure 6g–6i). The estimated location is still reliable in the presence of noise because the maximum of the pdf location is less than 30-m away from the true location.

Example 3

In this example, we test the strength of our approach when the velocity model used to locate events is an approximation of reality. Figure 7 displays the 68% confidence intervals built from the marginal pdf when the velocity model used for location is 20% slower than the true model. Figure 7a–7c represents the marginal pdf when only first arrivals are considered. For this case, the maximum of the posterior pdf (plus symbol) is more than 60-m away from the true location (multiplication symbol). The depth uncertainty is approximately 200 m, and the confidence regions are spread over approximately 230 m in the north direction and 170 m in the east direction. As illustrated in Figure 7g–7i, including reflected phases results in an estimated location that is less than 30-m away from the true location. The uncertainties are once again decreased by approximately 33%.

Figure 8 shows the 68% confidence intervals when the velocity model used for location is 20% faster than the true model. When only first arrivals are considered, the confidence regions are shifted with respect to the case of a slower velocity model and the intervals are more diffuse (Figure 8a–8c). The maximum of the posterior pdf is located in an incorrect layer, and it is more than 130-m away from the true location indicated by the multiplication symbol. The true location is not even included in the confidence intervals. As illustrated in Figure 8g–8i, including the reflected phases results in an approximately 33% decrease of the uncertainties. It also results in a much more accurate location because it is now less than 60-m away from the true location. This example shows that the addition of reflected arrivals allows us to compensate for the location error due to the wrong velocity model.

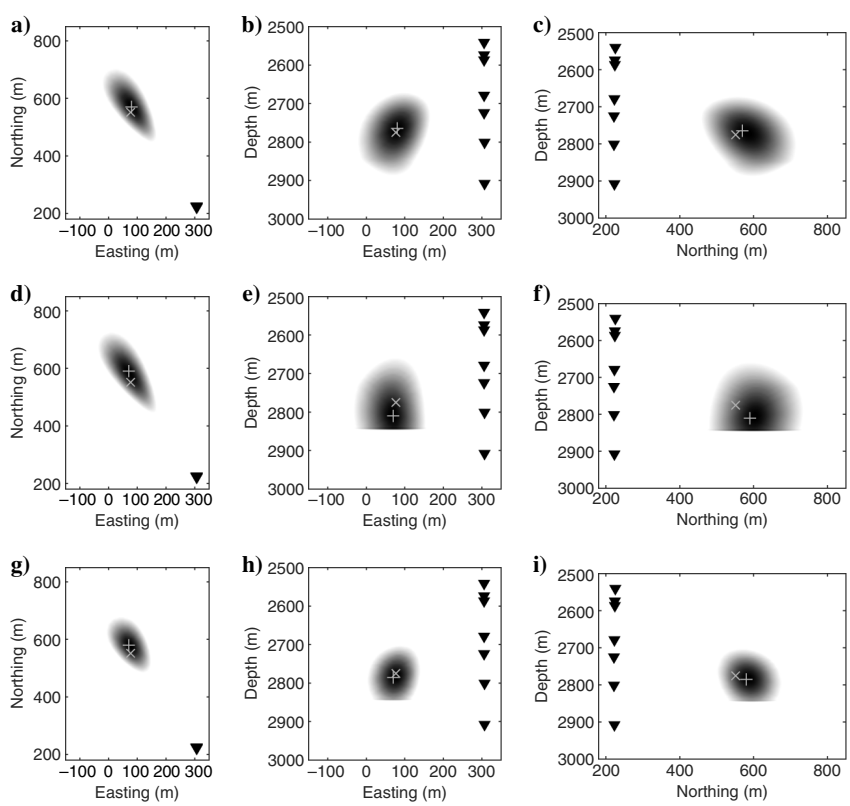

Figure 6. Uncertainties (68% confidence intervals) associated with the location of a synthetic microseismic event when Gaussian noise is added to the observed traveltime and polarization data. Information is plotted in the same way as in Figure 5.

Downloaded 03/30/16 to 93.3.150.44. Redistribution subject to SEG license or copyright; see Terms of Use at http://library.seg.org/

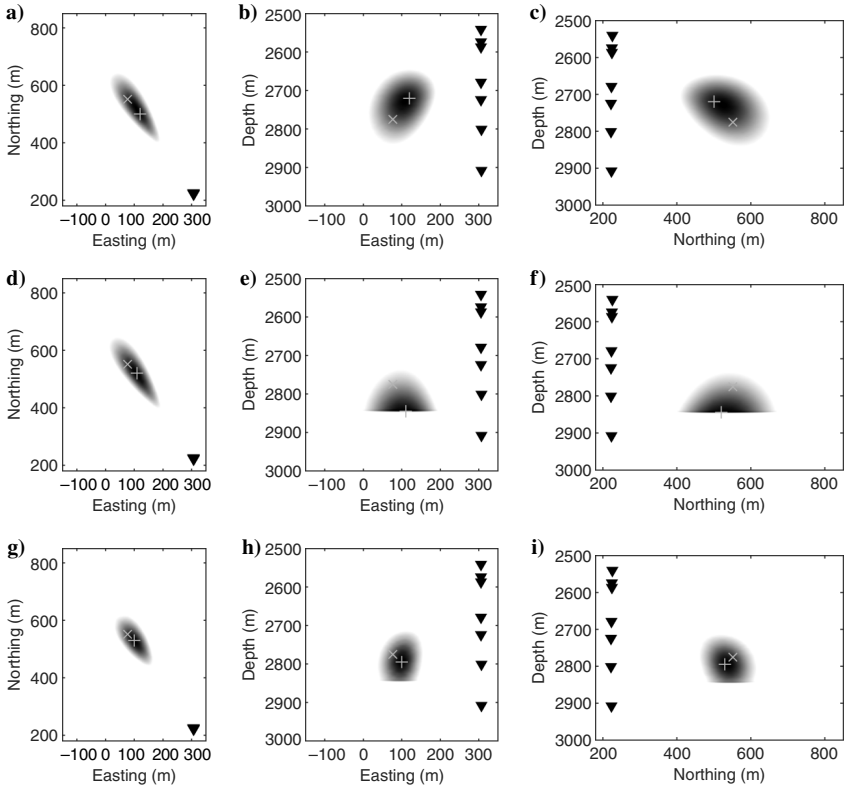

Figure 7. Uncertainties (68% confidence intervals) associated with the location of a synthetic microseismic event when Gaussian noise is added to the observed data (traveltimes and polarizations) and for a velocity model 20% slower than reality. Information is plotted in the same way as Figure 5.

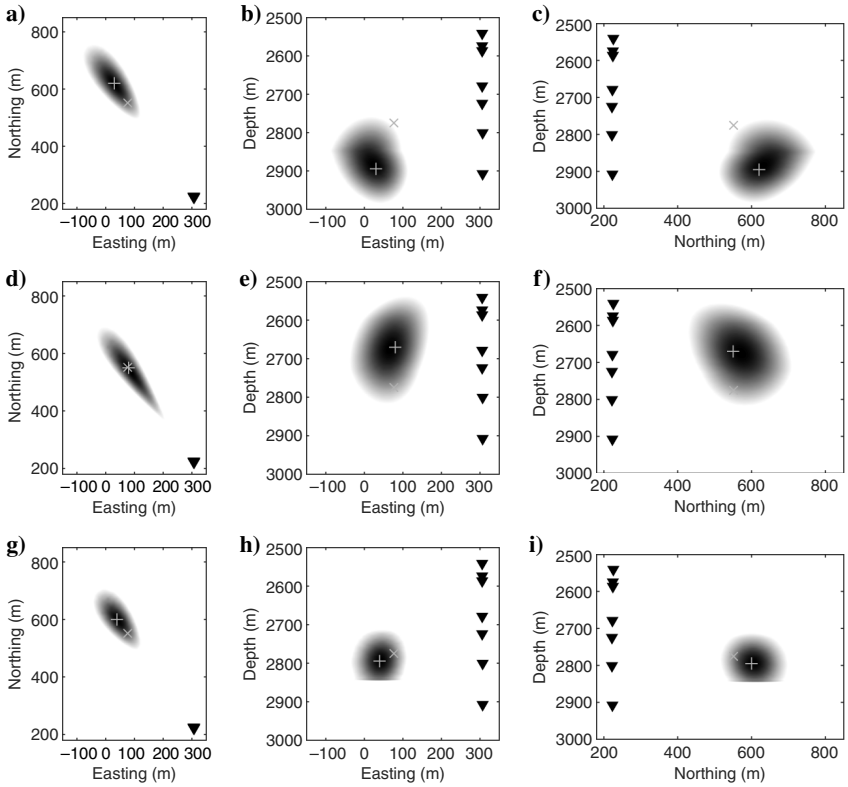

Figure 8. Uncertainties (68% confidence intervals) associated with the location of a synthetic microseismic event when Gaussian noise is added to the observed data (traveltimes and polarizations) and for a velocity model 20% faster than reality. Information is plotted in the same way as Figure 5.

Downloaded 03/30/16 to 93.3.150.44. Redistribution subject to SEG license or copyright; see Terms of Use at http://library.seg.org/

Downloaded 03/30/16 to 93.3.150.44. Redistribution subject to SEG license or copyright; see Terms of Use at http://library.seg.org/

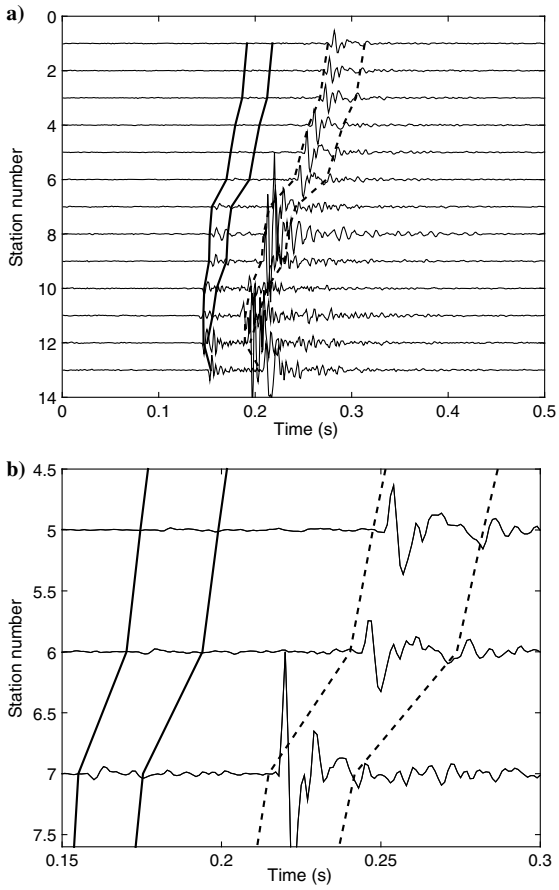

Figure 9. (a) Real seismograms (x-component) recorded at the 13 receivers represented in Figure 2 for the first real microseismic event. Some theoretical arrival times computed with our new ray-tracing algorithm are superimposed on the seismograms. The solid and the dashed lines represent the theoretical traveltimes of the first and reflected arrivals of P and S waves, respectively. (b) Magnification of three seismograms.

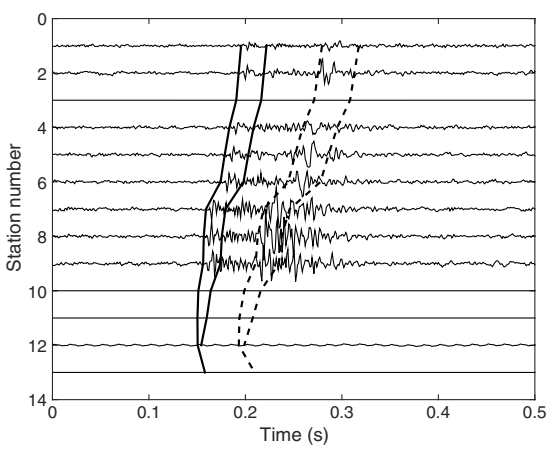

Figure 10. Real seismograms (x-component) recorded at the 13 receivers represented in Figure 2 for the second real microseismic event with a lower S/N. Some theoretical arrival times computed with our new ray-tracing algorithm are superimposed on the seismograms. The solid and the dashed lines represent the theoretical traveltimes of the first and reflected arrivals of P and S waves, respectively.

Cotton Valley real data example

The Carthage Cotton Valley gas field, Texas, was an extensively monitored fracking experiment as described in Rutledge and Phillips (2003) and Rutledge et al. (2004). The field covers a 1000-km^2 area in the north of the Gulf of Mexico basin. In the interest zone, the reservoir depth is approximately 2600 m. It is constituted of interbedded shales and low-permeability sands. The experiment consists of injections at different depths in two treatment wells. Data were collected from three phases with either single- or dual-well monitoring. We selected two events from phase 2, stage 1 of moment magnitude ($M_W < -1.2$). The events were detected on 13 3C receivers of array 2 deployed in well 22-09. The velocity model used to locate the seismic events was derived from sonic logs and calibrated with string shots (Walker, 1997). The velocity model (Figure 3) and the acquisition geometry (Figure 2) correspond to the ones used in the previous synthetic examples.

Figure 9a shows the seismograms (only the x-component) recorded at the 13 receivers for the first event. In addition to the first breaks, clear arrivals corresponding to reflections on the bottom interface can be picked for the P and S waves. Indeed, the superimposition of theoretical traveltimes computed with our new ray-tracing algorithm allows for reliable identification of these reflections. These theoretical times are calculated for a hypocenter location obtained using first arrivals only. The approximate locations are sufficient to plot the reflected times: Events are only required to be located in the same region to have similar seismograms. In fact, because we are interested in reflection, we should have the right relative position to the reflectors (i.e., above or below). In this example, the reflection on the top interface is too weak to be detected and is therefore discarded from the location process. A magnification of the seismograms (Figure 9b) leads us to set the picking uncertainty of these observed data to 5 ms for the P-waves and 7 ms for the S-waves. These values correspond to approximately half the periods of the P- and S-wave signals. Figure 10 shows the seismograms of a microseismic event with a lower S/N.

As for the previous example, we use the probabilistic approach to locate these seismic events. Figures 11 and 12 show the 68% confidence interval built from the marginal pdfs for the NE, ZE, and ZN planes using only first arrivals, only reflected arrivals, and using a combination of the first and reflected arrivals. When locating the seismic event using only the first arrivals, the 68% confidence intervals (Figures 11a–11c and 12a–12c) are spread over approximately 150 m in the east direction, 230 m in the north direction, and 200 m in depth. The depth uncertainty thus spreads over several geologic layers. When adding the reflected arrivals, the three 68% confidence intervals (Figures 11g–11i and 12g–12i) are reduced to approximately 100 m in the east direction, less than 170 m in the north direction, and less than 130 m in depth, and the uncertainty on the depth of the event is now fully included in only one layer. The estimated locations (plus symbols) are similar with first arrivals only or with the first and reflected arrivals. Compared to the synthetic examples (Figures 7 and 8), this could indicate that the velocity model considered for the location is not far from reality. For this real data application, adding the reflected waves in our probabilistic location does not change the estimated location of the seismic event, but this allows us to greatly decrease the uncertainties (approximately 33%) associated with the event location.

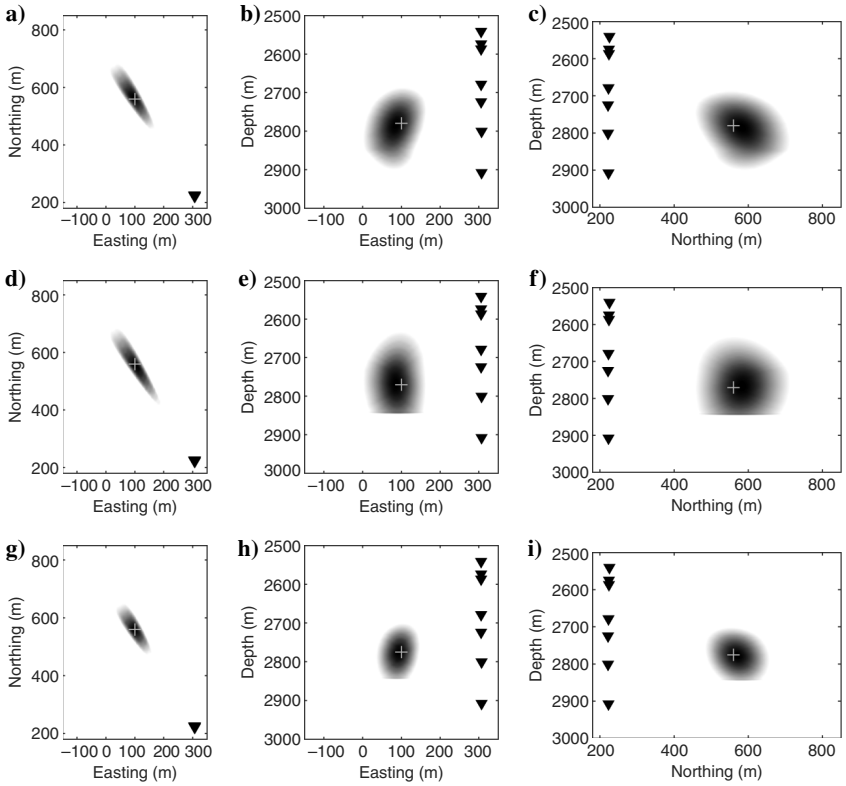

Figure 11. Uncertainties (68% confidence intervals) associated with the location of the first real microseismic event whose seismograms are represented in Figure 9. Information is plotted in the same way as Figure 5.

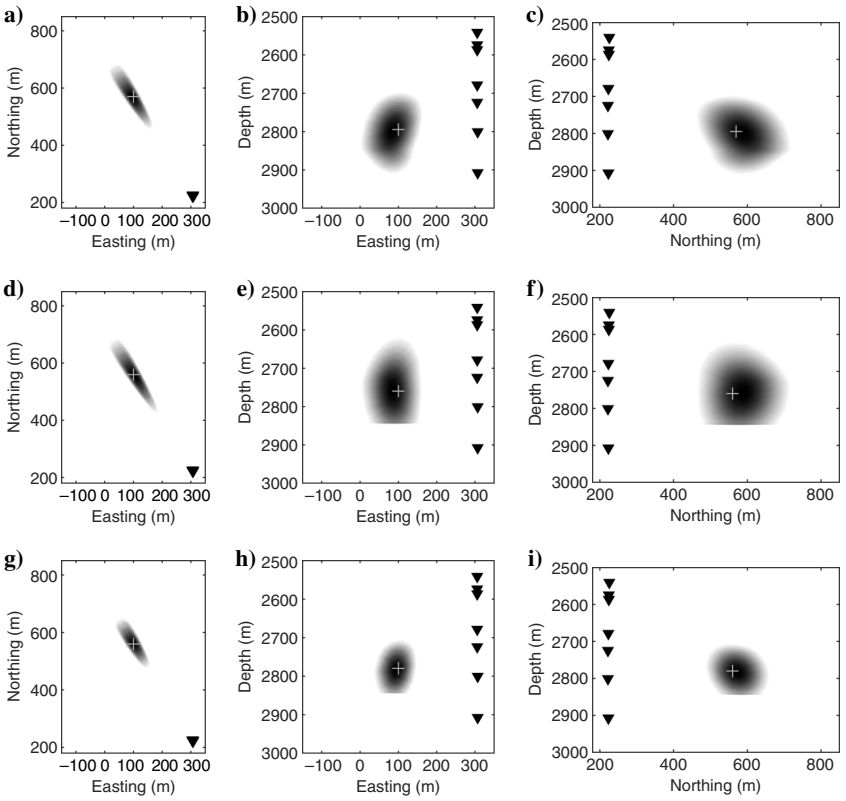

Figure 12. Uncertainties (68% confidence intervals) associated with the location of the second real microseismic event whose seismograms are represented in Figure 10. Information is plotted in the same way as Figure 5.

Downloaded 03/30/16 to 93.3.150.44. Redistribution subject to SEG license or copyright; see Terms of Use at http://library.seg.org/

Downloaded 03/30/16 to 93.3.150.44. Redistribution subject to SEG license or copyright; see Terms of Use at http://library.seg.org/

CONCLUSIONS

The first and reflected arrivals had been successfully used to improve the location accuracy of microseismic events. This was possible thanks to the new ray-tracing algorithm that we have developed. It enabled us to accurately and efficiently compute different arrivals. This algorithm is based on Snell's law to find the minimum traveltime between a source and a receiver. Furthermore, the reflected arrivals are obtained using an alternative mirrored velocity model. The second part of the location problem is the cost function used to find the position of the event that best fits the observed first and reflected traveltime picks. We use a global grid search to estimate the complete posterior pdf of the event location that is given by the probabilistic Bayesian formulation. This allows us to retrieve the global minimum of the misfit function and estimate the uncertainty. The advantage of this formulation is its flexibility with respect to the observed data; it accounts for different traveltimes and also for polarization in a straightforward way.

Our synthetic study is based on several examples for which we tested the robustness of our approach in the presence of noise and also for velocity model variations. The traveltimes are picked from synthetic gathers computed with independent software. For all the synthetic cases, we showed that the use of reflection data dramatically reduced the location uncertainty by approximately 33%. For more realistic cases in which the velocity model is an approximation of the reality, the methodology allows us to greatly improve the location accuracy. In the real case example, we used seismograms from the Cotton Valley data set. After analyzing the waveform, we detected reflected arrivals from the bottom of the reservoir. The use of this information in the objective function improves the location uncertainty.

Adding more arrivals to the location process enhances the quality of the results with a reduced cost. Depending on the velocity model and the acquisition geometry, different phases could be detected in the signal. For example, the converted arrivals and the multireflected arrivals could have a strong amplitude in highly contrasted reservoirs. The use of these arrivals could significantly improve the localization procedure.

In this paper, we assumed independency between azimuthal angles and traveltimes. Even though it is not critical for our applications, it could be worthwhile to develop the probabilistic methodology accounting for the dependency between the two parameters.

REFERENCES

Abel, J. S., S. Coffin, Y. Hur, and S. Taylor, 2011, An analytic model for microseismic event location estimate accuracy: First Break, **29**, 99–107.

Belayouni, N., 2013, Nouveaux algorithmes efficaces de modélisation 2d et 3d: Temps des premières arrivées, angles à la source et amplitudes: Ph.D. thesis, Ecole Nationale Supérieure des Mines de Paris.

Brent, R. P., 1973, Algorithms for minimization without derivatives: Courier Dover Publications.

Červený, V., 2000, Seismic ray method: Cambridge University Press.

Coffin, S., Y. Hur, J. S. Abel, B. Culver, R. Augsten, and A. Westlake, 2012, Beyond first arrivals: Improved microseismic event localization using both direct-path and head-wave arrivals: 82nd Annual International Meeting, SEG, Expanded Abstracts, doi: 10.1190/segam2012-1597.1.

Culver, B., R. Augsten, S. Coffin, Y. Hur, J. S. Abel, and A. Westlake, 2012, Interpretation of multipath-analysis localizations of microseismic data: An Alberta Montney shale example: 82nd Annual International Meeting, SEG, Expanded Abstracts, doi: 10.1190/segam2012-1597.1.

Eisner, L., P. Duncan, H. Werner, and W. Keller, 2009a, Uncertainties in passive seismic monitoring: The Leading Edge, **28**, 648–655, doi: 10.1190/1.3148403.

Eisner, L., T. Fischer, and J. T. Rutledge, 2009b, Determination of S-wave slowness from a linear array of borehole receivers: Geophysical Journal International, **176**, 31–39, doi: 10.1111/j.1365-246X.2008.03939.x.

Eisner, L., B. J. Hulsey, P. Duncan, D. Jurick, H. Werner, and W. Keller, 2010, Comparison of surface and borehole locations of induced seismicity: Geophysical Prospecting, **58**, 809–820, doi: 10.1111/j.1365-2478.2010.00867.x.

Evernden, J. F., 1969, Precision of epicenters obtained by small numbers of world-wide stations: Bulletin of the Seismological Society of America, **59**, 1365–1398.

Flinn, E. A., 1965, Confidence regions and error determinations for seismic event location: Reviews of Geophysics, **3**, 157–185, doi: 10.1029/RG003i001p00157.

Gesret, A., N. Desassis, M. Noble, T. Romary, and C. Maisons, 2015, Propagation of the velocity model uncertainties to the seismic event location: Geophysical Journal International, **200**, 52–66, doi: 10.1093/gji/ggu374.

Husen, S., E. Kissling, N. Deichmann, S. Wiemer, D. Giardini, and M. Baer, 2003, Probabilistic earthquake location in complex three-dimensional velocity models: Application to Switzerland: Journal of Geophysical Research, **108**, 2077–2096, doi: 10.1029/2002JB001778.

Husen, S., and R. Smith, 2004, Probabilistic earthquake location in three-dimensional velocity models for the Yellowstone National Park region, Wyoming: Bulletin of the Seismological Society of America, **94**, 880–896, doi: 10.1785/0120030170.

Jordan, T. H., and K. A. Sverdrup, 1981, Teleseismic location techniques and their application to earthquake clusters in the south-central pacific: Bulletin of the Seismological Society of America, **71**, 1105–1130.

Lahr, J., 1989, HYPOELLIPSE: A computer program for determining local earthquake hypocentral parameters, magnitude, and first motion pattern (Y2K compliant version): U.S. Geological Survey, Open-File Report.

Lahr, J., 2002, User's guide to HYPOINVERSE-2000: A Fortran program to solve for earthquake locations and magnitudes: U.S. Geological Survey, Open-File Report.

Lecomte, I., 1993, Finite difference calculation of first traveltimes in anisotropic media: Geophysical Journal International, **113**, 318–342, doi: 10.1111/j.1365-246X.1993.tb00890.x.

Lee, W., and J. Lahr, 1975, HYP071 (revised): A computer program for determining hypocenter, magnitude, and first motion pattern of local earthquakes: U.S. Geological Survey, Open-File Report.

Lomax, A., J. Virieux, P. Volant, and C. Berge-Thierry, 2000, Probabilistic earthquake location in 3D and layered models: Introduction of a Metropolis-Gibbs method and comparison with linear locations, *in* , C. H. Thurber, and N. Rabinowitz, eds., Advances in seismic event location 228 , Kluwer Academic, 101–134.

Lomax, A., A. Zollo, P. Capuano, and J. Virieux, 2001, Precise, absolute earthquake location under Somma-Vesuvius volcano using a new three-dimensional velocity model: Geophysical Journal International, **146**, 313–331, doi: 10.1046/j.0956-540x.2001.01444.x.

Maxwell, S., 2010, Microseismic: Growth born from success: The Leading Edge, **29**, 338–343, doi: 10.1190/1.3353732.

Maxwell, S. C., and T. I. Urbancic, 2001, The role of passive microseismic monitoring in the instrumented oil field: The Leading Edge, **20**, 636–639, doi: 10.1190/1.1439012.

Moser, T., T. van Eck, and G. Nolet, 1992, Hypocenter determination in strongly heterogeneous earth models using the shortest path method: Journal of Geophysical Research, **97**, 6563–6572, doi: 10.1029/91JB03176.

Noble, M., A. Gesret, and N. Belayouni, 2014, Accurate 3-D finite difference computation of traveltimes in strongly heterogeneous media: Geophysical Journal International, **199**, 1572–1585, doi: 10.1093/gji/ggu358.

Pei, D., J. A. Quirein, B. E. Cornish, D. Quinn, and N. R. Warpinski, 2009, Velocity calibration for microseismic monitoring: A very fast simulated annealing (VFSA) approach for joint-objective optimization: Geophysics, **74**, no. 6, WCB47–WCB55, doi: 10.1190/1.3238365.

Phillips, W. S., J. T. Rutledge, L. S. House, and M. C. Fehler, 2002, Induced microearthquake patterns in hydrocarbon and geothermal reservoirs: Six case studies, *in* C. I. Trifu, ed., The mechanism of induced seismicity: Springer, 345–369.

Podvin, P., and I. Lecomte, 1991, Finite difference computation of traveltimes in a very contrasted velocity models: Geophysical Journal International, **105**, 271–284, doi: 10.1111/j.1365-246X.1991.tb03461.x.

Poliannikov, O. V., M. Prange, A. Malcolm, and H. Djikpesse, 2013, A unified Bayesian framework for relative microseismic location: Geophysical Journal International, doi: 10.1093/gji/ggt119.

Rutledge, J., W. Phillips, and M. Mayerhofer, 2004, Faulting induced by forced fluid injection and fluid flow forced by faulting: An interpretation of hydraulic-fracture microseismicity, Carthage Cotton Valley gas field, Texas: Bulletin of the Seismological Society of America, **94**, 1817–1830, doi: 10.1785/012003257.

Rutledge, J. T., and W. S. Phillips, 2003, Hydraulic stimulation of natural fractures as revealed by induced microearthquakes, Carthage Cotton Valley gas field, east Texas: Geophysics, **68**, 441–452, doi: 10.1190/1.1567214.

Tarantola, A., 2005, Inverse problem theory and model parameter estimation: SIAM.
Tarantola, A., and B. Valette, 1982, Inverse problems = quest for information: Journal of Geophysics, **50**, 159–170.
Vidale, J. E., 1990, Finite difference calculation of travel times in three dimensions: Geophysics, **55**, 521–526, doi: 10.1190/1.1442863.
Walker, R. N., 1997, Cotton valley hydraulic fracture imaging project: Presented at Society of Petroleum Engineers Annual Technical Conference, 131–145.
Wittlinger, G., G. Herquel, and T. Nakache, 1993, Earthquake location in strongly heterogeneous media.: Geophysical Journal International, **115**, 759–777, doi: 10.1111/j.1365-246X.1993.tb01491.x.
Yue, T., and C. Xiao-Fei, 2005, A rapid and accurate two-point ray tracing method in horizontally layered velocity model: Acta Seismologica Sinica, **18**, 154–161, doi: 10.1007/s11589-005-0062-4.
Zimmer, U., 2010, Localization of microseismic events using head waves and direct waves: 80th Annual International Meeting, SEG, Expanded Abstracts, 2196–2200.

Downloaded 03/30/16 to 93.3.150.44. Redistribution subject to SEG license or copyright; see Terms of Use at http://library.seg.org/

Geophysical Journal International

Geophys. J. Int. (2016) **207,** 374–392
Advance Access publication 2016 July 25
GJI Seismology

doi: 10.1093/gji/ggw272

Stochastic seismic tomography by interacting Markov chains

Alexis Bottero,[1,2] Alexandrine Gesret,[1] Thomas Romary,[1] Mark Noble[1] and Christophe Maisons[3]

[1]*MINES ParisTech, PSL Research University, Centre de Geosciences,* 77 *Fontainebleau, France. E-mail:* alexis.bottero@gmail.com
[2]*LMA, CNRS UPR* 7051*, Aix-Marseille University, Centrale Marseille, F-*13453 *Marseille Cedex* 13*, France*
[3]*Magnitude SAS, Centre Regain, Route de Marseille,* 04 *Sainte-Tulle, France*

Accepted 2016 July 19. Received 2016 July 1; in original form 2016 March 11

SUMMARY

Markov chain Monte Carlo sampling methods are widely used for non-linear Bayesian inversion where no analytical expression for the forward relation between data and model parameters is available. Contrary to the linear(ized) approaches, they naturally allow to evaluate the uncertainties on the model found. Nevertheless their use is problematic in high-dimensional model spaces especially when the computational cost of the forward problem is significant and/or the *a posteriori* distribution is multimodal. In this case, the chain can stay stuck in one of the modes and hence not provide an exhaustive sampling of the distribution of interest. We present here a still relatively unknown algorithm that allows interaction between several Markov chains at different temperatures. These interactions (based on importance resampling) ensure a robust sampling of any posterior distribution and thus provide a way to efficiently tackle complex fully non-linear inverse problems. The algorithm is easy to implement and is well adapted to run on parallel supercomputers. In this paper, the algorithm is first introduced and applied to a synthetic multimodal distribution in order to demonstrate its robustness and efficiency compared to a simulated annealing method. It is then applied in the framework of first arrival traveltime seismic tomography on real data recorded in the context of hydraulic fracturing. To carry out this study a wavelet-based adaptive model parametrization has been used. This allows to integrate the *a priori* information provided by sonic logs and to reduce optimally the dimension of the problem.

Key words: Wavelet transform; Inverse theory; Tomography; Probability distributions.

1 INTRODUCTION

Tomographic inversion schemes aiming at reconstructing the subsurface structures from seismic traveltime data are widely used (e.g. Rawlinson *et al.* 2010). The obtained wave propagation velocity distribution is usually a starting point for further seismological, structural or tectonic analysis. For a reliable and quantitative interpretation of the tomographic solution, an accurate velocity model with its associated uncertainties are required. Very often, the tomographic inverse problem is solved with iterative linearized approaches that minimize a misfit function. The misfit function usually measures the difference between observed and computed traveltimes as a function of the velocity model parameters. When the data-model relationship is highly non-linear, the misfit surface has a complex shape. It is most likely multimodal with a global maximum, representing the most likely solution, and a large number of secondary maxima, representing other possible solutions. The linearization makes the implicit assumption of a unique solution which is chosen thanks to a regularization procedure that reduces the solution non-uniqueness (Menke 2012). This is generally achieved by imposing the solution to be somehow similar or close to an initial *a priori* model. If the initial model is too far from the global minimum, the method may stop the inversion at any point where the misfit function does not change significantly. This can happen even for very simple tomographic inversion problem with only two layers (Weber 2000). In addition, the linearized approaches are not really adapted to provide reliable uncertainties. This is due either to possible multiple minima of the objective functions or to badly constrained area where many candidate models are all equally likely. Rawlinson *et al.* (2014) provide an extensive description of the existing methods to estimate uncertainties with local approaches and illustrate that a probabilistic sampling of the *a posteriori* distribution within a Bayesian framework (Tarantola 2005) is much more suitable.

In their pioneering work, Tarantola & Valette (1982) propose to sample the *a posteriori* probability density of the velocity model parameters. This posterior probability density function summarizes how the information brought by the seismic traveltime data improves the *a priori* knowledge on the model parameters. Such a Bayesian approach is capable of dealing with highly non-linear problems. In the

© The Authors 2016. Published by Oxford University Press on behalf of The Royal Astronomical Society.

Bayesian framework, either a single model maximizing the posterior distribution is sought, this is an optimization problem or the complete shape of the *a posteriori* distribution is inferred, this is a sampling problem. The sampling of the whole posterior distribution allows for an unbiased estimation of the velocity model uncertainties (Debski 2010) without any assumption on the shape of the misfit surface.

We focus here on Markov chain Monte Carlo (MCMC) methods introduced by Metropolis *et al.* (1953) for the universality of the method and the ease of its implementation. Monte Carlo type algorithms are useful to generate a large number of samples of statistically near-independent velocity models distributed according to the posterior distribution (Koren *et al.* 1991; Mosegaard & Tarantola 1995; Bodin & Sambridge 2009). In other words, their frequency of occurrence approximates the posterior probability density function. For example, the classical Metropolis–Hastings algorithm is known to converge towards the true posterior distribution (Robert & Casella 2013). However, the convergence can be quite slow. To overcome this drawback, during the first iterations of the algorithm, the true posterior distribution can be replaced by a tempered distribution. This corresponds to the simulated annealing (SA) algorithm which is commonly used in an optimization prospect where the final best velocity model is reached when the annealing temperature is close to zero (Salamon *et al.* 2002). Although particularly well suited for sampling and optimization (Robert & Casella 2013), two major impediments of classical MCMC methods exist. First, if the dimension of the problem is very large or if the forward problem is computationally expensive, the number of iterations needed for an adequate sampling of the posterior will never be reached. In addition, if the *a posteriori* distribution is multimodal, the chain may be stuck in one of the secondary modes. In order to sample very efficiently complex *a posteriori* distributions, it is possible to allow several Markov chains to interact at different temperatures, for example, according to the parallel tempering scheme (Geyer 1991). Recently Sambridge (2014) proposed to use parallel tempering for probabilistic sampling and multimodal optimization. Randomized swaps between any pair of adjacent temperature levels allow to significantly accelerate the convergence of the MCMC process. However in the parallel tempering algorithm exchanges can only occur between simultaneous states of the chains.

We go here a step forward by proposing an interacting MCMC (IMCMC) algorithm based on the population importance-resampling (PIR) MCMC sampler introduced by Andrieu *et al.* (2011) where exchanges are proposed taking advantage of the whole history of the chains. Romary (2009) and Romary (2010a) showed that this interaction scheme improves significantly the mixing properties and the convergence speed of the chains over other parallel MCMC schemes, including parallel tempering. This ensures better sampling and thus better results with less iterations for Bayesian inversion purpose. We first compare this IMCMC algorithm to a common SA algorithm for a highly multimodal function in order to test its robustness and efficiency. We then apply the IMCMC algorithm to invert a set of perforation shots recorded in the context of induced microseismicity. In this context, the calibrated velocity model has to be accurate since it is subsequently used for precise microseismic event locations that required for safety and exploitation optimization. In routine microseismic monitoring of hydraulic fracturing projects, sonic logs are used to construct a layered velocity model, which is then usually calibrated with the perforation shots from known locations (Eisner *et al.* 2009; Maxwell 2010). We propose an adaptive parametrization based on a optimally truncated decomposition of the sonic logs on a variable wavelet functions basis. This allows to use the sonic log as a prior information by describing a complex velocity model with a restricted number of wavelet coefficients. The wavelet type together with the coefficients become the model parameters of the inversion. We illustrate the efficiency and the robustness of our algorithm by applying it to the perforation shot data.

The paper is organized as follows. We first recall the formalism of the Bayesian inversion and briefly present the classical MCMC Metropolis–Hastings and SA algorithms. We then introduce our IMCMC algorithm and illustrate its performance for a highly multimodal distribution. We finally apply our approach to a real data set with an original adaptive model parametrization based on wavelet decomposition of sonic logs.

1.1 Mathematical setting, Bayesian context

The aim of traveltime tomography is to infer the spatial structure $\mathcal{S}$ of the seismic wave velocity field using observed traveltimes. It falls into the wide category of inverse problems. On the system $\mathcal{S}$ we have a finite set of L imperfect indirect measurements $\mathbf{d}^{\text{obs}} = (d_1^{\text{obs}}, \ldots, d_L^{\text{obs}})$ belonging to the data space $\mathcal{D} \subset \mathbb{R}^L$, the measurement error being most of the time not perfectly known. The sought physical system $\mathcal{S}$ is usually a continuous function of a general variable $\mathbf{x}$ (space here) $\mathcal{S}(\mathbf{x})$. Practically, to reduce the dimension of the problem, this unknown system is approximated as a given function $\mathcal{G}_{\mathbf{b}}(\mathbf{x})$ that can be fully described by a finite set of N parameters $\mathbf{b} = (b_1, \ldots, b_N) \in \mathcal{M}$. $\mathcal{M} \subset \mathbb{R}^N$ is commonly called the model space

$$\mathcal{S}(\mathbf{x}) \approx \mathcal{G}_{\mathbf{b}}(\mathbf{x}). \tag{1}$$

Knowing $\mathcal{S}$ reduces then to find the best set of parameters $\mathbf{b}$. This approximation is called parametrization and can obviously affect the solution (e.g. Hartzell & Langer 1993; Köhn *et al.* 2012; Rawlinson *et al.* 2014). A good parametrization should extract the maximum information from the observed data, without introducing unjustified complexity to the model structure. The forward problem that predicts the synthetic measurements $\mathbf{d}$ from a set of model parameters $\mathbf{b}$ writes

$$\mathbf{d} = \mathbf{F}(\mathbf{b}) \tag{2}$$

where $\mathbf{F}$ is the physical coupling that links the data $\mathbf{d}$ to a given model $\mathbf{b}$. This function $\mathbf{F}$, generally non-linear, can only be imperfectly modeled. The inverse problem consists in finding the parameters $\mathbf{b}$ for which $\mathbf{d} = \mathbf{F}(\mathbf{b}) \approx \mathbf{d}^{\text{obs}}$. In the following, we adopt the classical Bayesian framework (Tarantola 2005) in which all information is represented by probability distributions. This approach allows to transform the prior knowledge on model parameters into a posterior distribution while accounting properly for both the measurement and theoretical

uncertainties. For a given model $\mathbf{b}$, the forward problem is represented by the following N-dimensional probability distribution:

$$P(\mathbf{d}^{\text{obs}}|\mathbf{b}) \qquad \text{probability of observing the data } \mathbf{d}^{\text{obs}} \text{given the model } \mathbf{b} \tag{3}$$

commonly called the likelihood. It is a quantitative measure of the difference between the observed data $\mathbf{d}^{\text{obs}}$ and the synthetic data $\mathbf{d} \in \mathcal{D}$ computed from $\mathbf{b} \in \mathcal{M}$. This distribution depends on the stochastic noise associated to the observed data. It is common nevertheless to make the (simplifying) assumption that it has an uncorrelated Gaussian form:

$$P(\mathbf{d}^{\text{obs}}|\mathbf{b}) = e^{\frac{-\Delta(\mathbf{b})}{2}}, \tag{4}$$

in which $\Delta(\mathbf{b})$ is a simple least-squares misfit function

$$\Delta(\mathbf{b}) = \left\| \frac{\mathbf{F}(\mathbf{b}) - \mathbf{d}^{\text{obs}}}{\sigma_{\mathbf{d}}} \right\|^2 \tag{5}$$

where $\sigma_{\mathbf{d}}$ is the estimated standard deviation of the measurement errors that are assumed uncorrelated here. Some *a priori* information about the system is often available. This knowledge is expressed in terms of an *a priori* N-dimensional probability distribution on the values of the model parameters:

$$P(\mathbf{b}) \qquad \textit{a priori} \text{ probability of the model } \mathbf{b} \tag{6}$$

The result of a non-linear inversion is not a unique value of $\mathbf{b}$ but the following N-dimensional *a posteriori* probability distribution on the values of the parameters.

$$P(\mathbf{b}|\mathbf{d}^{\text{obs}}) \qquad \textit{a posteriori} \text{ probability of the model } \mathbf{b} \text{ given the data } \mathbf{d}^{\text{obs}} \tag{7}$$

Bayes' rule (Bayes & Price 1763) allows to express explicitly this probability distribution:

$$P(\mathbf{b}|\mathbf{d}^{\text{obs}}) = \frac{P(\mathbf{d}^{\text{obs}}|\mathbf{b})P(\mathbf{b})}{P(\mathbf{d}^{\text{obs}})}. \tag{8}$$

Note that the term $P(\mathbf{d}^{\text{obs}}) \equiv \int_{\mathcal{M}} P(\mathbf{d}^{\text{obs}}|\mathbf{b})P(\mathbf{b})\,\mathrm{d}\mathbf{b}$, often called the probability of the data or the evidence (Sambridge *et al.* 2006), is generally intractable in high-dimensional problems but does not depend on any particular state of the system and can therefore be considered as a normalization constant. Hence, the problem to be solved amounts to evaluate

$$P(\mathbf{b}|\mathbf{d}^{\text{obs}}) \propto P(\mathbf{d}^{\text{obs}}|\mathbf{b})P(\mathbf{b}) = P(\mathbf{b}) \exp\left(-\frac{1}{2} \left\| \frac{\mathbf{F}(\mathbf{b}) - \mathbf{d}^{\text{obs}}}{\sigma_{\mathbf{d}}} \right\|^2 \right). \tag{9}$$

Knowing (9) exhaustively implies then to calculate the forward problem for all $\mathbf{b} \in \mathcal{M} \subset \mathbb{R}^N$ or at least on a very large sample of models whose dimension makes the problem intractable in practice. MCMC methods are then used to sample these probability distributions in an efficient way, as they only involve computations of ratios of such probabilities.

1.2 Markov chain Monte Carlo (MCMC)

In the field of geophysical inversion, several methods have been proposed for solving (9). In a sampling purpose, one can cite the neighborhood algorithm (Sambridge 1999a,b) which seems to be limited to low-dimensional problems, or, in an optimization prospect, the genetic algorithm (based on Holland 1975) and the Kitanidis–Oliver algorithm (see Kitanidis 1995; Oliver 1996) whose speed of convergence is controversial. The efficiency for optimization of the last two has impelled some attempts of modifying them, so that they could also be used for sampling a probability distribution (see Sen & Stoffa 2013) but without success so far (Mosegaard & Sambridge 2002). We focus here on MCMC for the universality of the method and the ease of its implementation. Introduced by Metropolis *et al.* (1953), the aim of MCMC methods can be either optimization or sampling. The basic idea is to generate a random sequence of parameters $\mathbf{b} \in \mathcal{M} \subset \mathbb{R}^N$

$$\mathbf{b}^0 \to \mathbf{b}^1 \to \mathbf{b}^2 \to \ldots \to \mathbf{b}^i \to \ldots \tag{10}$$

whose distribution $\boldsymbol{\mathcal{B}}$ equals asymptotically (and therefore approximately in finite time) the probability $P(\mathbf{b}|\mathbf{d}^{\text{obs}})$. The main characteristic of the chain is that every proposed state only depends on the previous one. The chain is said having converged when:

$$\boldsymbol{\mathcal{B}} \approx P(\mathbf{b}|\mathbf{d}^{\text{obs}}). \tag{11}$$

Before the convergence is reached the chain is performing what is commonly called a burn-in period. In real problems, several methods exist to assess the convergence (e.g. Cowles & Carlin 1996; Brooks & Roberts 1998; Robert & Casella 2013) but obviously do not allow to rigorously ensure it. It is an assumption which has to be made. A set κ containing K samples computed after the convergence of the chain $(\mathbf{b}^k)_{k\in\kappa} \in \mathcal{M}^K$ can then be used to estimate posterior expectations $I_\kappa(h)$ of any function $h(\mathbf{b})$:

$$I_\kappa[h] \approx \int_{\mathcal{M}^K} P(\mathbf{b}|\mathbf{d}^{\text{obs}})h(\mathbf{b})\,\mathrm{d}\mathbf{b} \approx \frac{1}{K}\sum_{k\in\kappa} h(\mathbf{b}^{\mathbf{k}}) \tag{12}$$

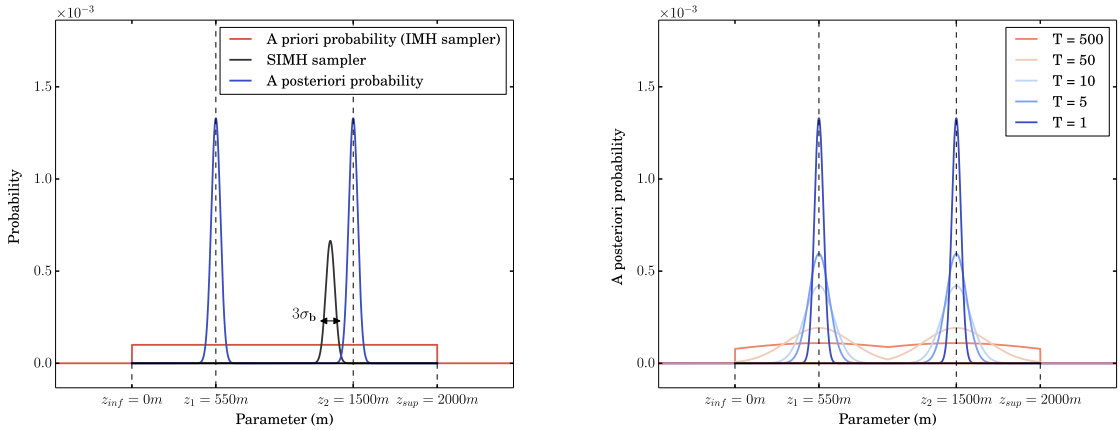

Figure 1. Left: example of a 1-D bimodal distribution with two samplers. The IMH sampler is not normalized. Right: effect of the temperature on this *a posteriori* example distribution $P(b|d^{\text{obs}})$.

and its associated variance:

$$\text{Var}_\kappa[h] = I_\kappa[(h - I_\kappa[h])^2] \approx \frac{1}{K}\sum_{k\in\kappa}(h(\mathbf{b}^k) - I_\kappa[h])^2. \tag{13}$$

For example, $h(\mathbf{b}) = \mathbf{b}$ gives the mean posterior model and (13) an estimation of the associated uncertainties. Assuming the convergence is reached (11), the error on the value decreases as $K^{-\frac{1}{2}}$ independently from the dimension of the space (Meyn & Tweedie 2012). However, if the Markov chain slowly moves in the model space, the states are highly correlated with each other and the chain is said to have poor mixing properties. In that case, the choice of the samples to be used $(\mathbf{b}^k)_{k\in\kappa} \in \mathcal{M}^K$ is often made by taking off one sample out of several after the burn-in period to reduce the variance of the estimator $I_\kappa[h]$. As an illustration Bodin & Sambridge (2009) have used less than one sample out of 150 for their tomography of the Australian continent. The interest of this process called thinning is controversial and induces a considerable waste of resources. MacEachern & Berliner (1994) showed that more precise posterior estimates are obtained if the entire Markov chain is used.

1.2.1 MCMC sampling: the Metropolis–Hastings algorithm

The Metropolis–Hastings algorithm is an MCMC construction which can be tailored to sample from any target distribution, including posterior distributions in the Bayesian inversion context. As every state of a Markov chain only depends on the previous one, the chain behaviour depends on the rule chosen to go from one state to another. In the Metropolis–Hastings algorithm, a move is made in two steps. First, from the current state $\mathbf{b}^i$ of the chain, a potential transition to a state $\mathbf{b}^\star$ is proposed following an instrumental distribution $q(\mathbf{b}^i, \mathbf{b}^\star,)$ (probability of proposing a transition to $\mathbf{b}^\star$ from $\mathbf{b}^i$), which has to be compatible with the prior. This distribution is called the sampler or the proposal distribution. The transition to $\mathbf{b}^\star$ is then accepted with a probability $\alpha(\mathbf{b}^i, \mathbf{b}^\star)$ defined as:

$$\alpha(\mathbf{b}^i, \mathbf{b}^\star) = \begin{cases} \min\left(1, \frac{P(\mathbf{b}^\star|\mathbf{d}^{\text{obs}})q(\mathbf{b}^\star,\mathbf{b}^i)}{P(\mathbf{b}^i|\mathbf{d}^{\text{obs}})q(\mathbf{b}^i,\mathbf{b}^\star)}\right) & \text{if} \quad P(\mathbf{b}^i|\mathbf{d}^{\text{obs}})q(\mathbf{b}^i, \mathbf{b}^\star) \neq 0, \\ 1 & \text{else.} \end{cases} \tag{14}$$

If the transition is accepted, $\mathbf{b}^{i+1} = \mathbf{b}^\star$; otherwise $\mathbf{b}^\star$ is rejected and the chain stays in the same state: $\mathbf{b}^{i+1} = \mathbf{b}^i$.

Several possibilities exist for the choice of the proposal distribution q (Robert & Casella 2013) and this choice strongly determines the inversion. For example, the Gibbs sampler is widely used for inverse problems (Mosegaard & Sambridge 2002) but the important number of calls to the forward problem limits its relevancy for seismic tomography applications. We here introduce two widely used proposal distributions that we have implemented:

(i) The independent sampler (IMH): $q(\mathbf{b}^i, \mathbf{b}^\star) = q(\mathbf{b}^\star)$ where q is generally the *a priori* probability distribution (6) in Bayesian inversion. The proposed states are independent, they do not depend on the current one but are suggested according to the *a priori* information.

(ii) The symmetric increment random-walk sampler (SIMH): $q(\mathbf{b}^i, \mathbf{b}^\star) = q(|\mathbf{b}^i - \mathbf{b}^\star|)$. With this sampler, new states are proposed according to their distance to the current one. $q(\mathbf{b}^\star, \mathbf{b}^i) = q(\mathbf{b}^i, \mathbf{b}^\star)$, the acceptance probability then simplifies:

$$\alpha(\mathbf{b}^i, \mathbf{b}^\star) = \begin{cases} \min\left(1, \frac{P(\mathbf{b}^\star|\mathbf{d}^{\text{obs}})}{P(\mathbf{b}^i|\mathbf{d}^{\text{obs}})}\right) & \text{if} \quad P(\mathbf{b}^i|\mathbf{d}^{\text{obs}}) \neq 0 \\ 1 & \text{else.} \end{cases} \tag{15}$$

We illustrate the two samplers in Fig. 1. For this 1-D bi-modal distribution example, the IMH sampler (red curve) equals the *a priori* distribution. It only depends on the state $\mathbf{b}^\star$. The chain has thus good mixing properties since the successive states are not correlated (when the transition is accepted). In this sense, it is a global sampler that allows to explore coarsely the whole parameter space $\mathcal{M}$ but commonly fails to identify the different modes (the different maxima) of the *a posteriori* distribution $P(\mathbf{b}|\mathbf{d}^{\text{obs}})$, especially in large dimensions. We also

represent in black in Fig. 1 an SIMH sampler $q(\mathbf{b}^\star|\mathbf{b}^i)$ based on a normal distribution $\mathcal{N}_N(\mathbf{b}^i, \boldsymbol{\sigma}_\mathbf{b}^2)$ centred on the current state $\mathbf{b}^i$ and with a standard deviation $\boldsymbol{\sigma}_\mathbf{b}$. The closer a state $\mathbf{b}^\star$ is from $\mathbf{b}^i$, the more likely it may be proposed. It is clear that for a small $\boldsymbol{\sigma}_\mathbf{b}$ value (as shown here), the chain can spend a lot of iterations in the low probability area, it will then detect and permit a fine exploration of one of the modes. The SIMH is in this case a local sampler that will hardly leave a local mode. It does not give a wide overview of the distribution $P(\mathbf{b}|\mathbf{d}^{\text{obs}})$, the chain has low mixing properties as the successive states are strongly correlated. Conversely, if $\boldsymbol{\sigma}_\mathbf{b}$ is too large, the sampler proposes large moves that are mostly rejected: the chain can eventually detect both modes but will probably not sample them correctly. For this sampler, an appropriate $\boldsymbol{\sigma}_\mathbf{b}$ has to be chosen. It is a difficult tuning problem generally tackled by trial and error.

1.2.2 MCMC optimization: the simulated annealing algorithm (SA)

The SA has been introduced by Metropolis *et al.* (1953) and then generalized by Kirkpatrick *et al.* (1983) in the framework of optimization. It is a specialization of the previously introduced Metropolis–Hastings algorithm, the fundamental idea being to control the amplitude of the accepted perturbations thanks to a positive parameter T called the temperature. By considering the Gaussian likelihood (4) and defining the energy of the system as $E(\mathbf{b}) \equiv \frac{\Delta(\mathbf{b})}{2} - \ln(P(\mathbf{b}))$, we can rewrite the *a posteriori* distribution (8) as

$$P(\mathbf{b}|\mathbf{d}^{\text{obs}}) = \frac{e^{-E(\mathbf{b})}}{\int_{\mathcal{M}} e^{-E(\mathbf{b})}\,\mathrm{d}\mathbf{b}} \tag{16}$$

and recognize a Gibbs–Boltzmann distribution of energy E. As for (9), we simply write:

$$P(\mathbf{b}|\mathbf{d}^{\text{obs}}) \propto e^{-E(\mathbf{b})}. \tag{17}$$

The SA consists in choosing a maximum temperature $T_{\max}$ and performing a classical MCMC sampling (for instance using an SIMH sampler) of the following deformed (or tempered) *a posteriori* Gibbs–Boltzmann distribution:

$$P_T(\mathbf{b}|\mathbf{d}^{\text{obs}}) \propto e^{-\frac{E(\mathbf{b})}{T}}. \tag{18}$$

The influence of the temperature parameter on a multimodal distribution is shown in Fig. 1 (right). It can be seen that at high temperature the *a posteriori* distribution gets close to a uniform distribution, the two modes are connected. Indeed at $T \to +\infty$

$$P_T(\mathbf{b}|\mathbf{d}^{\text{obs}}) \underset{T\to+\infty}{\to} \text{uniform distribution}. \tag{19}$$

Decreasing the temperature parameter allows to detect and progressively reveal the modes. Obviously, at $T = 1$:

$$P_1(\mathbf{b}|\mathbf{d}^{\text{obs}}) = P(\mathbf{b}|\mathbf{d}^{\text{obs}}). \tag{20}$$

The temperature is slowly lowered from $T_{\max}$ to $T = 0$ during the run. Close to $T = 0$, the distribution approximates a Dirac distribution at the global minimum for $E(\mathbf{b})$ (if it is unique).

Using the energy the acceptance probability can be rewritten

$$\alpha(\mathbf{b}^i, \mathbf{b}^\star) = \min\left(1, e^{\frac{E(\mathbf{b}^i)-E(\mathbf{b}^\star)}{T}}\right). \tag{21}$$

Hence at $T \to +\infty$, every new model is accepted while at $T \to 0$, only the less energetic (the most probable) have a chance to be accepted. Since T decreases along the algorithm, the acceptance probability $\alpha(\mathbf{b}^i, \mathbf{b}^\star)$ varies with time and SA can be viewed as a non-homogeneous version of Metropolis–Hastings algorithm. Consequently, classical theoretical results on Markov chains do not apply for SA. Rigorously speaking, under some broad conditions, the algorithm converges to the global minimum of $E(\mathbf{b})$ for a starting temperature high enough and a cooling in $T \propto \frac{1}{\log(n)}$ (with n the iteration). This theoretical optimal cooling rate is intractable in practice and a geometrically decreasing sequence is generally used. The choice of the maximum temperature is done by considering some heuristic rules based on the acceptance rate (14) at $T_{\max}$ (Robert & Casella 2013).

Sampling a probability distribution with SA can be considered by stopping the cooling at $T = 1$ and continuing a Metropolis–Hastings exploration. Nevertheless, for a multimodal posterior distribution, if the cooling has been made too fast and the chain is on a local minimum of energy far from the global minimum (in term of $\boldsymbol{\sigma}_\mathbf{b}$ of the sampler), the chain will have an infinitely small probability to move toward and sample around the global minimum.

As just detailed, sampling correctly a complex posterior distribution and estimating the uncertainties may be problematic with classical Metropolis–Hastings or SA algorithms. Moreover, the number of iterations needed for a good sampling can be unreachable if the forward problem is too computationally expensive or the number of model parameters to retrieve too large. To cope with these impediments, we introduce in the next section a more elaborated algorithm.

2 INTERACTING MARKOV CHAINS

2.1 Theory and setting

2.1.1 Presentation

We present here a still relatively unknown algorithm that brings a solution to the drawbacks of classical MCMC methods and seems therefore particularly suited for complex sampling problems such as Bayesian inversion. The basic idea is to run several chains at different temperatures and allow them to interact in order to sample efficiently an *a posteriori* distribution. The idea first appears in Geyer (1991). Its algorithm is called parallel tempering and has been originally applied in physicochemical simulations [see Earl & Deem (2005) and references therein]. Undoubtedly Monte Carlo algorithms are particularly adapted to parallel computing (see Rosenthal 2000; Hall *et al.* 2014). Nevertheless, even if parallel computing allows to explore a bigger part of the model space, the previously mentioned drawbacks of MCMC still exist: the procedure neither improves the convergence speed nor the mixing properties of the non-interacting chains. Most samples are still discarded either during burn-in or thinning and this constitutes a considerable waste of resources.

If running several non-interacting Markov chains in parallel is already widely used for inverse problems (e.g. Agostinetti *et al.* 2015), less studies have applied interacting Markov chains. This approach is also known under the names of exchange Monte Carlo or Metropolis coupled chains (Iba 2001). More recently, the statistical community paid attention to interacting Markov chains and proposed a theoretical background and new algorithms. In this approach, the chains at different temperatures can exchange information along their run. The term of these exchanges can be defined in several ways. For example, Sambridge (2014) recently used the basic parallel tempering algorithm where exchanges occur between simultaneous states of the chains. However, this approach had been compared with two other interaction schemes [equi-energy sampler Kou *et al.* (2006) and PIR of Andrieu *et al.* (2011)] in Romary (2009). These numerical results showed that the latter outperforms the other two for Bayesian inversion purpose. Indeed, it is based on a powerful interaction scheme making use of the whole history of the chains rather than the simultaneous states only. Our work is thus based on PIR interaction schemes which allows the low-temperature chains to access the history of the adjacent higher temperature ones. The first applications of the method in geosciences are Romary (2009, 2010a,b) where it has been used for reservoir characterization.

The previous discussions about MCMC and SA allows us to present easily this approach in the Bayesian inversion context. In a few words, several chains are run simultaneously, each one at a different temperature in the sense of SA. Instead of performing only Metropolis–Hasting updates, every chain can also jump to any past state of the chain at the next higher temperature with a probability defined by importance weights that will foster the low-energy states. The transition probability is then governed by eq. (26). Let us describe the approach in a more mathematical way.

2.1.2 Mathematical setting

We recall that we aim at sampling from the posterior distribution (17). K Markov chains are running in parallel, each one at a different temperature T_l with $l = 1, \ldots, K$ in the sense of SA. The chain l is actually exploring the following tempered version of $P(\mathbf{b}|\mathbf{d}^{\text{obs}})$:

$$P_l(\mathbf{b}|\mathbf{d}^{\text{obs}}) \propto e^{-\frac{E(\mathbf{b})}{T_l}}. \tag{22}$$

We note $q_l(\mathbf{b}, \mathbf{b}^\star)$ the sampler of chain l (see Section 1.2.1). The temperature ladder verifies:

$$T_1 = 1 < T_2 < \cdots < T_K = T_{\max}. \tag{23}$$

In this approach, the chains at different temperatures can exchange information along their run. PIR allows importance sampling swaps between chains at adjacent temperatures. At each iteration, a swap move is proposed to any single chain (except the highest temperature one) with a probability θ.

(i) If it is rejected, the chain performs a classical Metropolis–Hastings iteration as described in Section 1.2.1.

(ii) If it is accepted, an importance swap is proposed. It potentially allows the chain to move to any past state of the chain at the next higher temperature. This step is described below.

If we note $\mathbf{b}^{(l,n)} = (b_1^{(l,n)}, b_2^{(l,n)}, \ldots, b_N^{(l,n)}) \in \mathcal{M}$ the state number n generated by the chain l (at temperature T_l), a state $\mathbf{b}^{(l+1,*)}$ is picked among the past states of the adjacent higher temperature chain:

$$H_{n-1}^{(l+1)} \equiv \left\{\mathbf{b}^{(l+1,1)}, \mathbf{b}^{(l+1,2)}, \mathbf{b}^{(l+1,3)}, \ldots, \mathbf{b}^{(l+1,n-1)}\right\}.$$

To each past state of that chain, $\mathbf{b}^{(l+1,i)}$, $i = 1, \ldots, (n-1)$ is associated an importance weight:

$$r^{(l)}\left(\mathbf{b}^{(l+1,i)}\right) = \frac{P_l\left(\mathbf{b}^{(l+1,i)}|\mathbf{d}^{\text{obs}}\right)}{P_{l+1}\left(\mathbf{b}^{(l+1,i)}|\mathbf{d}^{\text{obs}}\right)} = \frac{e^{-\frac{E(\mathbf{b}^{(l+1,i)})}{T_l}}}{e^{-\frac{E(\mathbf{b}^{(l+1,i)})}{T_{l+1}}}} = e^{-E(\mathbf{b}^{(l+1,i)})\left(\frac{1}{T_l} - \frac{1}{T_{l+1}}\right)}. \tag{24}$$

which is the un-normalized ratio of the tempered distributions at T_l and T_{l+1}. Sampling a state $\mathbf{b}^{(l+1,i^*)}$ of the chain $l+1$, that is, virtually distributed according to $P_{l+1}(\mathbf{b}^{(l+1,i^*)}|\mathbf{d}^{\text{obs}})$, with respect to this weight allows this state to be considered as distributed according to $P_{l+1}(\mathbf{b}^{(l+1,i^*)}|\mathbf{d}^{\text{obs}})$ following the principle of importance sampling (Robert & Casella 2013).

• The idea is pretty simple. Considering two probability density function, f and g, and a variable X that follows f. We can write:

$$E(h(X)) = \int h(x)f(x)dx = \int h(x)\frac{f(x)}{g(x)}g(x)dx. \tag{25}$$

Therefore, this expectation can be computed by Monte Carlo integration using random numbers following g and reweighted by the ratio $\frac{f(x)}{g(x)}$.

• This method gives more chance to the less energetic states of the chain $l+1$ to be proposed.

• The transition is then accepted or not with probability:

$$\beta(\mathbf{b}^{(l,n)}, \mathbf{b}^{(l+1,i^*)}) = \min\left(1, \frac{r^{(l)}(\mathbf{b}^{(l+1,i^*)})}{r^{(l)}(\mathbf{b}^{(l,n)})}\right) \tag{26}$$

$$= \min\left(1, \exp\left(\left(\frac{1}{T_l} - \frac{1}{T_{l+1}}\right)(E(\mathbf{b}^{(l,n)}) - E(\mathbf{b}^{(l+1,i^*)}))\right)\right). \tag{27}$$

If the energy of the proposed state $\mathbf{b}^{(l+1,i^*)}$ is lower than that of $\mathbf{b}^{(l,n)}$, the exchange will be systematically accepted.

The efficiency of the algorithm relies on the type of sampler used by each chain. The highest temperature chain might use a global sampler (e.g. IMH) and thus explores coarsely the whole model space while the lower temperature chains use local samplers (e.g. SIMH) and thus are able to sample thoroughly the interesting regions discovered by the higher temperature chains. The standard deviation of the normal distribution of each SIMH sampler may also decrease with the temperature. We added a detailed flowchart of the algorithm in Appendix. As any MCMC-based inference method, the algorithm here proposed needs to be tuned. The parameters that have to be chosen are:

(i) The number K of chains.
(ii) The sequence $(T_l)_l$ of temperatures.
(iii) The samplers at each temperature $q_l(\mathbf{b}^\star|\mathbf{b})$.
(iv) The probability θ of proposing a swap.

The approach is purely empirical, based on numerical experiments. Romary (2010a) summarizes the existing guidelines and rules of thumb. Hence, for example, the number of chains to use should be the minimum number that ensures a good overlapping of the histograms of the tempered energies. For the choice of $T_{\max}$ however it seems more suitable to us to run a single chain at temperature 1 sampling independently the prior distribution (6) during say, $N = 500$ iterations: $(\mathbf{b}^k)_{0\leq k\leq 500}$. The resulting energy distribution $(E(\mathbf{b}^k))_{0\leq k\leq 500}$ can then be used to choose $T_{\max}$ in order to obtain a satisfactory transition acceptance rate (21) at the highest temperature: between 0.6 and 0.75 in practice. Knowing the number of chains and the maximum temperature, the temperature ladder can be built, for example, as a geometrical progression between 1 and $T_{\max}$.

2.1.3 Theoretical improvements

As we have seen, without exchange, the highest temperature chain would sample coarsely large volumes of the model space $\mathcal{M}$ whereas low-temperature chains would precisely sample local regions but could become trapped in local energy minima. Allowing the lowest temperature chains to be regenerated in an interesting low energetic location previously sampled by the upper chains significantly enhances their mixing (Romary 2010a; Andrieu *et al.* 2011) and their speed of convergence toward the stationary regime, especially the lowest temperature one. Each chain can run physically in parallel, that is on different processors. However, if not working on a CPU cluster, running K chains rather than 1 during n iterations requires more computational effort. Nevertheless, the sampling will clearly be more efficient than running a single chain during nK iterations. Indeed, in practice, a single chain would not have been able to access to the whole region which is always within reach of the highest temperature chains during the parallel interacting sampling. Moreover, as shown in Romary (2010a), the states generated by parallel IMCMC are far less correlated than the ones generated by an SA or a classical Metropolis–Hastings algorithm thus providing less variable estimates. To estimate posterior expectations $I[h]$ of a function $h(\mathbf{b})$ (see eq. (12)) every sample generated at each temperature can also be used. Every state $\mathbf{b}^{(l,n)}$ of the chain at temperature T_l just having to be weighted by the following importance weights:

$$\eta^{ln} = e^{-E(\mathbf{b}^{(l,n)})\left(1-\frac{1}{T_l}\right)}. \tag{28}$$

Therefore, the estimate of $I[h]$ after N iterations of K chains will take the form:

$$I[h] \approx \frac{1}{K}\sum_{l=1}^{K}\frac{\sum_{n=1}^{N}\eta^{ln}h(\mathbf{b}^{(l,n)})}{\sum_{n=1}^{N}\eta^{ln}}. \tag{29}$$

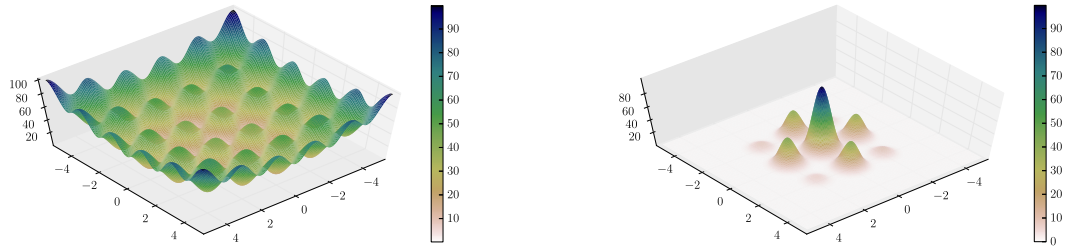

Figure 2. Left: 2-D Rastrigin function $\mathbf{b} \mapsto \mathcal{R}(\mathbf{b})$. Right: KDE of the *a posteriori* distribution sought $P(\mathbf{b}|\mathbf{d}^{\text{obs}}) = P(\mathbf{b})e^{-\frac{1}{2}\left|\frac{\mathcal{R}(\mathbf{b})}{\sigma_d}\right|^2}$.

Table 1. Features of the run for the interacting MCMC.

Number K of chains	3		
Probability θ of proposing a swap	25 per cent		
Sequence $(T_l)_l$ of temperatures	Geometric sequence between $T_{\max} = 50$ and $T = 1$:		
	$T_0 = 1$	$T_1 = \sqrt{50}$	$T_{\max} = 50$
Samplers at each temperature	SIMH	SIMH	IMH
$q_l(\mathbf{b}^\star\|\mathbf{b})$:	$\mathcal{N}_2(\mathbf{b}, \mathbb{1}_2\,\sigma_{\mathbf{b}}^2)$	$\mathcal{N}_2(\mathbf{b}, \mathbb{1}_2\,\sigma_{\mathbf{b}}^2)$	$P(\mathbf{b}^\star)$
$\sigma_{\mathbf{b}} = (\sigma_x, \sigma_y)$:	Linear decreasing functions of T:		
	$\sigma_x = \sigma_y = \frac{5.12+5.12}{50}$	$\sigma_x = \sigma_y = \frac{5.12+5.12}{20.62}$	

With its estimated variance:

$$\text{Var}[h] \approx \frac{1}{K}\sum_{l=1}^{K}\frac{\sum_{n=1}^{N}\eta^{ln}(h\left(\mathbf{b}^{(l,n)}\right) - I[h])^2}{\sum_{n=1}^{N}\eta^{ln}}. \tag{30}$$

Kou *et al.* (2006) have shown that using this weighted sum over the chains provides better estimates than using only the states generated by the lowest temperature chain (even if in practice the η^{ln} are very small).

2.2 Test on a highly multimodal distribution

In order to illustrate the efficiency and the robustness of the algorithm, we apply it to sample a 2-D multimodal distribution. The forward problem (2) is the following 2-D Rastrigin function $\mathcal{R}$ depicted in Fig. 2 (left):

$$\mathcal{R} : \left| \begin{array}{l} [-5.12, 5.12]^2 \longrightarrow \mathbb{R} \\ \quad \mathbf{b} = (x, y) \longmapsto \mathcal{R}(\mathbf{b}) = \mathcal{R}(x, y) = 20 + (x^2 - 10\cos(\pi x)) + (y^2 - 10\cos(\pi y)). \end{array} \right.$$

It was first proposed by Torn & Zilinskas (1989) as a 2-D function and has been generalized for N-dimensions by Mühlenbein *et al.* (1991). It is a typical example of a non-linear multimodal function useful to test the performance of a sampling algorithm. It has a global minimum in $(x, y) = (0, 0)$ and several local minima. For this test, following the notations of the previous section, a state $\mathbf{b}$ is composed of two parameters x and y belonging to the model space $\mathcal{M} = [-5.12, 5.12]^2$. Our *a priori* knowledge on the values of these parameters is a uniform distribution over $\mathcal{M}$ (every value of (x, y) has the same *a priori* probability):

$$\forall \mathbf{b} \in [-5.12, 5.12]^2 \qquad P(\mathbf{b}) = \frac{1}{(5.12 + 5.12)^2}. \tag{31}$$

The data $\mathbf{d}^{\text{obs}}$ are 0 with a significant standard deviation $\sigma_{\mathbf{d}} = \sigma_d = \sqrt{50}$. Then, the energy $E(\mathbf{b})$ of a state $\mathbf{b}$ is

$$E(\mathbf{b}) = \frac{1}{2}\left|\frac{\mathcal{R}(\mathbf{b})}{\sigma_d}\right|^2 - \ln(P(\mathbf{b})) \tag{32}$$

and the sought *a posteriori* distribution is

$$\mathbf{b} \mapsto P(\mathbf{b}|\mathbf{d}^{\text{obs}}) = e^{-E(\mathbf{b})} = P(\mathbf{b})e^{-\frac{1}{2}\left|\frac{\mathcal{R}(\mathbf{b})}{\sigma_d}\right|^2}. \tag{33}$$

We have sampled it perfectly by an accept/reject method using 100 000 samples and used a kernel density estimator (KDE, see Silverman 1986) to represent the resulting density. It is shown in Fig. 2 (right). We run two algorithms to sample this distribution: the IMCMC and an SA. Their features are shown in Tables 1 and 2. Having a look at these tables, it is important to note that the temperature sequences and the amplitudes of the proposed moves have been chosen in the same way for the two algorithms. In other words, when the SA chain is at the same

Table 2. Features of the run for the simulated annealing.

Evolution of T with the iteration n	Geometric sequence. A decrease from $T_{\max} = 50$ to $T = 1$ is achieved in 2000 iterations the temperature being updated every 50 iterations: $T_n = 50^{-\frac{50}{2000}(\text{floor}[\frac{2000-n}{50}]+1)}$
Sampler chosen $q(\mathbf{b}^\star\|\mathbf{b})$:	SIMH
$q_l(\mathbf{b}^\star\|\mathbf{b})$:	$\mathcal{N}_2(\mathbf{b}, \sigma_{\mathbf{b}}^2)$
$\sigma_{\mathbf{b}} = (\sigma_x, \sigma_y)$:	Linear decrease between $\frac{5.12+5.12}{4}$ at $T_{\max}$ and $\frac{5.12+5.12}{50}$ at $T = 1$ Particularly: $\sigma_x(T = \sqrt{50}) = \frac{5.12+5.12}{20.62}$

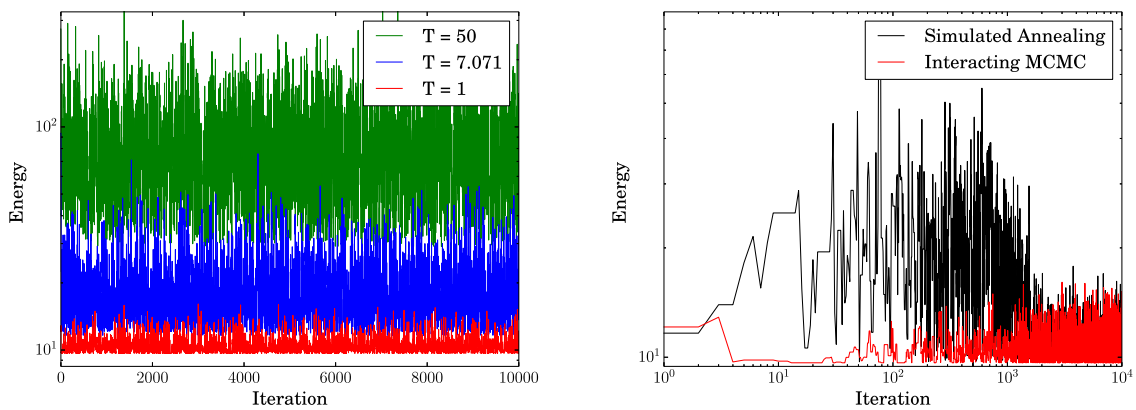

Figure 3. Left: energies of the interacting chains as a function of the iteration. Right: convergence in term of energy for the lowest temperature chain of interacting Markov chains algorithm (red) and the SA (black). Low-energy (high probability) regions are reached very quickly with interacting Markov chains algorithm.

temperature as one of the interacting chains they behave alike (they can propose the same moves). The only difference being their ability to interact or not. The three interacting Markov chains ran during $N = 10\,000$ iterations whereas the SA ran during 30 000 iterations after the 2000 burn-in iterations. The energies of states (x, y) generated by the IMCMC are shown in Fig. 3 (left). We observe a good overlapping of the energy domain explored by the three chains ensuring a satisfactory exchange rate between the chains. Fig. 3 (right) is a comparison of the energy evolution for the 10 000 first samples of each algorithm, it demonstrates clearly the higher speed of convergence of the IMCMC algorithm compared to the SA. No burn-in is required with IMCMC, whereas more than 1000 iterations are needed by SA to converge. The posterior distributions simulated by each algorithm are then constructed from the generated samples using a KDE. The results shown in Fig. 4 have to be compared to the theoretical density drawn in Fig. 2 (right). At $T = 1$, the standard deviation of the sampler $\sigma_x = \sigma_y = \frac{5.12+5.12}{50}$ gives a chance to the chain to go from one mode to another. Nevertheless, the SA algorithm ends stuck in one or several modes and does not succeed in identifying the central mode as the principal one (Fig. 4, left). The results presented here are the best we managed to obtain in term of sampling with the SA method (it has detected seven of the nine modes) and a standard deviation of the sampler at $T = 1$ similar as the one used by the lowest temperature chain of the IMCMC algorithm. It seems important to highlight the high variability of the results obtained by SA as the chain ends stuck in different modes for each different run. The IMCMC detected the nine principal modes (Fig. 4, right) in 100 per cent of the runs performed, even with far less iterations (down to 2000). The consequences are huge in term of computational cost. Most important, the estimations of the uncertainties on the values of the parameters $\mathbf{b} = (x, y)$ would be much more reliable with the IMCMC. The algorithm gives thus a robust way to evaluate the uncertainties associated with the model parameters and it is interesting because of its speed of convergence and its stability.

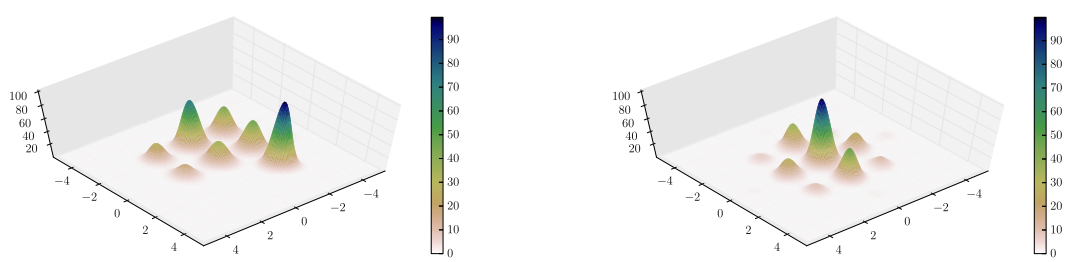

Figure 4. Left: KDE of the posterior distribution simulated by simulated annealing. Right: KDE of the posterior distribution simulated by the interacting Markov chains. To be compared with Fig. 2.

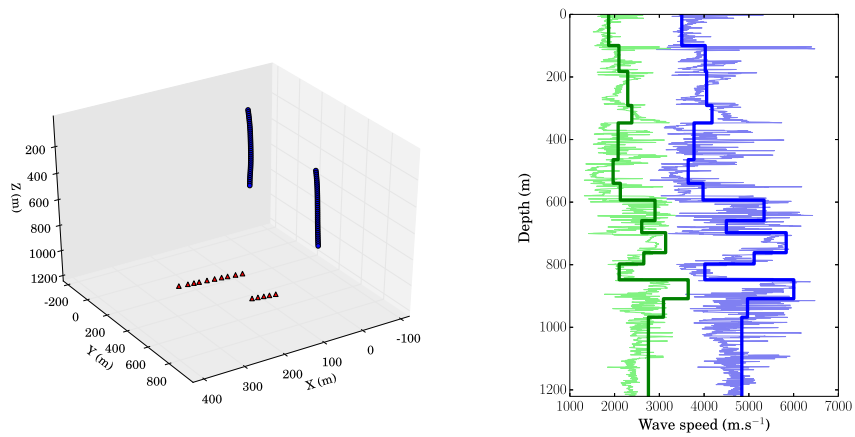

Figure 5. This figure illustrates the *a priori* knowledge on the area studied. Left: geometrical setting for the first arrival times recorded. The circles represent the receivers and the triangles are the sources. Right: light blue and green curves are, respectively, *P*- and *S*-wave velocity profiles (sonic logs) acquired on the site. These curves are noted $V^P_{\log}(z)$ and $V^S_{\log}(z)$ in the text. Dark blue and green curves are, respectively, V_P and V_S vertical profiles of the 1-D reference calibrated velocity model.

3 REAL DATA CASE STUDY

In this last section, we present the results of our inversion approach applied to a real data set recorded in the context of hydraulic fracturing. We have two types of measurements available: a sonic log which informs on the wave propagation velocity of the medium at a given frequency and some traveltimes from perforation shots. We first build the prior model from the sonic logs. We then update this prior knowledge on the model parameters by estimating the posterior distribution of the model parameters knowing the traveltime data.

3.1 Setting of the problem

The acquisition geometry is represented in Fig. 5 (left) in a relative Cartesian coordinate system. The monitoring network consisted of two wireline arrays of 40 3C-receivers that were deployed in two different vertical wells (circles in Fig. 5, left). The depth range of these arrays is between about 50 and 750 m. Fifteen perforation shots performed along two horizontal wells (triangles in Fig. 5, left) at a depth of 1050 m have been considered. For each of the 15 perforation shots, almost all 80 first *P*-wave and approximately 40 *S*-wave arrivals could be picked. These *P* and *S* first arrival traveltimes constitute our data set for the inversion. Following the notations introduced in Section 1, we write:

$$\mathbf{d}^{\text{obs}} = \left(d_P^1, \ldots, d_P^{15\times 80}, d_S^1, \ldots, d_S^{15\times 40}\right) \in \mathcal{D} = \mathbb{R}^{\times 15\times(80+40)}. \tag{34}$$

Over the entire data set, we estimate the average *P*- and *S*-wave picking uncertainties to be around 2.5 and 5 ms, respectively. Compressive and shear velocity logs represented in Fig. 5 (right, light curves) have also been acquired in one of the wells using a sonic wireline tool that emits a signal with a central frequency around 3 kHz. They will be noted $V^P_{\log}(z)$ and $V^S_{\log}(z)$, respectively. The measurements have been made every half-foot. These logs are obtained at a very high frequency and, assuming that the medium is dispersive, probably do not represent the subsurface as seen by the seismic waves in the frequency band of the microseismic events. Indeed disagreements between seismic data and sonic log data are often recognized (Sheriff & Geldart 1995). However, they can be considered as *a priori* information for an inversion. The sonic logs are generally used to build a layered velocity model, which is then calibrated with a tomography using perforation shots from known locations (e.g. Bardainne & Gaucher 2010). In this example, a velocity model was derived from the logs and from *a priori* geological information (subhorizontal layers). The resulting 1-D calibrated velocity model consisted of a blocky horizontal model with 15 layers (see dark curves in Figs 5, right). *P* velocities range from 3500 to 6000 ms^{-1} and V_P/V_S ratio varies from 1.6 to 1.95.

For this example, a layered geometrical parametrization is not necessarily appropriate: how many layers do we need to describe the subsurface? Is it physically relevant to work with layers and not with a smoother representation? This parametrization is by itself a strong *a priori* assumption since the number of layers is fixed. Most important, this representation is not optimum in term of dimension since $2N$ parameters (V_P and V_S in each layer) are needed to represent N static horizontal layers. If the interface depths are also considered as unknowns, $3N - 1$ parameters are required. In a Bayesian context, the computational cost depends on the number of model parameters to retrieve, the dimension of the problem should thus be just sufficient for the resolution needed. We propose here to use a parametrization based on a optimally truncated decomposition of the velocity logs on wavelet functions basis. This allows to describe complex velocity models with a restricted number of parameters.

3.2 A self-parametrizing approach using wavelet theory

3.2.1 The wavelet decomposition, a multiscale analysis tool

Since the 1980s, wavelet theory has developed rapidly and has become an important tool for multiscale signal analysis (see Burrus *et al.* 1997; Mallat 1999). It has been applied successfully in many different fields, such as image compression and processing, optimum signal smoothing or speech analysis. It has also been used several times for model parametrization [Chiao & Kuo (2001), Bennett & Malinverno (2005), Loris *et al.* (2007), Tikhotsky & Achauer (2008), Simons *et al.* (2011) or more recently Hawkins & Sambridge (2015)]. The original goal of wavelet theory is to build orthonormal basis of the Hilbert space $L^2(\mathbb{R})$ of square integrable functions of $\mathbb{R}$, expressed as:

$$\{\psi_{jk}(x) : (j,k) \in \mathbb{Z}^2\} = \{2^{\frac{j}{2}}\psi(2^j x - k) : (j,k) \in \mathbb{Z}^2\} \tag{35}$$

that is, composed of dyadic translations and dilations of a unique function, preferably regular and localized, called the mother wavelet ψ. This basis is orthonormal:

$$\forall j,k,l,m \qquad \langle \psi_{jk}, \psi_{lm} \rangle = \delta_{jl}\delta_{km} \tag{36}$$

where δ_{jl} is the Kronecker delta and $\langle f, g \rangle$ is the standard inner product $\langle f, g \rangle = \int_{-\infty}^{\infty} f(x)\overline{g(x)}\,\mathrm{d}x$ of $L^2(\mathbb{R})$. Every function $h \in L^2(\mathbb{R})$ can be expanded in a unique way in this basis as:

$$h(x) = \sum_{j=-\infty}^{\infty}\sum_{k=-\infty}^{\infty} a_{jk}\psi_{jk}(x) \tag{37}$$

with convergence of the series understood to be convergent in norm. Such a representation of a function h is known as a wavelet series. In the discrete case $h = (h(x_j))_{j=1,\ldots,N} \in \mathbb{R}^N$ can be fully described by N coefficients:

$$h(x_j) = \sum_{i=1}^{N} a_i \psi_i(x_j). \tag{38}$$

The first coefficients describe the global shape of the function while the last ones characterize its small-scale details. From (38), by keeping the M most energetic coefficients (i.e. the biggest $|a_i|^2$) and setting the other coefficients to 0, we construct the following approximation h_M of h:

$$h_M(x_j) = \sum_{i=1}^{M} c_{i'}\psi_{i'}(x_j) \tag{39}$$

where i' is the index of the ith most energetic coefficient (see Jansen 2012). It is interesting to note (and very convenient) that h_M is an optimal approximation in the mean-square sense. Moreover, this thresholding does not cause any phase shift nor ringing as the Gibbs phenomenon for filtering in frequency domain.

Fig. 6 shows examples of filtering of the P-wave velocity log (blue curve) using three different wavelets and 15 coefficients (red curves). The mother wavelet determines the global appearance of the profile and the first coefficients mainly control its lowest frequency variations.

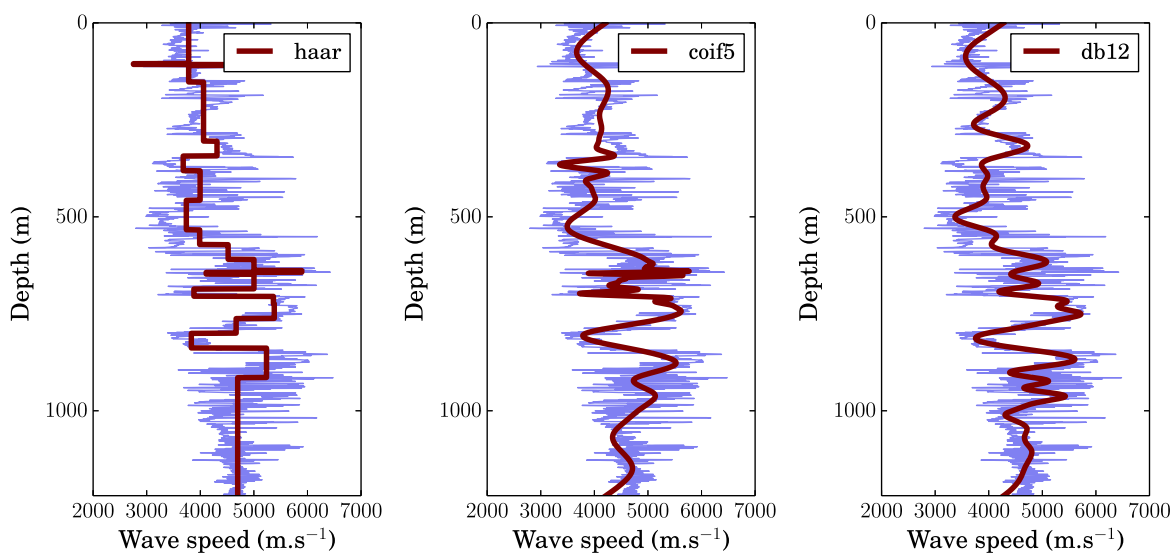

Figure 6. Left: filtering of the P-wave velocity log using a Haar wavelet and 15 coefficients. Middle: filtering of the P-wave velocity log using a Coiflet wavelet with five vanishing moments and 15 coefficients. Right: filtering of the P-wave velocity log using a Daubechie wavelet with 12 vanishing moments and 15 coefficients. This illustrates the global aspect of the profiles based on the different wavelets. Coiflet 3 is very similar to Coiflet 5 and Daubechie 8 is similar to Daubechie 12.

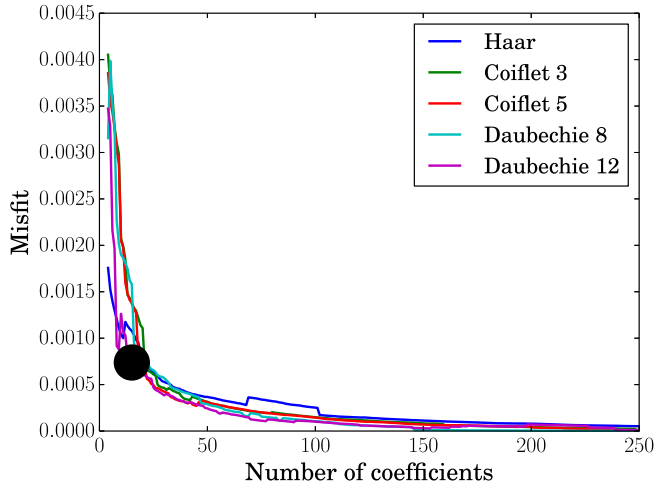

Figure 7. Least-squares misfit in term of traveltimes between the raw P-wave velocity log $V^P_{\log}(z)$ and the filtered logs $V^{P\,M}_{\log,\psi}(z)$ as a function of the number M of coefficients kept and for the set of mother wavelets ψ considered in this paper. The black dot spots the selected configuration, namely: 15 coefficients.

Rather complex features of the velocity log are described with 15 coefficients. With a geometrical-layered parametrization, 15 parameters represent only eight layers, a very small number compared to the layer number obtained with the Haar wavelet parametrization (Fig. 6, left).

3.2.2 The parametrization chosen

The velocity profile parametrization is based on the filtering described above. Indeed, a velocity profile can be constructed from the choice of a mother wavelet ψ and a set $\mathbf{c}$ of coefficients c_i through the relation (39). The idea is to use the mother wavelet's type and its coefficients as the parameters $\mathbf{b}$ of the inversion. Letting the wavelet type be part of the inversion is a similar approach to the Bayesian Model averaging (Hoeting *et al.* 1999). The mother wavelets belong to a discrete space $\{\psi_1, \psi_2, \psi_3, \dots\}$. The number of coefficients to keep have still to be determined. We adopt the following approach: from the raw P-wave velocity log $V^P_{\log}(z)$ represented in light colours in Fig. 5 (right), we generate synthetic first arrival times $\mathbf{d}_0$ with the eikonal solver of Noble *et al.* (2014) for an arbitrary shot located near the bottom of the profile (at $z = 900$ m) and recorded at synthetic receivers located close to the surface ($z = 50$ m). $V^P_{\log}(z)$ is then iteratively filtered with a truncated wavelet decomposition. We note $V^P_{\log,M}(z)$ the filtered P-wave sonic log reconstructed from M coefficients. For each truncated profile, first arrival times $\mathbf{d}_M$ are computed with the eikonal solver and a misfit $\Delta_M = ||\mathbf{d}_0 - \mathbf{d}_M||^2$ is calculated. In Fig. 7, we represent this misfit with respect to the number of coefficients kept to describe the velocity model for five different mother wavelets. The best trade-off between a minimum number of coefficients and a resolution sufficient to explain the synthetic data $\mathbf{d}_0$ seems to be a filtering with $M \approx 15$ coefficients regardless of the mother wavelet type. Hence, for the inversion, a state of the Markov chain will contain the wavelet type plus 30 parameters: 15 for the P-wave velocity and 15 for S-wave velocity. We note: $\mathbf{b} = (\psi, c^P_1, \dots, c^P_{15}, c^S_1, \dots, c^S_{15}) \equiv (\psi, c_1, \dots, c_{30})$ and $\mathcal{M} \subset \mathbb{N} \times \mathbb{R}^{30}$. The *a priori* knowledge on the values of the parameters $\mathbf{b}$ can be represented by a 31-D probability distribution: $P(\mathbf{b})$. For this problem we choose, *a priori*, five different wavelet types: Haar wavelet, Daubechie wavelets with 8 and 12 vanishing moments and Coiflet wavelets with 3 and 5 vanishing moments, these mother wavelets having, *a priori*, the same chance to be drawn. These different wavelets provide velocity profiles with distinct aspect. The reader can make up his mind by looking at Fig. 6 which illustrates the appearance of the profiles based on the different wavelets. Coiflet 3 is very similar to Coiflet 5 and Daubechie 8 is similar to Daubechie 12. We also suppose a uniform *a priori* probability distribution on each coefficient c_j, that is, for each wavelet type ψ_i and each coefficient c_j we define an interval $[\inf_{\psi_i}(c_j), \sup_{\psi_i}(c_j)]$ on which c_j can take any value with the same probability. Out of this domain any value has a probability 0. Hence, the *a priori* probability is:

$$P(\mathbf{b}) = \begin{cases} \displaystyle\prod_{i=1}^{5}\prod_{j=1}^{30} \frac{1}{\sup_{\psi_i}(c_j) - \inf_{\psi_i}(c_j)} & \text{if} \quad \forall k \quad c_k \in [\inf_{\psi}(c_k), \sup_{\psi}(c_k)] \\ 0 & \text{else.} \end{cases} \tag{40}$$

We note $V^{P\,15}_{\log,\psi}(z)$ and $V^{S\,15}_{\log,\psi}(z)$ the P- and S-wave velocity logs filtered by truncated wavelet decomposition using wavelet ψ and 15 coefficients. Three examples of filtering are shown in Fig. 6. Filtered sonic logs are fully described by their 15 wavelet coefficients that we will note: $(l^P_{1,\psi}, \dots, l^P_{15,\psi})$ and $(l^S_{1,\psi}, \dots, l^S_{15,\psi})$. In order to generate models not too far from $V^{P\,15}_{\log,\psi}(z)$ and $V^{S\,15}_{\log,\psi}(z)$, we have chosen to sample around the $l^P_{i,\psi}$ and $l^S_{i,\psi}$. Hence, we have chosen $\inf_{\psi_i}(c^P_j) = 0.6 l^P_{j,\psi_i}$, $\sup_{\psi_i}(c^P_j) = 1.4 l^P_{j,\psi_i}$, $\inf_{\psi_i}(c^S_j) = 0.6 l^S_{j,\psi_i}$ and $\sup_{\psi_i}(c^S_j) = 1.4 l^S_{j,\psi_i}$. To summarize, the parameters of the inversion are perturbed wavelet coefficients of the filtered logs. This strategy allows us to include the *a priori* information brought by the seismic logs while keeping a relatively wide model space. A sample of P- and S-wave velocity profiles generated with this prior can be seen in Fig. 8 together with the P- and S-wave measured velocity logs.

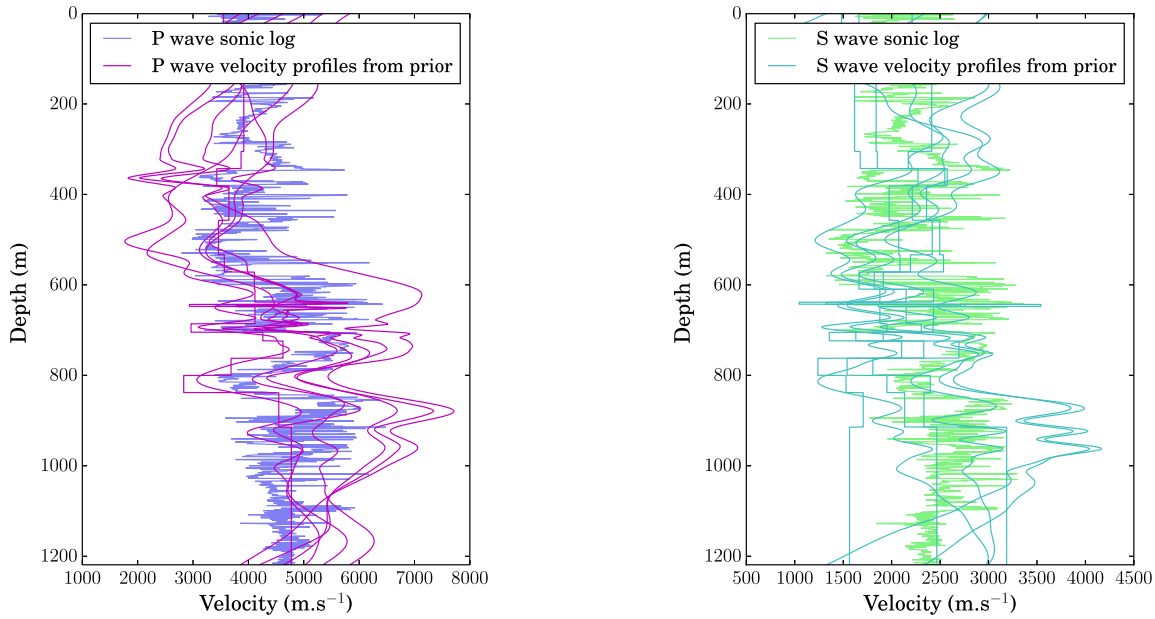

Figure 8. Samples of *P*- and *S*-wave velocity profiles from prior shown together with the sonic logs. It illustrates the diversity of profiles reachable *a priori*.

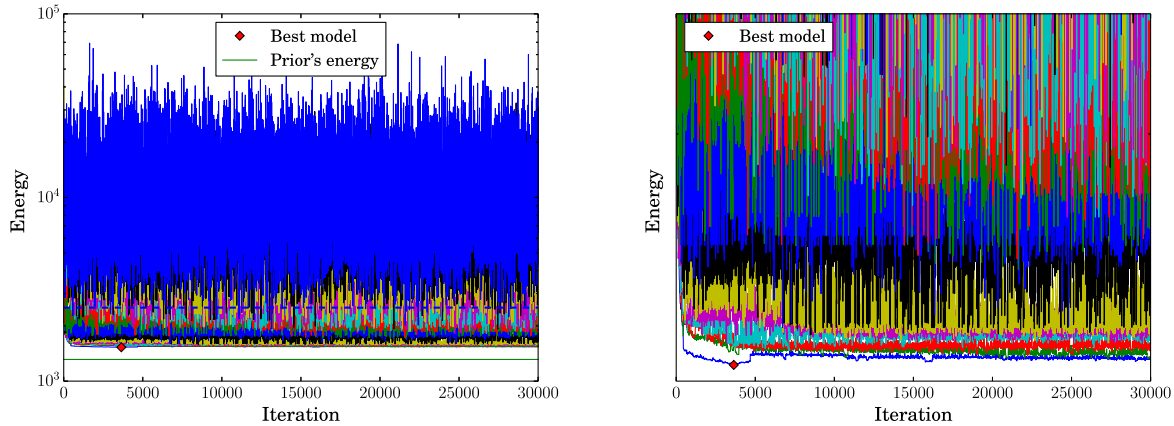

Figure 9. Energies of the interacting Markov chains as a function of the iteration for the real case study. The red diamond spots the best model generated. The dashed blue line represents the threshold below which the models generated are acceptable (one standard deviation of difference between synthetic and real data). The right figure is a zoom on the lowest temperature chains. These figures illustrate the efficiency of the algorithm especially showing the large number of acceptable models sampled from the first iterations.

3.3 Results and discussion

For this traveltime tomography, the forward problem is the 3-D computation of the theoretical traveltimes **d** that a configuration of the velocity model produces. The velocity model is discretized on a rectangular grid ($n_x = 35 \times n_y = 35 \times n_z = 80$) and a new eikonal solver (Noble *et al.* 2014) is used to calculate, for each perforation shot (triangles in Fig. 5, left), the traveltimes at the receiver positions (circles in Fig. 5, left). The forward problem is the most resource demanding part of the algorithm. A parallel network of 30 CPUs (Intel®Xeon®CPU E5-2407 @ 2.20 GHz) has been used, at each iteration, to run the eikonal solver for both *P* and *S* waves for the 15 shots. As seen in Section 1 (eqs (8) and (16)) an energy is computed afterward from a least-squares misfit between **d** and $\mathbf{d}^{\text{obs}}$. Fifteen interacting Markov chains ran during $N = 30\,000$ iterations. This number ensured a good overlapping of the histograms of the tempered energies and allows them to satisfactorily exchange their states. The whole tomography lasted ∼8 hr. We represent the energies of the different chains with respect to the iteration number in Fig. 9. In that figure, the dashed blue line represents the threshold below which the models generated are acceptable (one standard deviation of difference between synthetic and real data). It illustrates the high number of acceptable models found. It has to be noted that the best model tested has been found rather quickly but not reached again during the simulation indicating that, providing the algorithm has finally converged, it probably corresponds to a thin mode which did not need to be sampled to give a good overview of the *a posteriori* probability distribution. The algorithm converges in less than 5000 iterations for the features indicated in Table 3. We first estimate the *P* and *S* best models (green curves in Fig. 10) and average models (dark blue curves in Fig. 10) applying the formula (29). In this case, the obtained profiles seem coherent with the sonic logs. In order to estimate the velocity model uncertainties, we represent marginal posterior probability density function for V_P and V_S velocity profiles. The resulting density plots are shown in Fig. 10 with darker colours representing higher probability.

Table 3. Features of the run for the interacting MCMC applied to the real case study. We note $\sigma_{\mathbf{c}} = (\sigma_{c_1}, \ldots, \sigma_{c_{30}})$ and $\sigma_{\mathbf{c}}^2 = (\sigma_{c_1}^2, \ldots, \sigma_{c_{30}}^2)$.

Number K of chains	15
Probability θ of proposing a swap	25 per cent
Sequence $(T_k)_k$ of temperatures	Geometric sequence between $T_{14} = T_{\max} = 10\,000$ and $T_0 = 1$: $\forall k \in \{0, 1, \ldots, 14\} \quad T_k = T_{\max}^{\frac{k}{14}}$
Number of parameters changed at each iteration (including wavelet type)	1 if $T = 1$ 31 if $T = T_{\max}$ 4 otherwise
Samplers at each temperature	SIMH if $T \neq T_{\max}$ IMH otherwise
$q_l(\mathbf{b}^\star \vert \mathbf{b})$	$\mathcal{N}_{30}(\mathbf{c}, \mathbb{I}_{30}\, \sigma_{\mathbf{c}}^2)$ if $T \neq T_{\max}$ $P(\mathbf{b}^\star)$ otherwise
$\forall j \quad \sigma_{c_j}$	If $T \neq T_{\max}$ $\sigma_{c_j} = \frac{\inf_{\psi_i}(c_j) - \inf_{\psi_i}(c_j)}{5}$

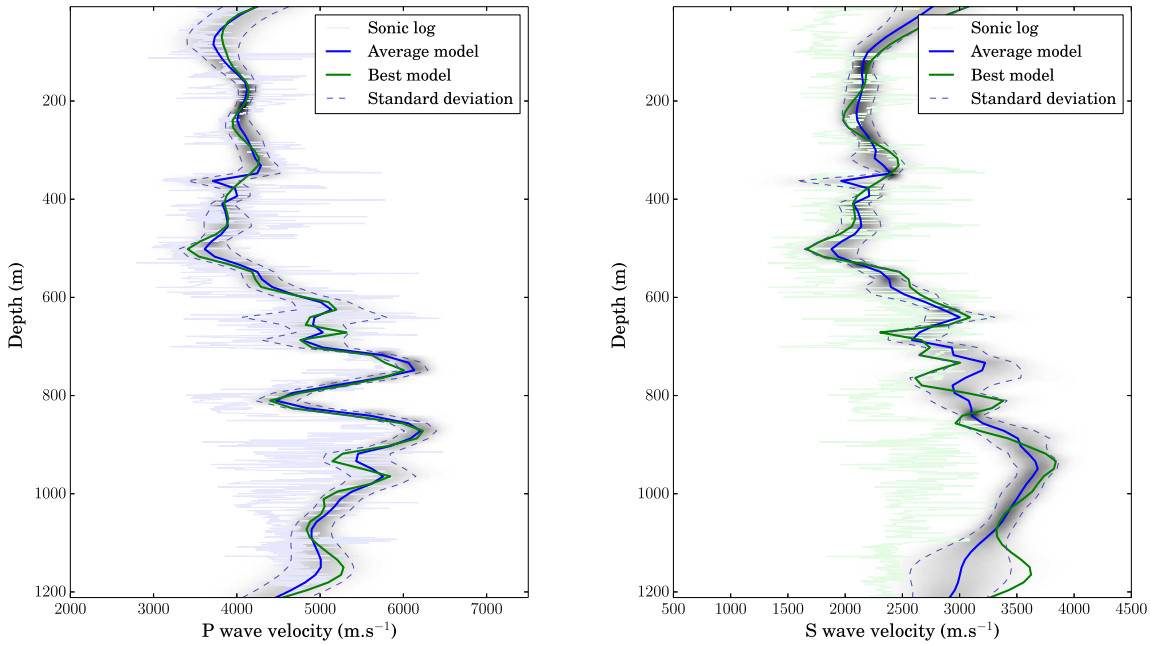

Figure 10. Left: results of the tomography for P-wave velocities. The figure shows the average model (blue) and *a posteriori* standard deviation (dashed blue)—calculated with the formulae (29) and (30)—together with the best model (green) and the measured sonic log (bright blue). The resulting density plots are also shown with darker colours representing higher probability. Right: same for S-wave velocities. The most valuable information obtained are the standard deviations which tell us about the knowledge on the area obtained by the inversion.

We also estimate the standard deviation (dashed blue lines in Fig. 10) from all the samples generated by the chains. This figure illustrates that between 200 and 750 m (in particular for S waves), the velocity model is well constrained and thus reliable. This is in agreement with the ray coverage linked to the source and receiver positions since both receiver arrays cover this depth range. We also represent average V_P/V_S and associated standard deviation in Fig. 11, this allows us to check the validity of our approach since the obtained ratios for the average model are in an acceptable range, between about 1.5 and 2. Differences between the confidence intervals and the sonic logs between 750 and 1000 m are fairly notable. This discrepancy seems higher for the S velocities. A very plausible explanation in this acquisition context could be the presence of mycolour dispersive and/or very strong anisotropic layers not accounted for in our isotropic eikonal solver.

We finally compare the residuals obtained with the reference calibrated velocity model (dark curves in Fig. 5, right) and with the new average model (blue curves in Fig. 10). Black crosses in Fig. 12 represent residuals at the receivers of the first antenna (at $Y = -200$ m), red crosses at the receivers of the second antenna (at $Y = 400$ m) and the 15 shots are separated by the vertical dashed lines. For this reference velocity model, most of the residuals are smaller than the standard deviation of the picking uncertainty (0.0025 s for P waves and 0.005 s for S waves). However, the residuals are not at random for the mycolour last five shots since they are distributed with almost all the positive for the first antenna and almost all the negative for the second antenna. This particular distribution is confirmed by the P (Fig. 14) and S (Fig. 15) residual histograms sorted by antenna and by shot line (upper figures). This specific distribution is not retrieved with the average model based on a wavelet parametrization since the P and S residuals for the last five shots are centred on zero for both antenna (Figs 13–15). The best model gives similar residuals as those obtained with the average model with a good distribution and most of the residuals smaller than the standard deviations of the picking uncertainties. This comparison illustrates the gain in accuracy provided by the wavelet-based parametrization compared to the layer-based parametrization with much better residual distribution. Moreover, the classical parametrization with layers is dependent of the operator who has to determine an initial velocity model from the sonic logs. With the wavelet parametrization, no operator is involved and the parametrization is only driven by the sonic log data.

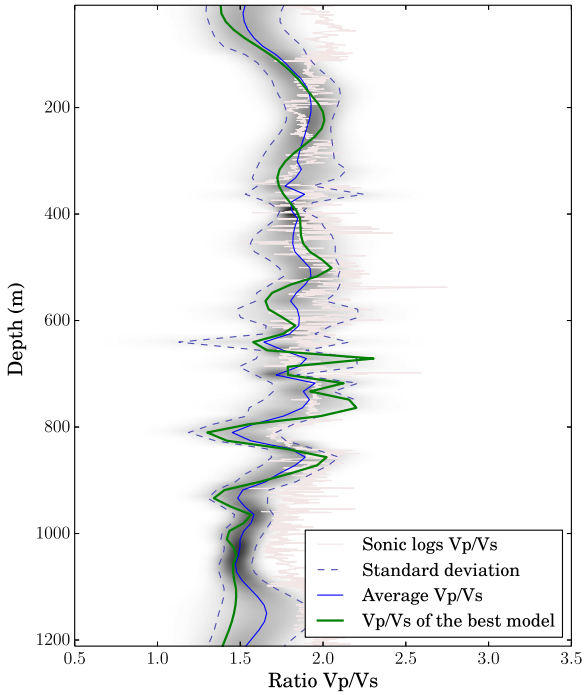

Figure 11. In green, the ratio $V_P(z)/V_S(z)$ for the best model and in blue, the average $V_P(z)/V_S(z)$. The standard deviation is drawn as two dashed blue lines and the ratio $V^P_{\log}(z)/V^S_{\log}(z)$ for the sonic logs is drawn in bright red. Darker colours of the density plot represent higher probability. The obtained ratios for the average model are in an acceptable range, between about 1.5 and 2.

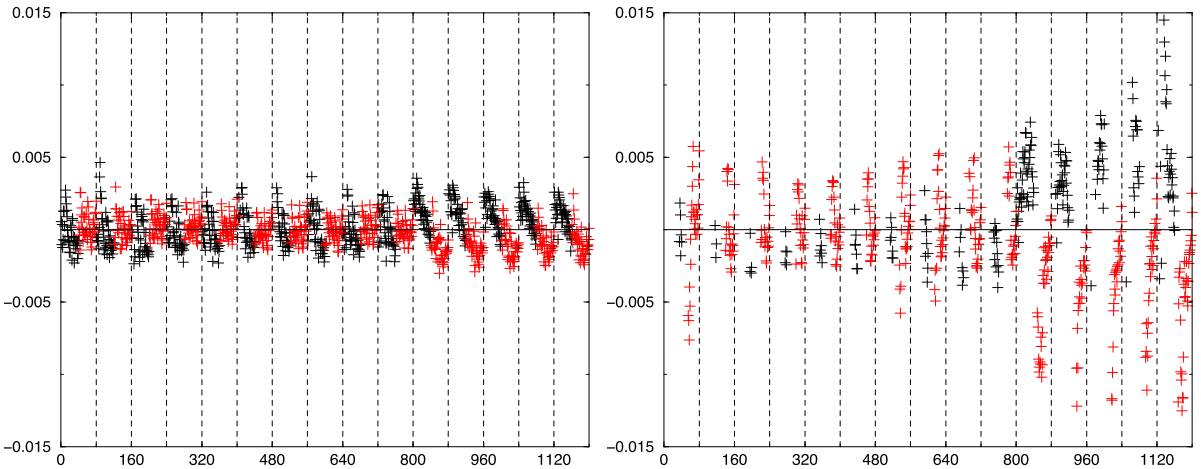

Figure 12. Left: *P*-wave arrival time residuals for the reference calibrated velocity model of Fig. 5 (right, dark blue curve). The 15 perforation shots are separated by vertical dashed lines. Black crosses represent residuals for the first receiver antenna and red crosses for the second receiver antenna. Right: same for *S*-wave arrival times. Residuals are not at random for the last five shots since they are almost all positive (respectively, negative) for the first (respectively, second) antenna.

This application of our new efficient Bayesian tomography algorithm to real data with an adaptive model parametrization based on wavelet coefficients is very convincing. Indeed, this first attempt gives, with only 30 parameters, elaborated final *P* and *S* velocity models with reliable associated uncertainty estimations indicating regions where the velocities are well constrained and thus reliable and also the regions where the velocities are poorly constrained.

4 CONCLUSIONS

In this paper, we have described and applied a still relatively unknown algorithm for Bayesian inversion. The main idea is to sample the *a posteriori* distribution using several interacting Markov chains evolving at different scales. The exchanges between the chains allow a precise sampling of the high probability zones of the model space while avoiding the chains becoming stuck in a local probability maxima. The algorithm has first been tested on a synthetic multimodal 2-D distribution where it has shown its robustness and efficiency for sampling compared to an SA approach. No burn-in period was required to be compared to more than 1000 iterations needed by SA to converge. It

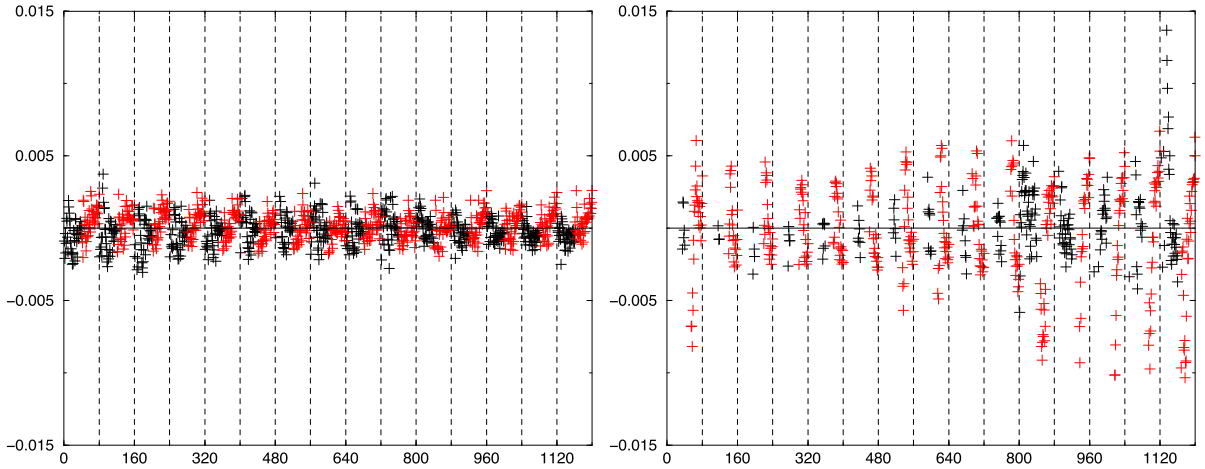

Figure 13. Residuals for the new average model (blue curve in Fig. 10). Information is plotted in the same way as Fig. 12. Good distribution of residuals that are centred on 0 for the last five shots.

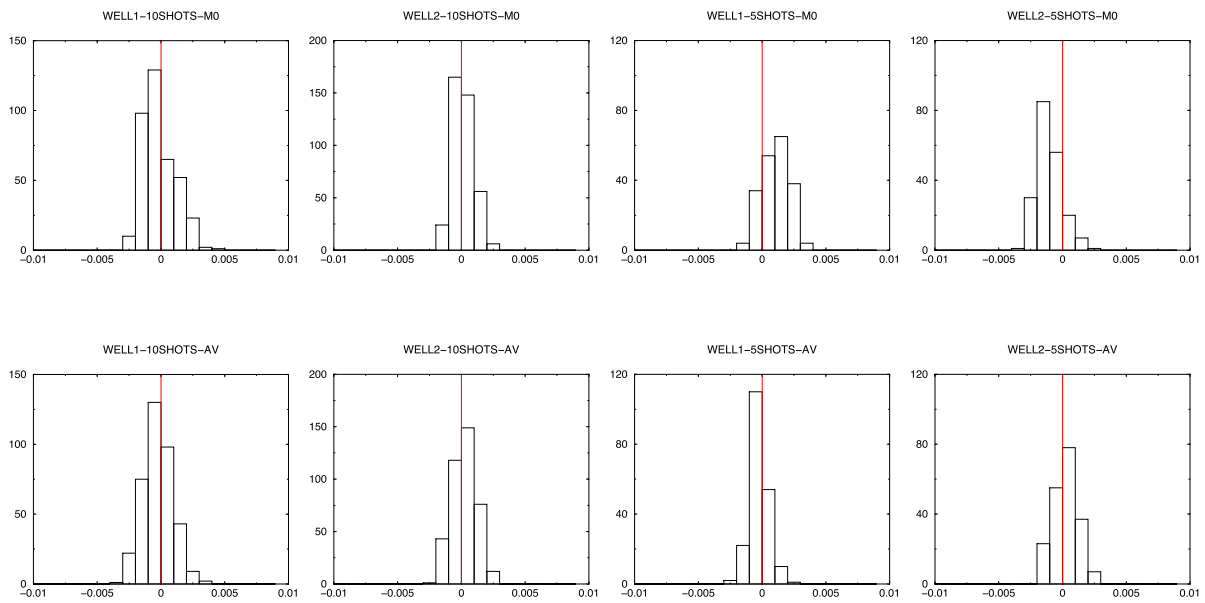

Figure 14. Top figures: histograms of the *P*-wave arrival time residuals for the reference calibrated velocity model of Fig. 5 (right, dark blue curve). From left to right: histogram for the 10 shots (at $Y = 100$ m) recorded at the first receiver antenna (at $Y = -200$ m), for the 10 shots (at $Y = 100$ m) recorded at the second receiver antenna (at $Y = 400$ m), for the five shots (at $Y = 400$ m) recorded at the first receiver antenna (at $Y = -200$ m) and for the five shots (at $Y = 400$ m) recorded at the second receiver antenna (at $Y = 400$ m). Bottom: same for the new average model (blue curve in Fig. 10).

has then been implemented for a 3-D seismic first arrival traveltime tomography on a real data example in an efficient way. Agostinetti *et al.* (2015) have recently presented a 3-D probabilistic local earthquake tomography with a Voronoi cell parametrization. They report very long computation times with several independent Markov chains. We could expect a great decrease in running time by using interacting instead of independent MCMC. Moreover, in the examples presented in this paper, only the computation of the forward problem has been performed on several processors. All the chains have run together on a single CPU and the algorithm already gave good results in a very efficient way. The evolution of each chain could also be parallelized on a CPU cluster, enhancing even more its performances. Communications between processors would be limited since only one energy value has to be sent by each processor at each iteration.

On the real-data example typical of hydraulic fracturing context, instead of using a geometrical parametrization with a layered velocity model built from the sonic logs, we have developed an adaptive wavelet-based model parametrization. This allowed us to reduce the dimension of the problem while including properly on the inversion the *a priori* information provided by sonic logs, without involving any operator. Our stochastic tomography of perforation shots provided reliable estimates of the uncertainties. This is important, in particular in the microseismic context where the final velocity model is further used to locate seismic events. With a standard linearized inversion method or global optimization approach, the errors on the resulting velocity model cannot be properly taken into account in the seismic event location. On the contrary, the samples of velocity model provided by our stochastic approach could be used to propagate velocity model uncertainties to the seismic event location uncertainties (Gesret *et al.* 2015). The 1-D velocity model assumption seems valid for this case study but for more complex media, such as generally faced in seismic refraction, the parametrization methodology should be extended using 2-D or

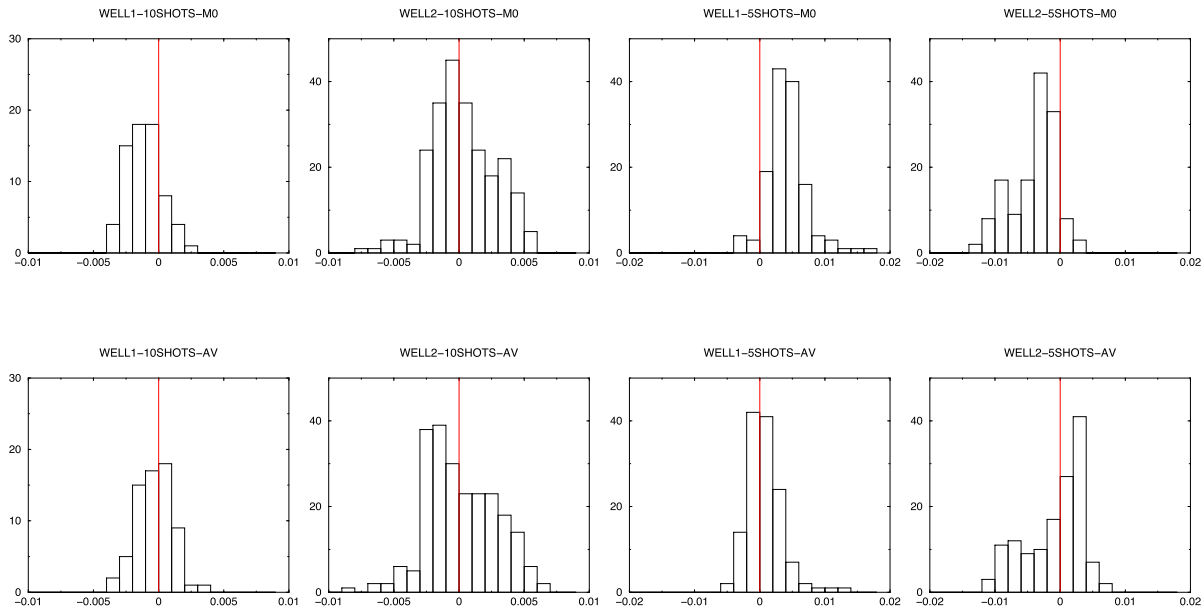

Figure 15. Histograms of the *S*-wave arrival time residuals. Information is plotted in the same way as Fig. 14.

3-D wavelet bases. We noted that anisotropy could explain the discrepancy between well logs and tomography results below 750 m, it would thus be interesting to do a future inversion including anisotropic parameters.

In this paper, the number of wavelet coefficients has been fixed. Future development should be made on the algorithm to allow transdimensional inversions such as proposed by Malinverno (2002) or Bodin *et al.* (2012) with our adaptive wavelet-based parametrization. For example, the reversible jump algorithm of Green (1995) could be adapted to multichain sampling. The number of wavelet coefficients to be kept would hence become part of the inversion, leading to a resolution adapted to the observed data. The algorithm would then adapt to the complexity of the medium and become an even more efficient approach to tomography.

Our software package is collaborative and available open-source at: https://github.com/bottero/IMCMCrun, it includes all the tools necessary to reproduce the results presented in this paper.

ACKNOWLEDGEMENTS

We are grateful to N. Desassis and F. Ors (Mines ParisTech, Centre de Géosciences, Fontainebleau, France) for fruitful discussions. The internship of AB has been made possible by IPGP and ENS Cachan, France. We also thank Michael Afanasiev and an anonymous reviewer for their useful comments that improved the manuscript.

REFERENCES

Agostinetti, N.P., Giacomuzzi, G. & Malinverno, A., 2015. Local three-dimensional earthquake tomography by trans-dimensional Monte Carlo sampling, *Geophys. J. Int.,* **201**(3), 1598–1617.

Andrieu, C., Jasra, A., Doucet, A. & Del Moral, P., 2011. On nonlinear Markov Chain Monte Carlo, *Bernoulli,* **17**(3), 987–1014.

Bardainne, T. & Gaucher, E., 2010. Constrained tomography of realistic velocity models in microseismic monitoring using calibration shots, *Geophys. Prospect.,* **58**(5), 739–753.

Bayes, M. & Price, M., 1763. An essay towards solving a problem in the doctrine of chances. By the late rev. Mr. Bayes, FRS communicated by Mr. Price, in a letter to John Canton, AMFRS, *Phil. Trans.,* **53,** 370–418.

Bennett, N.N. & Malinverno, A., 2005. Fast model updates using wavelets, *Multiscale Model. Simul.,* **3**(1), 106–130.

Bodin, T. & Sambridge, M., 2009. Seismic tomography with the reversible jump algorithm, *Geophys. J. Int.,* **178**(3), 1411–1436.

Bodin, T., Sambridge, M., Rawlinson, N. & Arroucau, P., 2012. Transdimensional tomography with unknown data noise, *Geophys. J. Int.,* **189**(3), 1536–1556.

Brooks, S.P. & Roberts, G.O., 1998. Convergence assessment techniques for Markov Chain Monte Carlo, *Stat. Comput.,* **8**(4), 319–335.

Burrus, C.S., Gopinath, R.A. & Guo, H., 1997. *Introduction to Wavelets and Wavelet Transforms: A Primer,* Prentice Hall, 268 pp.

Chiao, L.-Y. & Kuo, B.-Y., 2001. Multiscale seismic tomography, *Geophys. J. Int.,* **145,** 517–527.

Cowles, M.K. & Carlin, B.P., 1996. Markov Chain Monte Carlo convergence diagnostics: a comparative review, *J. Am. Stat. Assoc.,* **91**(434), 883–904.

Debski, W., 2010. Seismic tomography by Monte Carlo sampling, *Pure appl. Geophys.,* **167**(1–2), 131–152.

Earl, D.J. & Deem, M.W., 2005. Parallel tempering: theory, applications, and new perspectives, *Phys. Chem. Chem. Phys.,* **7**(23), 3910–3916.

Eisner, L., Duncan, P.M., Heigl, W.M. & Keller, W.R., 2009. Uncertainties in passive seismic monitoring, *Leading Edge,* **28**(6), 648–655.

Gesret, A., Desassis, N., Noble, M., Romary, T. & Maisons, C., 2015. Propagation of the velocity model uncertainties to the seismic event location, *Geophys. J. Int.,* **200**(1), 52–66.

Geyer, C.J., 1991. Markov chain Monte Carlo maximum likelihood, in *Computer Science and Statistics: Proceedings of 23rd Symposium on the Interface,* pp. 156–163, ed. Keramigas, E.M., Interface Foundation, Fairfax Station, VA.

Green, P.J., 1995. Reversible jump Markov Chain Monte Carlo computation and Bayesian model determination, *Biometrika,* **82**(4), 711–732.

Hall, C., Ji, W. & Blaisten-Barojas, E., 2014. The metropolis Monte Carlo method with cuda enabled graphic processing units, *J. Comput. Phys.,* **258,** 871–879.

Hartzell, S. & Langer, C., 1993. Importance of model parameterization in finite fault inversions: application to the 1974 Mw 8.0 peru earthquake, *J. geophys. Res.,* **98**(B12), 22 123–22 134.

Hawkins, R. & Sambridge, M., 2015. Geophysical imaging using trans-dimensional trees, *Geophys. J. Int.,* **203**(2), 972–1000.

Hoeting, J.A., Madigan, D., Raftery, A.E. & Volinsky, C.T., 1999. Bayesian model averaging: a tutorial, *Stat. Sci.,* **14**(4), 382–417.

Holland, J.H., 1975. *Adaptation in Natural and Artificial System: An Introduction with Application to Biology, Control and Artificial Intelligence,* University of Michigan Press.

Iba, Y., 2001. Extended ensemble Monte Carlo, *Int. J. Mod. Phys. C,* **12**(05), 623–656.

Jansen, M., 2012. *Noise Reduction by Wavelet Thresholding,* Vol. 161, Springer Science & Business Media.

Kirkpatrick, S., Gelatt, C.D. & Vecchi, M.P., 1983. Optimization by simulated annealing, *Science,* **220**(4598), 671–680.

Kitanidis, P.K., 1995. Quasi-linear geostatistical theory for inversing, *Water Resour. Res.,* **31**(10), 2411–2419.

Köhn, D., De Nil, D., Kurzmann, A., Przebindowska, A. & Bohlen, T., 2012. On the influence of model parametrization in elastic full waveform tomography, *Geophys. J. Int.,* **191**(1), 325–345.

Koren, Z., Mosegaard, K., Landa, E., Thore, P. & Tarantola, A., 1991. Monte Carlo estimation and resolution analysis of seismic background velocities, *J. geophys. Res.,* **96**(B12), 20 289–20 299.

Kou, S., Zhou, Q. & Wong, W.H., 2006. Discussion paper equi-energy sampler with applications in statistical inference and statistical mechanics, *Ann. Stat.,* **34**(4), 1581–1619.

Loris, I., Nolet, G., Daubechies, I. & Dahlen, F., 2007. Tomographic inversion using ℓ_1-norm regularization of wavelet coefficients, *Geophys. J. Int.,* **170**(1), 359–370.

MacEachern, S.N. & Berliner, L.M., 1994. Subsampling the gibbs sampler, *Am. Stat.,* **48**(3), 188–190.

Malinverno, A., 2002. Parsimonious Bayesian Markov Chain Monte Carlo inversion in a nonlinear geophysical problem, *Geophys. J. Int.,* **151**(3), 675–688.

Mallat, S., 1999. *A Wavelet Tour of Signal Processing,* Academic Press.

Maxwell, S., 2010. Microseismic: growth born from success, *Leading Edge,* **29**(3), 338–343.

Menke, W., 2012. *Geophysical Data Analysis: Discrete Inverse Theory,* Academic Press.

Metropolis, N., Rosenbluth, A.W., Rosenbluth, M.N., Teller, A.H. & Teller, E., 1953. Equation of state calculations by fast computing machines, *J. Chem. Phys.,* **21**(6), 1087–1092.

Meyn, S.P. & Tweedie, R.L., 2012. *Markov Chains and Stochastic Stability,* Springer Science & Business Media.

Mosegaard, K. & Sambridge, M., 2002. Monte Carlo analysis of inverse problems, *Inverse Probl.,* **18**(3), R29–R54.

Mosegaard, K. & Tarantola, A., 1995. Monte Carlo sampling of solutions to inverse problems, *J. geophys. Res.,* **100**(B7), 12 431–12 447.

Mühlenbein, H., Schomisch, M. & Born, J., 1991. The parallel genetic algorithm as function optimizer, *Parallel Comput.,* **17**(6), 619–632.

Noble, M., Gesret, A. & Belayouni, N., 2014. Accurate 3-d finite difference computation of traveltimes in strongly heterogeneous media, *Geophys. J. Int.,* **199**(3), 1572–1585.

Oliver, D.S., 1996. On conditional simulation to inaccurate data, *Math. Geol.,* **28**(6), 811–817.

Rawlinson, N., Pozgay, S. & Fishwick, S., 2010. Seismic tomography: a window into deep earth, *Phys. Earth Planet. Inter.,* **178**(3), 101–135.

Rawlinson, N., Fichtner, A., Sambridge, M. & Young, M.K., 2014. Chapter one—seismic tomography and the assessment of uncertainty, *Adv. Geophys.,* **55,** 1–76.

Robert, C. & Casella, G., 2013. *Monte Carlo Statistical Methods,* Springer Science & Business Media.

Romary, T., 2009. Integrating production data under uncertainty by parallel interacting Markov Chains on a reduced dimensional space, *Comput. Geosci.,* **13**(1), 103–122.

Romary, T., 2010a. Bayesian inversion by parallel interacting Markov Chains, *Inverse Probl. Sci. Eng.,* **18**(1), 111–130.

Romary, T., 2010b. History matching of approximated lithofacies models under uncertainty, *Comput. Geosci.,* **14**(2), 343–355.

Rosenthal, J.S., 2000. Parallel computing and monte carlo algorithms, *Far East J. Theor. Stat.,* **4**(2), 207–236.

Salamon, P., Sibani, P. & Frost, R., 2002. *Facts, Conjectures, and Improvements for Simulated Annealing,* SIAM.

Sambridge, M., 1999a. Geophysical inversion with a neighbourhood algorithm—I. Searching a parameter space, *Geophys. J. Int.,* **138**(2), 479–494.

Sambridge, M., 1999b. Geophysical inversion with a neighbourhood algorithm—II. Appraising the ensemble, *Geophys. J. Int.,* **138**(3), 727–746.

Sambridge, M., 2014. A parallel tempering algorithm for probabilistic sampling and multimodal optimization, *Geophys. J. Int.,* **196,** 357–374.

Sambridge, M., Gallagher, K., Jackson, A. & Rickwood, P., 2006. Trans-dimensional inverse problems, model comparison and the evidence, *Geophys. J. Int.,* **167**(2), 528–542.

Sen, M.K. & Stoffa, P.L., 2013. *Global Optimization Methods in Geophysical Inversion,* Cambridge Univ. Press.

Sheriff, R.E. & Geldart, L.P., 1995. *Exploration Seismology,* Cambridge Univ. Press.

Silverman, B.W., 1986. *Density Estimation for Statistics and Data Analysis,* Vol. 26, CRC press.

Simons, F.J. *et al.*, 2011. Solving or resolving global tomographic models with spherical wavelets, and the scale and sparsity of seismic heterogeneity, *Geophys. J. Int.,* **187**(2), 969–988.

Tarantola, A., 2005. *Inverse Problem Theory and Methods for Model Parameter Estimation,* SIAM, Philadelphia, Pennsylvania, USA.

Tarantola, A. & Valette, B., 1982. Generalized nonlinear inverse problems solved using the least squares criterion, *Rev. Geophys. Space Phys.,* **20**(2), 219–232.

Tikhotsky, S. & Achauer, U., 2008. Inversion of controlled-source seismic tomography and gravity data with the self-adaptive wavelet parametrization of velocities and interfaces, *Geophys. J. Int.,* **172**(2), 619–630.

Torn, A. & Zilinskas, A., 1989. *Global Optimization,* Springer-Verlag.

Weber, Z., 2000. Seismic traveltime tomography: a simulated annealing approach, *Phys. Earth Planet. Inter.,* **119**(1), 149–159.
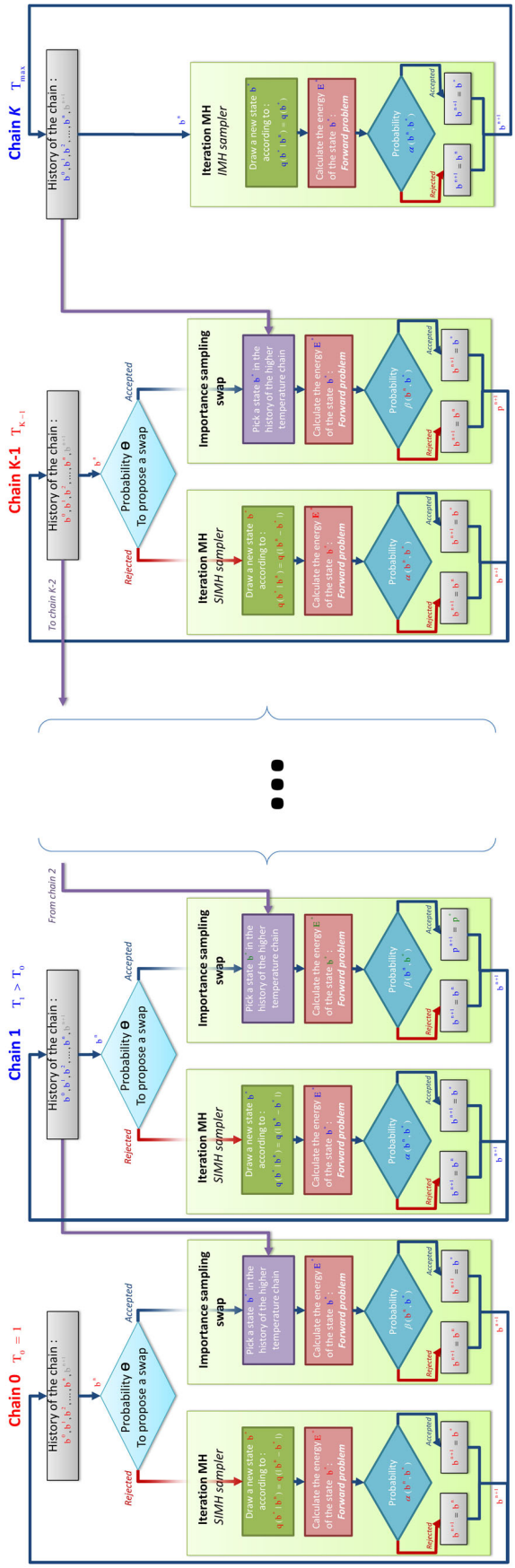
APPENDIX: FLOWCHART OF THE INTERACTING MCMC ALGORITHM PRESENTED